Orbital condensates in higher Bloch bands of an optical boron-nitride lattice

DISSERTATION

zur Erlangung des Doktorgrades
an der Fakultät für Mathematik, Informatik und Naturwissenschaften
Fachbereich Physik
der Universität Hamburg

vorgelegt von
ALEXANDER ILIN
HAMBURG
2022

Gutachter/innen der Dissertation:	Prof. Dr. Klaus Sengstock
	Prof. Dr. Henning Moritz
Zusammensetzung der Prüfungskommission:	Prof. Dr. Klaus Sengstock
	Prof. Dr. Henning Moritz
	Prof. Dr. Ludwig Mathey
	Prof. Dr. Markus Drescher
	Prof. Dr. Andreas Hemmerich
Vorsitzender der Prüfungskommission:	Prof. Dr. Ludwig Mathey
Datum der Disputation:	07.12.2022
Vorsitzender Promotionsausschuss Physik:	Prof. Dr. Wolfgang J. Parak
Leiter des Fachbereichs Physik:	Prof. Dr. Günter H. W. Sigl
Dekan der Fakultät MIN:	Prof. Dr. Heinrich Graener

Eidesstattliche Versicherung:

Hiermit versichere ich an Eides statt, die vorliegende Dissertationsschrift selbst verfasst und keine anderen als die angegebenen Hilfsmittel und Quellen benutzt zu haben.

Hamburg, 4. Juli 2022

Alexander Ilin

To N.M.H.

Abstract

Ultracold atoms in higher lattice orbitals give new impetus to the established field of quantum simulation of solids by extending the class of lattice Hamiltonians that can be modeled. At the same time, they offer unique possibilities to realize and study exotic quantum many-body states that have no analogue in conventional condensed matter systems and that originate from the interplay of orbital degrees of freedom, atom-atom interactions, and lattice geometry.

This thesis reports on the investigation and creation of Bose-Einstein condensates in higher Bloch bands of a two-dimensional optical boron-nitride lattice. A central result is the realization of an unconventional condensate in the second band that breaks time-reversal symmetry and provides evidence for the emergence of a chiral superfluid order. In particular, experiments presented here make use of rapid quenches of the sublattice energy offset to accomplish a Landau-Zener type transfer of an initially incoherent bosonic ensemble from the lowest band to a higher target band. For appropriate quench parameters, the subsequent relaxation dynamics exhibits a fast build-up of coherence and long-range order in the second and fourth band, signaling the system's evolution to a transient orbital condensate. Specifically, condensation in the second band occurs at the two degenerate Dirac points, where corresponding Bloch orbitals feature rectified phase vortices that support a globally finite angular momentum with opposite orientation. For the case of a single-mode condensate, numerical calculations show that the mean-field interaction energy is minimized by condensation in a single Dirac point. Hence, the formation of chiral condensates should be favored. Initial evidence of a corresponding symmetry breaking in the momentum distribution has been experimentally observed. Several aspects of condensate formation and dissolution in higher bands are discussed, including relevant processes for intraband and interband relaxation. The results make essential contributions to quantum engineering of unconventional condensates and superfluid states in higher Bloch bands.

Furthermore, this thesis reports on time-resolved measurements of the anomalous velocity for condensates in an accelerated optical lattice. The value of the Berry curvature along the forced trajectory in reciprocal space can be precisely inferred from the observed Hall response in momentum space. For condensates in the second band, geometric pumping and a bosonic counterpart of the valley Hall effect have been realized. The findings provide essential insights into semiclassical wave-packet dynamics beyond Bloch oscillations and elucidate the coherent interference mechanism that underlies the anomalous velocity.

Zusammenfassung

Ultrakalte Atome in höheren Gitterorbitalen geben neue Anstöße im etablierten Feld der Quantensimulation von Festkörpern, indem sie die Klasse modellierbarer Hamilton-Operatoren beträchtlich erweitern. Gleichzeitig bieten sie einzigartige Möglichkeiten zur Realisierung exotischer Quanten-Vielteilchen-Zustände, für die es keine Entsprechung in konventionellen Systemen kondensierter Materie gibt. Solche Zustände entstehen durch das Zusammenspiel orbitaler Freiheitsgrade, zwischenatomarer Wechselwirkung und der Gittergeometrie.

Diese Arbeit widmet sich der Untersuchung und experimentellen Erzeugung von Bose-Einstein Kondensaten in höheren Blochbändern eines zweidimensionalen hexagonalen optischen Gitters. Ein zentrales Ergebnis ist die Realisierung eines exotischen Kondensats im zweiten Band, das die Zeitumkehrinvarianz bricht und auf das Vorliegen eines chiralen Ordnungsparameters hindeutet. Die hier vorgestellten Experimente beruhen auf der gezielten Anregung eines anfänglich inkohärenten Quantengases von Bosonen in höhere Blochbänder durch eine schnelle Transformation an beiden Untergittern. Bei geeigneter Wahl der Transformationsparameter zeigt das System im zweiten und vierten Blochband eine schnelle Ausbildung von Kohärenz und beschreibt eine Entwicklung zu einem metastabilen orbitalen Kondensat. Im zweiten Band findet die Kondensation insbesondere an den zwei entarteten Dirac-Punkten statt. Die Phase der zugehörigen Blochorbitale weist hier spezifische Vortexstrukturen auf, die einen global nicht verschwindenden Drehimpuls mit jeweils entgegengesetzter Orientierung hervorrufen. Numerische Berechnungen zeigen, dass für einen nicht fragmentierten Zustand die Wechselwirkungsenergie durch Kondensation in einem einzelnen Dirac-Punkt minimiert und folglich die Ausbildung eines chiralen Kondensats bevorzugt wird. Eine entsprechende Symmetriebrechung in der Impulsverteilung konnte experimentell beobachtet werden. Unterschiedliche Aspekte der Kondensation und des Zerfalls von Kondensaten in höheren Blochbändern, einschließlich relevanter Intraband- und Interband-Relaxationsprozesse, werden eingehend untersucht. Die Ergebnisse dieser Arbeit leisten einen wesentlichen Beitrag zum Verständnis und zur Erforschung exotischer Kondensate und suprafluider Phasen in höheren Blochbändern.

Darüber hinaus wurden im Rahmen dieser Arbeit zeitaufgelöste Messungen der anomalen Geschwindigkeit für Kondensate in einem beschleunigten optischen Gitter vorgenommen. Die Messungen erlauben eine präzise Bestimmung der Berry-Krümmung entlang der zurückgelegten Trajektorie im reziproken Raum. Für Kondensate im zweiten Band konnte ein geometrisches Pumpen sowie das bosonische Gegenstück zum Valley-Hall-Effekt realisiert werden. Die Ergebnisse liefern, über gewöhnliche Bloch-Oszillationen hinaus, wesentliche Einsichten in die semiklassische Dynamik von Wellenpaketen bei Anwesenheit einer nicht verschwindenden Berry-Krümmung und verdeutlichen auf eindrückliche Weise den der anomalen Geschwindigkeit zugrundeliegenden kohärenten Interferenzmechanismus.

Contents

Contents

1 Introduction

During the past 25 years, sparked by the first experimental realizations of Bose-Einstein condensates (BEC) [1–3] and quantum degenerate Fermi gases [4], experimental platforms of ultracold atoms have evolved into fantastic playgrounds for exploring intriguing phenomena in the field of quantum many-body physics. Seminal experiments comprise the observation and investigation of such paradigmatic and diverse concepts as the BEC-BCS (Bardeen-Cooper-Schrieffer) crossover [5–7], Efimov states [8–11], the Berezinskii–Kosterlitz–Thouless transition [12–16], quantum thermalization in isolated systems [17–20], and many-body localization [21–23], only to name a few. Results like these became possible only thanks to groundbreaking technological advancements in cooling, trapping, manipulating, and detecting neutral atoms, all of which are now subsumed under *quantum engineering*.

Today's state of the art quantum gas experiments offer an extraordinary degree of control and tunability of basically all system parameters. These encompass the number and type of atoms – be it bosons, fermions, or mixtures thereof – the energy landscape for the atomic internal and external degrees of freedom, and the sign and strength of interatomic interactions, which can be tuned via optical or magnetic Feshbach resonances [24]. In addition, advanced diagnostic tools in combination with a variety of spectroscopic probes [25] give access to a precise state and system characterization, even down to the single-atom level, as enabled by quantum gas microscopes [26] or more recently developed ion microscopes [27, 28]. Generally speaking, these attributes make ultracold atoms ideal model systems for implementing a large class of different Hamiltonians and for investigating the emergent phenomena and properties that come along with them. As such, ultracold atom systems are ideally suited for quantum simulation, much as initially envisioned by Feynman [29].

Typically, quantum simulation seeks to provide insights into some complex target quantum systems $\mathcal{S}_\mathrm{t}$, say an actual piece of solid-state material, by implementing and studying a particular model Hamiltonian $\hat{H}_\mathrm{mod}$ through a well controllable artificial quantum system $\mathcal{S}_\mathrm{a}$, where $\hat{H}_\mathrm{mod}$ is supposed to capture the essential physics of $\mathcal{S}_\mathrm{t}$ [30, 31]. In a broader sense, however, quantum simulation can be understood as exploring the physics of an artificial quantum system under some general model Hamiltonian of interest, which must not necessarily represent an abstraction of a Hamiltonian of another real system. From this viewpoint, quantum simulation with cold atoms provides unique opportunities to realize and explore truly novel quantum states of matter and phenomena unattainable in other settings. Investigating such novel quantum states of matter is a hallmark of modern physics and a central element of this work.

An important and well-established class of quantum simulators are atoms in optical lattices, i.e. atoms loaded into artificial crystals of light created from the interference of laser beams. These systems are particularly suited to mimic phenomena from condensed matter physics [32–34], where the atom replaces the role of the electron. Indeed,

atoms in optical lattices yield almost perfect implementations of the famous bosonic or fermionic Hubbard model, originally devised to study magnetism and electrical conduction in solids. In this context, an early success of quantum simulation was the first observation of a quantum phase transition from a superfluid to a Mott insulating state for bosons in a three-dimensional cubic lattice, following the seminal proposal by Jaksch et al. [35]. Meanwhile, such quantum phase transitions have been observed in a variety of lattice geometries and dimensions [36–39], even with fermionic atoms [40, 41] and molecules [42]. Other notable examples of quantum simulation along these lines are the observation of long-range antiferromagnetic ordering [43] or incommensurate magnetism [44] in doped Fermi-Hubbard systems. Such experiments directly probe the rich phase diagram of the fermionic Hubbard model and may help unravel the origins of high-temperature superconductivity [45, 46].

A major limitation in the analogy between atoms in optical lattices and electrons in solids is that atoms are charge neutral and thus do not couple to electromagnetic fields as prescribed by minimal coupling. Consequently, many fascinating phenomena, especially those that rely on the electron coupling to magnetic fields via the Lorentz force – like the quantum Hall effect – cannot be directly simulated with optical lattices. In recent years, the concept of Floquet engineering [47] has significantly advanced the field of quantum simulation in this direction by enabling the creation of artificial gauge fields [48, 49], which can mimic the presence of magnetic fields and give rise to complex tunneling matrix elements. This in turn has set the stage, for example, for quantum simulation of frustrated magnetism [50, 51], the Hofstadter model [52–55], and the Haldane model [56]. Floquet engineering has also allowed exploring new exotic states of matter, such as anomalous Floquet topological states [57] or dissipative Floquet time crystals [58, 59]. Furthermore, by incorporating synthetic dimensions [60] encoded through the atomic internal degrees of freedom, Floquet engineering bears exciting possibilities for realizing and studying topological physics in higher dimensions, such as a four-dimensional quantum Hall effect [61, 62]. On top of that, optical flux lattices [63] promise to reach the regime of strongly correlated topological phases in the form of fractional Chern insulators [64], which are closely related to the fractional quantum Hall states.

Similar to Floquet engineering, atoms in higher bands add exciting new aspects to quantum simulation with optical lattices by providing access to orbital degrees of freedom, which are relevant to many phenomena in condensed matter systems [65]. In particular, as we detail further below, the presence of orbital degrees of freedom can result in a plethora of yet unobserved quantum states of matter [66]. Following the general spirit of quantum simulation, this work focuses on the experimental realization of unconventional superfluid states in higher Bloch bands and the investigation of geometric phase effects. Our findings rely on experiments with a bosonic quantum gas in an optical boron-nitride lattice. A central concept is the time-dependent manipulation of the energy landscape for the atomic external degrees of freedom, either by quenching the sublattice energy offset or by accelerating the lattice, both of which drive the quantum system out of equilibrium. In the following, we briefly introduce the main topics and results covered in this thesis.

Orbital condensates

The lowest energy eigenstates in higher Bloch bands are often degenerate and feature complex phase profiles or intricate nodal structures. These eigenstates define what is often subsumed under the general term of *orbital degrees of freedom*. As a result of orbital degrees of freedom, atoms loaded into higher Bloch bands can provide natural realizations of various types of extended Hubbard models [67], thereby significantly expanding the scope for quantum simulation of solid-state phenomena. In addition, they offer unique opportunities to realize and study exotic quantum many-body states that have no analogue in other systems.

For bosonic ensembles, orbital degrees of freedom can result in a plethora of unconventional superfluid states realized in the form of orbital condensates that exhibit spontaneous time-reversal symmetry breaking and are characterized by a complex order parameter beyond Feynman's no-node theorem [68]. Moreover, due to the rich interplay between orbital degrees of freedom and interactions, these complex order parameters can manifest in a variety of ways that may involve new exotic properties, such as quantum stripe ordering [69], antiferromagnetic orbital angular momentum ordering [70, 71], or intertwined superfluidity and density wave order [72]. Moreover, the associated superfluid states can host different kinds of topological excitations [73–75].

While there is already quite a large body of theoretical work devoted to exploring novel quantum states of matter in higher lattice orbitals [76], experimental research in this direction has so far mainly focused on weakly interacting bosonic ensembles in higher bands of a bipartite square lattice, leading to the seminal observation of long-lived chiral condensates that exhibit staggered orbital angular momentum ordering [77–79]. Recently, also quantum degenerate fermionic atoms have been successfully loaded into higher bands of a bipartite square lattice [80].

Within the scope of this thesis, we have realized and studied condensates in higher Bloch bands of an optical boron-nitride lattice, i.e. orbital condensates in a lattice with hexagonal symmetry. Here, a new kind of interaction-induced chiral superfluid is expected in the second band, exhibiting rectified phase currents that give rise to a finite global orbital angular momentum (see Figure 1.1). The realization of such an unconventional state of matter was one of the central goals of this thesis. To this end, we have established and characterized an efficient method for populating higher Bloch bands of a boron-nitride lattice that features a spin-dependency resulting from a non-vanishing vector light shift. A quench of the sublattice energy offset through a fast rotation of the external quantization field allows for a controlled Landau-Zener type transfer of atoms from the lowest into higher bands. The nonequilibrium states initialized in this way exhibit fascinating relaxation dynamics. For certain quench parameters, we observe the interaction-driven, transient evolution to an orbital condensate in the second and fourth band. More specifically, condensation in the second band occurs at the two degenerate Dirac points. Furthermore, this unconventional condensate shows clear signatures of time-reversal symmetry breaking, indicating the emergence of a chiral order. Our observations are consistent with the presence of a chiral single-mode condensate, which minimizes its mean-field interaction energy by condensing in a single Dirac point. In comparison, condensation in the fourth band occurs at zero quasimomentum, analogous to conventional superfluid states.
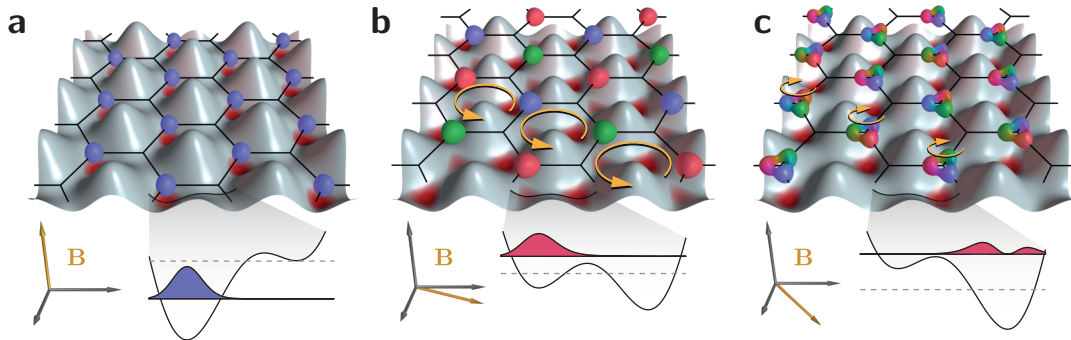
Fig. 1.1: Illustration of superfluid states in a boron-nitride lattice, where the sublattice energy offset can be tuned by a rotation of the quantization field **B**. Different colors represent the phase of the order parameter. **a** Ground state superfluid with real-valued order parameter. **b** Chiral superfluid in the second band with complex order parameter exhibiting phase windings around each lattice plaquette (circular arrows). **c** Chiral superfluid in the second band with complex order parameter exhibiting onsite phase vortices, leading to a finite onsite angular momentum.

At present, the lifetime of the chiral condensate is insufficient to establish pronounced chirality and impedes adiabatic transport to a regime where the formation of a macroscopically large orbital angular momentum can occur. Quite generally, the realization of long-lived orbital condensates is challenging since they correspond to metastable states that are prone to decay into the lowest Bloch band. In this thesis, we therefore discuss several fundamental aspects of condensate formation and dissolution in higher bands. By including relevant processes for intraband and interband relaxation, we identify central ingredients for creating long-lived orbital condensates. For chiral condensates in the second band of a bipartite square lattice, it has been shown [81] that the relaxation into the lowest band is inhibited by the destructive many-body interference of two principal decay channels, which leads to significantly increased lifetimes. We find evidence that a similar mechanism might be at work also for condensates in the second and fourth band of the boron-nitride lattice.

At the start of this project, to the best of our knowledge, no systematic experimental investigation of orbital condensates in a hexagonal boron-nitride lattice had been pursued. Meanwhile, two groups have reported on the realization of such condensates in a similar lattice geometry. Jin et al. [82] claim the observation of a Potts-nematic quantum phase in the second band, whose emergence is explained by renormalization effects. These results are not compatible with ours. In contrast, the recent observation of a chiral superfluid in the second band by Wang et al. [83] is in excellent agreement with our findings.

Anomalous velocity

In his famous paper from 1984 [84], Michael Berry considered the quantum mechanical evolution of an energy eigenstate in response to an adiabatic change of a generic external system parameter that follows a closed path in parameter space. He showed that, in addition to the usual dynamical phase, the eigenstate acquires a gauge-invariant phase,
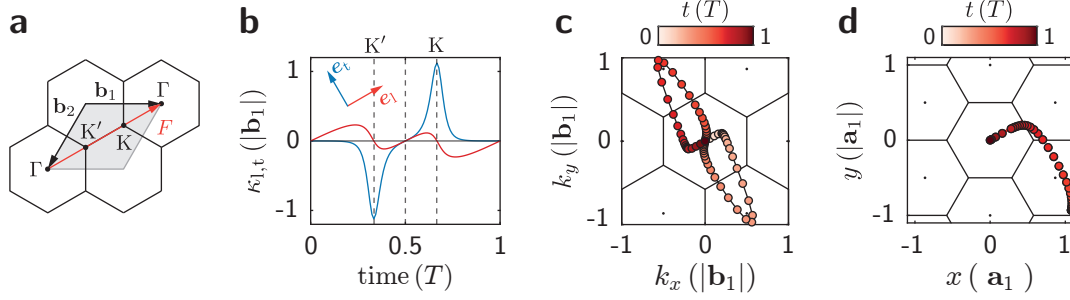
Fig. 1.2: Anomalous velocity induced by forcing in a hexagonal lattice. **a** Exemplary forcing trajectory in reciprocal space, passing Dirac points at K and K′. **b** Induced Bloch oscillations (red) with anomalous velocity (blue). The latter results from a non-vanishing Berry curvature at the Dirac points. **c** Evolution of the mean velocity in momentum space. **d** Associated real-space orbit. Time is in units of the period T of the induced motion.

today known as the Berry phase or adiabatic geometric phase, that does not depend upon the time it takes to complete the path but only on its geometry. Moreover, he showed that this phase can be written as the integral of another gauge-invariant quantity, the Berry curvature, over the surface bounded by the closed path. Just like magnetic fields, the Berry phase and Berry curvature have fundamental implications for the quantum mechanical motion of particles. In fact, as pointed out by Berry himself, the Berry phase is closely related to the celebrated Aharonov-Bohm phase for a charged particle that moves around a solenoid producing a magnetic field.

Owing to their generality, Berry's results attracted much attention across all areas of quantum physics and triggered an enormous amount of theoretical and experimental research on geometric phase effects in different systems. Thouless [85], for instance, gave an early demonstration of Berry phase effects in solids in his thought experiment of a slowly varying lattice potential, resulting in quantized particle transport for a one-dimensional band insulator. This so-called Thouless topological charge pump has now found its realization in experiments with ultracold bosonic and fermionic atoms [86, 87]. Another prime example of Berry phase effects in crystalline solids is the anomalous velocity or anomalous Hall response, which lies at the heart of various non-quantized and quantized Hall effects [88].

The anomalous velocity is best illustrated in the framework of semiclassical wave-packet dynamics for a particle that is localized in reciprocal space and whose quasimomentum is changed by an external force (see Figure 1.2). Here, the resulting, time-dependent quasimomentum takes the role of the external system parameter in Berry's original formulation, and the Brillouin zone of the crystal lattice naturally defines the parameter space, forming a closed manifold that can exhibit regions of non-vanishing Berry curvature. Subtle considerations of the semiclassical equations of motion unveil that the particle acquires a velocity component transverse to the direction of the external force whenever the quasimomentum visits regions of nonzero Berry curvature [89, 90]. This anomalous velocity is an explicit manifestation of the geometric properties of Bloch states and can be directly related to the topological Chern number formulation of the quantum Hall effect [91].

Measuring the anomalous velocity in real solid-state materials is challenging as a di-

rect observation of electron wave-packet dynamics is usually impeded by scattering off lattice defects or blurred by other extrinsic, interfering effects. Ultracold atoms in optical lattices instead provide ideal platforms to investigate this phenomenon and related effects in the general spirit of quantum simulation. For example, measurements of in situ Hall deflections resulting from the anomalous velocity have successfully revealed the topological character of various engineered quantum states [54, 56, 57, 92]. However, while also the Berry phase [93], the Berry curvature [94], and extended concepts such as Wilson lines [95] have been precisely measured with atoms in optical lattices, no quantitative measurements of the anomalous velocity itself have been presented so far.

In the scope of this thesis, we have performed time-resolved measurements of the anomalous velocity for condensates in an accelerated optical boron-nitride lattice. In particular, for condensates prepared in a given band, we consider forcing along different trajectories in reciprocal space and examine the resulting momentum distributions obtained from conventional time-of-flight images. In the adiabatic limit, the Berry curvature along the forced trajectory can be precisely inferred from the observed Hall response, even though the corresponding real-space Hall deflections may amount to only a few nanometers. When adiabaticity breaks down, the anomalous Hall response becomes more intriguing and requires a generalization to a multiband setting. Using an orbital condensate in the second band, we have also realized a bosonic counterpart of the valley Hall effect [96, 97], where atoms in different valleys of the band experience a net anomalous transport into opposite directions. Our results provide essential insights into the coherent interference mechanism that underlies the anomalous velocity.

Structure of the thesis

For this thesis, we have adopted the following structure. For readers convenience, the corresponding abstracts are repeated at the beginning of each chapter.

- **Chapter 2** gives an overview of the experimental apparatus and the main experimental techniques used throughout this work to create, manipulate, and detect Rubidium-87 Bose-Einstein condensates. The order of presentation complies with the steps of the experimental sequence, starting with the state preparation that involves several lasers and magnetic fields for loading, cooling, and trapping atoms, through to state manipulation and detection of individual spin states. The focus is mainly on concrete experimental implementations of specific methods rather than the physical concepts behind them. The only exception we make in this regard is the detailed discussion of the interaction of neutral atoms with a non-resonant monochromatic light field, which is particularly relevant to this thesis.

- **Chapter 3** is dedicated to the formal description of ultracold bosonic atoms in optical lattices and its application to central experimental techniques. For this reason, I briefly review the Bloch formalism, established for the description of non-interacting particles in periodic potentials, and present exact numerical calculations of the eigenspace and eigenspectrum for our spin-dependent optical boron-nitride lattice. Particular emphasis is put on an accurate characterization

of higher Bloch orbitals and their physical properties, such as the intrinsic orbital angular momentum. Furthermore, we elaborate on the central experimental observables and probing methods used throughout this work. Based on this, I demonstrate how amplitude-modulation spectroscopy and Kapitza-Dirac diffraction can be used to calibrate the lattice depth and in situ orientation of the external quantization field, respectively.

- **Chapter 4** reports on the realization of condensates in higher Bloch orbitals of an optical boron-nitride lattice. We start with a general overview of the field of ultracold bosonic atoms in higher lattice orbitals and elucidate the primary goals and prospects of studying these systems. Following this, we examine the main method used in this work for transferring atoms into higher Bloch bands via quenches of the sublattice energy offset. Next, we present measurements that provide compelling evidence for the emergence of unconventional orbital condensates in the second and fourth band of the boron-nitride lattice. Specifically, for condensates in the second band, we analyze signatures of time-reversal symmetry breaking and find evidence for a chiral superfluid order. Next, by examining the condensation and relaxation dynamics, we identify relevant processes that lead to an eventual dissolution of orbital condensates in higher bands. Finally, additional transfer methods into higher Bloch bands are explored.

- **Chapter 5** reports on measurements of the anomalous velocity for bosonic atoms in an accelerated optical boron-nitride lattice. We start with a brief introduction to the Berry calculus and provide results of a numerical calculation of the Berry curvature. Based on this, we discuss the semiclassical equations of motion for Bloch states subject to a uniform force field and illustrate the resulting trajectories in momentum and real space for different types of forcing. Next, the experimental approach for inertial forcing via lattice acceleration is presented, and the transformation into the comoving frame is reviewed. Following this, we examine the coherent evolution of Bloch states in a moving lattice to first order in adiabatic perturbation theory and establish an explicit connection to experimentally observed momentum distributions after time-of-flight. Finally, we present measurements of the anomalous velocity for different forcing protocols and compare the results to numerical calculations.

2 Overview of the experimental setup

This chapter gives an overview of the experimental apparatus and the main experimental techniques used throughout this work to create, manipulate, and detect Rubidium-87 Bose-Einstein condensates. The order of presentation complies with the steps of the experimental sequence, starting with the state preparation that involves several lasers and magnetic fields for loading, cooling, and trapping atoms, through to state manipulation and detection of individual spin states. The focus is mainly on concrete experimental implementations of specific methods rather than the physical concepts behind them. The only exception we make in this regard is the detailed discussion of the interaction of neutral atoms with a non-resonant monochromatic light field, which is particularly relevant to this thesis.

Within the scope of this work, experiments were conducted at the *Spinor* project at the Institut of Laser Physics in the group of Klaus Sengstock. The experimental apparatus is a quantum gas machine that produces Rubidium-87 Bose-Einstein condensates (BECs) at a cycle time of 30 s to 40 s. Since the first creation of a Rubidium-87 BEC at the *Spinor* experiment by H. Schmaljohann [98] and M. Erhard [99], the experimental setup has undergone extensive modifications with numerous enhancements by the works of J. Kronjäger, C. Becker, P. Soltan-Panahi, J. Struck, M. Weinberg, and C. Ölschläger [100–105]. Recent technical developments have been advanced by J. Seeger [106] and T. Klafka [107], including the design and implementation of an active magnetic field stabilization and a new system for intensity and phase control of the lattice laser beams. Given the long timeline of *Spinor* history, we provide a detailed account of the current experimental sequence to produce, manipulate, and detect a Rubidium-87 BEC. Before doing so, however, I will quickly summarize the latest technical upgrades achieved in the course of this thesis.

2.1 Latest upgrades

Large parts of the latest experimental upgrades have been realized through teamwork by J. Seeger, T. Klafka, and the author under supervision of Juliette Simonet. Here, we provide a summary of those that are most relevant to this thesis. An in-depth discussion of specific technical aspects can be found in the PhD theses of J. Seeger [106] and T. Klafka [107].

At the beginning of this project, we replaced our depleted set of Rubidium-87 dispensers by a new set of two Rubidium-87 and two Potassium-39 dispensers. Regarding the close similarity of the optical properties between ^{87}Rb and ^{39}K, the upgrade towards Potassium is natural in the way that the existing setup is easily extended to support the generation of ^{39}K BECs without the need for an excessive redesign of the main

experimental unit and a large number of additional new laser sources. In principle, a single new laser source will suffice. The design and implementation of this system, however, is not part of this work and will be treated elsewhere. We merely conclude by noting that the accessibility of multiple magnetic Feshbach resonances for ^{39}K [108] with a resonance width of several gauss is a great benefit. Compared to the mostly narrow magnetic Feshbach resonances in ^{87}Rb [109], this allows for a very precise and flexible control of the interatomic scattering length over a wide range of parameters. The inclusion of this additional degree of freedom into existing experimental protocols will be the goal of future experiments. Apart form the replacement of the dispensers, which was the most invasive surgery, there were further upgrades that are notable as well.

T. Klafka and I have completely revised the laboratory computer infrastructure for the experimental control. The old set of laboratory computers that were still running on Microsoft Windows 7 have been replaced by a single high-performance Windows 10 computer. Simultaneously, the ancient LabVIEW virtual instrument (VI) for programming the experimental sequence was abandoned in favor of the latest VI group development from the *Femto* experiment. We have supplemented this VI with additional functionalities, such as the so-called *protocol generator* introduced by D. Vogel [110]. This now allows to run sequences with arbitrarily complex variations of parameters. On this occasion, we emphasize that the actual orchestration of the various digital and analog outputs for the experimental control is still accomplished by an ADwin Pro system[1] that offers a time step resolution of 10 μs. As part of the modernization we have also replaced our old detection camera pco.pixelfly qe by a pco.pixelfly USB that offers overall improved performance in terms of bit depth, readout noise, and readout speed. Correspondingly, a new VI for the camera control and image acquisition has been designed and implemented by the author into the experimental control environment. In the same way, the existing VI for our second detection camera Andor iKon-M 934 has been completely revised.

Further improvements include the reconstruction of the optical pathway taken by the detection beam for the exposure of the Andor camera. Originally, due to several constraints in the optical access to the science cell, a flipping mirror was used to promote the detection beam for absorption imaging, which caused apparent shot-to-shot fluctuations in the center of mass position of the BEC. Although these fluctuations, originating from the pointing instability of the detection beam, can be removed in principle via post-processing algorithms (cf. e.g. [111]), the latter do not always produce reliable results and it is generally advised to avoid their application in the first place. By reorganizing parts of the magneto-optical trap (MOT) setup, we were able to circumvent the flipping mirror for the detection beam, thus significantly improving the pointing stability and thereby obviating any needs for post-processing image data.

J. Seeger and T. Klafka made huge efforts in developing from scratch and implementing a new intensity and phase control system for our lattice beams, involving commercial high-speed servo controllers[2], digital drivers for the acousto-optic modulators (dAOM) [110, 112], newly developed fast photodiode buffers and voltage-controlled RF attenu-

---

[1] Jäger Messtechnik, processor module T10.
[2] New Focus LB1005.
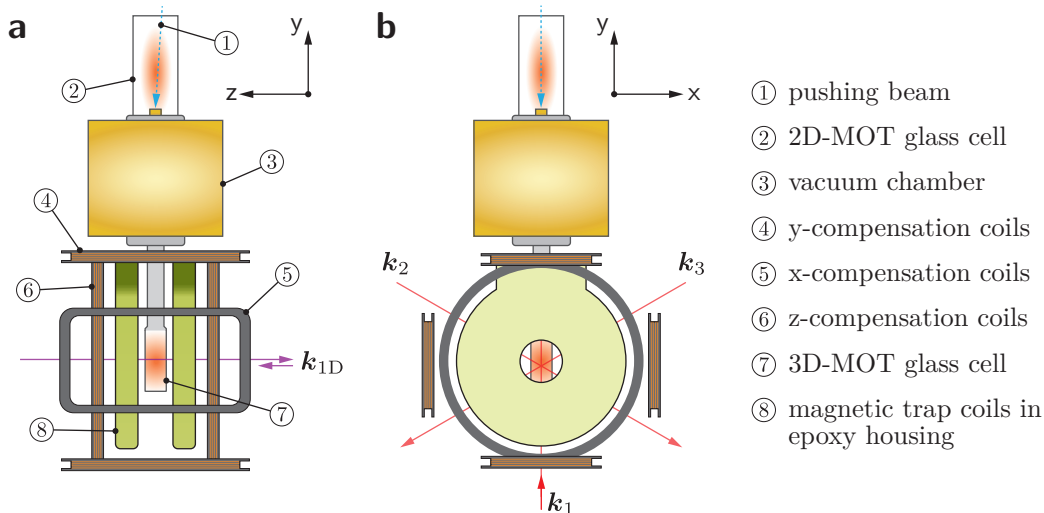
Fig. 2.1: Schematic overview of the main experimental unit consisting of an upper glass cell and a lower glass cell (science cell), hold together by a vacuum chamber with several connections and ports for gauges and pumps, which are omitted for clarity. **a** Side view corresponding to the detection field of view of the PCO camera, with wave vector k_{1D} for the 1D retro-reflected lattice. **b** Side view corresponding to the detection field of view of the Andor camera, with the three wave vectors k_1, k_2, k_3 for the 2D running-wave three-beam lattice.

ators (VVA) [106], and a new design for a phase detector [106]. These developments contributed to a significant improvement in intensity and phase noise suppression for our running-wave three-beam lattice. An important aspect in this regard was also the elimination of parasitic etalons in the optical paths for the intensity control, which caused spurious amplitude fluctuations among the different lattice beams.

Last but not least, T. Klafka and I have implemented a grey molasses cooling for Rubidium-87. The implementation will be discussed in more detail in the next section. We simply mention that, as a main result, we were able to reduce the cycle time of the experimental sequence by almost 10 s without loss in performance, corresponding to a speedup of nearly 25% as compared to former experimental protocols based on bright molasses cooling.

2.2 State preparation

For the experimental studies presented in this thesis we have worked with Rubidium-87 Bose-Einstein condensates. The preparation of the BEC takes place in the main experimental unit that is made of two glass cells joined by a vacuum chamber and coupled via a differential pumping stage [98, 99]. Figure 2.1 gives a rough schematic of this unit. To begin with, we create an atomic cloud of Rubidium-87 that is supplied from dispensers in the upper glass cell, maintaining a constant background pressure of 10^{-9} mbar. A small fraction of the cloud is captured and precooled by a two-dimensional magneto-optical trap (2D-MOT) that serves as a particle reservoir for loading the 3D-MOT in the lower glass cell (science cell) at a pressure of 10^{-11} mbar. The loading

procedure lasts about $10\,\mathrm{s}$ to $15\,\mathrm{s}$ and is accomplished by means of a near-resonant pushing beam that transfers the atoms from the 2D-MOT into the 3D-MOT. Once the 3D-MOT is loaded, subsequent cooling is provided by a grey molasses for a duration of $6\,\mathrm{ms}$. Afterwards, the atoms are optically pumped from the $\{|F = 2, m_F\rangle\}$ to the $\{|F = 1, m_F\rangle\}$ hyperfine manifold and transferred to a magnetic trap that is based on a hybrid *cloverleaf/4-dee* coil configuration [113]. Next, we perform RF-forced evaporative cooling for $10\,\mathrm{s}$ until the thermal atomic cloud reaches a temperature and density that is close to quantum degeneracy. For the last cooling step we employ a crossed optical dipole trap in which the final evaporation to a BEC is performed by linearly lowering the intensities of the corresponding laser beams. Eventually, we end up with a BEC that consists of typically 3×10^5 atoms.

2.2.1 Grey molasses cooling

In the course of this thesis, T. Klafka and I have implemented a grey molasses cooling for Rubidium-87 in our experimental cycle. The scheme is based on a Λ-enhanced grey molasses on the D_2 line, as reported by Rosi et al. [114]. However, instead of realizing the grey molasses via a cooler(repumper) on the open transition $F = 2(1) \rightarrow F' = 2$ between the ground state hyperfine level F and the excited state hyperfine level F', we employ for technical reasons the open transition $F = 2(1) \rightarrow F' = 1$.

The cooler light for the grey molasses in our case is derived from the same laser source that is used for cooling in the MOT, and the required phase-coherent repumper is generated from a sideband by means of a resonant electro-optic phase modulator[3] (PM). An additional acousto-optic modulator[4] (AOM) serves to shift the frequency of the cooler from being red-detuned with respect to $F' = 3$ during the MOT to being blue-detuned with respect to $F' = 1$ for the grey molasses. We stress that the AOM is placed in series to the PM and operated in a double-pass configuration such that we effectively end up using the same optical branch for the MOT-cooler and the grey molasses. A selective switching is then realized simply by simultaneously turning on or off the AOM and PM. As a technical detail, we remark that the 0th diffraction order from the AOM should be shuttered during the grey molasses to prevent the presence of undesired frequency components.

Using this scheme, we have achieved sub-Doppler cooling for ^{87}Rb with temperatures as low as $5.3(4)\,\mathrm{\mu K}$ [115]. What is more, the phase-space density increased by a factor of ten compared to the previous bright molasses. With that, we could afford to reduce the MOT loading time as well as the subsequent evaporation time in the magnetic trap to a minimum, leading to cycle times that are shorter by $10\,\mathrm{s}$ while maintaining the same temperature and atom number in the final BEC. For an exhaustive discussion of the parameter optimization for the grey molasses and further aspects of the experimental implementation we refer to the theses of R. Conrad, P. Groß, and T. Klafka [107, 115, 116]. An excellent recent treatment of the principles and simulations of Λ-enhanced grey molasses cooling can be found in the publications of Grier et al. [117] and Sievers et al. [118]. For an original perspective on grey molasses cooling we encourage the reader

---

[3]QUBIG PM-Rb_6.8.
[4]Crystal Technology AOMO 3200-121.

to consult the pioneering works by Dalibard and Cohen-Tannoudji [119], Grynberg and Courtois [120], Weidemüller et al. [121], Boiron et al. [122], and Esslinger et al. [123].

2.2.2 Magnetic fields and magnetic traps

All magnetic fields that are used for trapping and manipulating a BEC in our experiment are generated by the so-called magnetic trap coils and compensation coils. As it stands, in the current setup they have been implemented by C. Ölschläger during his PhD thesis [105].

Magnetic trap coils   The magnetic trap coils are made of two independent sets of winding patterns, referred to as Helmholtz coils (HC) and gradient coils (GC), that are arranged in a hybrid *cloverleaf/4-dee* configuration with the principal symmetry axis along the z-direction, as implied in Figure 2.2. The implemented design is attributed to R. Dinter [113] but goes back to the original works by M. Kottke [124]. Since the magnetic trap is operated at large currents, the coils are located in a sealed epoxy resin housing equipped with separate water circulation for cooling.

The HC coils in this setup are multipurpose coils that can work in two distinct modes to create either the anti-Helmholtz field required for the 3D-MOT or a Helmholtz field that is necessary for setting the offset bias field in the magnetic trap. In anti-Helmholtz mode (1) the resulting field at the center exhibits a radial gradient of $\partial_\rho B_\rho^{\mathrm{HC},1}/I = 0.5\,\mathrm{G\,cm^{-1}\,A^{-1}}$ [125]. Complementary, in Helmholtz mode (2) they produce a field along the axial direction $\boldsymbol{e}_z$ with a strength of $B_0^{\mathrm{HC},2}/I = 7.67\,\mathrm{G\,A^{-1}}$. Typically, the HC coils are operated at currents between $0\,\mathrm{A}$ to $40\,\mathrm{A}$ and are also frequently used to generate magnetic fields for a strong quantization axis along the z-direction.

The GC coils, on the other hand, are used for realizing a tight radial confinement in the magnetic trap and for Stern-Gerlach separation of the various Zeeman substates of a given hyperfine manifold $\{|F, m_F\rangle\}$. They are operated at a current of $110\,\mathrm{A}$ and produce a magnetic field configuration at the trap center with a radial gradient of approximately $\partial_\rho B_\rho^{\mathrm{GC}} \equiv B_\rho' = 168\,\mathrm{G\,cm^{-1}}$ and an axial curvature of $\partial_z^2 B_z^{\mathrm{GC}} \equiv B_z'' = 77\,\mathrm{G\,cm^{-2}}$. In combination with the offset bias $\mathbf{B}_0 = B_0 \boldsymbol{e}_z$ from the HC coils, this results in an Ioffe-Pritchard like trap potential [126] for which the geometry is controlled by varying the field magnitude B_0. Figure 2.2 illustrates the magnetic field lines in the center of our magnetic trap for two different trap geometries at a field magnitude of $B_0 = 192\,\mathrm{G}$ and $B_0 = 0.5\,\mathrm{G}$, respectively. For a strong offset bias, the field strength distribution is clearly isotropic over a large volume, allowing for an efficient transfer from the 3D-MOT into the magnetic trap. By contrast, for a weak offset bias the field configuration becomes highly anisotropic with a tight radial confinement, leading to high collision rates that are crucial for efficient RF-forced evaporative cooling in the magnetic trap.

Given the multipole expansion of the Ioffe-Pritchard field [127], one easily verifies that for a non-vanishing B_0 the total field strength $|\mathbf{B}|$ at the center of the trap can be
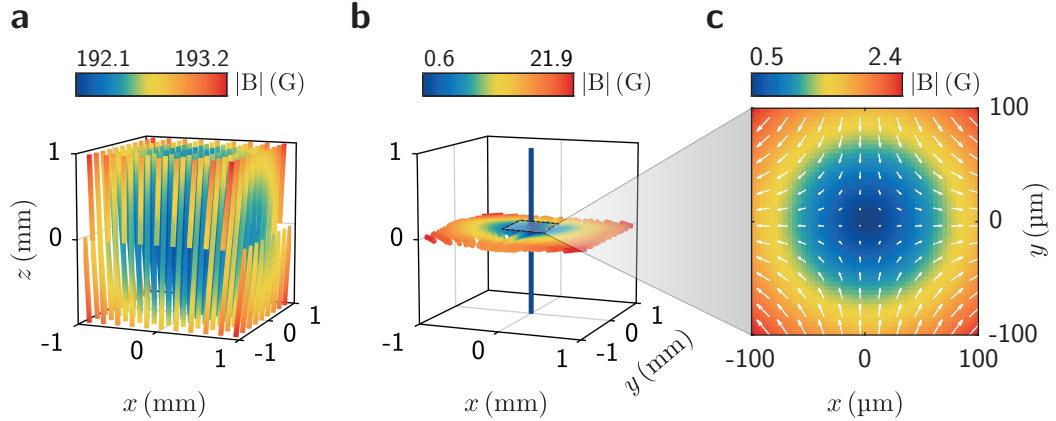
Fig. 2.2: Magnetic field configurations close to the center (origin) of the magnetic trap for a strong **a** and weak **b** offset bias B_0, as used in our experiment for the transfer from the MOT to the magnetic trap and RF-forced evaporative cooling, respectively. **a** For an offset bias of $B_0 = 192\,\text{G}$, the field lines emerging in the xy-plane (radial plane) at $z = 0$ in the vicinity of the trap center are nearly parallel to the z-axis (axial direction) and the field magnitude (color code) increases isotropically away from the center. **b** For an offset bias of $B_0 = 0.5\,\text{G}$, the field configuration becomes highly anisotropic, with field lines strongly bending inwards the radial plane for increasing values of $\rho = \sqrt{x^2 + y^2}$. Only in a close neighborhood to $\rho = 0$, field lines remain parallel to the z-axis over a macroscopic range, defining a unique quantization axis for a BEC. The field magnitude increases strongly along the radial coordinate, whereas it remains almost constant (on this scale) along the axial direction. **c** Field distribution over a microscopic region in the radial plane for $z = 0$ as shown in **b**, emphasizing the axial symmetry and parabolic confinement. White arrows represent the projection of the local magnetic field vector onto the radial plane, with the length being proportional to its magnitude.

written as

$$|\mathbf{B}(\rho, \phi, z = 0)| = |\mathrm{B}_0| + \frac{1}{2}\mathrm{B}''_\rho \rho^2 + \mathcal{O}(\rho^3), \tag{2.1a}$$

$$|\mathbf{B}(\rho = 0, \phi, z)| = |\mathrm{B}_0| + \frac{1}{2}\mathrm{B}''_z \mathrm{sgn}(\mathrm{B}_0)z^2 + \mathcal{O}(z^3), \tag{2.1b}$$

where the effective radial curvature is defined as

$$\mathrm{B}''_\rho \equiv \frac{\mathrm{B}'^2_\rho}{|\mathrm{B}_0|} - \frac{\mathrm{B}''_z}{2}\mathrm{sgn}(\mathrm{B}_0), \tag{2.2}$$

with values for B'_ρ and B''_z as stated above. We stress that only for $\mathrm{sgn}(\mathrm{B}_0) = +1$ it is possible to achieve a single extremum in the center of the trap, which is the configuration that we always work with. According to Wing [128], this necessarily corresponds to a local minimum in the field strength of the magnetic field. Assuming an adiabatic spin motion for a single Zeeman substate $|F, m_F\rangle$, the trapping potential resulting from the Zeeman energy $E_\mathrm{M} = -\hat{\boldsymbol{\mu}}_F \mathbf{B} \equiv \mu_\mathrm{B} g_F m_F |\mathbf{B}|$ is thus parabolic close to the center, with trap frequencies along radial and axial directions given by

$$\omega_\rho = \left(\frac{\mu_\mathrm{B} g_F m_F}{m}\mathrm{B}''_\rho\right)^{1/2}, \tag{2.3a}$$

$$\omega_z = \left(\frac{\mu_\mathrm{B} g_F m_F}{m}\mathrm{B}''_z\right)^{1/2}, \tag{2.3b}$$

respectively, where μ_B is the Bohr magneton, g_F is the hyperfine Landé g-factor, m_F denotes the magnetic quantum number of the total angular momentum F of the atom, and m is the mass of the atom. Note that for atoms in the Zeeman substate $|F, m_F\rangle$, the potential has a stable point at the origin for $\mathrm{sgn}(g_F)\,\mathrm{sgn}(m_F) = +1$ and an unstable point for $\mathrm{sgn}(g_F)\,\mathrm{sgn}(m_F) = -1$. In other words, only the low-field seeking states can be confined in the magnetic trap.

In a typical experimental cycle, precooled Rubidium-87 atoms derived from the MOT and the grey molasses are optically pumped to the hyperfine structure manifold $\{|F = 1, m_F\rangle\}$ of the ground state and immediately transferred into the magnetic trap by a sudden switch-on of the GC coils at a bias field of $\mathrm{B}_0 = 192\,\mathrm{G}$. The bias field is then gradually reduced within $1.5\,\mathrm{s}$ to a final value of $\mathrm{B}_0 \approx 0.5\,\mathrm{G}$, where RF-forced evaporative cooling is initiated by driving an RF signal through an antenna located in the vicinity of the science cell. Specifically, the evaporation is accomplished by exponentially sweeping the frequency of the output signal of an RF source[5] from $12\,\mathrm{MHz}$ to $1\,\mathrm{MHz}$ within $10\,\mathrm{s}$. Eventually, we obtain a fully polarized and nearly degenerate cloud of cold atoms in the Zeeman substate $|F = 1, m_F = -1\rangle$ at the center of the trap. The radial and axial magnetic trap frequencies at this stage amount to $\omega_\rho = 2\pi \cdot 214\,\mathrm{Hz}$ and $\omega_\rho = 2\pi \cdot 8\,\mathrm{Hz}$, respectively, and the cloud is sufficiently cold and dense for an efficient transfer into an optical dipole trap in which the final evaporation to a BEC is performed by lowering the intensities of the corresponding laser beams. Details of the transfer procedure are described in the next subsection 2.2.3. For further details on our

---

[5]Photonics Technologies Versatile Frequency Generator VFG-150.

magnetic trap design we refer to the theses of R. Dinter [113] and C. Ospelkaus [129]. A brief overview about magnetic traps in the context of cold atoms is readily provided in reference [130].

Compensation coils   As illustrated in Figure 2.1, the magnetic trap is surrounded by three additional pairs of coils with their principal symmetry axis oriented along the x-, y-, and z-direction, respectively. These coils are universal coils that are typically used for compensating external magnetic stray fields and for setting a well-defined quantization axis $\mathbf{Q}$ along an arbitrary direction in configuration space once the magnetic trap is turned off. The coils and the corresponding mounting cages were designed by A. Bick [125] during his PhD studies at the *Nano* project. Each pair of coils consists of three independent subcoils with different winding numbers that produce highly homogenous field distributions close to the geometric center when operated in Helmholtz mode. An overview of the respective field strengths is provided in reference [105].

In this work, we focus on two particular subsets $\{\mathbf{Q}_x, \mathbf{Q}_y, \mathbf{Q}_z\}$ and $\{\mathbf{C}_x, \mathbf{C}_y, \mathbf{C}_z\}$ of coils that are used to generate a well-defined quantization axis and to cancel external magnetic stray fields, respectively. Note that in this convention we identify each pair of coils by the corresponding magnetic field distribution, e.g. $\mathbf{Q}_x = Q_x \boldsymbol{e}_x$, that is created in Helmholtz mode. The individual pairs have the following characteristics:

$$Q_x/I = 0.546\,\mathrm{G\,A^{-1}}, \quad Q_y/I = 0.21\,\mathrm{G\,A^{-1}}, \quad Q_z/I = 0.66\,\mathrm{G\,A^{-1}} \tag{2.4}$$

for the quantization axis coils, and

$$C_x/I = 0.26\,\mathrm{G\,A^{-1}}, \quad C_y/I = 0.63\,\mathrm{G\,A^{-1}}, \quad C_z/I = 0.33\,\mathrm{G\,A^{-1}} \tag{2.5}$$

for the compensation coils.

We stress that setting a well-defined quantization axis with an exactly known field magnitude and direction requires an accurate cancelation of all in situ magnetic stray fields from laboratory equipment, the earth's magnetic field, and other external sources. Generally, stray fields can be classified into static and time-dependent ones. The compensation of static stray fields by an appropriate choice of $\{\mathbf{C}_x, \mathbf{C}_y, \mathbf{C}_z\}$ is straight forward in principle but requires a meticulous procedure. Active compensation of time-dependent magnetic fields, on the other hand, is more involved and necessitates real-time monitoring of AC magnetic field components with external field sensors. A thorough treatment of active magnetic field compensation for our experiment is provided, for example, by T. Klafka [107]. All experiments conducted in this work were performed without an active magnetic field compensation.

Finally, let us remark that it is possible to realize not only static quantization axes $\mathbf{Q} = Q_i \boldsymbol{e}_i$ along arbitrary directions, but also complex time-dependent versions $\mathbf{Q}(t) = Q_i(t)\boldsymbol{e}_i$ by driving the currents in the individual coils according to some prescribed protocol. For instance, a simple uniform rotation of the quantization axis within the xz-plane is accomplished by

$$\mathbf{Q}(t) = Q_0 \cos(\omega t + \phi)\boldsymbol{e}_x + Q_0 \sin(\omega t + \phi)\boldsymbol{e}_z, \tag{2.6}$$

where $Q_0 = I_x(Q_x/I) = I_y(Q_y/I)$ is the desired field magnitude, ω is the angular
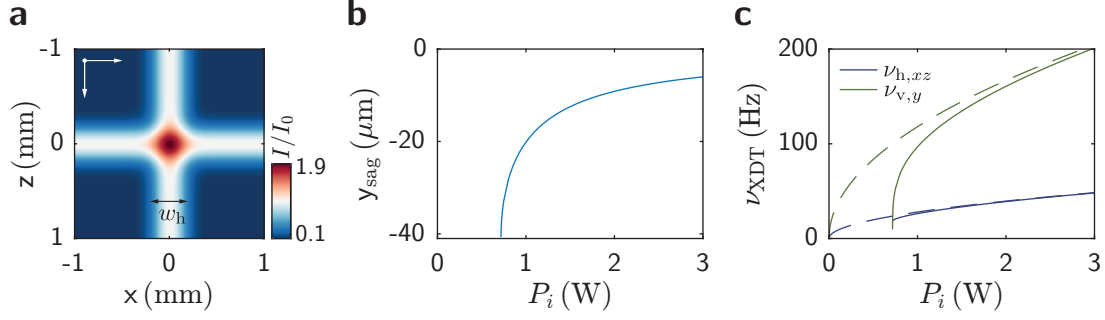
Fig. 2.3: Setup of the crossed optical dipole trap (XDT) generated by the interference of two elliptical Gaussian laser beams with identical beam power and a horizontal (vertical) waist size $w_{\mathrm{h}} \approx 245\,\mu\mathrm{m}$ ($w_{\mathrm{v}} \approx 82\,\mu\mathrm{m}$). **a** The XDT intensity profile I in units of the peak intensity I_0 of a single beam is visualized in the horizontal xz-plane for $y = 0$. **b** The gravitational sag y_{sag} along the vertical direction is plotted as a function of the individual beam power P_i. The minimum value $y_{\mathrm{sag,min}} = w_{\mathrm{v}}/2 \approx 41\,\mu\mathrm{m}$ is reached for the least holding power $P_{i,\mathrm{min}} \approx 0.72\,\mathrm{W}$. **c** Horizontal and vertical trap frequencies $\nu_{\mathrm{h},xz}$ and $\nu_{\mathrm{v},y}$ (solid lines) as functions of P_i, with corresponding bare frequencies that neglect the influence of gravitation (dashed lines). The minimal horizontal trap frequency at $P_i = P_{i,\mathrm{min}}$ is given by $\nu_{\mathrm{h,min}} \approx 18\,\mathrm{Hz}$.

frequency, and ϕ is an arbitrary phase constant. This kind of uniform rotation of the quantization axis is central to the preparation of ultracold bosonic ensembles in higher Bloch bands of our spin-dependent optical lattice, as further discussed in chapter 4 of this thesis.

2.2.3 Crossed optical dipole trap

As already mentioned in the previous subsection, the final evaporative cooling towards a BEC in our experiment is performed in an optical dipole trap after the transfer from the magnetic trap. Working in an optical dipole trap has the main advantage that it provides a trapping potential not only for the low-field seeking states, but also for arbitrary mixtures of Zeeman substates of the full ground state hyperfine manifold $\{|F, m_F\rangle\}$. In our experiment we employ a crossed optical dipole trap (XDT) that is generated by the combined intensity distribution of two elliptical Gaussian laser beams propagating along the x- and z-direction, respectively, and intersecting in the horizontal plane at their corresponding waists under an angle of approximately $90°$. The situation is illustrated in Figure 2.3a. The original design and implementation of the trap is due to J. Struck [103]. The beams have a wavelength of $\lambda_{\mathrm{XDT}} = 1064\,\mathrm{nm}$ and an elliptical profile with principal waist radii $w_{\mathrm{v}} \approx 82\,\mu\mathrm{m}$ and $w_{\mathrm{h}} \approx 245\,\mu\mathrm{m}$ along the vertical and horizontal direction, respectively. To avoid interference terms in the time-averaged intensity distribution, the frequencies of the two beams are shifted against each other by at least $100\,\mathrm{MHz}$. Thus, the total intensity distribution of the XDT can be written

as the incoherent sum of the two Gaussian beams:

$$I_{\mathrm{XDT}}(\boldsymbol{r}) = I_1(\rho_1, z_1) + I_2(\rho_2, z_2) \equiv I_1(\rho_1, z) + I_2(\rho_2, x)$$
$$= \frac{2P_1}{\pi w_{\mathrm{h}}(z) w_{\mathrm{v}}(z)} \exp\left(\frac{-2x^2}{w_{\mathrm{h}}(z)^2} + \frac{-2y^2}{w_{\mathrm{v}}(z)^2} \right)$$
$$+ \frac{2P_2}{\pi w_{\mathrm{h}}(x) w_{\mathrm{v}}(x)} \exp\left(\frac{-2z^2}{w_{\mathrm{h}}(x)^2} + \frac{-2y^2}{w_{\mathrm{v}}(x)^2} \right), \quad (2.7)$$

where P_i denotes the power of the i-th beam. The waist sizes $w_{\mathrm{h,v}}(z_i)$ for the horizontal and vertical direction are functions of the local axial coordinates $z_i \in \{z, x\}$, with $w_{\mathrm{h,v}}(z_i) \equiv w_{\mathrm{h,v}}(1 + z_i^2/z_{\mathrm{R_{h,v}}}^2)^{-1/2}$ and the Rayleigh range $z_{\mathrm{R_{h,v}}} \equiv \pi w_{\mathrm{h,v}}^2/\lambda$ for the respective plane of symmetry. As we will discuss in more detail in section 2.3, the resulting XDT trapping potential V_{XDT} for Rubidium-87 atoms is to very good approximation given by the simple relation $V_{\mathrm{XDT}}(\boldsymbol{r}) = u(\omega) I_{\mathrm{XDT}}(\boldsymbol{r})$. Here, $u(\omega)$ is a frequency-dependent conversion factor that is defined in terms of the conventional dynamical scalar polarizability $\alpha_s(\omega)$ as $u(\omega) \equiv -\alpha_s(\omega)/(2\varepsilon_0 c)$, with the electric constant ε and the speed of light in vacuum c. For Rubidium-87 in the ground state $(5^2 S_{1/2})$ and $\lambda_{\mathrm{XDT}} = 1064\,\mathrm{nm}$, this evaluates to $u(\omega_{\mathrm{XDT}}) = -2.1 \times 10^{-36}\,\mathrm{m^2\,s}$. With that, one may easily calculate the expected trap frequencies in the center of the XDT as a function of the beam parameters. By neglecting the individual contributions from the axial confinements of the corresponding beams, one can find the following analytical results for the trap frequencies $\Omega_{\mathrm{h},xz}$ and $\Omega_{\mathrm{v},y}$ along the horizontal and vertical principal directions [131]:

$$\Omega_{\mathrm{h},x}^2 = \overline{\Omega}_{\mathrm{h},x}^2 \exp\left(-2y_{\mathrm{sag}}^2/w_{\mathrm{v}}^2\right), \quad \Omega_{\mathrm{h},z}^2 = \overline{\Omega}_{\mathrm{h},z}^2 \exp\left(-2y_{\mathrm{sag}}^2/w_{\mathrm{v}}^2\right), \quad (2.8a)$$

$$\Omega_{\mathrm{v},y}^2 = \overline{\Omega}_{\mathrm{v},y}^2 \exp\left(-2y_{\mathrm{sag}}^2/w_{\mathrm{v}}^2\right) \left(1 - 4y_{\mathrm{sag}}^2/w_{\mathrm{v}}^2\right). \quad (2.8b)$$

The expressions for $\Omega_{\mathrm{h},xz}$ and $\Omega_{\mathrm{v},y}$ include the effects from the local gravitational acceleration g along the $-y$-direction, whereas the quantities $\overline{\Omega}$ refer to the corresponding *bare* frequencies in the absence of gravitation. Obviously, both are connected by a simple factor that incorporates the gravitational sag y_{sag}. In our case, the bare frequencies can be expressed as

$$\overline{\Omega}_{\mathrm{h},x}^2 = -\frac{4\mathrm{A}_1}{m w_{\mathrm{h}}^2}, \quad \overline{\Omega}_{\mathrm{h},z}^2 = -\frac{4\mathrm{A}_2}{m w_{\mathrm{h}}^2}, \quad \overline{\Omega}_{\mathrm{v},y}^2 = -\frac{4\mathrm{A}}{m w_{\mathrm{v}}^2}, \quad (2.9)$$

where m is the mass of the atom and we employ the definitions $\mathrm{A}_i \equiv \frac{2P_i}{\pi w_{\mathrm{v}} w_{\mathrm{h}}} u(\omega)$, $\mathrm{A} \equiv \mathrm{A}_1 + \mathrm{A}_2$. The gravitational sag, on the other hand, is obtained from

$$y_{\mathrm{sag}} = -\frac{w_{\mathrm{v}}}{2}\sqrt{-W_0(C)}, \quad C \equiv -\left[\frac{mg w_{\mathrm{v}}}{2A}\right]^2, \quad (2.10)$$

with W_0 denoting the first principal branch of the Lambert W-function. W_0 supports real solutions only if the argument is greater or equal to $-1/e$, which gives a condition on the minimal holding power P_{min} such that for $P = P_1 + P_2 < P_{\mathrm{min}}$ the XDT

cannot sustain a trapping configuration against gravity and thus the atoms get lost from the trap. By assuming that the individual beams have equal power, we find that $P_{i,\text{min}} = mge^{1/2}\pi w_{\text{v}}^2 w_{\text{h}}/(8|u(\omega)|) \approx 0.72\,\text{W}$, which agrees well with our experimental findings. The gravitational sag and the vertical and horizontal trap frequencies for our XDT potential are shown in Figure 2.3 as functions of the beam power P_i. It is easy to verify that the lower bound on the horizontal trap frequencies is given by

$$\Omega_{\text{h,min}} = \left(-\text{sgn}\left(u(\omega)\right) g w_{\text{v}}/w_{\text{h}}^2\right)^{1/2}.$$ (2.11)

This shows that an elliptical dipole trap with its minor axis oriented along the vertical direction allows for lower trap frequencies than a circular trap with the same minimal holding power. In this sense, elliptical beam profiles can compensate for the effects of gravitation.

In our experiment, the two laser beams that create the XDT are derived from a commercial master oscillator power amplifier[6] that provides a laser power of up to $3\,\text{W}$ per beam. After the RF-forced evaporation in the magnetic trap, the transfer into the XDT is realized by first ramping up the individual beam powers linearly from $0\,\text{W}$ to $3\,\text{W}$ in $350\,\text{ms}$. The magnetic confinement is then gradually reduced at a constant beam power by increasing the bias field B_0 from $0.5\,\text{G}$ to around $50\,\text{G}$ in $300\,\text{ms}$. Subsequently, the GC coils are switched off abruptly with an insulated-gate bipolar transistor (IGBT) circuit and the magnetic trap is released. This completes the transfer procedure into the XDT and we proceed with the final evaporation to a BEC in the XDT by lowering the individual beam powers within $7\,\text{s}$ to roughly $0.75\,\text{W}$. We emphasize that a finite bias field B_0 remains from the HC coils during this ramp to preserve the original spin polarization from the magnetic trap. As a result, we obtain a BEC in the Zeeman substate $|F = 1, m_F = -1\rangle$ of the ground state hyperfine level $F = 1$ with no discernible thermal fraction and with a typical particle number of 3×10^5 atoms. The trap frequencies in the final configuration amount to $\boldsymbol{\Omega}_{\text{XDT}} = (\Omega_{\text{h},x}, \Omega_{\text{v},y}, \Omega_{\text{h},z}) \approx 2\pi \cdot (20,\ 50, 20)\,\text{Hz}$, which results in approximate Thomas-Fermi radii $\mathbf{R}_{\text{TF}} \approx (18,\ 7, 18)\,\mu\text{m}$. In general, this configuration is our starting point for all further experimental methods to prepare and to manipulate the internal and external degrees of freedom of an ultracold bosonic ensemble of Rubidium-87.

2.2.4 Optical lattice implementations

At the *Spinor* experiment we have two sets of distinct optical lattices created by the interference of various lattice beams. A highly versatile two-dimensional (2D) optical lattice in the vertical xy-plane that features a hexagonal symmetry, and an additional one-dimensional (1D) optical lattice along the orthogonal z-direction. The setup has been designed and implemented by C. Becker [101]. Many of the first pioneering results of ultracold bosons in hexagonal optical lattices have been achieved in the context of his PhD thesis. The following paragraphs will provide a short overview of the basic characteristics of the corresponding setups and describe the standard configurations that are used in this work. Special emphasis is put on the global macroscopic confine-

---

[6]Coherent Mephisto MOPA.

ment induced by the lattice beams. For further details on the optical setup, including experimental schemes for the lattice beam alignment and polarization adjustment, we refer to the PhD thesis of C. Becker [101]. A thorough treatment of the laser system and our experimental techniques for intensity stabilization and phase noise cancelation of the lattice beams is provided by J. Seeger [106] and T. Klafka [107].

2D running-wave three-beam lattice   The 2D optical lattice is generated by the interference of three Gaussian laser beams $\{\mathcal{G}_i\}$ whose waists intersect in the vertical xy-plane under a mutual angle of $120°$. The beams with wavelength $\lambda_{\mathrm{L}} = 830\,\mathrm{nm}$ and circular waist $w_0 = 115\,\mathrm{\mu m}$ are derived from a commercial Ti:sapphire laser[7] that provides a typical maximum output power of $1\,\mathrm{W}$ per lattice beam. In terms of the cartesian basis $(\boldsymbol{e}_i)$, the individual wave vectors $\boldsymbol{k}_i$ of the three lattice beams are given by

$$\boldsymbol{k}_1 = k_{\mathrm{L}}\boldsymbol{e}_y, \qquad \boldsymbol{k}_2 = \frac{k_{\mathrm{L}}}{2}\left(\sqrt{3}\boldsymbol{e}_x - \boldsymbol{e}_y\right), \qquad \boldsymbol{k}_3 = -\frac{k_{\mathrm{L}}}{2}\left(\sqrt{3}\boldsymbol{e}_x + \boldsymbol{e}_y\right), \qquad (2.12)$$

with the wavenumber $k_{\mathrm{L}} = 2\pi/\lambda_{\mathrm{L}}$. The beams in our setup are linearly polarized and the polarization vectors $\boldsymbol{\epsilon}_i$ can be set independently by means of corresponding half-wave plates. Moreover, the individual beam intensities I_i can be set independently. For all experiments presented in this thesis, the default configuration amounts to an in-plane polarization for each lattice beam, that is to say $\boldsymbol{\epsilon}_i = (\boldsymbol{k}_i \times \boldsymbol{e}_z)/k_{\mathrm{L}}$, and balanced beam intensities $I_i = I_0$. We will frequently refer to this configuration as the ideal p-polarization configuration. Then, since the lattice beams are set to have equal frequencies ω_{L}, the time-averaged intensity distribution $I_{\mathrm{L}}(\boldsymbol{r})$ of the lattice is given by the coherent superposition of the three Gaussian beams. The resulting spatially varying periodic intensity profile in the region of intersection is illustrated in Figure 2.4a, where the local maxima of $I_{\mathrm{L}}(\boldsymbol{r})$ form a graphene-like bipartite lattice in the xy-plane, known as the two-dimensional honeycomb lattice. This periodic structure features a hexagonal symmetry and a lattice constant $a = 2\lambda_{\mathrm{L}}/3$. In addition, in Figure 2.4b we show a corresponding isosurface representation that exemplifies the three-dimensional character of the system as a 2D periodic array of tubes arranged on a honeycomb lattice. Note that the tubes are expanded along the transverse direction to the lattice plane, which illustrates the weak confinement from the Gaussian beam profiles along the z-direction. By turning off selectively one of the three lattice beams, we can also realize three equivalent 1D running-wave lattices with different orientations of the principal axis. For instance, the combination of lattice beams $\mathcal{G}_2$ and $\mathcal{G}_3$ crates a 1D lattice with the principal lattice axis along the horizontal x-direction and a lattice spacing $a_{\mathrm{1D}} = \sqrt{3}a/2$, as depicted in Figure 2.4c. Similar to the 2D lattice, the isosurface representation in Figure 2.4d exemplifies the three-dimensional character of the system as a 1D periodic array of pancakes arranged along the horizontal x-axis. This time, the large expansion along the transverse directions signifies the weak confinement from the Gaussian beam profiles along the y- and z-directions. At this point, let me emphasize that the actual lattice potentials arising from the light distributions as described above are central to this work. I therefore devote a separate section 2.3 for a detailed discussion. For the

---

[7]Coherent MBR 110 pumped by Verdi V18.
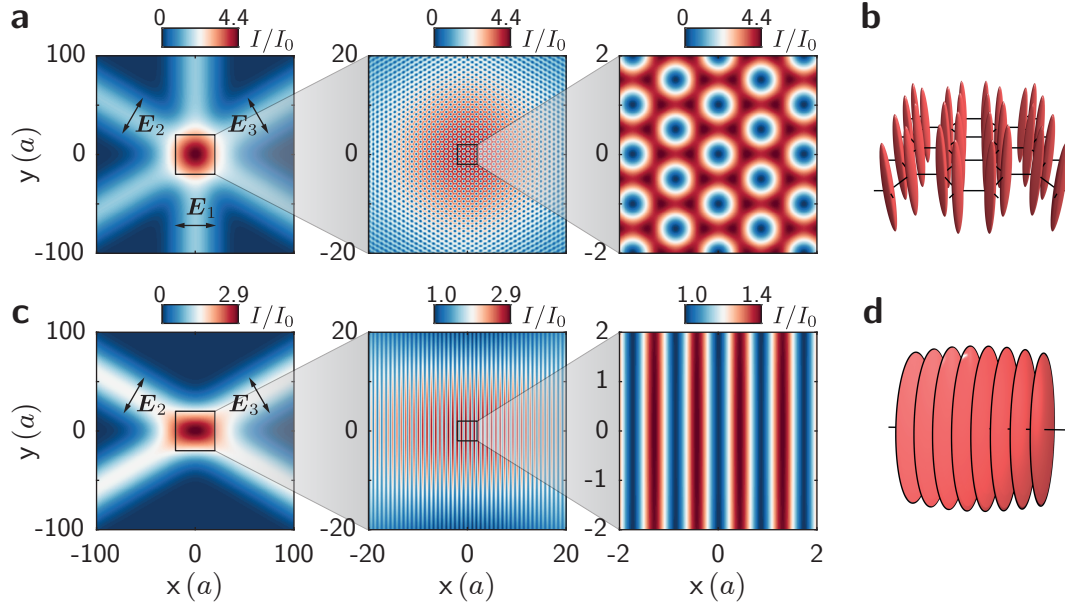
Fig. 2.4: The running-wave three-beam 2D (1D) lattice setup generated by the interference of three (two) Gaussian laser beams with wavelengths $\lambda_\mathrm{L} = 830\,\mathrm{nm}$, identical beam power, circular waists $w_0 = 115\,\mathrm{\mu m}$, and in-plane polarization $\{\boldsymbol{E}_i\}$ for all beams. **a** The 2D lattice intensity profile I in units of the peak intensity I_0 of a single beam is visualized in the vertical xy-plane for $z = 0$. The coordinates are given in units of the fundamental lattice constant $a = 2\lambda_\mathrm{L}/3$ and the cascade of close-ups emphasizes the intensity profile at different length scales. For illustration, the plots were generated for a waist size of $w_0/10$. **b** The isosurface representation of the 2D lattice intensity distribution exemplifies the three-dimensional character of the system as a 2D periodic array of lattice tubes with hexagonal symmetry and lattice constant a. **c** Similar to **a** but for the running-wave 1D lattice produced by lattice beams $\mathcal{G}_2$ and $\mathcal{G}_3$. The principal axis is oriented along the horizontal x-direction and the lattice spacing is given by $a_\mathrm{1D} = \sqrt{3}a/2$. **d** The isosurface representation of the 1D lattice intensity distribution exemplifies the three-dimensional character of the system as a 1D periodic array of lattice pancakes separated by the distance a_1D.

time being, we mainly focus on a few specific aspects related to the trap frequencies induced by the global macroscopic confinement of the XDT plus lattice potential of the ideal p-polarization configuration.

In general, our lattice potential $V_{\mathrm{L}}(\boldsymbol{r})$ for Rubidium-87 in its ground state, as opposed to the XDT potential, cannot be expressed only in terms of the intensity distribution $I_{\mathrm{L}}(\boldsymbol{r})$. The reason is that for $\lambda_{\mathrm{L}} = 830\,\mathrm{nm}$ the so-called dynamical vector polarizability $\alpha_v(\omega_{\mathrm{L}})$ will typically result in a non-negligible contribution to the total light shift, as explained in section 2.3. Although the inclusion of the corresponding vector light shift is straightforward in principle, we may avoid this complication for now by assuming that the vector term is identical zero, which can be justified for Zeeman substates $|F, m_F = 0\rangle$ of the ground state hyperfine levels in the presence of a strong external magnetic field. In this case, like for the XDT potential, we may simply write $V_{\mathrm{L}}(\boldsymbol{r}) = u(\omega_{\mathrm{L}})I_{\mathrm{L}}(\boldsymbol{r})$, now with $u(\omega_{\mathrm{L}}) = -9.4 \times 10^{-36}\,\mathrm{m^2\,s}$. This allows for a direct calculation of the total trap frequencies induced by the global confinement of the XDT plus lattice potential of the ideal p-polarization configuration. For all other states $|F, m_F \neq 0\rangle$, the reasoning applied here can be adopted by including the light shift from the vector polarizability, which yields a small correction to the trap frequencies presented below.

We note that the lattice potential in our experiment is in general superimposed on the XDT by ramping up exponentially the beam intensities to some final target value, thereby loading the BEC into the optical lattice. We make sure to adjust the lattice beams such that the geometric center of the lattice is aligned with the position of the BEC in the XDT. In other words, the global minimum of the lattice potential and the global minimum of the XDT potential plus gravity mostly coincide. In this case, the bare trap frequencies Ω_μ of the lattice confinement along the cartesian axes $\mu \in \{x, y, z\}$ simply add quadratically to the XDT frequencies in equation (2.8). For Ω_μ one should actually distinguish between the local ω_i and global $\overline{\Omega}$ trap frequencies induced by the lattice confinement, where the former refers to the trap frequencies of a single lattice tube or pancake at space point $\boldsymbol{r}_i$, while the latter accounts for the global macroscopic confinement defined in terms of the intensity envelope $\overline{I}$ at the center of the trap. For the 2D lattice configuration presented in Figure 2.4a we then find the following expressions for the trap frequencies

$$\text{2D:} \quad \overline{\Omega}_x^2 = -\frac{9A}{mw_0^2}, \quad \overline{\Omega}_y^2 = -\frac{9A}{mw_0^2}, \quad \omega_{0z}^2 = -\frac{18A}{mw_0^2}, \tag{2.13}$$

with $A \equiv 2P_0 u(\omega_{\mathrm{L}})/(\pi w_0^2)$, where we assume that all lattice beams have equal power $P_i = P_0$. Here, ω_{0z} denotes the trap frequency of the central lattice tube along the weakly confined axial z-direction, i.e. orthogonal to the lattice plane. Correspondingly, for the 1D lattice configuration in Figure 2.4c we obtain

$$\text{1D:} \quad \overline{\Omega}_x^2 = -\frac{3A}{mw_0^2}, \quad \omega_{0y}^2 = -\frac{9A}{mw_0^2}, \quad \omega_{0z}^2 = -\frac{12A}{mw_0^2}, \tag{2.14}$$

where ω_{0y} and ω_{0z} are now the trap frequencies of the central lattice pancake along the two weakly confined radial principal directions, i.e. orthogonal to the lattice axis. We note that the different factors in front of A have a simple geometric origin and are a consequence of the relative alignment and interference of the three (two) lattice beams.
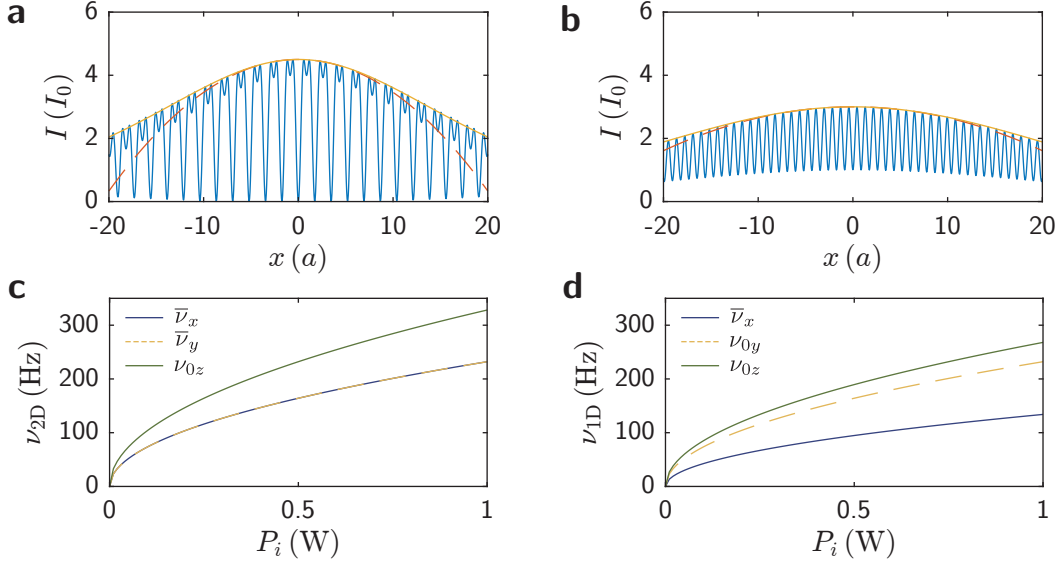
Fig. 2.5: Trap frequencies resulting from the global macroscopic confinement of the 2D and 1D lattice configuration with in-plane polarization. **a** The cross section (blue) $I = I(x, 0, 0)$ of the 2D lattice intensity distribution is plotted against the x-coordinate together with the intensity envelope $\bar{I}$ (yellow) and corresponding Taylor approximation to second order (red dashed). Intensities are specified in units of the peak intensity I_0 of a single beam. The x-coordinate is in units of the lattice constant $a = 2\lambda_{\mathrm{L}}/3$. For illustration, the plot was generated for a waist size of $w_0/10$. **b** Similar to **a** but for the 1D lattice intensity distribution. **c** The in-plane trap frequencies $\bar{\nu}_x = \overline{\Omega}_x/(2\pi)$ and $\bar{\nu}_y = \overline{\Omega}_y/(2\pi)$ of the 2D lattice intensity envelope $\bar{I}$ and the axial trap frequency $\nu_{0z} = \omega_{0z}/(2\pi)$ of the central lattice tube are shown as functions of the individual lattice beam power P_i. **d** Same as in **c** but for the 1D lattice, with envelope trap frequency $\bar{\nu}_x = \overline{\Omega}_x/(2\pi)$ along the lattice axis and principal radial trap frequencies $\nu_{0y} = \omega_{0y}/(2\pi)$ and $\nu_{0z} = \omega_{0z}/(2\pi)$ of the central pancake.

In Figure 2.5, we plot the resulting lattice trap frequencies as functions of the individual lattice beam power P_i for the two relevant configurations discussed above. Obviously, for powers of the lattice beams exceeding $100\,\mathrm{mW}$, the resulting trap frequencies are larger than the final XDT frequencies and will quickly dominate the global macroscopic confinement. In particular, the trap frequency along the initially weakly confined z-direction is strongly affected by the presence of the 2D lattice, as indicated by the strong increase of ν_{0z} in Figure 2.5c. These aspects relating to the global macroscopic confinement induced by the lattice beams should be kept in mind when examining the physics of neutral atoms in optical lattices. Besides, the trap frequencies discussed here should be contrasted with another class of local trap frequencies $\omega_{i\parallel}$ that naturally appear in the context of optical lattices, and which are related to the *microscopic* confinement exerted by a single lattice tube or pancake along the directions of periodic intensity modulation, i.e. parallel to the principal lattice axes. A detailed analysis of these microscopic trap frequencies for our lattice setup is given by T. Klafka [107]. Here, I have focused on the macroscopic counterparts because these are the ones that are frequently swept under the rug.

1D retro-reflected lattice The 1D lattice along the z-direction, i.e. perpendicular to the 2D lattice plane, is realized as an ordinary standing wave lattice by retro-reflecting a Gaussian laser beam with wave vector $\boldsymbol{k}_\perp = k_\perp \boldsymbol{e}_z = (2\pi/\lambda_\perp)\boldsymbol{e}_z$. As a laser source we use a commercial Nd:YAG laser at a wavelength $\lambda_\perp = 1064\,\text{nm}$, yielding a maximal output power of $1\,\text{W}$. The prograde and retrograde lattice beams have a circular waist profile with a minimal spot size $w_\perp = 150\,\mu\text{m}$ located near the center of the running-wave 2D lattice. Analogous to the running-wave 1D lattice, the time-averaged intensity distribution of the standing light wave creates a periodic array of pancakes with lattice spacing $a_\perp = \lambda_\perp/2 = 532\,\text{nm}$. The trap frequency Ω_ρ of the central pancake along the radial coordinate $\rho^2 = x^2 + y^2$ is given by

$$\Omega_\rho^2 = -\frac{16\text{A}}{mw_\perp^2}. \tag{2.15}$$

Since the 1D retro-reflected lattice is oriented perpendicular to the running-wave 2D lattice, we will refer to it as the *transverse* 1D lattice. Finally, we note that the transverse 1D lattice can be used in combination with the 2D lattice to create three-dimensional optical lattices that are separable along the z-direction plus xy-plane.

2.3 Optical lattices with scalar and vector light shifts

This section gives a detailed and general account of the lattice potentials for arbitrary configurations of our 2D optical lattice. We shall mainly focus on the local microscopic properties of the periodic potentials rather than on the global confinement from the finite extent, which we touched on in the previous section. The 2D optical lattice is at the heart of the *Spinor* setup and it has been the starting point for many pioneering experiments covered in the PhD theses of P. Soltan-Panahi, J. Struck, M. Weinberg and C. Ölschläger [102–105]. To all of those experiments and experiments presented in this work, it is of utmost significance that the interaction between atoms and light in the off-resonant semiclassical regime gives rise to nearly conservative optical potentials for the atomic center of mass motion. For this reason, I will start with a short review of the main aspects of optical potentials and present a systematic and general analysis of the AC Stark shift experienced by an atom under the influence of a non-resonant monochromatic electric field. The treatment of this subject will rely on a tensor operator formalism and the notion of the reduction into irreducible tensor components, which will provide a clear understanding of the different underlying physical effects, known as the scalar, vector, and tensor light shifts. Next, we will apply our findings to the case of our 2D optical lattice to derive a general and basis-independent representation of the resulting lattice potentials for Rubidium-87 atoms in the ground state hyperfine levels $F = 1, 2$. We will put special emphasis on the role of the external quantization field and the emergence of an effective lattice potential in the limit of strong external magnetic fields. Finally, we discuss the specific case of the ideal p-polarization configuration that corresponds, to a good approximation, to the actual 2D optical lattice configuration used for experiments presented in this work.

There are multiple literature sources that cover the broad field of atom-light interaction in full generality. Here, we will focus on a few selected aspects relevant to our

discussion of atoms in optical lattices. For a general and extensive survey of atoms in laser fields, we can recommend, for instance, the seminal report by Manakov et al. [132]. An original perspective on the tensor operator formalism for the semiclassical description of atom-light interaction is provided by Happer and Mathur [133]. Its application to the calculation of light shifts in Rubidium-87 is treated by the same authors in reference [134]. For the systematic analysis of the AC Stark shift as presented below, we closely follow the work by Le Kien et al. [135] and Deutsch and Jessen [136].

2.3.1 AC Stark shift and dynamical polarizability

In general, provided that the integrity of the atom remains unaffected by ionization or other disruptive processes, the action of a light field on a neutral atom gives rise to a radiative force that may be split into *dissipative* and *reactive* parts [137]. The dissipative part, known as the radiation pressure or spontaneous force, is related to the resonant absorption and subsequent spontaneous emission of photons from the light field and can be used for optical cooling techniques, such as the grey molasses cooling presented in subsection 2.2.1. The reactive part, on the other hand, originates from non-resonant coherent absorption and stimulated emission of photons through virtual excitations and is usually referred to as the *dipole force*. It corresponds to a conservative force because it derives from a potential that coincides with the interaction energy of an induced electric dipole moment in the external field. This interaction energy, also known as the AC Stark shift or light shift, will be the focus of our following discussion as it forms the basis for optical traps, including our XDT and optical lattices.

The main aspects of the AC Stark shift can be understood in terms of a semiclassical description where an electric field $\mathbf{E}(\boldsymbol{r}, t)$ couples to the atomic dipole operator $\hat{\boldsymbol{d}}$ according to

$$\hat{V}(\boldsymbol{r}, t) = -\hat{\boldsymbol{d}}\,\mathbf{E}(\boldsymbol{r}, t)\,. \tag{2.16}$$

Equation (2.16) characterizes the interaction energy between an atom and a light field in the famous dipole approximation. Specifically, consider the case of a non-resonant monochromatic wave

$$\mathbf{E}(\boldsymbol{r}, t) = \boldsymbol{\mathcal{E}}^{+}(\boldsymbol{r})e^{-\mathrm{i}\omega t} + \boldsymbol{\mathcal{E}}^{-}(\boldsymbol{r})e^{+\mathrm{i}\omega t} \equiv 2\mathrm{Re}\left(\boldsymbol{\mathcal{E}}^{+}(\boldsymbol{r})e^{-\mathrm{i}\omega t}\right)\,, \tag{2.17}$$

with frequency ω and complex electric strength vector $\boldsymbol{\mathcal{E}}^{+}(\boldsymbol{r})$, coupling to an atom in an eigenstate $|a\rangle$ of the bare atomic Hamiltonian at a fixed position $\boldsymbol{r}$. Then, in response to this coupling, the associated eigenenergy $E_a = \hbar\omega_a$ will shift by an amount ΔE_a. To second order perturbation theory one finds that [132, 135, 138]

$$\begin{aligned}
\Delta E_a(\boldsymbol{r}) &= -\mathcal{E}_i^{-}(\boldsymbol{r})\mathcal{E}_j^{+}(\boldsymbol{r})\alpha_{ij}^a(\omega) \\
&\equiv -\mathcal{E}_i^{-}(\boldsymbol{r})\mathcal{E}_j^{+}(\boldsymbol{r})\frac{1}{\hbar}\sum_b \mathrm{Re}\left(\frac{\langle a|\hat{d}_i|b\rangle\,\langle b|\hat{d}_j|a\rangle}{\omega_b - \omega_a - \omega - \mathrm{i}\gamma_{ba}/2}\right. \\
&\qquad\qquad\qquad\qquad\left. + \frac{\langle a|\hat{d}_j|b\rangle\,\langle b|\hat{d}_i|a\rangle}{\omega_b - \omega_a + \omega + \mathrm{i}\gamma_{ba}/2}\right)\,.
\end{aligned} \tag{2.18}$$

Equation (2.18) is known as the second order AC Stark shift or light shift of a nonde-

generate energy level E_a for an atom in an oscillating electric field. The sum in the last line is over all unperturbed eigenstates $|b\rangle$ with energies $E_b = \hbar\omega_b$, and $\gamma_{ba} \equiv \gamma_a + \gamma_b$ denotes the transition linewidth between states $|a\rangle$ and $|b\rangle$ with spontaneous decay rates γ_a and γ_b, respectively. The indices i and j refer to the cartesian coordinates and we employ the convention of summation over repeated indices. Moreover, we have defined the dynamical linear polarizability tensor $\alpha_{ij}^a(\omega)$ for an atom in the state $|a\rangle$. We point out that the AC Stark shift $\Delta E_a(\boldsymbol{r})$ is the origin of the *dipole potential* from which the dipole force derives in the usual way according to $\mathbf{F}_{\text{dip}} = -\boldsymbol{\nabla}\left(\Delta E_a(\boldsymbol{r})\right)$ [139].

In the following, we will be interested in examining the AC Stark shift for an atom in the manifold of a single hyperfine structure (hfs) state $|a\rangle \equiv |nJF\rangle$. Our basic assumption will be that the AC Stark shift is a small perturbation to the hfs splitting. Thus, no mixing is induced among different hfs states, and the total angular momentum F remains a good quantum number. In other words, we require that the full Hamiltonian of atom plus atom-light interaction remains nearly block diagonal in the quantum numbers F so that restricting the analysis of the AC Stark shift to the subspace of a single hfs state is well justified. This condition is always fulfilled for the electric field strengths and detunings employed in our experiment. For the moment, we will also assume that there is no external quantization field that breaks the degeneracy among the different Zeeman substates $|(nJF)m_F\rangle$ of the relevant hyperfine manifold. Modifications that result from the inclusion of the Zeeman interaction with a finite external magnetic field will be treated later in this section. To proceed, we note that with $A_i B_j = (\mathbf{A} \otimes \mathbf{B})_{ij}$ for any vectors $\mathbf{A}$ and $\mathbf{B}$, where $(\mathbf{A} \otimes \mathbf{B})_{ij}$ are the components with respect to the cartesian tensor basis $\{\boldsymbol{e}_i \otimes \boldsymbol{e}_j\}$, one can rewrite equation (2.18) in the form

$$\Delta E_a(\boldsymbol{r}) = -\langle a|\left(\boldsymbol{\mathcal{E}}^-(\boldsymbol{r}) \otimes \boldsymbol{\mathcal{E}}^+(\boldsymbol{r})\right)_{ij}(\hat{\boldsymbol{\alpha}}^a(\omega))_{ij}|a\rangle, \qquad (2.19)$$

where we have introduced the rank-2 polarizability tensor operator

$$\hat{\boldsymbol{\alpha}}^a(\omega) \equiv \hat{\boldsymbol{d}} \otimes \left(\hat{R}_+^a(\omega)\hat{\boldsymbol{d}}\right) + \hat{\boldsymbol{d}} \otimes \left(\hat{R}_-^a(\omega)\hat{\boldsymbol{d}}\right), \qquad (2.20)$$

with the following abbreviations

$$\hat{R}_\pm^a(\omega) \equiv \frac{1}{\hbar}\sum_b \text{Re}\left(\frac{1}{E_b - E_a \mp \omega \mp \mathrm{i}\gamma_{ba}/2}\right)|b\rangle\langle b|. \qquad (2.21)$$

We now define the *AC Stark operator* $\hat{V}_{\text{AC}}$ for the a-th energy level as

$$\hat{V}_{\text{AC}}(\boldsymbol{r}) \equiv -\hat{P}_a\langle\boldsymbol{\mathcal{E}}^-(\boldsymbol{r}) \otimes \boldsymbol{\mathcal{E}}^+(\boldsymbol{r}), \hat{\boldsymbol{\alpha}}^a(\omega)\rangle_{\text{F}}\hat{P}_a. \qquad (2.22)$$

Here, $\hat{P}_a \equiv |a\rangle\langle a|$ is the projector onto the a-th energy level, and $\langle\cdot,\cdot\rangle_{\text{F}}$ refers to the Frobenius inner product of the two dyadics $(\boldsymbol{\mathcal{E}}^-(\boldsymbol{r}) \otimes \boldsymbol{\mathcal{E}}^+(\boldsymbol{r}))$ and $\hat{\boldsymbol{\alpha}}^a$. We note that $\Delta E_a(\boldsymbol{r})$ is just the expectation value $\langle a|\hat{V}_{\text{AC}}|a\rangle$ and that the Frobenius inner product can be evaluated with respect to any tensor basis. As in reference [135], we will now assume that the AC Stark operator $\hat{V}_{\text{AC}}$ not only correctly describes the AC Stark shift of a non-degenerate energy level but also the mixing between degenerate states in case that the bare atomic eigenenergy E_a has a g-fold degeneracy, i.e. $\hat{P}_a = \sum_{i=1}^g |a_i\rangle\langle a_i|$.

To analyze the effect of the Stark operator onto the given hyperfine manifold, we must thus diagonalize $\hat{V}_{\mathrm{AC}}$ in the subspace of Zeeman states $|(nJF)m_F\rangle$ to the fixed quantum numbers (nJF), where for the sake of brevity we will suppress the numbers n and J hereafter. For the evaluation of the corresponding matrix elements $\langle Fm_F|\hat{V}_{\mathrm{AC}}|Fm_F'\rangle$, it is instructive to expand the two operands in equation (2.22) in a tensor basis that provides a decomposition into irreducible components and allows to identify the distinct physical effects that underlie the AC Stark shift. To this end, let us first introduce the spherical basis $\{e_q\}$ with $q \in \{-1, 0, +1\}$, which is defined in terms of the cartesian basis as

$$e_{-1} \equiv \frac{1}{\sqrt{2}}\left(e_x - \mathrm{i}e_y\right), \qquad e_0 \equiv e_z, \qquad e_{+1} \equiv -\frac{1}{\sqrt{2}}\left(e_x + \mathrm{i}e_y\right). \qquad (2.23)$$

Note that any complex vector $\mathbf{A}$ can be expanded in the spherical basis as $\mathbf{A} = A^q e_q = \langle \mathbf{A}, e_q \rangle e_q$, where A^q denotes the contravariant spherical component and $\langle \cdot, \cdot \rangle$ is the standard scalar product on $\mathbb{C}^3$. Similarly, any rank-2 tensor $\mathbf{T}$ can be expanded in the spherical tensor basis $\{e_q \otimes e_{q'}\}$ according to $\mathbf{T} = T^{qq'}(e_q \otimes e_{q'})$. To proceed, we will now define the *coupled spherical tensor basis* $\{e_{Km}\}$ as

$$e_{Km} \equiv \sum_{qq'} C^{Km}_{1q,1q'}\left(e_q \otimes e_{q'}\right), \qquad (2.24)$$

with $K \in \mathcal{S} \equiv \{0, 1, 2\}$ and $m \in \mathcal{S}_K \equiv \{-K, -K+1, \ldots, +K\}$, which provides a natural decomposition of any rank-2 tensor into a sum of its irreducible scalar $(K = 0)$, vector $(K = 1)$, and tensor $(K = 2)$ components. Here, the coefficients $C^{Km}_{1q,1q'}$ are the Clebsch-Gordan coefficients in the notation

$$\begin{aligned} C^{jm}_{j_1 m_1, j_2 m_2} &= (-1)^{j_1 - j_2 + m}\sqrt{2j+1}\begin{pmatrix} j_1 & j_2 & j \\ m_1 & m_2 & -m \end{pmatrix} \\ &\equiv (-1)^{j_1 - j_2 + m}\sqrt{2j+1}\,W^{j_1, j_2, j}_{m_1, m_2, -m}, \end{aligned} \qquad (2.25)$$

with the definition $W^{j_1, j_2, j}_{m_1, m_2, -m}$ for the Wigner 3-j symbol. The expansion of $\mathbf{T}$ in the coupled spherical tensor basis reads

$$\mathbf{T} = \sum_{K \in \mathcal{S}} \sum_{m \in \mathcal{S}_K} T^{Km} e_{Km}, \quad T^{Km} = \sum_{qq'} T^{qq'} C^{Km}_{1q,1q'}. \qquad (2.26)$$

By expanding the dyadic $\left(\boldsymbol{\mathcal{E}}^-(\boldsymbol{r}) \otimes \boldsymbol{\mathcal{E}}^+(\boldsymbol{r})\right)$ and $\hat{\boldsymbol{\alpha}}^a$ in the same way, and taking the Zeeman basis $|Fm_F\rangle$ as the standard angular momentum basis that complies with the definition of the spherical basis in equation (2.23), one can derive the following result for the matrix elements of the AC Stark operator [135]

$$\langle Fm_F|\,\hat{V}_{\mathrm{AC}}(\boldsymbol{r})\,|Fm_F'\rangle = \sum_{K \in S} \sum_{m_K \in S_K} \left(\boldsymbol{\mathcal{E}}^-(\boldsymbol{r}) \otimes \boldsymbol{\mathcal{E}}^+(\boldsymbol{r})\right)^{Km_K}$$

$$\times (-1)^{(F-m_F)}\begin{pmatrix} F & K & F \\ -m_F & -m_K & m_F' \end{pmatrix}\alpha^{(K)}_F(\omega). \quad (2.27)$$

Here, the coefficients $\alpha_F^{(K)}(\omega)$ are known as the *reduced* dynamical scalar $(K = 0)$, vector $(K = 1)$, and tensor $(K = 2)$ polarizabilities defined by

$$\alpha_F^{(K)}(\omega) \equiv (-1)^{(K+F+1)}(2F+1)\sqrt{2K+1} \sum_{n'J'} |\langle n'J'\|d\|nJ\rangle|^2$$

$$\times \sum_{F'}(-1)^{F'}(2F'+1) \begin{Bmatrix} 1 & K & 1 \\ F & F' & F \end{Bmatrix} \begin{Bmatrix} F & 1 & F' \\ J' & I & J \end{Bmatrix}^2 \Delta_{n'J'F',nJF}^{(K)}(\omega), \quad (2.28)$$

with the following abbreviations

$$\Delta_{n'J'F',nJF}^{(K)}(\omega) = \frac{1}{\hbar}\text{Re}\left(\frac{1}{\omega_{n'J'F'} - \omega_{nJF} - \omega - \mathrm{i}\gamma_{n'J'F',nJF}/2}\right.$$

$$\left. + \frac{(-1)^K}{\omega_{n'J'F'} - \omega_{nJF} + \omega + \mathrm{i}\gamma_{n'J'F',nJF}/2}\right). \quad (2.29)$$

The sum in equation (2.28) is over all atomic quantum numbers $(n'J'F')$ and the curly brackets denote the Wigner 6-j symbols. The term $|\langle n'J'\|d\|nJ\rangle|$ refers to the absolute value of the reduced matrix element of the rank-1 dipole operator in the following convention:

$$\langle n'J'm'|\hat{d}_q|nJm\rangle = (-1)^{J'-m'} \begin{pmatrix} J' & 1 & J \\ -m' & q & m \end{pmatrix} \langle n'J'\|d\|nJ\rangle. \quad (2.30)$$

For practical purposes one should note that the reduced matrix elements may be inferred from the spontaneous transition rates Γ according to [140][8]

$$|\langle n'J'\|d\|nJ\rangle|^2 = \frac{\omega_0^3}{3\pi\varepsilon_0\hbar c^3} \cdot \begin{cases} (2J'+1)\Gamma_{n'J'\to nJ}, & \text{for } \omega_{n'J'} > \omega_{nJ} \\ (2J+1)\Gamma_{nJ\to n'J'}, & \text{for } \omega_{nJ} > \omega_{n'J'} \end{cases}, \quad (2.31)$$

with $\omega_0 \equiv |\omega_{n'J'} - \omega_{nJ}|$.

We point out that the right hand side of equation (2.27) seemingly differs from the result in reference [135] by a factor $(-1)^{K+m_K}$ inside the sum. Yet, both results agree for we use the contravariant instead of the covariant components of $(\boldsymbol{\mathcal{E}}^-(\boldsymbol{r}) \otimes \boldsymbol{\mathcal{E}}^+(\boldsymbol{r}))$. Indeed, it is easy to show that both components with respect to the coupled spherical tensor basis are simply related by $T^{Km} = (-1)^{K+m}T_{Km}$ for any rank-2 tensor $\mathbf{T}$.

Equation (2.27) can be used to calculate the matrix elements $\langle Fm_F| \hat{V}_{\text{AC}}(\boldsymbol{r})|Fm_F'\rangle$ of any atom in a given hyperfine level F and for arbitrary monochromatic light fields. Specifically, the amplitude and polarization of $\boldsymbol{\mathcal{E}}^+(\boldsymbol{r})$ can be any function of the position variable $\boldsymbol{r}$. The only constraint we want to impose is that the variations in space remain small compared to the size of the atom to be consistent with the dipole approximation. This condition is certainly fulfilled for all light fields employed in our experiment. Thus, we will use equation (2.27) in the following subsection 2.3.2 to derive the general form of our 2D optical lattice potential for Rubidium-87 atoms in the ground state $(5^2S_{1/2})$

---

[8]See also [140] for a discussion of different conventions for the normalization of reduced matrix elements.

hyperfine levels $F = 1, 2$.

Let us now focus on the physical meaning behind the different terms $K = 1, 2, 3$ in equation (2.27). In fact, the decomposition into irreducible tensor components corresponds to a partition of the AC Stark operator into a sum $\hat{V}_{\mathrm{AC}} = \hat{V}^s + \hat{V}^v + \hat{V}^t$ of scalar, vector, and tensor light-shift operators, which reflect the separate transformation behavior under simultaneous rotations of the position space basis $\{e_{Km}\}$ and the Hilbert space Zeeman basis $\{|F, m_F\rangle\}$. From this, one can deduce, for example, that the scalar light shift must be independent of the magnetization $\langle \hat{\boldsymbol{F}} \rangle$, i.e. independent of the magnetic quantum numbers m_F. Hence, it cannot depend on the polarization of the light field but only on the total light intensity $I(\boldsymbol{r}) = 2\varepsilon_0 c \langle \boldsymbol{\mathcal{E}}^+(\boldsymbol{r}), \boldsymbol{\mathcal{E}}^+(\boldsymbol{r}) \rangle = 2\varepsilon_0 c |\boldsymbol{\mathcal{E}}^+(\boldsymbol{r})|^2$. In contrast, the vector light shift depends on both of them. These insights are most evident in a basis-independent representation of $\hat{V}_{\mathrm{AC}}$, which can be derived from equation (2.27) [135, 136]:

$$\hat{V}_{\mathrm{AC}}(\boldsymbol{r}) = -\alpha_F^s |\boldsymbol{\mathcal{E}}^+(\boldsymbol{r})|^2 \, \mathrm{id}_F + \alpha_F^v \frac{\mathrm{i} \left[\boldsymbol{\mathcal{E}}^-(\boldsymbol{r}) \times \boldsymbol{\mathcal{E}}^+(\boldsymbol{r}) \right] \hat{\boldsymbol{F}}}{2F}$$
$$- \alpha_F^t \frac{3 \left(\boldsymbol{\mathcal{E}}^-(\boldsymbol{r}) \hat{\boldsymbol{F}} \right) \left(\boldsymbol{\mathcal{E}}^+(\boldsymbol{r}) \hat{\boldsymbol{F}} \right) + 3 \left(\boldsymbol{\mathcal{E}}^+(\boldsymbol{r}) \hat{\boldsymbol{F}} \right) \left(\boldsymbol{\mathcal{E}}^-(\boldsymbol{r}) \hat{\boldsymbol{F}} \right) - 2 |\boldsymbol{\mathcal{E}}^+(\boldsymbol{r})|^2 \hat{\boldsymbol{F}}^2}{2F(2F-1)} \, , \quad (2.32)$$

where id_F is the identity map and $\hbar \hat{\boldsymbol{F}} = \hat{\mathbf{F}}$ is the standard angular momentum operator or spin operator acting on the given hyperfine manifold F. The factors α_F^s, α_F^v, α_F^t are the *conventional* dynamical scalar, vector, and tensor polarizabilities defined in terms of the reduced polarizabilities (equation (2.28)) as

$$\alpha_F^s(\omega) = \sqrt{\frac{1}{3(2F+1)}} \, \alpha_F^{(0)}(\omega) \, , \quad \alpha_F^v(\omega) = -\sqrt{\frac{2F}{(F+1)(2F+1)}} \, \alpha_F^{(1)}(\omega) \, ,$$
$$\alpha_F^t(\omega) = -\sqrt{\frac{2F(2F-1)}{3(F+1)(2F+1)(2F+3)}} \, \alpha_F^{(2)}(\omega) \, . \quad (2.33)$$

By inspecting equation (2.32), one can see that the vector light shift corresponds to a Zeeman interaction $\hat{V}_{\mathrm{Z}} = -\hat{\boldsymbol{\mu}}_F \mathbf{B}^{\mathrm{fict}} \equiv \mu_{\mathrm{B}} g_F \hat{\boldsymbol{F}} \mathbf{B}^{\mathrm{fict}}$ with a fictitious magnetic field [133, 135, 136]

$$\mathbf{B}^{\mathrm{fict}}(\boldsymbol{r}) \equiv \frac{\alpha_F^v(\omega)}{2\mu_{\mathrm{B}} g_F F} \mathrm{i} \left(\boldsymbol{\mathcal{E}}^-(\boldsymbol{r}) \times \boldsymbol{\mathcal{E}}^+(\boldsymbol{r}) \right) \, , \quad (2.34)$$

first experimentally observed by Cohen-Tannoudji and Dupont-Roc [141]. It should therefore come as no surprise that the AC Stark operator $\hat{V}_{\mathrm{AC}}$, depending on the orientation of $\mathbf{B}^{\mathrm{fict}}$, will generally be non-diagonal in the standard Zeeman basis. Note that $\mathbf{B}^{\mathrm{fict}}$, however, depends on the polarization and frequency of the light field and vanishes for a linear polarization. We emphasize that the fictitious magnetic field has been used successfully for coherent spin manipulation of Zeeman sublevels in the near-resonant [142, 143] and far-off-resonance [144] regime. Moreover, it has great significance to the field of optical lattice clocks and precision measurements with neutral atoms [145, 146]. In view of our 2D optical lattice, it would be particularly interesting to explore the possibility to use the fictitious magnetic field for the creation of a two-dimensional

spin-orbit coupling. As regards the tensor light shift, which corresponds to the last term in equation (2.32), there is no simple analogy and interpretation as for the vector light shift. The general observation is that it describes a nonlinear light shift that induces spin dynamics in the hyperfine manifold, going beyond simple SU(2) rotations [136].

It is important to note that the structure of equation (2.28) implies a natural ordering $|\alpha_F^t/\alpha_F^v| < |\alpha_F^v/\alpha_F^s| < 1$ of the relative strengths of the conventional dynamical scalar, vector, and tensor polarizabilities in the limit of large detunings, i.e. when the light frequency ω stays far off resonance to any atomic transition line. In particular, these ratios decrease as the detuning increases. Loosely speaking, the vector polarizability $\alpha_F^v(\omega)$ and thus the vector light shift might become appreciable only if the detuning to a predominant transition line (n') in equation (2.28) is of the same order as the fine structure splitting of this level. Similarly, the tensor polarizability $\alpha_F^t(\omega)$ and thus the tensor light shift might become relevant only if the detuning to a predominant transition line $(n'J')$ is of the same order as the hyperfine structure splitting of this level. For instance, for Rubidium-87 in the ground state hfs level $F = 1$ we find in case of our 2D optical lattice ($\lambda_L = 830$ nm) that $|\alpha^v/\alpha^s| \approx 0.13$ and $|\alpha^t/\alpha^v| \approx 1.3 \times 10^{-5}$, while for the XDT ($\lambda_{XDT} = 1064$ nm) we have $|\alpha^v/\alpha^s| \approx 0.02$ and $|\alpha^t/\alpha^v| \approx 9 \times 10^{-6}$. In any case, the tensor light shifts may be safely ignored. Furthermore, since our XDT has linear polarization, the fictitious magnetic field is identical zero and the only relevant contribution to the dipole potential comes from the scalar part. On the other hand, as we will outline in subsection 2.3.3, our 2D optical lattice in the p-polarization configuration involves circular components in the polarization of the total electric field, leading to a non-vanishing fictitious magnetic field and a substantial contribution of the vector light shift.

In Figure 2.6, we show the calculated ground state scalar and vector polarizabilities of Rubidium-87 as a function of the wavelength $\lambda = 2\pi c/\omega$ in the vicinity of the D_1 and D_2 transition lines. The domain comprises large detunings near the limits of the horizontal axis and small detunings close to the transitions, marked by vertical red lines. We stress that the tensor polarizabilities are not resolved on this scale because they manifest only within of a few GHz around the D_1 and D_2 lines [147]. For the calculations according to equations (2.28) and (2.33), we have considered only the dominant coupling of the light field to the hyperfine levels of the excited states $5^2P_{1/2}$ and $5^2P_{3/2}$, and legitimately ignored the coupling to all distant higher energy levels. For completeness, we also show similar plots in the lower panel of Figure 2.6 for the other species available in our experiment, Potassium-39. It is worth noting that the scalar polarizabilities vanish at points between the D_1 and D_2 lines, whereas the vector polarizabilities remain finite. In case of our 2D optical lattice, this could be used in principle to create pure vector light-shift periodic potentials with fictitious magnetic field strengths as large as a few gauss, where the relevant wavelengths are easily accessed by the wide tuning range of the Ti:sapphire laser source. However, one should keep in mind that in this regime of small detunings, the spontaneous force due to photon scattering may become significant and constitute a serious source of heating, promoting decoherence, and limiting the atom's lifetime in the optical lattice. As far as we are concerned with the default wavelength $\lambda_L = 830$ nm for our 2D optical lattice, we can practically assume to operate in the far-off-resonance regime and generally neglect the effects from the spontaneous force.
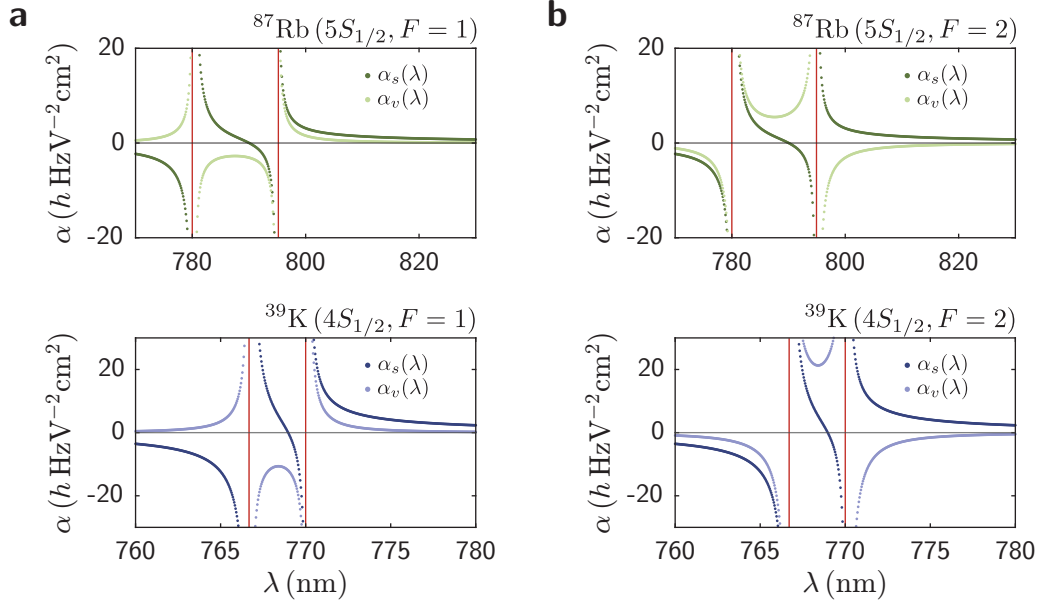
Fig. 2.6: Calculated dynamical ground state scalar and vector polarizabilities $\alpha_{s,v}(\lambda)$ for Rubidium-87 and Potassium-39 as a function of the laser wavelength λ near the corresponding D_1 and D_2 transition lines. **a** For the ground state hyperfine structure (hfs) level $F = 1$ and **b** for the ground state hfs level $F = 2$. Note that the scalar polarizabilities vanish at points in between the D_1 and D_2 lines, whereas the vector polarizabilities remain finite. Also note the different sign of vector polarizabilities for $F = 1$ in **a** compared to $F = 2$ in **b**. We stress that the tensor polarizabilities $\alpha_t(\lambda)$ are not resolved on the wavelength scale as presented here.

2.3.2 Scalar and vector light-shift periodic potentials

We will now apply the findings from the previous subsection 2.3.1 to derive a general and basis-independent representation of the lattice potential for arbitrary configurations of our 2D optical lattice. To be precise, by lattice potential we shall always mean the position-dependent AC Stark shift experienced by Rubidium-87 atoms in the ground state hyperfine levels $F = 1, 2$ inside the light field distribution of the 2D optical lattice. As outlined before, for $\lambda_{\mathrm{L}} = 830\,\mathrm{nm}$ we are dealing with the situation where the tensor light shift can be neglected so that we will focus only on the contributions from the scalar and vector terms. Our results are more general than those obtained in previous works[9], especially insofar as we do not require the presence of a uniform external magnetic field $\mathbf{B}_{\mathrm{ext}}$ that dominates over the fictitious field $\mathbf{B}^{\mathrm{fict}}(\boldsymbol{r})$ from equation (2.34). As a consequence, $\mathbf{B}^{\mathrm{fict}}(\boldsymbol{r})$ can induce a position-dependent mixing of the various Zeeman substates, which results in qualitatively new effects. In fact, for lattice configurations that involve a non-vanishing fictitious field, the periodicity of the lattice implies a periodic structure of $\mathbf{B}^{\mathrm{fict}}(\boldsymbol{r})$ reminiscent of *magnetic lattices*.[10]

Recall now that our 2D optical lattice (paragraph 2.2.4) is generated by the interference of three linearly polarized Gaussian laser beams with distinct wave vectors

---

[9]See, for example, P. Soltan-Panahi [102] and M. Weinberg [104].

[10]Though C. Becker [101] has emphasized the possibility to generate effective magnetic landscapes with the 2D optical lattice, a detailed consideration has remained unexplored so far.

$\boldsymbol{k}_1, \boldsymbol{k}_2, \boldsymbol{k}_3$ of equal norm k_{L}. In the vicinity of the lattice center we can approximate the electric field of a single lattice beam by a plane wave

$$\mathbf{E}_i(\boldsymbol{r}, t) = \boldsymbol{E}_i \cos(\boldsymbol{k}_i \boldsymbol{r} + \phi_i - \omega_{\mathrm{L}} t) \equiv \boldsymbol{\mathcal{E}}_i^+(\boldsymbol{r}) e^{-\mathrm{i}\omega_{\mathrm{L}} t} + \boldsymbol{\mathcal{E}}_i^-(\boldsymbol{r}) e^{+\mathrm{i}\omega_{\mathrm{L}} t}, \tag{2.35}$$

where ϕ_i are arbitrary phases and we have defined the complex electric strength vectors $\boldsymbol{\mathcal{E}}_i^{\pm}(\boldsymbol{r}) \equiv \boldsymbol{E}_i \exp(\pm\mathrm{i}(\boldsymbol{k}_i \boldsymbol{r} + \phi_i))/2$. Thus, the total electric field distribution at the lattice center is given by

$$\mathbf{E}_{\mathrm{L}}(\boldsymbol{r}, t) = \sum_i \boldsymbol{\mathcal{E}}_i^+(\boldsymbol{r}) e^{-\mathrm{i}\omega_{\mathrm{L}} t} + \text{c.c.} \equiv \boldsymbol{\mathcal{E}}_{\mathrm{L}}^+(\boldsymbol{r}) e^{-\mathrm{i}\omega_{\mathrm{L}} t} + \text{c.c.} \tag{2.36}$$

By inserting this into equation (2.32) and ignoring the tensor light shift, we obtain the following basis-independent representation of the lattice potential operator

$$\hat{V}_{\mathrm{L}}(\boldsymbol{r}) = \hat{V}_{\mathrm{L}}^s(\boldsymbol{r}) + \hat{V}_{\mathrm{L}}^v(\boldsymbol{r}) = -\frac{\alpha_F^s(\omega_{\mathrm{L}})}{4} \sum_{ijk} \left(\boldsymbol{E}_i^2 + \epsilon_{ijk}^2 \boldsymbol{E}_i \boldsymbol{E}_j \cos(\mathbf{b}_k \boldsymbol{r} + \Delta_k) \right) \mathrm{id}_F$$

$$+ \frac{\alpha_F^v(\omega_{\mathrm{L}})}{8F} \sum_{ijk} \epsilon_{ijk} \left(\boldsymbol{E}_i \times \boldsymbol{E}_j \right) \sin(\mathbf{b}_k \boldsymbol{r} + \Delta_k) \cdot \hat{\boldsymbol{F}}. \tag{2.37}$$

Here, $\hat{V}_{\mathrm{L}}^s$ and $\hat{V}_{\mathrm{L}}^v$ are the lattice scalar and vector light-shift operators, respectively. Furthermore, ϵ_{ijk} denotes the Levi-Civita symbol and we have defined the primitive reciprocal lattice vectors $\mathbf{b}_k \equiv \epsilon_{ijk}(\boldsymbol{k}_i - \boldsymbol{k}_j)/2$ and the relative phases $\Delta_k \equiv \epsilon_{ijk}(\phi_i - \phi_j)/2$, where summation is implied over indices that appear twice. Following the definition in equation (2.34), we see that the fictitious magnetic field for the lattice potential is given by

$$\mathbf{B}_{\mathrm{L}}^{\mathrm{fict}}(\boldsymbol{r}) = \frac{\alpha_F^v(\omega_{\mathrm{L}})}{8\mu_{\mathrm{B}} g_F F} \sum_{ijk} \epsilon_{ijk} \left(\boldsymbol{E}_i \times \boldsymbol{E}_j \right) \sin(\mathbf{b}_k \boldsymbol{r} + \Delta_k). \tag{2.38}$$

We note that any pair $(\mathbf{b}_i, \mathbf{b}_j)_{i \neq j}$ from the set of primitive vectors $\{\mathbf{b}_1, \mathbf{b}_2, \mathbf{b}_3\}$ – only two of which are linearly independent – forms a basis of the two-dimensional subspace, known as the reciprocal space, that defines the lattice plane. In particular, any pair $(\mathbf{b}_i, \mathbf{b}_j)_{i \neq j}$ spans the two-dimensional reciprocal Bravais lattice

$$\mathcal{G}_{\mathrm{B}} = \{\mathbf{G} = n_1 \mathbf{b}_i + n_2 \mathbf{b}_j \mid n_1, n_2 \in \mathbb{Z} \wedge i \neq j\}, \tag{2.39}$$

which denotes the set of all possible reciprocal lattice vectors $\mathbf{G}$. As usual, the associated two-dimensional real-space Bravais lattice is obtained from the dual basis $(\mathbf{a}_i, \mathbf{a}_j)_{i \neq j}$, with the defining relation $\mathbf{a}_i \mathbf{b}_j = 2\pi \delta_{ij}$, according to

$$\mathcal{R}_{\mathrm{B}} = \{\mathbf{R} = n_1 \mathbf{a}_i + n_2 \mathbf{a}_j \mid n_1, n_2 \in \mathbb{Z} \wedge i \neq j\}. \tag{2.40}$$

Evidently, the lattice scalar and vector light shift $\hat{V}_{\mathrm{L}}^s(\boldsymbol{r})$ and $\hat{V}_{\mathrm{L}}^v(\boldsymbol{r})$ in equation (2.37) are invariant with respect to discrete translations $T_{\mathbf{R}} : \boldsymbol{r} \mapsto (\boldsymbol{r} + \mathbf{R})$ by an arbitrary lattice vector $\mathbf{R} \in \mathcal{R}_{\mathrm{B}}$. Hence, the total lattice potential $\hat{V}_{\mathrm{L}}(\boldsymbol{r})$ is periodic in accordance with the notion of optical lattices, and the primitive real-space lattice vectors are given by the duals $\mathbf{a}_i$. Obviously, the fictitious magnetic field $\mathbf{B}_{\mathrm{L}}^{\mathrm{fict}}(\boldsymbol{r})$ in equation (2.38) corresponds

to a periodic vector field with the same periodicity. All in all, the lattice potential $\hat{V}_L(\boldsymbol{r})$ constitutes a scalar plus vector light-shift periodic potential. Also note that variations of the relative phases Δ_k in equation (2.37) correspond to translations of the lattice potential. In particular, as is thoroughly discussed in section 5.2, by modulating the frequencies of the individual lattice beams according to some prescribed protocol, it is possible to move the lattice potential $\hat{V}_L(\boldsymbol{r})$ along arbitrary time-dependent trajectories $\mathbf{R}_0(t)$ within the lattice plane. However, for the moment we will assume that the relative phases Δ_k have a fixed but arbitrary value.

So far, we have made no explicit reference to the three wave vectors $\boldsymbol{k}_i$ as defined in equation (2.12) of subsection 2.2.4. As it stands, equation (2.37) and the subsequent results are completely general in the sense that the orientation of the three wave vectors $\{\boldsymbol{k}_i\}$ with common wavenumber k_L can be arbitrary provided that they correspond to the three edges of a generalized tetrahedron that meet at one vertex. Then, the resulting primitive reciprocal lattice vectors $\{\mathbf{b}_k\}$ literally form the three remaining edges of a triangle base. Moreover, the amplitudes E_i, linear polarizations $\boldsymbol{\epsilon}_i = \boldsymbol{E}_i/E_i$, and phases ϕ_i of the individual lattice beams in equation (2.37) can be set arbitrarily, which enables the investigation of a large variety of distinct lattice potentials for all possible configurations of our 2D optical lattice. For the same reason, equation (2.37) is useful to deal with experimental imperfections related to deviations from ideal lattice configurations. This means that one can easily incorporate the effects of geometric misalignments of the wave vectors $\boldsymbol{k}_i$, polarization maladjustments, and intensity imbalances among the individual lattice beams.[11] For the rest of our discussion, we will therefore proceed in this general spirit of arbitrary lattice configurations. Only in the next subsection 2.3.3 will we focus on the specific case of the ideal p-polarization configuration and provide a reduced expression for the corresponding lattice potential.

Role of the external quantization axis Let us now inspect the influence of a static and uniform external magnetic field $\mathbf{B}_{ext}$ that gives rise to an additional Zeeman interaction $\hat{V}_Z = \mu_B g_F \hat{\boldsymbol{F}} \mathbf{B}_{ext}$. We will allow $\mathbf{B}_{ext}$ to point into an arbitrary direction, but we shall assume that the field magnitude is not exceedingly large so that we stay in the regime of the linear Zeeman effect with respect to the magnetic quantum numbers m_F. This condition is always satisfied for the typical experimental scenarios with field values up to a maximum of a few gauss. Then, if there is no strict hierarchy in the magnitudes of the fictitious and the external magnetic field, we have to treat $\mathbf{B}_L^{fict}(\boldsymbol{r})$ and $\mathbf{B}_{ext}$ on an equal footing. In other words, to obtain the new internal eigenstates and eigenvalues in the presence of the Zeeman interaction with the external field, we must diagonalize the total potential $\hat{V}(\boldsymbol{r}) = \hat{V}_L(\boldsymbol{r}) + \hat{V}_Z$.

Following the recipe from the previous subsection 2.3.1, we expand the fields in the spherical basis according to $\mathbf{B}_L^{fict}(\boldsymbol{r}) = B_L^q(\boldsymbol{r})\boldsymbol{e}_q$, and $\mathbf{B}_{ext} = B_{ext}^q \boldsymbol{e}_q$. Similarly, the spin operator can be expanded in the dual basis as $\hat{\boldsymbol{F}} = \hat{F}_q \boldsymbol{e}^q$. With this, the matrix

---

[11]This will be crucial in our study of the anomalous velocity presented in chapter 5.

elements of $\hat{V}(\boldsymbol{r})$ with respect to the standard Zeeman basis $|Fm_F\rangle$ evaluate to

$$
\begin{aligned}
\langle Fm_F|\,\hat{V}_{\mathrm{L}}(\boldsymbol{r})\,|Fm_F'\rangle = {} & V_{\mathrm{L}}^s(\boldsymbol{r})\delta_{m_F m_F'} \\
& + \mu_{\mathrm{B}} g_F (-1)^{F-m_F}\sqrt{F(2F+1)(F+1)}\sum_q B_{\mathrm{L}}^q(\boldsymbol{r})\begin{pmatrix} F & 1 & F \\ -m_F & q & m_F' \end{pmatrix}
\end{aligned}
\tag{2.41}
$$

for the lattice potential $\hat{V}_{\mathrm{L}}(\boldsymbol{r})$, and

$$
\begin{aligned}
\langle Fm_F|\,\hat{V}_{\mathrm{Z}}\,|Fm_F'\rangle = {} & \mu_{\mathrm{B}} g_F (-1)^{F-m_F}\sqrt{F(2F+1)(F+1)} \\
& \times \sum_q B_{\mathrm{ext}}^q \begin{pmatrix} F & 1 & F \\ -m_F & q & m_F' \end{pmatrix}
\end{aligned}
\tag{2.42}
$$

for the Zeeman interaction part $\hat{V}_{\mathrm{Z}}$ with the external field. In equation (2.41), we have defined $V_{\mathrm{L}}^s(\boldsymbol{r})$ simply as $\hat{V}_{\mathrm{L}}^s(\boldsymbol{r})$ with the identity operator id_F stripped off. We stress that the spherical components $B_{\mathrm{L}}^q(\boldsymbol{r})$ are obtained from the scalar products $\langle\mathbf{B}_{\mathrm{L}}^{\mathrm{fict}}, \boldsymbol{e}_q\rangle$, with the fictitious field as defined in equation (2.38). Besides, one easily verifies that equation (2.41) is completely consistent with equation (2.27) by examining the relations in equation (2.26). As a whole, equations (2.41) and (2.42) can be used to diagonalize the total potential $\hat{V}(\boldsymbol{r})$ for arbitrary lattice configurations and external magnetic fields.

Experimentally, we will most often deal with a situation where the external magnetic field $\mathbf{B}_{\mathrm{ext}}$ dominates over the fictitious field $\mathbf{B}_{\mathrm{L}}^{\mathrm{fict}}(\boldsymbol{r})$. For instance, the typical peak magnitudes of the fictitious field in the setting of our ideal p-polarization configuration amount only to a few milligauss such that external fields on the order of a few gauss are already sufficient. In this case, it is customary to apply a basis transformation and to consider the basis $\{\bar{\boldsymbol{e}}_q\}$, which results from a proper rotation of the spherical basis that maps $\boldsymbol{e}_0$ onto the direction of $\mathbf{B}_{\mathrm{ext}}$. Let us denote by $\{|F, \bar{m}_F\rangle\}$ the accordingly rotated Zeeman basis. In this representation, the matrix elements of the total potential $\hat{V}(\boldsymbol{r})$ are then given by

$$
\begin{aligned}
\langle F\bar{m}_F|\,\hat{V}(\boldsymbol{r})\,|F\bar{m}_F'\rangle = {} & V_{\mathrm{L}}^s(\boldsymbol{r})\delta_{\bar{m}_F \bar{m}_F'} \\
& + \mu_{\mathrm{B}} g_F (-1)^{F-\bar{m}_F}\sqrt{F(2F+1)(F+1)}\sum_q \bar{B}_{\mathrm{L}}^q(\boldsymbol{r})\begin{pmatrix} F & 1 & F \\ -\bar{m}_F & q & \bar{m}_F' \end{pmatrix} \\
& + \mu_{\mathrm{B}} g_F \bar{m}_F \bar{B}_{\mathrm{ext}}^0 \delta_{\bar{m}_F \bar{m}_F'}\,.
\end{aligned}
\tag{2.43}
$$

Here, we use the notation $\bar{A}^q$ for the contravariant components of a vector $\mathbf{A} = \bar{A}^q \bar{\boldsymbol{e}}_q$ with respect to the rotated spherical basis, and by $\bar{m}_F$ we denote the magnetic quantum numbers of the correspondingly rotated Zeeman basis. Since by assumption $|\bar{B}_{\mathrm{ext}}^0| \gg |\bar{B}_{\mathrm{L}}^q(\boldsymbol{r})|$, the Zeeman states $\{|F, \bar{m}_F\rangle\}$ are asymptotic eigenstates to $\hat{V}(\boldsymbol{r})$. Thus, one can usually neglect the mixing among different Zeeman substates by discarding the off-diagonal elements from the fictitious field. In other words, in the presence of a strong external magnetic field that defines the quantization axis, the spin mixing is frozen out effectively. By considering only the diagonal elements, we then arrive at the following

effective lattice potential for an atom in a Zeeman substate $|F, \bar{m}_F\rangle$:

$$V_{F,\bar{m}_F}(\boldsymbol{r}) \equiv V_{\mathrm{L}}^s(\boldsymbol{r}) + \mu_{\mathrm{B}} g_F \bar{m}_F \left(\bar{B}_{\mathrm{L}}^0(\boldsymbol{r}) + \bar{B}_{\mathrm{ext}}^0 \right). \tag{2.44}$$

It is evident that the term $\mu_{\mathrm{B}} g_F \bar{m}_F \bar{B}_{\mathrm{L}}^0(\boldsymbol{r})$ describes a spin-dependent or m_F-dependent part of the effective lattice potential that is determined by the projection of the fictitious field $\mathbf{B}_{\mathrm{L}}^{\mathrm{fict}}(\boldsymbol{r})$ onto the direction of the external field $\mathbf{B}_{\mathrm{ext}}$, i.e.

$$\bar{B}_{\mathrm{L}}^0(\boldsymbol{r}) \equiv \langle \mathbf{B}_{\mathrm{L}}^{\mathrm{fict}}(\boldsymbol{r}), \bar{e}_0 \rangle = |\mathbf{B}_{\mathrm{L}}^{\mathrm{fict}}(\boldsymbol{r})| \cos(\theta_{\mathrm{B}}(\boldsymbol{r})), \tag{2.45}$$

where $\theta_{\mathrm{B}}(\boldsymbol{r})$ denotes the local angle between the fictitious and external magnetic field. Hence, in the limit $|\mathbf{B}_{\mathrm{ext}}| \gg |\mathbf{B}_{\mathrm{L}}^{\mathrm{fict}}(\boldsymbol{r})|$, the spin-dependent part of the effective lattice potential, if it is non-vanishing, can be dynamically tuned by changing the orientation of the external magnetic field. This aspect will be discussed further in subsection 2.3.3 for the specific case of the ideal p-polarization configuration that gives rise to a tunable spin-dependent boron-nitride lattice.

Although the above line of reasoning concerning the derivation of an effective lattice potential in the limit of a dominating external magnetic field might seem appropriate, we give a fair warning that it is not entirely correct in general. The reason is that the energy spectrum associated with the external (center of mass) degrees of freedom of the individual Zeeman substates in an optical lattice consists of distinct energy bands, which can be tuned into resonance by the external magnetic field $\mathbf{B}_{\mathrm{ext}}$. As a result, even in the case where the external field is dominant, the off-diagonal elements from the fictitious field $\mathbf{B}_{\mathrm{L}}^{\mathrm{fict}}(\boldsymbol{r})$ can play a crucial role by inducing hybridization, i.e. mixing of $\bar{m}_F$ levels that belong to different bands. Obviously, for a correct description one must then resort to equation (2.43). In future experiments, one may closely inspect these so-called interband spin-mixing processes. For the time being, we shall assume that they are not relevant.

For completeness, we point out that the effective lattice potential (equation (2.44)) can be rewritten in terms of the local polarization intensities $I^q(\boldsymbol{r}) \equiv 2\varepsilon_0 c \, |\langle \boldsymbol{\mathcal{E}}_{\mathrm{L}}^+(\boldsymbol{r}), \bar{e}_q \rangle|^2$ of the lattice electric field.[12] By noting that the total light intensity $I_{\mathrm{L}}(\boldsymbol{r})$ is given by

$$I_{\mathrm{L}}(\boldsymbol{r}) = \sum_q I^q(\boldsymbol{r}) = \frac{\varepsilon_0 c}{2} \sum_{ijk} \boldsymbol{E}_i^2 + \epsilon_{ijk}^2 \boldsymbol{E}_i \boldsymbol{E}_j \cos(\mathbf{b}_k \boldsymbol{r} + \Delta_k), \tag{2.46}$$

and the differential polarization $I_{\mathrm{P}}(\boldsymbol{r}) \equiv I^{+1}(\boldsymbol{r}) - I^{-1}(\boldsymbol{r})$ is given by

$$\begin{aligned} I_{\mathrm{P}}(\boldsymbol{r}) \equiv I^{+1}(\boldsymbol{r}) - I^{-1}(\boldsymbol{r}) &= -\frac{4\varepsilon_0 c F}{\alpha_F^v(\omega_{\mathrm{L}})} \mu_{\mathrm{B}} g_F \bar{B}_{\mathrm{L}}^0(\boldsymbol{r}) \\ &= -\frac{\varepsilon_0 c}{2} \sum_{ijk} \epsilon_{ijk} \left(\boldsymbol{E}_i \times \boldsymbol{E}_j \right) \sin(\mathbf{b}_k \boldsymbol{r} + \Delta_k) \cdot \bar{e}_0, \end{aligned} \tag{2.47}$$

---

[12]The conventional notation of the polarization intensities is given by the identification $(-1, 0, +1) \simeq (\sigma^-, \pi, \sigma^+)$.

the effective lattice potential reads

$$V_{F,\bar{m}_F}(\boldsymbol{r}) = -\frac{\alpha_F^s(\omega_{\mathrm{L}})}{2\varepsilon_0 c}I_{\mathrm{L}}(\boldsymbol{r}) - \frac{\alpha_F^v(\omega_{\mathrm{L}})}{4\varepsilon_0 cF}\bar{m}_F I_{\mathrm{P}}(\boldsymbol{r}) + \mu_{\mathrm{B}}g_F\bar{m}_F\bar{B}_{\mathrm{ext}}^0\,. \tag{2.48}$$

Naturally, $I_{\mathrm{P}}(\boldsymbol{r})$ depends on the orientation of the external magnetic field in the same way as $\bar{B}_{\mathrm{L}}^0(\boldsymbol{r})$. Equation (2.48) can be simplified further by noting that the ground state scalar and vector polarizabilities of Rubidium-87 for the wavelength $\lambda_{\mathrm{L}} = 830\,\mathrm{nm}$ are approximately given by

$$\alpha_F^s(\omega_{\mathrm{L}}) \approx \pi\varepsilon_0 c^3\left(\mathcal{D}_1 + 2\mathcal{D}_2\right), \quad \alpha_F^v(\omega_{\mathrm{L}}) \approx -2\pi\varepsilon_0 c^3 g_F F\left(\mathcal{D}_1 - \mathcal{D}_2\right), \tag{2.49}$$

where

$$\mathcal{D}_i \equiv \frac{\Gamma_i}{\omega_{D_i}^3}\left(\frac{1}{\omega_{D_i} - \omega_{\mathrm{L}}} + \frac{1}{\omega_{D_i} + \omega_{\mathrm{L}}}\right) \tag{2.50}$$

denote the coupling strengths to the D_1 and D_2 transition lines, with natural linewidths $\Gamma_{1,2}$ and transition frequencies $\omega_{D_{1,2}}$. The approximations in equation (2.49) are easily derived from equations (2.28) and (2.33) by taking into account only the predominant coupling to the D_1 and D_2 transition lines and neglecting the hyperfine structure splittings in the transition frequencies, which gives accurate results as long as the detuning stays large compared to the ground and excited state hyperfine structure splittings. With this, equation (2.48) reduces to the same form – aside from a constant Zeeman energy – as presented in earlier works [102–105].

2.3.3 Tunable spin-dependent boron-nitride lattice

Up to now, our considerations regarding lattice potentials have remained general and valid for arbitrary configurations of the 2D optical lattice. For clarity, we now focus on the ideal p-polarization configuration (subsection 2.2.4), which defines the standard configuration for experiments presented in this work. Moreover, we shall assume the presence of a uniform external magnetic field that dominates over the fictitious field. This corresponds to a typical experimental situation where the external quantization axis is generated and controlled by means of our compensation coils (subsection 2.2.2), which provide magnetic field strengths on the order of a few gauss. Hence, we will limit our discussion to effective lattice potentials as introduced in the previous subsection.

Recall now that the ideal p-polarization configuration is characterized by wave vectors $\boldsymbol{k}_i$ as defined in equation (2.12), linear in-plane polarizations $\boldsymbol{\epsilon}_i = (\boldsymbol{k}_i \times \boldsymbol{e}_z)/k_{\mathrm{L}}$ for each lattice beam, and balanced electric field amplitudes $E_i = E_0$. It then follows that the primitive reciprocal lattice vectors $\mathbf{b}_k$ are given by

$$\mathbf{b}_1 = b\boldsymbol{e}_x, \qquad \mathbf{b}_2 = -\frac{b}{2}\left(\boldsymbol{e}_x + \sqrt{3}\boldsymbol{e}_y\right), \qquad \mathbf{b}_3 = -\frac{b}{2}\left(\boldsymbol{e}_x - \sqrt{3}\boldsymbol{e}_y\right), \tag{2.51}$$

with $b \equiv \sqrt{3}k_{\mathrm{L}}$. The associated primitive real-space lattice vectors $\mathbf{a}_i$ read

$$\mathbf{a}_1 = \frac{a}{2}\left(\sqrt{3}\boldsymbol{e}_x - \boldsymbol{e}_y\right), \qquad \mathbf{a}_2 = -a\boldsymbol{e}_y, \qquad a \equiv 2\lambda_{\mathrm{L}}/3 \tag{2.52}$$
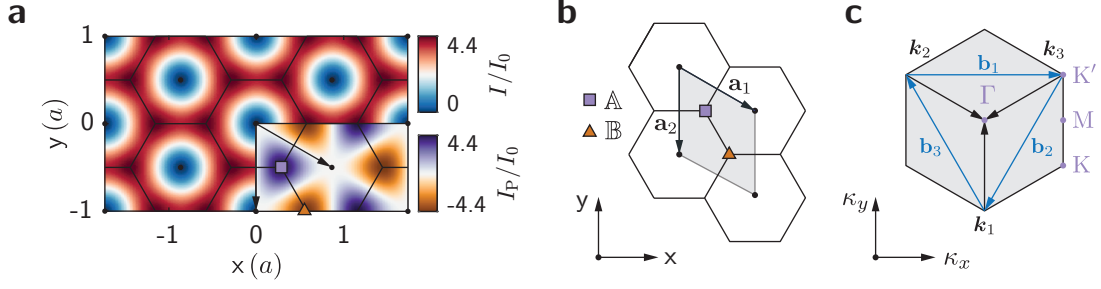
Fig. 2.7: Optical boron-nitride lattice. **a** Total intensity profile I_L and differential polarization I_P in units of the peak intensity I_0 of a single lattice beam, visualized in the vertical xy-plane for $z = 0$. The coordinates are given in units of the fundamental lattice constant $a = 2\lambda_\mathrm{L}/3$ and the quantization axis for I_P was set to $\bar{\boldsymbol{e}}_0 \equiv \boldsymbol{e}_z$. The local maxima of I_L reproduce a two-dimensional bipartite hexagonal lattice with a shallow channel structure around the steep minima of I_L. Local maxima and minima of I_P alternate from $\mathbb{A}$ to $\mathbb{B}$ sublattice site, indicated by a small square and a triangle. **b** Hexagonal Bravais lattice spanned by the primitive lattice vectors $\mathbf{a}_1$ and $\mathbf{a}_2$, with sublattice sites $\mathbb{A}$ and $\mathbb{B}$. The grey rhombus represents the primitive unit cell, and the surrounding hexagons correspond to Wigner-Seitz cells. **c** Reciprocal lattice vectors $\mathbf{b}_i$ and wave vectors $\boldsymbol{k}_i$ arranged inside the Brillouin zone (grey hexagon), with selected high-symmetry points denoted by Γ, M, K, K′.

if we define $(\mathbf{b}_1, \mathbf{b}_2)$ as the standard basis of the two-dimensional reciprocal space. In Figure 2.7b, we show the lattice vectors $\mathbf{a}_1$ and $\mathbf{a}_2$, spanning the primitive unit cell (grey rhombus) of the real-space Bravais lattice. In addition, Figure 2.7c depicts the three wave vectors $\boldsymbol{k}_i$ and their relation to the reciprocal lattice vectors $\mathbf{b}_k$ arranged inside the hexagonal Brillouin zone (grey hexagon). It is evident that the Bravais lattice obtained from equations (2.39) and (2.40) is a two-dimensional hexagonal lattice, characterized by the point group D_6 of sixfold rotations and reflections.

According to equation (2.48), the effective lattice potential for an atom in a Zeeman substate $|F, \bar{m}_F\rangle$ is determined by the total light intensity $I_\mathrm{L}(\boldsymbol{r})$ and the differential polarization $I_\mathrm{P}(\boldsymbol{r})$, which evaluate to

$$I_\mathrm{L}(\boldsymbol{r}) = \frac{\epsilon_0 c E_0^2}{2} \sum_k 3 - \cos(\mathbf{b}_k \boldsymbol{r} + \Delta_k) \,, \tag{2.53}$$

$$I_\mathrm{P}(\boldsymbol{r}) = \frac{\epsilon_0 c \sqrt{3} E_0^2}{4} \langle \boldsymbol{e}_z, \bar{\boldsymbol{e}}_0 \rangle \sum_k \sin(\mathbf{b}_k \boldsymbol{r} + \Delta_k) \,. \tag{2.54}$$

Here, $\langle \boldsymbol{e}_z, \bar{\boldsymbol{e}}_0 \rangle = \cos(\theta_\mathrm{B})$ defines the angle θ_B between the z-axis and the external quantization axis, which, by definition, corresponds to the direction of the external magnetic field $\mathbf{B}_\mathrm{ext}$. Note that the expression for $I_\mathrm{P}(\boldsymbol{r})$ follows from the fact that the fictitious magnetic field $\mathbf{B}_\mathrm{L}^\mathrm{fict}(\boldsymbol{r})$ for the ideal p-polarization configuration is given by

$$\mathbf{B}_\mathrm{L}^\mathrm{fict}(\boldsymbol{r}) = -\frac{\alpha_F^v(\omega_\mathrm{L})}{8\mu_\mathrm{B} g_F F} \frac{\sqrt{3} E_0^2}{2} \sum_k \sin(\mathbf{b}_k \boldsymbol{r} + \Delta_k) \boldsymbol{e}_z \,. \tag{2.55}$$

Figure 2.7a shows a profile of the total light intensity $I_\mathrm{L}(\boldsymbol{r})$ in the vertical xy-plane at

$z = 0$, together with a corresponding profile of the differential polarization $I_P(\boldsymbol{r})$ for a quantization axis $\bar{\boldsymbol{e}}_0 \equiv \boldsymbol{e}_z$, i.e. $\theta_B = 0°$. Clearly, the local maxima of $I_L(\boldsymbol{r})$ trace out hexagons that are arranged around the respective local minima. In particular, they form a two-dimensional graphene-like lattice with hexagonal symmetry and lattice constant $a = 2\lambda_L/3$. As evident from Figure 2.7b, the lattice structure of $I_L(\boldsymbol{r})$ is equivalent to the honeycomb or symmetric boron-nitride lattice, described as a hexagonal Bravais lattice with two sublattice sites $\mathbb{A}$ and $\mathbb{B}$ per unit cell. The latter are located at the vertices of the Wigner-Seitz cell and represent a symmetric twofold atomic basis. When the symmetry of the twofold basis is broken, the lattice corresponds to a proper boron-nitride lattice. Note that both honeycomb and boron-nitride lattices are bipartite, i.e. they can be divided into disjoint sublattices $\mathcal{A}$ and $\mathcal{B}$ such that all nearest-neighbor lattice sites to any $\mathbb{A} \in \mathcal{A}$ lie in $\mathcal{B}$ and vice versa.

Regarding the differential polarization $I_P(\boldsymbol{r})$ in Figure 2.7a, the local maxima and minima of the corresponding profile alternate from $\mathbb{A}$ to $\mathbb{B}$. In particular, for the choice $\theta_B = 0°$ it is evident that the light field is completely $\sigma^+(\sigma^-)$-polarized on the sublattice site $\mathbb{A}(\mathbb{B})$. Obviously, atoms in Zeeman substates $|F, \bar{m}_F\rangle$ with $\bar{m}_F \neq 0$ will therefore experience different light shifts on $\mathbb{A}$ and $\mathbb{B}$. As a result, the lattice potential given by equation (2.48) will correspond to a pure honeycomb lattice for $\bar{m}_F = 0$, while for $\bar{m}_F \neq 0$ and $\theta_B = 0°$ it will exhibit a broken inversion symmetry with a non-vanishing energy offset Δ_{AB} between sublattice sites $\mathbb{A}$ and $\mathbb{B}$, and thus resemble a hexagonal boron-nitride lattice. Specifically, from equations (2.53) and (2.54) it follows that the effective lattice potential of the ideal p-polarization configuration is given by

$$V_{F,\bar{m}_F}(\boldsymbol{r}) = -\frac{V_0(\omega_L)}{8} \sum_k \Big(6 - 2\cos(\mathbf{b}_k \boldsymbol{r} + \Delta_k)$$

$$+ \sqrt{3}\,\bar{m}_F \cos(\theta_B)\eta(\omega_L; F) \sin(\mathbf{b}_k \boldsymbol{r} + \Delta_k)\Big). \quad (2.56)$$

Equation (2.56) will be referred to as the spin-dependent boron-nitride lattice. Note that we have excluded the constant Zeeman energy from the interaction with the external magnetic field. Moreover, we have employed the definitions

$$V_0(\omega_L) \equiv \alpha_F^s(\omega_L)E_0^2 \,, \quad \eta(\omega_L; F) \equiv \frac{\alpha_F^v(\omega_L)}{F\alpha_F^s(\omega_L)} \,. \quad (2.57)$$

The factor $V_0(\omega_L)/8 \equiv V_{2D}$ in equation (2.56) is conveniently defined as the *lattice depth*, which is typically expressed in units of the recoil energy $E_{\mathrm{rec}} = \hbar^2 k_L^2/(2m)$ for an atom of mass m. The frequency-dependent and F-dependent numerical factor $\eta(\omega_L; F)$ describes the relative contribution of the vector light shift. Note that the lattice depth V_{2D} defined in this way refers to the modulation depth along adjacent sublattice sites $\mathbb{A}$ and $\mathbb{B}$ in case of a symmetric boron-nitride lattice, and thus accounts for the shallow channel structure in the intensity profile of I_L. The overall *potential depth* is obviously much larger, which is clear from Figure 2.7a and the fact that the intensity modulation along adjacent minima is large compared to the modulation along adjacent maxima.

From equation (2.56), one can easily deduce that the amplitude of the spin-dependent term, which is responsible for the symmetry breaking discussed above, can be continu-

ously tuned by rotating the external quantization field, i.e. by changing the angle θ_{B}. This implies, for instance, that for Zeeman substates with $\bar{m}_F \neq 0$ the energy offset Δ_{AB} is maximized or minimized at $\theta_{\mathrm{B}} = 0°$, vanishes at $\theta_{\mathrm{B}} = 90°$, i.e. when the quantization axis lies within the lattice plane, and becomes maximally inverted at $\theta_{\mathrm{B}} = 180°$. In particular, from equation (2.56) it follows that the energy offset between two sublattice sites $\mathbb{A}$ and $\mathbb{B}$ is given by

$$\Delta_{\mathrm{AB}} \equiv V_{F,\bar{m}_F}(\boldsymbol{r}_{\mathrm{B}}) - V_{F,\bar{m}_F}(\boldsymbol{r}_{\mathrm{A}}) = 9V_{\mathrm{2D}}\bar{m}_F \cos(\theta_{\mathrm{B}})\eta(\omega_{\mathrm{L}}; F) \,, \qquad (2.58)$$

where $\boldsymbol{r}_{\mathrm{A}}$ and $\boldsymbol{r}_{\mathrm{B}}$ denote their corresponding locations. For example, $\boldsymbol{r}_{\mathrm{A}} \equiv (\mathbf{a}_1 + \mathbf{a}_2)/3$ and $\boldsymbol{r}_{\mathrm{B}} \equiv 2(\mathbf{a}_1 + \mathbf{a}_2)/3$. As will be discussed in chapter 4, the controlled rotation of the external quantization field and the accompanied dynamical change of the energy offset Δ_{AB} constitute the central experimental technique in our setup for the coherent transfer of Rubidium-87 atoms into the higher Bloch bands of an optical boron-nitride lattice.

Finally, two aspects concerning our lattice potentials should be noted. First, the actual lattice configuration of the 2D optical lattice inevitably exhibits deviations from the ideal p-polarization configuration as examined here. Although these deviations are small and usually have no profound influence on the physical properties of bosons in the lowest band of an optical lattice[13], for some settings that we are going to investigate in the following chapters they prove to be crucial. In that case, we will revert to the general expression of the lattice potential as presented in subsection 2.3.2. Second, apart from the ideal p-polarization configuration, there exist additional ideal configurations that yield further lattice potentials, including a *triangular lattice* or a purely spin-dependent *polarization lattice*. A thorough treatment, albeit one that ignores the possibility of vector light-shift-induced spin mixing, is provided, for example, in the works of P. Soltan-Panahi [102] and M. Weinberg [104]. We note that the inclusion of light-shift-induced spin mixing can be accomplished with the general formulas presented in subsection 2.3.2.

2.4 State detection and manipulation

In this final section of chapter 2, we briefly review the methods that are relevant to this thesis for the state detection and state manipulation of a Rubidium-87 quantum gas. We start with a rough sketch of our implementations for absorption imaging along two orthogonal directions, and then comment on the spin-state manipulation by means of RF pulses and RF sweeps.

2.4.1 Absorption imaging after time-of-flight

The standard method for state detection of a cloud of Rubidium-87 atoms at the *Spinor* experiment is based on conventional resonant absorption imaging after a variable time-of-flight (TOF) [148]. Following the main experimental cycle, we switch off all trapping potentials and let the atomic cloud freely expand under the influence of gravity. After

---

[13]See, for instance, Ölschläger [105].

a time t_{TOF}, the cloud is illuminated by a resonant laser beam on the cycling transition $F = 2 \to F' = 3$ of the D_2 line for a duration of $50\,\mu\mathrm{s}$, and the resulting absorption profile $I_{\mathrm{abs}}(\boldsymbol{r}_\perp)$, i.e. the intensity distribution of the detection beam behind the cloud, is imaged with a CCD camera.[14] Here, $\boldsymbol{r}_\perp$ denotes the position vector in the image plane. Naturally, the atomic cloud is destroyed in the process of imaging. A subsequent image recorded at the same parameters without atoms provides the genuine intensity profile $I_{\mathrm{ref}}(\boldsymbol{r}_\perp)$ of the detection beam, serving as a reference. Typically, an additional pair of successive dark images is recorded in absence of the detection beam to account for diffuse background light that falls onto the CCD. Eventually, the intensity distributions on the absorption and reference image can be related via the Beer-Lambert law to yield the optical density OD of the atomic cloud [149–151]

$$\mathrm{OD}(\boldsymbol{r}_\perp) = \sigma_{\mathrm{eff}} n_{\mathrm{2D}}(\boldsymbol{r}_\perp) = -\ln\left(\frac{\eta(\boldsymbol{r}_\perp)I_{\mathrm{abs}}(\boldsymbol{r}_\perp)}{I_{\mathrm{ref}}(\boldsymbol{r}_\perp)}\right). \tag{2.59}$$

Here, $\eta(\boldsymbol{r}_\perp) \equiv \exp\left(-\Delta(\boldsymbol{r}_\perp)/I_{\mathrm{sat}}\right) \in (0, 1]$, with $\Delta \equiv I_{\mathrm{ref}}(\boldsymbol{r}_\perp) - I_{\mathrm{abs}}(\boldsymbol{r}_\perp)$, describes a correction factor due to saturation effects. For all experiments presented within this work, the optical density constitutes the central observable. According to equation (2.59), it is proportional to $n_{\mathrm{2D}}(\boldsymbol{r}_\perp)$, the atomic density distribution integrated along the imaging direction, with a proportionality constant given by the effective cross section σ_{eff} of the detection transition. Importantly, depending on how the trapping potentials are switched off in time, the optical density can contain different information about the system. We will discuss this in more detail in section 3.2 for the particular case of an atomic cloud released from an optical lattice.

The *Spinor* experiment provides two orthogonal detection directions oriented along the -x-axis (PCO) and -z-axis (Andor), respectively. They conform to the fields of view as presented Figure 2.1. The corresponding imaging systems have magnifications $M \approx 3.1$ (PCO) and $M \approx 2.7$ (Andor), and provide a maximum optical resolution in the image plane that is greater than or equal to $10\,\mu\mathrm{m}$. At present, the PCO axis is operated with a pco.pixelfly USB compact CCD camera that offers a dynamic range of 14 bit, a pixel size of $[6.45\,\mu\mathrm{m} \times 6.45\,\mu\mathrm{m}]$, and a quantum efficiency of $15\,\%$ at the detection wavelength $\lambda_{\mathrm{det}} = 780\,\mathrm{nm}$. As a unique feature, it allows for an extremely short interframing time between absorption and reference image down to $1\,\mu\mathrm{s}$. Although such small values are not required in general, an interframing time on the order of $1\,\mathrm{ms}$ is desired to reduce the appearance of fringe patterns on the OD that result from mechanical vibrations, causing shifts in the optical path lengths.

On the other hand, the Andor axis is operated with an Andor iKon-M 934 low noise CCD camera that offers a dynamic range of 16 bit, a pixel size of $[13\,\mu\mathrm{m} \times 13\,\mu\mathrm{m}]$, and a high quantum efficiency of $95\,\%$ at the wavelength $\lambda_{\mathrm{det}} = 780\,\mathrm{nm}$. By means of a special double-shutter acquisition mode, the Andor camera enables a minimum interframing time of $3\,\mathrm{ms}$.

---

[14]To detect atoms in the hyperfine level $F = 1$, the cloud is simultaneously illuminated by a repumper on the open transition $F = 1 \to F' = 2$.

2.4.2 Spin-state manipulation

A central feature of our setup is the ability to prepare Rubidium-87 atoms in a variety of different well-defined spin states of the ground state hyperfine manifold $F = 1, 2$. The necessary experimental techniques have been implemented and pioneered in previous works [98–101]. Usually, the starting point is a spin-polarized BEC in the Zeeman substate $|F = 1, m_F = -1\rangle$ for some fixed quantization field $\mathbf{B}_{\text{ext}}$. To change the spin state, we induce magnetic dipole transitions[15] by coupling to an oscillating magnetic field

$$\mathbf{B}_{\text{rf}}(t) = \mathbf{B}_{\text{rf}} \cos\left(\phi(t)\right). \tag{2.60}$$

Here, $\mathbf{B}_{\text{rf}}$ is a uniform real-valued magnetic strength vector and $\phi(t)$ denotes a time-dependent phase. In general, the oscillating magnetic field is generated by an RF or microwave (MW) source that drives an appropriate signal through an RF antenna or waveguide located in the vicinity of the science cell, respectively. For the controlled spin-state manipulation we work in the regime $|\mathbf{B}_{\text{ext}}| \gg |\mathbf{B}_{\text{rf}}|$, where we distinguish between the two following techniques:

RF pulses By choosing a monochromatic drive with a frequency $\dot{\phi}(t) \equiv \omega_{\text{rf}}$ that matches the Zeeman splitting in the external field, we induce multilevel Rabi cycles in the spin space of a given hyperfine level F. In particular, for a quantization field on the order of a few gauss, the quadratic Zeeman effect can be neglected and the Zeeman splitting $\Delta E_{\text{Z}} = \hbar\omega_{\text{Z}} \equiv |\mu_{\text{B}}g_F B_{\text{ext}}|$ between adjacent sublevels is equidistant, where ω_{Z} denotes the corresponding Larmor frequency. In this case, it turns out that the Hamiltonian that characterizes the spin dynamics in the rotating wave approximation is of the form

$$\hat{H}_F = \hbar\Omega(\boldsymbol{u} \cdot \hat{\boldsymbol{F}}), \tag{2.61}$$

with a unit vector $\boldsymbol{u}$ and a generalized Rabi frequency $\Omega = \left(\Delta^2 + \Omega_{\text{rf}}^2\right)^{\frac{1}{2}}$. For the latter, we have defined the detuning $\Delta \equiv \omega_{\text{Z}} - \omega_{\text{rf}}$ and the normal Rabi frequency $\Omega_{\text{rf}} \equiv \mu_{\text{B}}g_F B_{\text{rf}}^{\perp}/(2\hbar)$, where $B_{\text{rf}}^{\perp}$ is the norm of the field component $\mathbf{B}_{\text{rf}}^{\perp}$ that is perpendicular to $\mathbf{B}_{\text{ext}}$. As before, by the operator $\hbar\hat{\boldsymbol{F}} = \hat{\mathbf{F}}$ we denote the standard angular momentum or spin operator acting in the given hyperfine manifold F. The unit vector $\boldsymbol{u}$ in equation (2.61) is defined by

$$\boldsymbol{u} \equiv \frac{\Delta}{\Omega}\frac{\mathbf{B}_{\text{ext}}}{B_{\text{ext}}} + \frac{\Omega_{\text{rf}}}{\Omega}\frac{\mathbf{B}_{\text{rf}}^{\perp}}{B_{\text{rf}}^{\perp}}. \tag{2.62}$$

Assume now that $\mathbf{B}_{\text{rf}}(t)$ is turned on at some time t_0. Then, since the Hamiltonian $\hat{H}_F$ is time-independent, the time-evolution operator for times $t \geq t_0$ reads

$$\hat{U}(t) = \exp\left(-\frac{\text{i}}{\hbar}\hat{H}_F(t - t_0)\right) = \exp\left(-\text{i}\Omega(t - t_0)(\boldsymbol{u} \cdot \hat{\boldsymbol{F}})\right), \tag{2.63}$$

which describes a spin rotation around the axis $\boldsymbol{u}$ at an angular velocity Ω. Specifically, if the driving frequency ω_{rf} is in resonance with the Larmor frequency ω_{Z}, the axis of

---

[15]See, for example, Sobel'Man [152].

rotation will be perpendicular to $\mathbf{B}_{\mathrm{ext}}$.

A common use case for spin rotations in our experiment is a π-pulse, where a resonant field $\mathbf{B}_{\mathrm{rf}}(t)$ is turned on for a duration $\tau \equiv t - t_0$ such that $\Omega\tau = \pi$. For instance, given the initial state $|1, -1\rangle$, this will cause a complete transfer (spin flip) to the state $|1, +1\rangle$. We stress that by choosing different pulse lengths or detunings, it is also possible to realize superpositions of different Zeeman substates $|F, \bar{m}_F\rangle$ with well-defined relative phases. Within this thesis, RF pulses for spin-state manipulation are usually employed at moderate quantization fields on the order of $1\,\mathrm{G}$ to $3\,\mathrm{G}$. We note that the different Zeeman substates can be detected individually by a conventional Stern-Gerlach separation and subsequent absorption imaging after TOF.

RF and MW sweeps   Another approach for controlled spin-state manipulation is based on the adiabatic passage through an avoided crossing [153]. Here, one may induce a complete population transfer between two spin states adhering to $\Delta m_F = 0, \pm 1$ and $\Delta F = 0, \pm 1$ by sweeping the frequency of the driving field $\mathbf{B}_{\mathrm{rf}}(t)$ across the relevant transition line ω. In practice, the sweep is accomplished from an initial frequency value $\dot{\phi}(t_0) = \omega - |\delta|$ to an end value $\dot{\phi}(t_{\mathrm{e}}) = \omega + |\delta|$ via a constant sweep slope $\ddot{\phi}(t) = c > 0$, where $2|\delta|$ is the sweep range, which must be chosen appropriately. If the sweep is sufficiently slow, the initial state will adiabatically follow its instantaneous eigenstate, thus giving rise to an adiabatic passage. We emphasize that the driving signal is turned off at the end of the sweep at time t_{e}, similar to the pulse technique from the previous paragraph. This type of sweep signal is hence identical to what is known as a chirped pulse.

To selectively address transitions $\Delta m_F = \pm 1$ for the case $\Delta F = 0$, i.e. within a given hyperfine manifold F, the external quantization field $\mathbf{B}_{\mathrm{ext}}$ should lift the degeneracy in the splittings of adjacent sublevels. In fact, this is a crucial requirement to avoid the follow-up population of consecutive Zeeman substates during the sweep. We typically choose $|\mathbf{B}_{\mathrm{ext}}| = 30\,\mathrm{G}$, which induces a quadratic Zeeman shift that results in a frequency *difference* on the order of $2\pi \cdot 100\,\mathrm{kHz}$ among neighboring transitions. An example for an adiabatic passage in this case is provided by a complete transfer $|1, -1\rangle \to |1, 0\rangle$ via a frequency sweep from $2\pi \cdot 20.6\,\mathrm{MHz}$ to $2\pi \cdot 21.6\,\mathrm{MHz}$ in $20\,\mathrm{ms}$. The corresponding RF sweep signal or chirped pulse is generated by a versatile frequency generator.[16]

In a similar way, it is possible to realize hyperfine level changing transitions $\Delta F = \pm 1$. Here, a strong external field $\mathbf{B}_{\mathrm{ext}}$ is not required to address the individual transitions $\Delta m_F = 0, \pm 1$, since the corresponding manifolds are separated by the ground state hyperfine splitting $\omega_{\mathrm{hfs}} \approx 2\pi \cdot 6.835\,\mathrm{GHz}$. For this reason, it is sufficient to stay in the linear Zeeman regime, say with $|\mathbf{B}_{\mathrm{ext}}|$ on the order of $1\,\mathrm{G}$, to lift the degeneracies of the transition lines. In practice, to bridge the hyperfine splitting, the RF sweep signal is combined with a suitable frequency offset from a microwave generator. The mixed signal gives a MW sweep that is used, for example, to perform a complete adiabatic transfer $|1, -1\rangle \to |2, -2\rangle$.

We note that, in comparison to RF pulses, RF and MW sweeps are generally less sensitive to fluctuations in the external magnetic field strength and driving field amplitude, thus enabling accurate and faultless spin-state manipulation with a high fidelity.

---

[16]Photonics Technologies Versatile Frequency Generator VFG-150.

It is also possible to combine RF and MW sweeps with RF pulses in multiple sequences to prepare a multitude of different spin states. Moreover, non-adiabatic sweeps can be performed that yield Landau-Zener type transitions and allow for the creation of fine-tuned spin mixtures. For further details regarding these aspects, we refer to the theses of H. Schmaljohann, M. Erhard, J. Kronjäger, and C. Becker [98–101].

3 Ultracold atoms in a tunable spin-dependent boron-nitride lattice

This chapter is dedicated to the formal description of ultracold bosonic atoms in optical lattices and its application to central experimental techniques. For this reason, I briefly review the Bloch formalism, established for the description of non-interacting particles in periodic potentials, and present exact numerical calculations of the eigenspace and eigenspectrum for our spin-dependent optical boron-nitride lattice. Particular emphasis is put on an accurate characterization of higher Bloch orbitals and their physical properties, such as the intrinsic orbital angular momentum. Furthermore, we elaborate on the central experimental observables and probing methods used throughout this work. Based on this, I demonstrate how amplitude-modulation spectroscopy and Kapitza-Dirac diffraction can be used to calibrate the lattice depth and in situ orientation of the external quantization field, respectively.

The main objective in the study of atoms in optical lattices is to understand the dynamical evolution as well as the stationary equilibrium properties of a system of N particles (atoms) subject to a variety of different external conditions in the presence of a periodic potential. Formally, this requires to solve the many-body Schrödinger equation for elements $|\Psi\rangle$ of the N-particle Hilbert space $\mathscr{H}_N$, which, however, is a formidable and usually intractable task for systems with large particle numbers and interactions among the individual constituents. The main difficulty can be traced back to the fact that the size of $\mathscr{H}_N$ grows exponentially with N. Therefore, one has to rely on adequate approximations that reduce the complexity of the problem while preserving the key aspects and ingredients that provide insights into important physical observables.

In the case of ultracold *bosonic* atoms in optical lattices, being the focus of our discussion here, a natural starting point for approximation schemes as well as exact numerical and analytical methods is provided by the Bose-Hubbard model (BHM) and its various extensions. Indeed, bosonic atoms in optical lattices constitute nearly perfect realizations of the BHM, allowing for a strong interconnection between experiment and theory. Most prominently, the BHM has been successful in predicting a quantum phase transition from a superfluid to a Mott insulating state [154], which was experimentally verified in optical lattices [155] soon after a proposal by Jaksch et al. [35]. In principle, the BHM captures most of the physics of bosonic atoms in optical lattices, but explicit calculations within this model are typically quite involved.[1]

When interactions are small and correlations among the atoms can be ignored, a conceptually and technically more simple approach is suitable. Commonly, this is provided

---

[1]An excellent review of the BHM and related methods in the context of optical lattices is provided by Lewenstein et al. [32].

by the famous Gross-Pitaevskii equation (GPE).[2] The GPE yields an effective description of a weakly interacting bosonic ensemble in terms of a non-linear field equation for the order parameter ψ related to the macroscopic occupation of a single 1-particle state, i.e. the occurrence of a BEC. It has proved successful in the study of BECs in various trap configurations, including optical lattices. Essentially, the GPE builds on a self-consistent mean-field ansatz with the central premise that the system is present as a pure BEC. For this reason, strictly speaking, it cannot account for situations where this condition fails; for instance, at temperatures above zero where the presence of an additional thermal component must be included. Similarly, the GPE fails for systems with strong interactions or when correlations between atoms become important. Nevertheless, as long as the thermal and quantum depletion from the condensate remain small, the GPE is a valuable tool for the study of weakly interacting bosonic atoms in optical lattices, providing reasonable results in the superfluid low-temperature limit. Furthermore, the GPE can be refined and generalized to incorporate effects from coupling to a non-vanishing thermal component at finite temperatures [158, 159]. Based on the Hartree-Fock-Bogoliubov-Popov (HFBP) approximation [160], it is then possible to derive an effective finite-temperature theory of superfluid bosons in optical lattices [161], which allows for an accurate treatment under a large number of realistic experimental conditions.

By far the most simplistic approach to the N-particle problem is given by a free-particle (independent-particle) description, i.e. where the interaction among particles is completely ignored. The corresponding single-particle problem is always solvable and offers a well-established and transparent framework for understanding different fundamental concepts, such as band structures, the geometric phase, or non-interacting symmetry-protected topological (SPT) orders, including topological insulators and superconductors. Though the ambition and scope of this thesis is less generic or fundamental, in the majority of cases, for reasons of clarity and simplicity, we will mainly focus on single-particle calculations for comparison with experimental data. In fact, as we will see in this chapter and in the following ones, for our experimental settings in the weakly interacting superfluid regime, single-particle calculations are usually in good agreement with experimental observations. This can be understood from the point of view that we shall often be interested merely in the coarse-grained distribution of the high-momentum components of a BEC in an optical lattice, which is determined primarily by the microscopic periodic structure of the lattice potential itself. Interactions, on the other hand, mainly affect the details of the momentum distribution on a smaller scale, which can be frequently ignored. By the same reason, it is often justified to neglect the additional external harmonic confinement from the overall trapping potential. Yet, it is clear that other observables, in general, might be more susceptible to interactions and the external harmonic confinement. In that case, single-particle calculations are inadequate but may still provide a qualitative agreement and form the basis for more sophisticated approaches like those discussed above, which include effects from interactions at different levels of approximation.

---

[2]For an extensive discussion of the GPE and its application, we refer to the standard monographs by Pitaevskii and Stringari [156] and Pethick and Smith [157].

3.1 Non-interacting atoms in a spin-dependent boron-nitride lattice

In this section, I introduce some of the basic notations and formal relations that will guide our studies in subsequent chapters. We shall start our discussion with a preparatory note on the adiabatic approximation for the quantum mechanical motion of atoms in an optical lattice. Based on this, we review the physics of non-interacting atoms in periodic potentials by providing a brief survey of the Bloch formalism, which is an indispensable tool for understanding condensates in optical lattices. The concise notation that we follow is largely self-contained. Finally, I present exact numerical calculations of Bloch bands and Bloch states for our spin-dependent boron-nitride lattice and elaborate on important physical properties, such as the mean momentum and mean orbital angular momentum of Bloch states.

3.1.1 Adiabatic approximation

The total single-particle Hilbert space of an atom is usually defined as the tensor product $\mathscr{H}_{\mathrm{atom}} = \mathscr{H}_{\mathrm{int}} \otimes \mathscr{H}_{\mathrm{ext}}$ of the Hilbert space $\mathscr{H}_{\mathrm{int}}$ of internal electronic states and the Hilbert space $\mathscr{H}_{\mathrm{ext}}$ of external motional states that represent the atomic center of mass motion in configuration space. So far, in our discussion of the AC Stark shift and the optical lattice potentials in chapter 2, we have ignored the dynamical evolution of the atomic external degrees of freedom and treated the coordinate $\boldsymbol{r}$ as a fixed parameter of configuration space. In the following, we will promote it to a dynamical variable, i.e. we will replace $\boldsymbol{r}$ by the position operator $\hat{\boldsymbol{r}}$ that acts on $\mathscr{H}_{\mathrm{ext}}$, and ask for the full quantum mechanical motion of atoms under the action of the augmented AC Stark operator $\hat{V}_{\mathrm{AC}}(\boldsymbol{r}) \rightarrow \hat{V}_{\mathrm{AC}}(\hat{\boldsymbol{r}}) \equiv \hat{\mathcal{V}}_{\mathrm{AC}}$. In what follows, operators in calligraphic letters will denote operators that act on the total space $\mathscr{H}_{\mathrm{atom}}$.

First, consider a general *local* interaction operator $\hat{\mathcal{V}}$ on $\mathscr{H}_{\mathrm{atom}}$. Let $\{|a\rangle\}$ and $\{|\boldsymbol{r}\rangle\}$ denote a complete orthonormal basis of $\mathscr{H}_{\mathrm{int}}$ and $\mathscr{H}_{\mathrm{ext}}$, respectively. Then, $\{|a\rangle \otimes |\boldsymbol{r}\rangle\}$ provides a corresponding tensor basis of $\mathscr{H}_{\mathrm{atom}}$ such that $\hat{\mathcal{V}}$ can be expanded as

$$\hat{\mathcal{V}} = \sum_{ab} \int \mathrm{d}\boldsymbol{r}\, \mathrm{d}\boldsymbol{r}'\, V_{ab}(\boldsymbol{r},\boldsymbol{r}')\, |a\rangle\langle b| \otimes |\boldsymbol{r}\rangle\langle \boldsymbol{r}'| = \sum_{ab} \int \mathrm{d}\boldsymbol{r}\, V_{ab}(\boldsymbol{r})\, |a\rangle\langle b| \otimes |\boldsymbol{r}\rangle\langle \boldsymbol{r}| \,. \tag{3.1}$$

Here, $V_{ab}(\boldsymbol{r},\boldsymbol{r}')$ are the defining matrix elements of $\hat{\mathcal{V}}$ in the tensor basis $\{|a\rangle \otimes |\boldsymbol{r}\rangle\}$, and we require that they are diagonal in $\boldsymbol{r}$, i.e. $V_{ab}(\boldsymbol{r},\boldsymbol{r}') = V_{ab}(\boldsymbol{r})\, \delta(\boldsymbol{r} - \boldsymbol{r}')$. Accordingly, $\hat{\mathcal{V}}$ is called a *local* operator. For clarity, we will now assume that the elements $|a\rangle$ represent the atomic bare internal states, that is the eigenstates of the atomic internal Hamiltonian $\hat{H}_{\mathrm{int}}$ in the absence of atom-light interaction. In the latter case, the total atomic Hamiltonian has a simple form:

$$\hat{\mathcal{H}}^0 = \hat{H}_{\mathrm{int}} \otimes \mathrm{id}_{\mathrm{ext}} + \mathrm{id}_{\mathrm{int}} \otimes \hat{T} \,, \tag{3.2}$$

where id denotes the identity operator on the respective space, and $\hat{T} = \hat{\boldsymbol{p}}^2/(2\mu)$ is the kinetic energy operator on $\mathscr{H}_{\mathrm{ext}}$ for an atom of mass μ. Note that the structure of the Hamiltonian $\hat{\mathcal{H}}^0$ allows to treat the atomic internal and external degrees of

freedom separately. By contrast, in the presence of the interaction $\hat{\mathcal{V}}$, the total atomic Hamiltonian

$$\hat{\mathcal{H}} = \hat{\mathcal{H}}^0 + \hat{\mathcal{V}} \tag{3.3}$$

induces a mixing between both spaces if $V_{ab}(\boldsymbol{r})$ is not a constant function of $\boldsymbol{r}$, and hence obstructs a simple decomposition of the equations of motion. In general, obtaining solutions of the Schrödinger equation for a Hamiltonian $\hat{\mathcal{H}}$ with arbitrary local interactions $\hat{\mathcal{V}}$ is a challenging task. A major simplification is achieved if it is possible to restrict considerations onto a subspace $\mathscr{H}_{\mathrm{int}}^F \subset \mathscr{H}_{\mathrm{int}}$ that is spanned by a finite number of bare internal states. At the simplest level, this amounts to solving the Schrödinger equation for the effective Hamiltonian

$$\hat{\mathcal{H}}_{\mathrm{eff}} \equiv \left(\hat{P}_F \otimes \mathrm{id}_{\mathrm{ext}} \right) \hat{\mathcal{H}} \left(\hat{P}_F \otimes \mathrm{id}_{\mathrm{ext}} \right), \tag{3.4}$$

where $\hat{P}_F$ is the projector onto the relevant internal subspace $\mathscr{H}_{\mathrm{int}}^F$. Note that this leads to an effective interaction

$$\hat{\mathcal{V}}_{\mathrm{eff}} = \sum_{ab \in \mathscr{H}_{\mathrm{int}}^F} \int \mathrm{d}\boldsymbol{r}\, V_{ab}(\boldsymbol{r})\, |a\rangle\langle b| \otimes |\boldsymbol{r}\rangle\langle \boldsymbol{r}|. \tag{3.5}$$

In view of the AC Stark shift discussed in section 2.3, the expression for the effective Hamiltonian becomes

$$\hat{\mathcal{V}}_{\mathrm{eff}} = \hat{V}_{\mathrm{AC}} = \sum_{mm'}^{M} \int \mathrm{d}\boldsymbol{r}\, V_{mm'}(\boldsymbol{r})\, |m\rangle\langle m'| \otimes |\boldsymbol{r}\rangle\langle \boldsymbol{r}|, \tag{3.6}$$

where $\mathscr{H}_{\mathrm{int}}^F$ is identified with the M-dimensional hyperfine manifold spanned by the set of $M = 2F + 1$ Zeeman substates $\{|a\rangle \equiv |(nJF)m_F\rangle\}$ to some fixed quantum numbers (nJF). We stress that the matrix elements $V_{mm'}(\boldsymbol{r}) \equiv \langle m|\hat{V}_{\mathrm{AC}}(\boldsymbol{r})|m'\rangle$ in equation (3.6) are directly obtained from equation (2.27) and that indices (nJF) have been suppressed for clarity. We now argue that the restriction onto the subspace of a single hyperfine manifold is justified in the case of the AC Stark shift for two reasons: First, we assume that it is a non-resonant and small perturbation at every point $\boldsymbol{r}$, in the sense that (nJF) remain good quantum numbers to a very good approximation. In other words, the AC Stark shift only weakly couples bare internal states $|a\rangle \equiv |(nJF)m_F\rangle$ with different (nJF). Apart from that, however, it may induce a strong coupling among Zeeman substates of the same hyperfine manifold, i.e. within the relevant subspace $\mathscr{H}_{\mathrm{int}}^F$. Second, we assume that the atoms move sufficiently slowly through configuration space such that motional coupling to internal states outside $\mathscr{H}_{\mathrm{int}}^F$ can be neglected. Of course, a general requirement is that $\mathscr{H}_{\mathrm{int}}^F$ is well separated in energy from the remaining states compared to the atomic kinetic energy. For the atomic levels that are relevant to our discussion here, this is certainly fulfilled under all realistic experimental scenarios. Taken together, an atom prepared in $\mathscr{H}_{\mathrm{int}}^F$ shall remain in that subspace throughout the dynamical evolution in configuration space. We note that this is similar to the adiabatic or Born-Oppenheimer approximation in molecular physics [162]. But, instead of an adiabatic following regarding a single dressed internal state, we consider here an adiabatic following with respect to a bare internal *subspace*. If no further

simplification is applicable or justified, we shall diagonalize the effective Hamiltonian $\hat{\mathcal{H}}_{\text{eff}} = \hat{\mathcal{H}}_{\text{eff}}^0 + \hat{\mathcal{V}}_{\text{AC}}$ in the restricted total subspace $\mathscr{H}_{\text{int}}^F \otimes \mathscr{H}_{\text{ext}}$. In the context of optical lattice potentials, where all elements $V_{mm'}(\boldsymbol{r})$ in equation (3.6) are periodic functions of $\boldsymbol{r}$, this is readily achieved in a momentum-spin basis $\{|m\rangle \otimes |\mathbf{G}\rangle\}$.[3] We also note that if an additional external magnetic field is present, $\hat{\mathcal{V}}_{\text{AC}}$ should be supplemented by a corresponding Zeeman interaction $\hat{\mathcal{V}}_{\text{AC}} \to \hat{\mathcal{V}}_{\text{AC}} + \hat{\mathcal{V}}_{\text{Z}}$. For instance, for our 2D optical lattice the matrix elements $V_{mm'}(\boldsymbol{r})$ in that case are explicitly given by equations (2.41) to (2.42).

Most often, we shall deal with a situation where an additional adiabatic decoupling within the subspace $\mathscr{H}_{\text{int}}^F$ is appropriate. In particular, as we examine below, under the premise of an adiabatic evolution of internal states in $\mathscr{H}_{\text{int}}^F$, one can derive a reduced Hamiltonian for the respective atomic center of mass motion. To this end, let us define $|\eta_m(\boldsymbol{r})\rangle \otimes |\boldsymbol{r}\rangle$ as an eigenstate to the operator $\hat{\mathcal{V}}_{\text{eff}} \equiv \hat{\mathcal{V}}_{\text{AC}} + \hat{\mathcal{V}}_{\text{Z}}$ that includes a Zeeman interaction with a uniform external magnetic field. This implies that the internal state $|\eta_m(\boldsymbol{r})\rangle$ is an eigenstate to $\hat{V}(\boldsymbol{r}) \equiv \hat{V}_{\text{AC}}(\boldsymbol{r}) + \hat{V}_{\text{Z}}$, specifically [48, 49]

$$\hat{V}(\boldsymbol{r}) |\eta_m(\boldsymbol{r})\rangle = v_m(\boldsymbol{r}) |\eta_m(\boldsymbol{r})\rangle. \tag{3.7}$$

Here, $v_m(\boldsymbol{r})$ denotes the corresponding eigenvalue. The different eigenstates $|\eta_m(\boldsymbol{r})\rangle$ are related to the bare internal states $|m\rangle$ by an $\boldsymbol{r}$-dependent unitary basis transformation

$$|\eta_m(\boldsymbol{r})\rangle = \hat{U}(\boldsymbol{r}) |m\rangle \equiv \sum_{m'}^M U_{m'm}(\boldsymbol{r}) |m'\rangle. \tag{3.8}$$

Note, however, that since the eigenstates $|\eta_m(\boldsymbol{r})\rangle$ are only unique up to a phase factor $\exp(\mathrm{i}\phi_m(\boldsymbol{r}))$, with arbitrary real-valued functions $\phi_m(\boldsymbol{r})$, the transformation $\hat{U}(\boldsymbol{r})$ is not uniquely defined as a function of $\boldsymbol{r}$. In the following, we will assume a phase gauge where all matrix elements $U_{m'm}(\boldsymbol{r})$ in equation (3.8) are smooth functions on the configuration space.[4] The set $\{|\eta_m(\boldsymbol{r})\rangle\}$ will be called an eigenbasis of local *dressed* internal states [48, 49]. For each value of $\boldsymbol{r}$, it constitutes a complete orthonormal basis of $\mathscr{H}_{\text{int}}^F$. Thus, any state $|\Psi\rangle \in \mathscr{H}_{\text{int}}^F \otimes \mathscr{H}_{\text{ext}}$ can be expanded as

$$|\Psi\rangle = \sum_m^M \int \mathrm{d}\boldsymbol{r}\, \psi_m(\boldsymbol{r}) |\eta_m(\boldsymbol{r})\rangle \otimes |\boldsymbol{r}\rangle\,, \tag{3.9}$$

where $\psi_m(\boldsymbol{r})$ is readily interpreted as the probability amplitude to find an atom in the m-th dressed internal state at point $\boldsymbol{r}$. To proceed, we will now invoke the adiabatic approximation, this time by assuming that the dressed eigenvalues $v_m(\boldsymbol{r})$ for all values of $\boldsymbol{r}$ are well-separated relative to the kinetic energy. In practice, this is accomplished by a suitable and sufficiently strong fictitious or external magnetic field that breaks the degeneracy among the Zeeman substates and provides the desired level of separation.

---

[3]The states $|\mathbf{G}\rangle \in \mathscr{H}_{\text{ext}}$ refer to discrete momentum states of the reciprocal lattice, as discussed in subsection 3.1.2.

[4]In general, the smoothness condition is incompatible with $U_{m'm}(\boldsymbol{r})$ being single-valued functions on the whole configuration space. Such peculiarities are related to the theory of complex vector bundles on a manifold M (see, for example, [163, 164]). For $M = \mathbb{R}^3$, as tacitly assumed here, there is no problem to it.

Thus, an atom prepared in a local dressed internal state shall remain in the corresponding manifold of adiabatically connected eigenstates. Under this adiabatic ansatz, one can now derive (see also [49]) a *reduced* Hamiltonian $\hat{H}_{\text{ext}}^m \equiv \langle m | \hat{\mathcal{H}}'_{\text{eff}} | m \rangle$ solely for the center of mass motion of the m-th dressed internal state by tracing out the bare internal state $|m\rangle$ in the transformed Hamiltonian $\hat{\mathcal{H}}'_{\text{eff}} \equiv \hat{\mathcal{U}}^\dagger (\hat{\mathcal{H}}_{\text{eff}}^0 + \hat{\mathcal{V}}_{\text{eff}}) \hat{\mathcal{U}}$, where

$$\hat{\mathcal{U}} \equiv \int \mathrm{d}\boldsymbol{r}\, \hat{U}(\boldsymbol{r}) \otimes |\boldsymbol{r}\rangle\langle\boldsymbol{r}| = \sum_{mm'}^M \int \mathrm{d}\boldsymbol{r}\, U_{mm'}(\boldsymbol{r}) |m\rangle\langle m'| \otimes |\boldsymbol{r}\rangle\langle\boldsymbol{r}|. \tag{3.10}$$

By construction, this transformation brings $\hat{\mathcal{V}}_{\text{eff}}$ into a diagonal form with respect to the bare internal states, i.e.

$$\hat{\mathcal{U}}^\dagger \hat{\mathcal{V}}_{\text{eff}} \hat{\mathcal{U}} = \sum_m^M \int \mathrm{d}\boldsymbol{r}\, v_m(\boldsymbol{r}) |m\rangle\langle m| \otimes |\boldsymbol{r}\rangle\langle\boldsymbol{r}|. \tag{3.11}$$

After a lengthy but straightforward calculation, it is verified that the reduced Hamiltonian $\hat{H}_{\text{ext}}^m$ can be written as (compare [48, 49, 165–167])

$$\hat{H}_{\text{ext}}^m \equiv \langle m | \hat{\mathcal{H}}'_{\text{eff}} | m \rangle = \frac{(\hat{\boldsymbol{p}} - \boldsymbol{A}_m(\hat{\boldsymbol{r}}))^2}{2\mu} + v_m(\hat{\boldsymbol{r}}) + w_m(\hat{\boldsymbol{r}}) + E_F. \tag{3.12}$$

Here, E_F refers to the bare atomic energy of the hyperfine manifold. The operators $\hat{\boldsymbol{p}}$ and $\hat{\boldsymbol{r}}$ denote the vector-valued momentum and position operator on $\mathscr{H}_{\text{ext}}$, respectively. Moreover, we have employed the definitions

$$\boldsymbol{A}_m(\boldsymbol{r}) = \boldsymbol{A}_{mm}(\boldsymbol{r}) \equiv \mathrm{i}\hbar \langle \eta_m(\boldsymbol{r}) | \boldsymbol{\nabla} \eta_m(\boldsymbol{r}) \rangle = \mathrm{i}\hbar \sum_n^M U_{nm}^*(\boldsymbol{r}) \boldsymbol{\nabla} U_{nm}(\boldsymbol{r}), \tag{3.13a}$$

$$\begin{aligned} w_m(\boldsymbol{r}) &\equiv \frac{1}{2\mu} \sum_{n \neq m}^M \boldsymbol{A}_{nm}(\boldsymbol{r}) \cdot \boldsymbol{A}_{mn}(\boldsymbol{r}) = \frac{\hbar^2}{2\mu} \sum_{n \neq m}^M |\langle \eta_n(\boldsymbol{r}) | \boldsymbol{\nabla} \eta_m(\boldsymbol{r}) \rangle|^2 \\ &= \frac{\hbar^2}{2\mu} \sum_{n \neq m}^M \sum_{ij}^M U_{in}^*(\boldsymbol{r}) U_{jn}(\boldsymbol{r}) \left[(\boldsymbol{\nabla} U_{im}(\boldsymbol{r})) \cdot (\boldsymbol{\nabla} U_{jm}^*(\boldsymbol{r})) \right]. \end{aligned} \tag{3.13b}$$

We emphasize that if $|\psi_m\rangle \in \mathscr{H}_{\text{ext}}$ defines an external eigenstate to $\hat{H}_{\text{ext}}^m$, the product state $|\Psi'_m\rangle \equiv |m\rangle \otimes |\psi_m\rangle$ yields the corresponding adiabatic solution $|\Psi_m\rangle$ with respect to the untransformed Hamiltonian $\hat{\mathcal{H}}_{\text{eff}}$ via

$$|\Psi_m\rangle \equiv \hat{\mathcal{U}} |\Psi'_m\rangle = \int \mathrm{d}\boldsymbol{r}\, \psi_m(\boldsymbol{r}) |\eta_m(\boldsymbol{r})\rangle \otimes |\boldsymbol{r}\rangle, \tag{3.14}$$

with $\psi_m(\boldsymbol{r}) \equiv \langle \boldsymbol{r} | \psi_m \rangle$.

It is interesting to observe that the Hamiltonian in equation (3.12), although we are dealing with charge neutral atoms, has a structure reminiscent of the minimal coupling for charged particles in the gauge theory of electrodynamics. In fact, expressions $\boldsymbol{A}_m(\boldsymbol{r})$ and $w_m(\boldsymbol{r})$ in equation (3.13) are frequently referred to as *artificial* gauge fields, which have attracted much attention over the recent years in the endeavor of simulating elec-

tronic solid-state phenomena by means of neutral atoms [48, 49, 167]. Obviously, here they result from the spatial dependence of the dressed internal states $|\eta_m(\boldsymbol{r})\rangle$. In more general terms, $\boldsymbol{A}_m(\boldsymbol{r})$ and $w_m(\boldsymbol{r})$ are also known as the geometric vector and scalar potential for the external motion of the m-th dressed internal state. The geometric potentials are intimately related to the famous (adiabatic) geometric phase, which has plenty of observable effects throughout different areas of physics and was first derived, alongside with the corresponding vector potential, by Mead and Truhlar [168] in the context of molecular physics. However, it was not until Berry [84], who considered generic quantum system under adiabatic cyclic evolutions, that a general notion of the geometric phase and the associated gauge potentials was established.

As we do not intend to go into further detail about the geometric scalar and vector potentials – a general and comprehensive presentation can be found, for instance, in the book by Bohm et al. [163] – we merely emphasize their significance in the adiabatic approximation in case where the dressed internal states within the given hyperfine manifold have a non-vanishing spatial dependence. For instance, for our 2D optical lattice this is generally expected when the fictitious magnetic field exhibits a non-collinear spatial profile while its magnitude is comparable to or larger than the external magnetic field. A detailed analysis of the artificial gauge fields that can be realized by tailoring the fictitious magnetic field is left for the future. It should be stressed that the above approach is not the only way to realize artificial gauge fields. To take a single example, Floquet engineering [47, 169, 170] via lattice shaking [171–174] has proved successful in the creation of artificial gauge fields that are associated to staggered magnetic fluxes [51, 56]. Further methods for the creation of artificial gauge fields, including non-abelian generalization, are presented in the exhaustive reviews by Dalibard et al. [48] and Goldman et al. [49].

In view of equations (3.12) and (3.13), a particularly simple situation arises in the limit of a dominating uniform external magnetic field, where the spatial dependence of the dressed internal states vanishes to very good approximation and thus the geometric vector and scalar potentials can be neglected. Specifically, for our 2D optical lattice we then have $|\eta_m(\boldsymbol{r})\rangle \approx |F, \bar{m}_F\rangle$, with approximate dressed eigenenergies $v_m(\boldsymbol{r}) \approx V_{F,\bar{m}_F}(\boldsymbol{r})$ given by equation (2.44).[5] As a consequence, the reduced Hamiltonian for the center of mass motion of atoms in our 2D optical lattice becomes

$$\hat{H}_{\text{ext}}^m \approx \frac{\hat{\boldsymbol{p}}^2}{2\mu} + V_{F,\bar{m}_F}(\hat{\boldsymbol{r}}). \tag{3.15}$$

Although this might look like a trivial result, it is in fact not: it relies on the validity of the sequence of adiabatic approximations applied. Equation (3.15) will correspond to the typical situation studied within this thesis, and it will be the focus of the next subsection. Nevertheless, one should keep in mind that when the dressed internal states become increasingly close in energy, the adiabatic approximation is doomed to fail and the internal and external degrees of freedom must be treated on an equal footing. In other words, one should always revert in that case to the effective Hamiltonian $\hat{\mathcal{H}}_{\text{eff}}$ on the tensor product $\mathscr{H}_{\text{int}}^F \otimes \mathscr{H}_{\text{ext}}$.

---

[5]See also the discussion in subsection 2.3.2.
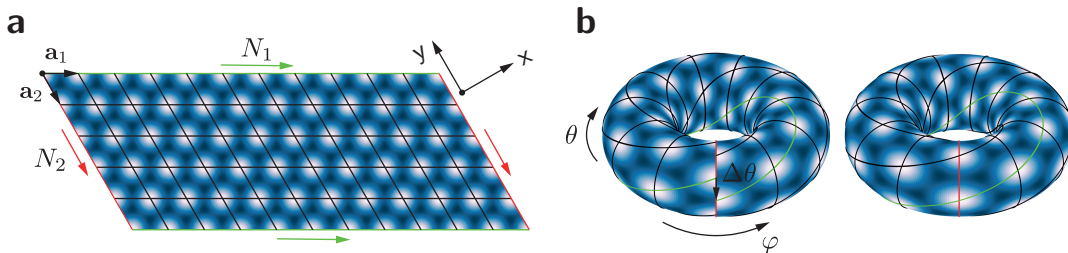
Fig. 3.1: Visualization of the Born-von-Karman periodic boundary conditions for a symmetric two-dimensional boron-nitride lattice (honeycomb lattice). **a** Quotient space of the boron-nitride lattice potential made of $N_1(N_2)$ unit cells arranged along the lattice vector $\mathbf{a}_1(\mathbf{a}_2)$. Red and green arrows identify equivalent points at the boundary of the parallelogram, resulting in a torus $\mathbf{T}^2$. Gluing opposite sides of the parallelogram in the orientation of the arrows yields an embedding **b** of the torus in $\mathbb{R}^3$, described by toroidal coordinates θ and φ. In fact, an embedding that respects the periodic boundary conditions corresponds to a uniformly *twisted* torus (right), where θ revolves by an additional angle $\Delta\theta = (N_1/N_2 \bmod 2)\,\pi$ for a single revolution around the coordinate φ.

3.1.2 Bloch formalism

In considering non-interacting atoms in optical lattices, we typically wish to solve the stationary Schrödinger equation

$$\hat{H}\,|\psi\rangle \equiv \left[\frac{\hat{\boldsymbol{p}}^2}{2m} + V(\hat{\boldsymbol{r}})\right]|\psi\rangle = E\,|\psi\rangle \tag{3.16}$$

for a single atom of mass m in a static periodic potential $V(\boldsymbol{r})$. Here, $\hat{\boldsymbol{p}}$ is the momentum operator and $\hat{\boldsymbol{r}}$ is the position operator, which act on elements $|\psi\rangle$ of the external single-particle Hilbert space $\mathscr{H}_{\mathrm{ext}}$. For the moment, we will ignore any reference to the internal state of the atom and assume that it remains in a fixed and well-defined local dressed internal state for all times. In addition, we will assume that the spatial dependence of the dressed internal states is negligible. Hence, we shall exclusively focus on the dynamics of the external degrees of freedom in configuration space in the limit of vanishing contributions from geometric scalar and vector potentials, as implied by equation (3.15) from the previous subsection.

In the following, the periodic potential $V(\boldsymbol{r})$ can correspond to lattices of arbitrary dimension d, but for clarity one may assume $d = 2$. Besides, to make the problem well-posed, it is necessary to enforce specific boundary conditions on $V(\boldsymbol{r})$. As usual, we will employ the Born-von-Karman periodic boundary conditions [175], resulting in a torus topology as exemplified in Figure 3.1 for our two-dimensional boron-nitride lattice. We emphasize that the torus topology rules out the emergence of edge or boundary states as encountered, for example, in real systems of topological insulators [176–179] with open boundaries. Although it is possible to generalize the Bloch formalism for arbitrary boundary conditions [180], which provides deep insights into the connection between bulk and boundary properties, we shall not complicate matters at this point and exclusively stick to periodic boundary conditions.

Translational invariance of the optical lattice implies that $V(\hat{\boldsymbol{r}}) = V(\hat{\boldsymbol{r}} + \mathbf{R})$ for any

Bravais lattice vector $\mathbf{R} \in \mathcal{R}_{\mathrm{B}}$. Therefore, it follows that the Hamiltonian $\hat{H}$ and the group of discrete translations $\{\hat{T}_{\mathbf{R}}\}$ form a set of commuting observables. According to Bloch's theorem, their common eigenbasis $\{|\psi_n\rangle\}$ can be classified by vector quantum numbers $\boldsymbol{k}$, known as crystal momenta or quasimomenta, that are uniquely defined within the first Brillouin zone (BZ_1) of the reciprocal Bravais lattice [181, 182]. The associated *Bloch states* $|\psi_{n\boldsymbol{k}}\rangle \equiv |n\boldsymbol{k}\rangle$ describe a complete set of common eigenstates

$$\hat{H}|n\boldsymbol{k}\rangle = \epsilon_n(\boldsymbol{k})|n\boldsymbol{k}\rangle, \quad \hat{T}_{\mathbf{R}}|n\boldsymbol{k}\rangle = e^{-\mathrm{i}\boldsymbol{k}\mathbf{R}}|n\boldsymbol{k}\rangle, \tag{3.17}$$

where the eigenvalues $\epsilon_n(\boldsymbol{k})$ represent energy bands or Bloch bands as functions of $\boldsymbol{k}$ that collectively form the band structure. For explicit calculations, it is helpful to rewrite the eigenvalue equation for $\hat{H}$ by exploiting the translational symmetries of the Bloch states $|n\boldsymbol{k}\rangle$. To this end, one typically establishes the ansatz $|n\boldsymbol{k}\rangle = e^{\mathrm{i}\boldsymbol{k}\hat{r}}|u_{n\boldsymbol{k}}\rangle$, which implies that the so-called *Bloch modes* $|u_{n\boldsymbol{k}}\rangle$ are invariant under the group of discrete translations $\{\hat{T}_{\mathbf{R}}\}$. With this, the left-hand side of equation (3.17) can be written in the form

$$e^{-\mathrm{i}\boldsymbol{k}\hat{r}}\hat{H}e^{\mathrm{i}\boldsymbol{k}\hat{r}}|u_{n\boldsymbol{k}}\rangle \equiv \hat{h}(\boldsymbol{k})|u_{n\boldsymbol{k}}\rangle = \epsilon_n(\boldsymbol{k})|u_{n\boldsymbol{k}}\rangle. \tag{3.18}$$

Here, we have introduced the so-called *Bloch Hamiltonian*

$$\hat{h}(\boldsymbol{k}) \equiv \frac{(\hat{\boldsymbol{p}} + \hbar\boldsymbol{k})^2}{2m} + V(\hat{\boldsymbol{r}}). \tag{3.19}$$

Thus, the Bloch modes $|u_{n\boldsymbol{k}}\rangle$ are eigenstates to the Bloch Hamiltonian, with eigenenergy $\epsilon_n(\boldsymbol{k})$. Note that for each $\boldsymbol{k}$ the corresponding eigenvalue problem has infinitely many countable solutions that are labeled by the additional *band index n*. Then, since the Bloch modes $|u_{n\boldsymbol{k}}\rangle$ are invariant under discrete translations $\hat{T}_{\mathbf{R}}$, i.e. periodic over primitive unit cells of the real-space Bravais lattice, we may expand them in the discrete Fourier basis $\{|\mathbf{G}\rangle\}$ of momentum states to the reciprocal lattice $\mathcal{G}_{\mathrm{B}}$ (compare equation (2.39)):

$$|u_{n\boldsymbol{k}}\rangle = \sum_{\mathbf{G}\in\mathcal{G}_{\mathrm{B}}} c_{n\boldsymbol{k}}(\mathbf{G})|\mathbf{G}\rangle. \tag{3.20}$$

In other words, we are provided with a suitable and complete set of orthogonal basis states that can be systematically truncated at $|\mathbf{G}| < M$ to arrive at an approximate solution for $|u_{n\boldsymbol{k}}\rangle$. From now on, we shall suppress the reference to $\mathcal{G}_{\mathrm{B}}$ in the sum over reciprocal lattice vectors $\mathbf{G}$. For clarity, we stress that the momentum state $|\mathbf{G}\rangle$ in our notation, by definition, is an eigenstate to the vector operator $\hat{\boldsymbol{p}}$ with eigenvalue $\hbar\mathbf{G}$. In position space representation, equation (3.20) therefore takes the familiar form[6]

$$u_{n\boldsymbol{k}}(\boldsymbol{r}) = \frac{1}{\sqrt{V}} \sum_{\mathbf{G}} c_{n\boldsymbol{k}}(\mathbf{G})e^{\mathrm{i}\mathbf{G}\boldsymbol{r}}. \tag{3.21}$$

The unknown expansion coefficients $c_{n\boldsymbol{k}}(\mathbf{G})$ uniquely determine each Bloch mode and

---

[6]We use that $u_{n\boldsymbol{k}}(\boldsymbol{r}) \equiv \langle \boldsymbol{r}|u_n(\boldsymbol{k})\rangle$ and $\langle \boldsymbol{r}|\boldsymbol{G}\rangle \equiv e^{\mathrm{i}\boldsymbol{G}\boldsymbol{r}}/\sqrt{V}$. The factor $1/\sqrt{V}$ accounts for the correct normalization by the system volume $V = Nv$, where N is the total number of unit cells contained in the lattice and v is the volume of a primitive unit cell.

Bloch state for fixed quantum numbers n and $\boldsymbol{k}$. They are easily obtained to leading order by solving the eigenvalue equation that results from the expansion of the Bloch Hamiltonian $\hat{h}(\boldsymbol{k})$ in a finite but sufficiently large Fourier basis $\{|\mathbf{G}\rangle\}_M$:

$$\sum_{\mathbf{G}'}^{M} \langle \mathbf{G}| \, \hat{h}(\boldsymbol{k}) \, |\mathbf{G}'\rangle \, c_{n\boldsymbol{k}}(\mathbf{G}') = \epsilon_n(\boldsymbol{k})c_{n\boldsymbol{k}}(\mathbf{G}) \quad :\Longleftrightarrow \quad \mathrm{H}(\boldsymbol{k})\mathbf{c}_{n\boldsymbol{k}} = \epsilon_n(\boldsymbol{k})\mathbf{c}_{n\boldsymbol{k}} \,. \qquad (3.22)$$

By noting that $V(\hat{\boldsymbol{r}}) = \sum_{\mathbf{G}} V_{\mathbf{G}} e^{i\mathbf{G}\hat{\boldsymbol{r}}}$, the components of the matrix $\mathrm{H}(\boldsymbol{k})$ read

$$\mathrm{H}_{\mathbf{G}\mathbf{G}'}(\boldsymbol{k}) \equiv \langle \mathbf{G}| \, \hat{h}(\boldsymbol{k}) \, |\mathbf{G}'\rangle = \frac{\hbar^2}{2m}(\mathbf{G} + \boldsymbol{k})^2 \delta_{\mathbf{G}\mathbf{G}'} + V_{\mathbf{G}-\mathbf{G}'} \,, \qquad (3.23)$$

and the reciprocal lattice vectors $\mathbf{G}$ can be ordered and numbered such that the subscripts refer to the corresponding numbers. The matrix elements in equation (3.23) are conveniently expressed in units of the recoil energy $E_{\mathrm{rec}} = \hbar^2 k_{\mathrm{L}}^2/(2m)$.

To obtain the full band structure and all Bloch modes or Bloch states of the particular problem at hand, it remains to diagonalize the matrix $\mathrm{H}_{\mathbf{G}\mathbf{G}'}(\boldsymbol{k})$ for all unique values of $\boldsymbol{k}$ that are allowed by the periodic boundary conditions. In general, given that $V(\boldsymbol{r})$ defines a finite d-dimensional lattice made of N_i unit cells along the primitive lattice vectors $\mathbf{a}_i$, the number of unique quasimomenta $\boldsymbol{k}$ is given by the total number of primitive unit cells $N = \prod_i^d N_i$. Usually, we are only interested in the limit of large N_i. In that case, the allowed quasimomenta are densely distributed within the first Brillouin zone, i.e. they vary quasi-continuously on a coarse-grained scale, and we must not bother with their precise values but tacitly assume that any $\boldsymbol{k} \in \mathrm{BZ}_1$ is compatible with the boundary conditions.

3.1.3 Band structure calculations

Based on the previous subsection, we now provide a brief account of the band structure of our spin-dependent boron-nitride lattice. The most striking feature, perhaps, is that it exhibits so-called *Dirac cones* in the limit of a vanishing sublattice energy offset. Dirac cones, first encountered by Wallace [183] in his studies of graphite, are conical intersections between two bands that are characterized by a linear dispersion relation and zero effective mass in the vicinity of the band touching points. As a consequence, particles near Dirac cones behave like ultra-relativistic particles that can be described by the massless Dirac equation, hence the name. Dirac cones are ubiquitous in the study of fermionic and bosonic Dirac matter and are associated with several remarkable transport properties. For example, the low-energy excitations in graphene, owing to the presence of Dirac cones, are massless chiral Dirac fermions that give rise to exotic phenomena such as Klein tunneling or the anomalous integer quantum Hall effect [184]. In close analogy to the two-dimensional honeycomb lattice of graphene, our tunable boron-nitride optical lattice can be considered a realization of artificial graphene with a tunable band gap.

In the following, we focus on the two extremal configurations $\theta_{\mathrm{B}} = 0°, 90°$ for our lattice potential, where θ_{B} denotes the angle between the z-axis and the external quantization field (see subsection 2.3.3). We assume a lattice depth of $V_{\mathrm{2D}} = 1\,E_{\mathrm{rec}}$ and atoms in the Zeeman substate $|2, -2\rangle$. The corresponding lattice potentials as well as
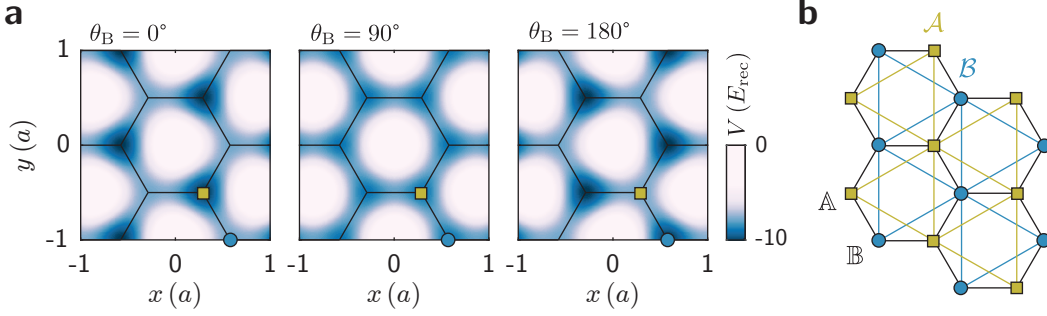
Fig. 3.2: Tunable spin-dependent boron-nitride lattice **a** for atoms in the Zeeman substate $|2, -2\rangle$ at a lattice depth $V_{2D} = 1\,E_{rec}$, and for varying angles $\theta_B = 0°,\ 90°, 180°$ of the external quantization field (left to right). **b** Sketch of the hexagonal lattice structure, with the definitions of the two triangular sublattices $\mathcal{A}$ and $\mathcal{B}$, and corresponding representative sublattice sites $\mathbb{A}$ and $\mathbb{B}$.

the associated triangular sublattices $\mathcal{A}$ and $\mathcal{B}$ are shown in Figure 3.2. Recall that the configuration $\theta_B = 0°$, i.e. a quantization field that points normal to the lattice plane, yields a maximum energy offset Δ_{AB} between the two sublattices. On the other hand, $\theta_B = 90°$ gives a vanishing energy offset $\Delta_{AB} = 0$ such that the boron-nitride lattice is transformed into a honeycomb lattice. For completeness, in Figure 3.2a we have included the case $\theta_B = 180°$ for which the energy offset is inverted compared to $\theta_B = 0°$. Note that the lattice potentials for $\theta_B = 0°$ and $\theta_B = 180°$ are linked by inversion. It is straightforward to show that potentials related by inversion have necessarily identical band structures. Thus, the case $\theta_B = 180°$ must not be considered separately.

The Bloch bands $\{\epsilon_n(\boldsymbol{k})\}$ for the two relevant lattice potentials at hand are obtained by exact numerical diagonalization of the Bloch matrix $H_{\mathbf{GG'}}(\boldsymbol{k})$ from equation (3.23) for different $\boldsymbol{k} \in \mathrm{BZ}_1$. The necessary matrix elements $V_{\mathbf{G}-\mathbf{G'}}$ can be directly inferred from equation (2.56). In Figure 3.3, we show the resulting band structures: For $\theta_B = 0°$, the finite value of Δ_{AB} breaks the inversion symmetry of the lattice potential, which manifests most prominently through a finite energy gap between the first and second Bloch band, as shown in Figure 3.3a. For $\theta_B = 90°$, on the other hand, the inversion symmetry is restored, leading to a honeycomb lattice featuring two conical intersections or Dirac cones between the first and second band. The corresponding band structure up to the fifth band is displayed in Figure 3.3b. Note that the Dirac cones are located at the two distinct vertices K and K' of the hexagonal Brillouin zone, and that similar Dirac cones also appear between the fourth and fifth band. For clarity, all Dirac cones at K have been marked by red circles. We stress that for each individual band, the quasimomenta K and K' always share the same energy due to time-reversal symmetry (see subsection 3.1.5). This holds regardless of the precise lattice configuration.

In Figure 3.3c, we provide further insights into the differences between the band structures of the two configurations $\theta_B = 0°$ and $\theta_B = 90°$ by inspecting cross sections along high-symmetry lines of the Brillouin zone. Most notably, apart from the degeneracies at K, which are lifted for $\theta_B \neq 90°$, there are additional degeneracies or band touching points at Γ between the third and fourth and between the fifth and sixth band. These are unaffected by modifications of the energy offset Δ_{AB} through
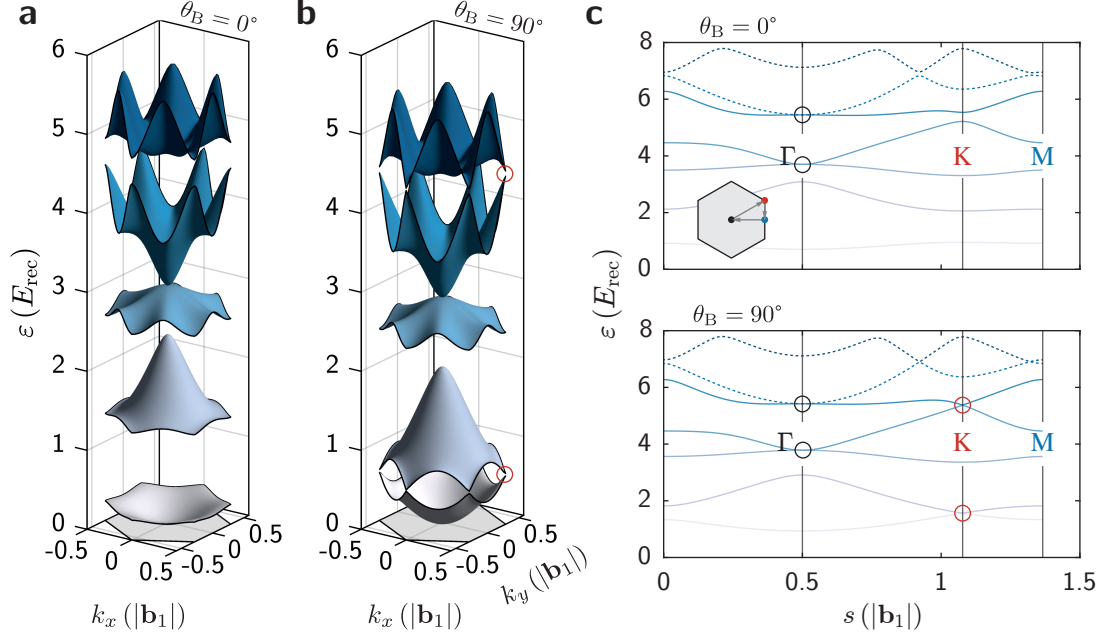
Fig. 3.3: Band structures of the spin-dependent boron-nitride lattice (equation (2.56)) for atoms in the Zeeman substate $|2, -2\rangle$. **a** For a lattice depth of $V_{2D} = 1\,E_{rec}$ and a quantization axis angle $\theta_B = 0°$, and **b** for $V_{2D} = 1\,E_{rec}$ and $\theta_B = 90°$. The first five bands for the two configurations are plotted in units of E_{rec} over the Brillouin zone (grey hexagon in the $k_x k_y$-plane). Coordinates of the quasimomentum space are given in units of the reciprocal lattice constant $|\mathbf{b}_1| = b$. **c** Sections of the band structures along a closed path in the Brillouin zone connecting points of high symmetry $M \to \Gamma \to K \to M$. The path length s is parametrized in units of $|\mathbf{b}_1|$. The degeneracies at K for the bands $(1, 2)$ and $(4, 5)$ are emphasized by red circles. They are lifted for $\theta_B \neq 90°$. Other degeneracies remain intact, such as $(3, 4)$ and $(5, 6)$ at Γ, marked by black circles. Dashed lines in **c** additionally show the 6th and 7th band, which have been omitted in **a** and **b** for clarity.

variations of θ_B. Besides, for $\theta_B = 90°$, another linear band touching point between the sixth and seventh band is encountered along the straight path $\Gamma \to K$ and $K \to M$. As with the Dirac cones, those degeneracies are absent for the case $\theta_B = 0°$. Clearly, it is possible to continuously tune between both band structures simply by rotating the quantization axis, i.e. by scanning the angle θ_B. This kind of manipulation of the band structure is central to this thesis and it will be extensively employed in chapter 4 for a Landau-Zener type transfer of atoms into higher Bloch bands. In particular, it enables to open and close the Dirac cones in a controlled manner, which has been used in previous experiments to study their influence on the lifetime of atoms in the second Bloch band [185].

Before we proceed with a discussion of Bloch orbitals in the next subsection, we note that Dirac cones are in general no static objects: their locations in the Brillouin zone can be manipulated by changing the lattice anisotropy. In fact, Dirac cones can be moved and even merged along different paths of the Brillouin zone [186–189]. Experimentally, this has been demonstrated in an optical honeycomb lattice by Tarruell et al. [190]. Based on a similar approach in our setup, the locations of Dirac cones can be easily

controlled by changing the intensities of the individual lattice beams, thereby introducing an intensity imbalance and asymmetry in the lattice potential. In view of this, it is illuminating to study the general requirements and conditions for the existence and stability of Dirac cones. While there has been a number of works devoted to it in the context of a minimal two-band model [191–194], we note that rigorous mathematical considerations in case of the full Bloch Hamiltonian (equation (3.19)) are rather rare.[7]

3.1.4 Bloch orbitals

We now turn our attention to Bloch states: The many-body ground state of an ideal BEC in an optical lattice is characterized by a macroscopic occupation of the lowest energy Bloch state $|n, \boldsymbol{k}\rangle = |1, \Gamma\rangle$. This situation constitutes the natural starting point for an ultracold bosonic ensemble loaded into a shallow optical lattice. On the other hand, the primary aim of this thesis was to achieve an unconventional BEC in higher Bloch states ($n > 1$) to some nonzero quasimomentum $\boldsymbol{k}$ (see chapter 4). Naturally, the properties of such an unconventional BEC will depend in a crucial way on the properties of the Bloch states that are occupied. Therefore, in preparation for the next chapter, we will provide a brief insight into some relevant Bloch states of our spin-dependent boron-nitride lattice. As an example, we consider the lattice potential for a quantization axis angle $\theta_{\mathrm{B}} = 0°$, a lattice depth $V_{\mathrm{2D}} = 4\,E_{\mathrm{rec}}$, and atoms in the Zeeman substate $|2, -2\rangle$. In this case, $\mathcal{A}$ defines the deeper sublattice (compare Figure 3.2) and the offset to $\mathcal{B}$ amounts to $\Delta_{\mathrm{AB}} \approx 9.2\,E_{\mathrm{rec}}$. In the following, we shall visualize the Bloch states in terms of their wave functions $\psi_{n\boldsymbol{k}}(\boldsymbol{r}) \equiv \langle \boldsymbol{r} | n\boldsymbol{k} \rangle$ over the configuration space, which will be termed *Bloch orbitals*.

In Figure 3.4, we plot the first four Bloch orbitals ($n = 1, \ldots, 4$) to the quasimomenta of high symmetry $\Gamma, \mathrm{K}, \mathrm{M}$. We note that the Fourier coefficients $\{c_{n\boldsymbol{k}}(\mathbf{G})\}$ to the Bloch states have been obtained by exact numerical diagonalization of the Bloch matrix $\mathrm{H}_{\mathbf{GG'}}(\boldsymbol{k})$ from equation (3.23). As would be expected, the Bloch orbital of the ground state $|n, \boldsymbol{k}\rangle = |1, \Gamma\rangle$ is localized essentially on the deeper sublattice $\mathcal{A}$. It has a trivial phase profile of constant value. On the other hand, higher Bloch orbitals are not necessarily localized on the deeper sublattice and possess more intriguing phase patterns. Note that the depicted orbitals $(2, \Gamma)$ and $(3, \Gamma)$ break the three-fold rotational symmetry, which is otherwise intact for Bloch orbitals at Γ. However, this symmetry breaking is just an artefact of their degeneracy, and it is perfectly possible to construct corresponding three-fold symmetric orbitals by appropriate superpositions of $(2, \Gamma)$ and $(3, \Gamma)$.

We stress that the phase profiles of higher Bloch orbitals to the quasimomenta Γ and M are characterized by domain-like structures, where domain walls correspond to node lines across which the phase makes a discontinuous jump by $\Delta\phi = \pi$. It is therefore clear that Bloch orbitals at Γ and M can always be chosen to be real-valued, in accordance with time-reversal symmetry (compare subsection 3.1.5). In contrast, Bloch orbitals at the quasimomentum K are genuinely complex. Most remarkably, the higher Bloch orbitals at K exhibit rectified phase windings on sublattices with a non-vanishing orbital

---

[7] Fefferman and Weinstein [195], for example, give a detailed proof that any periodic potential with *ideal* honeycomb symmetry features Bloch bands with conical intersections at each vertex of the Brillouin zone.
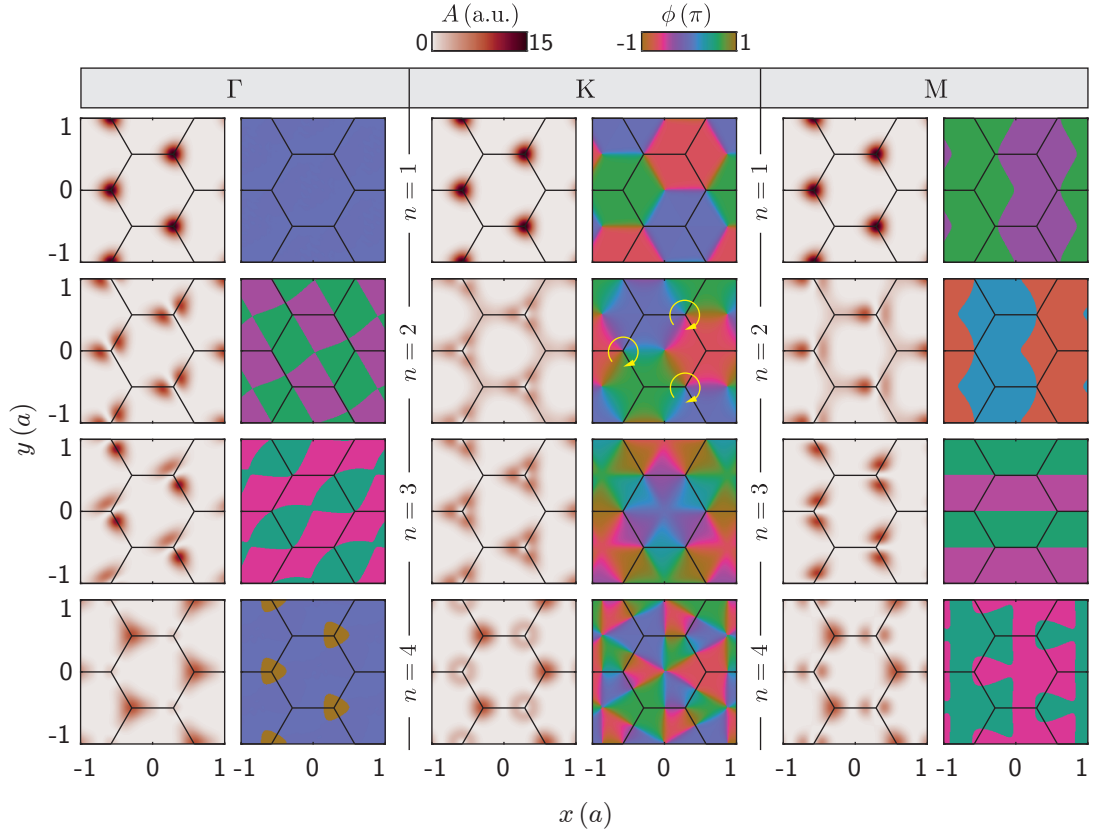
Fig. 3.4: First four Bloch orbitals of the spin-dependent boron-nitride lattice for parameters $\theta_B = 0°$, $V_{2D} = 4\,E_{rec}$, atoms in the Zeeman substate $|2, -2\rangle$, and selected quasimomenta. The plots are arranged into four rows that label the band indices $n = 1, \ldots, 4$, and three double-columns that refer to the quasimomenta Γ, K, M, as indicated on the top. Each double-column depicts the modulus squared A (on the left) and the phase ϕ (on the right) of Bloch orbitals over the real space lattice. The orbital $(1, \Gamma)$ represents the ground state, which is localized on deep lattice sites $\mathbb{A}$ of the underlying lattice potential and exhibits a constant phase profile. Higher Bloch orbitals possess nodes and more complex phase distributions. For instance, $(2, K)$ exhibits a clockwise phase winding on each lattice site $\mathbb{A}$ with a non-vanishing orbital weight that results in a finite onsite orbital angular momentum (OAM). The corresponding phase windings are emphasized by circular arrows. Note that the depicted orbitals $(2, \Gamma)$ and $(3, \Gamma)$ break the three-fold rotational symmetry, which is otherwise intact for orbitals at Γ. This is the result of the degeneracy between $(2, \Gamma)$ and $(3, \Gamma)$. It is possible, however, to construct new eigenfunctions that restore the symmetry. For convenience, all orbitals have been normalized such that integration of A over a primitive unit cell gives the volume v of that cell. Moreover, the global phase of each Bloch orbital has been gauged such that the zero-momentum component $c_{n\boldsymbol{k}}(\mathbf{G}_0)$ is real-valued.

weight, which is associated with a finite onsite orbital angular momentum (OAM). For example, the Bloch orbital $(2, \mathrm{K})$ has a clockwise phase winding on each sublattice site $\mathbb{A}$ with a finite orbital weight. As a consequence, a BEC in such a Bloch state is characterized by a macroscopic OAM. We will examine the orbital angular momentum of Bloch states in more detail in the following subsection 3.1.5.

3.1.5 Fundamental properties of Bloch states

For completeness, we now provide several fundamental properties of Bloch states that are relevant to this thesis.

Equivalence classes   Once a solution for a particular Bloch mode $|u_{n\boldsymbol{k}}\rangle$ is at hand, the associated Bloch state $|n\boldsymbol{k}\rangle$ is obtained via

$$|n\boldsymbol{k}\rangle \equiv e^{\mathrm{i}\boldsymbol{k}\hat{\boldsymbol{r}}} |u_{n\boldsymbol{k}}\rangle = e^{\mathrm{i}\boldsymbol{k}\hat{\boldsymbol{r}}} \sum_{\mathbf{G}} c_{n\boldsymbol{k}}(\mathbf{G}) |\mathbf{G}\rangle = \sum_{\mathbf{G}} c_{n\boldsymbol{k}}(\mathbf{G}) |\mathbf{G} + \boldsymbol{k}\rangle \,. \qquad (3.24)$$

We stress that two Bloch modes $|u_{n\boldsymbol{k}'}\rangle$ and $|u_{n\boldsymbol{k}}\rangle$ related by $\boldsymbol{k}' = \boldsymbol{k} + \mathbf{G}$, with arbitrary $\mathbf{G} \in \mathcal{G}_{\mathrm{B}}$, are in general not parallel, i.e. they correspond to distinct states in the Hilbert space $\mathscr{H}_{\mathrm{ext}}$. However, these states are equivalent in the sense that they yield the same Bloch state $|n\boldsymbol{k}'\rangle = e^{\mathrm{i}\phi} |n\boldsymbol{k}\rangle$ up to an irrelevant global phase factor.

Indeed, it is easy to verify that the Bloch mode $|u_{n\boldsymbol{k}'}\rangle = e^{-\mathrm{i}\mathbf{G}\hat{\boldsymbol{r}}} |u_{n\boldsymbol{k}}\rangle$ is an eigenstate to the Bloch Hamiltonian $\hat{h}(\boldsymbol{k}') \equiv \hat{h}(\boldsymbol{k} + \mathbf{G})$ with the same eigenvalue $\epsilon_n(\boldsymbol{k}') = \epsilon_n(\boldsymbol{k})$ as $|u_{n\boldsymbol{k}}\rangle$. The equality of Bloch states then follows immediately from the defining equation (3.24). Bloch states are thus class invariant under the equivalence relation defined by $\boldsymbol{k}' \sim \boldsymbol{k} :\Longleftrightarrow \boldsymbol{k}' = \boldsymbol{k} + \mathbf{G} \mid \mathbf{G} \in \mathcal{G}_{\mathrm{B}}$, which justifies the restriction of the quasimomentum onto the unique set of class representatives from the first Brillouin zone.

Time-reversal symmetry   Besides, it is illuminating to inspect the consequences of time-reversal symmetry (TRS) onto Bloch modes and Bloch states. To this end, let us first define the time-reversal operator $\hat{\Theta}$ acting in $\mathscr{H}_{\mathrm{ext}}$. For physical reasons, we will require that $\hat{\Theta}$ is an *anti-unitary* operator [196] that leaves the position states $|\boldsymbol{r}\rangle$ invariant up to a local gauge transformation, that means it will be uniquely defined by the following action:

$$\hat{\Theta}\left(\alpha |\boldsymbol{r}_1\rangle + \beta |\boldsymbol{r}_2\rangle\right) = \alpha^* \hat{\Theta} |\boldsymbol{r}_1\rangle + \beta^* \hat{\Theta} |\boldsymbol{r}_2\rangle \equiv \alpha^* e^{\mathrm{i}\vartheta(\boldsymbol{r}_1)} |\boldsymbol{r}_1\rangle + \beta^* e^{\mathrm{i}\vartheta(\boldsymbol{r}_2)} |\boldsymbol{r}_2\rangle \,, \qquad (3.25)$$

for arbitrary $\boldsymbol{r}_1, \boldsymbol{r}_2$, and $\alpha, \beta \in \mathbb{C}$, where we assume that $\vartheta(\boldsymbol{r})$ is a smooth, real-valued function. It is easy to verify that equation (3.25) implies that the position and canonical momentum operator transform according to

$$\hat{\Theta}\,\hat{\boldsymbol{r}}\,\hat{\Theta}^{-1} = \hat{\boldsymbol{r}}, \qquad \hat{\Theta}\,\hat{\boldsymbol{p}}\,\hat{\Theta}^{-1} = -\hat{\boldsymbol{p}} + \boldsymbol{\nabla}\vartheta(\hat{\boldsymbol{r}}) \,, \qquad (3.26)$$

where $\boldsymbol{\nabla}\vartheta(\hat{\boldsymbol{r}})$ is to be understood as an operator-valued function. We also note that $\hat{\Theta}^{-1} = \hat{\Theta}$, and we have the following useful identity:

$$\hat{\Theta}\,|\mathbf{G}\rangle = e^{\mathrm{i}\vartheta(\hat{\boldsymbol{r}})}\,|-\mathbf{G}\rangle\,. \tag{3.27}$$

Equation (3.27) simply tells that $\hat{\Theta}$ sends the momentum state $|\mathbf{G}\rangle$ to its opposite if $\vartheta(\boldsymbol{r}) = 0$ for all values of $\boldsymbol{r}$.

Now, a general Hamilton $\hat{H}$ is said to be time-reversal invariant or symmetric if there exists an anti-unitary operator $\hat{\Theta}$ such that $\hat{\Theta}\hat{H}\hat{\Theta}^{-1} = \hat{H}$. It is obvious that the lattice Hamiltonian in equation (3.16) is time-reversal symmetric under the trivial choice $\vartheta = 0$. This implies for the Bloch Hamiltonian in equation (3.19) that

$$\hat{h}(\boldsymbol{k}) = \hat{\Theta}\,\hat{h}(-\boldsymbol{k})\,\hat{\Theta}^{-1}, \quad \forall \boldsymbol{k} \in \mathrm{BZ}_1\,. \tag{3.28}$$

Conversely, equation (3.28) can be taken as a definition for the time-reversal symmetry of a Bloch Hamiltonian $\hat{h}(\boldsymbol{k})$. An immediate consequence of equation (3.28) is that Bloch modes $|u_{n\boldsymbol{k}}\rangle$ and $|u_{n,-\boldsymbol{k}}\rangle$, which are eigenstates to $\hat{h}(\boldsymbol{k})$ and $\hat{h}(-\boldsymbol{k})$ with eigenenergies $\epsilon_n(\boldsymbol{k})$ and $\epsilon_n(-\boldsymbol{k})$, respectively, are linked by $\hat{\Theta}$ according to

$$|u_{n,-\boldsymbol{k}}\rangle = \hat{\Theta}\,|u_{n\boldsymbol{k}}\rangle\,, \quad \epsilon_n(-\boldsymbol{k}) = \epsilon_n(\boldsymbol{k})\,, \tag{3.29}$$

being valid for all $\boldsymbol{k}$. Therefore, a time-reversal symmetric Bloch Hamiltonian has an inversion symmetric band structure with respect to the quasimomentum $\boldsymbol{k}$. A pair of Bloch modes for which equation (3.29) holds is called a time-reversal symmetric (TRS) pair. From equations (3.20) and (3.27) it then directly follows that the Fourier coefficients of a TRS pair are related by

$$c_{n,-\boldsymbol{k}}(\mathbf{G}) = [c_{n\boldsymbol{k}}(-\mathbf{G})]^*, \quad \forall \mathbf{G}\,. \tag{3.30}$$

Thus, the position space representations or wave functions $u_{n\boldsymbol{k}}(\boldsymbol{r}) \equiv \langle \boldsymbol{r}|u_{n\boldsymbol{k}}\rangle$ of TRS pairs are related by complex conjugation: $u_{n,-\boldsymbol{k}}(\boldsymbol{r}) = [u_{n\boldsymbol{k}}(\boldsymbol{r})]^*$. It is straightforward to show that the same holds for the respective Bloch wave functions $\psi_{n\boldsymbol{k}}(\boldsymbol{r}) \equiv \langle \boldsymbol{r}|n\boldsymbol{k}\rangle$. In particular, equation (3.30) implies that the wave functions to the time-reversal invariant quasimomenta $\boldsymbol{k} \in \{\Gamma, \mathrm{M}, \mathrm{M}', \mathrm{M}''\}$ can be chosen to be real-valued.

Bloch state momentum For atoms in optical lattices, the momentum distribution $f(\boldsymbol{q})$ provides a physical quantity that is directly accessible in absorption images after time-of-flight. Here, $\boldsymbol{q} = \boldsymbol{p}/\hbar \in \mathbb{R}^d$ is related to the kinetic momentum $\boldsymbol{p}$ by the De Broglie relation and is not to be confused with the quasimomentum $\boldsymbol{k} \in \mathrm{BZ}_1$. From equation (3.24), it immediately follows that the momentum distribution of a Bloch state is given by

$$f_{n\boldsymbol{k}}(\boldsymbol{q}) \equiv |\langle \boldsymbol{q}|n\boldsymbol{k}\rangle|^2 = \sum_{\mathbf{G}} |c_{n\boldsymbol{k}}(\mathbf{G})|^2\,\delta_{\boldsymbol{q},\mathbf{G}+\boldsymbol{k}}\,. \tag{3.31}$$

We can now define the corresponding density distribution $f'_{n\boldsymbol{k}}(\boldsymbol{q})$ according to

$$f'_{n\boldsymbol{k}}(\boldsymbol{q}) \equiv \sum_{\mathbf{G}} |c_{n\boldsymbol{k}}(\mathbf{G})|^2\,\delta\left(\boldsymbol{q} - (\mathbf{G}+\boldsymbol{k})\right), \tag{3.32}$$
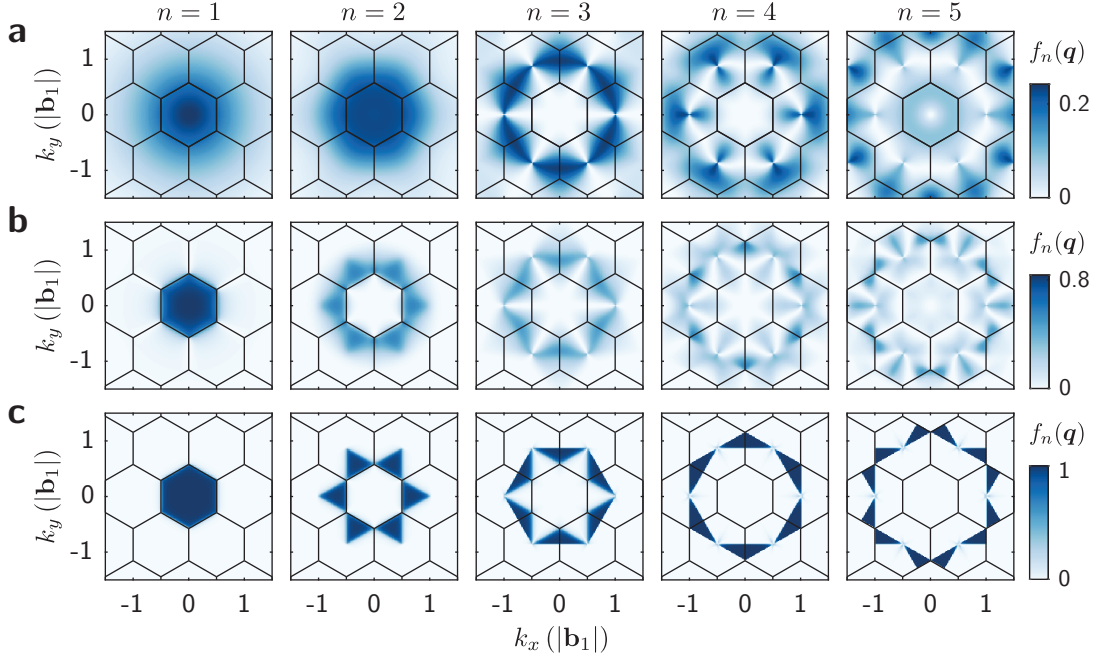
Fig. 3.5: Momentum-density distributions $f_n(\boldsymbol{q})$ of uniformly filled bands $n = 1, \ldots, 5$ for different configurations of the two-dimensional boron-nitride lattice, with atoms in the Zeeman substate $|2, -2\rangle$. **a** For a lattice depth $V_{2D} = 8\,E_{\text{rec}}$ and quantization axis angle $\theta_B = 106°$. **b** For $V_{2D} = 1\,E_{\text{rec}}$ and $\theta_B = 90°$. **c** For $V_{2D} = 0.1\,E_{\text{rec}}$ and $\theta_B = 90°$. Distributions $f_n(\boldsymbol{q})$ are plotted over the reciprocal space, with coordinates in units of the reciprocal lattice constant $|\mathbf{b}_1| = b$. For convenience, the color-coded densities have been normalized such that the integration of $f_n(\boldsymbol{q})$ over the entire reciprocal space gives the volume of the Brillouin zone. With increasing lattice depths, the respective distributions become broader. Note that in the limit $V_{2D} \to 0$, the momentum-density distribution of the n-th band approaches the characteristic function of the n-th Brillouin zone.

where $\delta(\boldsymbol{q})$ denotes the Dirac delta function on the reciprocal space. Based on this, it is straightforward to show that a normalized *quasimomentum* density distribution $\mathrm{B}_n(\boldsymbol{k})$ in the n-th band gives rise to the following momentum distribution:

$$F_n(\boldsymbol{q}) \equiv \int\limits_{\text{BZ}_1} \mathrm{d}\boldsymbol{k}\, \mathrm{B}_n(\boldsymbol{k}) f_{n\boldsymbol{k}}(\boldsymbol{q}) = \widetilde{\mathrm{B}}_n(\boldsymbol{q}) f_n(\boldsymbol{q})\,, \tag{3.33}$$

where $\widetilde{\mathrm{B}}_n(\boldsymbol{q})$ denotes the periodic extension of $\mathrm{B}_n(\boldsymbol{k})$ over the full reciprocal space, and we employed the definition

$$f_n(\boldsymbol{q}) \equiv \int\limits_{\text{BZ}_1} \mathrm{d}\boldsymbol{k}\, f'_{n\boldsymbol{k}}(\boldsymbol{q})\,. \tag{3.34}$$

Up to normalization, $f_n(\boldsymbol{q})$ corresponds to the momentum distribution of a uniformly filled band, described by $F_n(\boldsymbol{q})$ for the case $\mathrm{B}_n(\boldsymbol{k}) = 1/V_{\text{BZ}}$, where V_{BZ} is the volume of the Brillouin zone. In Figure 3.5, we depict the distributions $f_n(\boldsymbol{q})$ for the first five bands to three different configurations of the boron-nitride lattice. The functions $f_n(\boldsymbol{q})$ are

readily obtained from numerical diagonalization of the Bloch Hamiltonian over the first Brillouin zone and are also known as *Wannier envelopes*. In that context, they are often denoted by $|w_n(\boldsymbol{q})|^2$, where $w_n(\boldsymbol{q})$ is the Fourier transform of the n-th Wannier function $w_n(\boldsymbol{r})$ [197]. It is insightful to note that the density distributions $f_n(\boldsymbol{q})$ exhibit the hexagonal symmetry of the underlying lattice and approach the characteristic functions of the n-th Brillouin zone (BZ_n), respectively, for vanishing lattice depths $V_{2D} \to 0$. We note that the functions $f_n(\boldsymbol{q})$ can serve as reliable model functions for data fitting in TOF images to obtain accurate estimates of the quasimomentum distribution of thermal atoms in each band. As the main advantage, this could be used directly in connection with TOF images acquired after sudden release from the specified lattice potential, i.e. without the need to invoke the band mapping technique, which inherently suffers from non-adiabatic transfer and momentum redistribution during the lattice ramp [198]. However, since the individual supports of $f_n(\boldsymbol{q})$ tend to overlap for large lattice depths, we admit that the fits can become increasingly complex in situations where multiple bands are occupied.

Often, we will be interested in the mean kinetic momentum $\langle\hat{\boldsymbol{p}}\rangle_{n\boldsymbol{k}} \equiv \langle n\boldsymbol{k}|\hat{\boldsymbol{p}}|n\boldsymbol{k}\rangle$ of a Bloch state, which we call the Bloch state momentum. According to equation (3.24), it is given by

$$\langle\hat{\boldsymbol{p}}\rangle_{n\boldsymbol{k}} = \hbar \sum_{\mathbf{G}} |c_{n\boldsymbol{k}}(\mathbf{G})|^2 \left(\mathbf{G} + \boldsymbol{k}\right) . \tag{3.35}$$

We stress that Bloch states $|n\boldsymbol{k}\rangle$ are in general no eigenstates to the momentum operator $\hat{\boldsymbol{p}}$ and that TRS pairs obey the relation $\langle\hat{\boldsymbol{p}}\rangle_{n,-\boldsymbol{k}} = -\langle\hat{\boldsymbol{p}}\rangle_{n\boldsymbol{k}}$, as intuitively expected.

Bloch state orbital angular momentum   It addition to the mean kinetic momentum, it is tempting to consider the mean angular momentum $\langle\hat{\boldsymbol{L}}\rangle_{n\boldsymbol{k}} \equiv \langle n\boldsymbol{k}|\hat{\boldsymbol{L}}|n\boldsymbol{k}\rangle$ of a Bloch state, where $\hat{\boldsymbol{L}} = \hat{\boldsymbol{r}} \times \hat{\boldsymbol{p}}$ denotes the conventional angular momentum operator in three-dimensional Euclidean space. For clarity, we will focus on a two-dimensional ($d = 2$) lattice system in the xy-plane, with the relevant scalar operator $\hat{\ell}_z \equiv \hat{x}\hat{p}_y - \hat{y}\hat{p}_x$. In this case, a naive application of $\hat{\ell}_z$ to the Bloch states yields

$$\langle\hat{\ell}_z\rangle_{n\boldsymbol{k}} = \hbar \sum_{\mathbf{G},\mathbf{G}'} c_{n\boldsymbol{k}}^*(\mathbf{G})c_{n\boldsymbol{k}}(\mathbf{G}') \left[\left(G_y' + k_y\right)\langle\mathbf{G}|\hat{x}|\mathbf{G}'\rangle - \left(G_x' + k_x\right)\langle\mathbf{G}|\hat{y}|\mathbf{G}'\rangle\right] . \tag{3.36}$$

The terms $\langle\mathbf{G}|\hat{x}|\mathbf{G}'\rangle$ and $\langle\mathbf{G}|\hat{y}|\mathbf{G}'\rangle$ in equation (3.36) must be evaluated with respect to the torus topology imposed by the periodic boundary conditions. However, this cannot be accomplished in a unique way. In fact, although the operator $\hat{\ell}_z$ is well-defined locally on each open patch of the configuration space torus $\mathbf{T}^2$, it is not obvious how a global extension over the full manifold should look like.[8] At this point, we shall depart from mathematical rigor and attempt to make sense of equation (3.36) anyhow by evaluating $\langle\mathbf{G}|\hat{\mu}|\mathbf{G}'\rangle$ with $\mu = x, y$ over an unfolding $U \subseteq \mathbb{R}^2$ of the torus that exactly corresponds to the one shown in Figure 3.1a, i.e. we *define*

$$\langle\mathbf{G}|\hat{\mu}|\mathbf{G}'\rangle \equiv \frac{1}{V} \int_U \mu e^{\mathrm{i}(\mathbf{G}'-\mathbf{G})\boldsymbol{r}} \,\mathrm{d}x\mathrm{d}y . \tag{3.37}$$

---

[8]Problems of this kind are related to difficulties in formulating a consistent quantum theory in multiply-connected spaces. A general treatment of this subject can be found, for instance, in Dürr et al. [199].

Then, by partitioning U into primitive unit cells $U_{\mathbf{R}}$ that are located at lattice points $\mathbf{R}$ and using the periodicity of the Fourier basis we can write

$$\langle \mathbf{G}|\hat{\boldsymbol{r}}|\mathbf{G}'\rangle \equiv \sum_{\mathbf{R}}^{N} \langle \mathbf{G}|\hat{\boldsymbol{r}}|\mathbf{G}'\rangle_{U_{\mathbf{R}}} = \sum_{\mathbf{R}}^{N} \langle \mathbf{G}|\hat{\boldsymbol{r}}_{\mathbf{R}}+\mathbf{R}|\mathbf{G}'\rangle_{U_0}$$
$$= N\langle \mathbf{G}|\hat{\boldsymbol{r}}|\mathbf{G}'\rangle_{U_0} + \frac{1}{N}\sum_{\mathbf{R}}^{N} \mathbf{R}\,\delta_{\mathbf{G}\mathbf{G}'}\,, \tag{3.38}$$

where $\langle \mathbf{G}|\hat{\mu}|\mathbf{G}'\rangle_{U_0}$ shall denote the integral on the right-hand side of equation (3.37), restricted to the region of the *first* primitive unit cell U_0. With this, and by splitting equation (3.36) into off-diagonal and diagonal parts, we finally arrive at

$$\langle \hat{\ell}_z\rangle_{n\boldsymbol{k}} = \left(\boldsymbol{r}_s \times \langle \hat{\boldsymbol{p}}\rangle_{n\boldsymbol{k}}\right)_z + N\hbar \sum_{\mathbf{G},\mathbf{G}'}^{\mathbf{G}\neq\mathbf{G}'} c_{n\boldsymbol{k}}^*(\mathbf{G})c_{n\boldsymbol{k}}(\mathbf{G}')$$
$$\times \left[\left(G_y'+k_y\right)\langle \mathbf{G}|\hat{x}|\mathbf{G}'\rangle_{U_0} - \left(G_x'+k_x\right)\langle \mathbf{G}|\hat{y}|\mathbf{G}'\rangle_{U_0}\right]. \tag{3.39}$$

Clearly, the first term is just related to the contribution of the mean momentum to the angular momentum, where $\boldsymbol{r}_s$ is defined as the geometric center of the integration region U. It is always possible to make this term vanish by an appropriate transformation of the origin (reference point) in $\mathbb{R}^2$. Note that this transformation does not affect the second term in equation (3.39), which is off-diagonal in the momentum basis. Accordingly, we shall identify the second term with an *intrinsic* orbital angular momentum (OAM)

$$\langle \hat{s}_z\rangle_{n\boldsymbol{k}} \equiv N\hbar \sum_{\mathbf{G},\mathbf{G}'}^{\mathbf{G}\neq\mathbf{G}'} c_{n\boldsymbol{k}}^*(\mathbf{G})c_{n\boldsymbol{k}}(\mathbf{G}')$$
$$\times \left[\left(G_y'+k_y\right)\langle \mathbf{G}|\hat{x}|\mathbf{G}'\rangle_{U_0} - \left(G_x'+k_x\right)\langle \mathbf{G}|\hat{y}|\mathbf{G}'\rangle_{U_0}\right]. \tag{3.40}$$

It can be calculated numerically for any Bloch state once the expansion coefficients $c_{n\boldsymbol{k}}(\mathbf{G})$ are at hand. Yet, we stress that the value of the intrinsic orbital angular momentum is *not* unique. It depends on the choice of unfolding U or, to put it differently, on the chart that we choose to cover the torus. Indeed, there is a one-to-one correspondence in the ambiguity of $\langle \hat{s}_z\rangle_{n\boldsymbol{k}}$ and the measure of the distance between points on the torus. We will not go into further details but simply mention that, from a physical point of view, the ambiguity is rooted in the fact that Bloch states, in general, do not only possess local phase windings (phase vortices) but also global phase patterns that wrap around the configuration space torus. The latter are responsible for the non-uniqueness of $\langle \hat{s}_z\rangle_{n\boldsymbol{k}}$. Despite that, equation (3.40) can still be used to quantify the amount of nontrivial phase windings that inhere in Bloch states like those discussed in the previous subsection 3.1.4.

In Figure 3.6, as an example, we plot the calculated values of $\langle \hat{s}_z\rangle_{n\boldsymbol{k}}$ for different Bloch states of the boron-nitride lattice as functions of the quantization axis angle θ_{B}, which controls the energy offset between the two sublattice sites $\mathbb{A}$ and $\mathbb{B}$ according to equation (2.58). In particular, we focus on the first few Bloch states $n = 1,\ldots,5$ to the
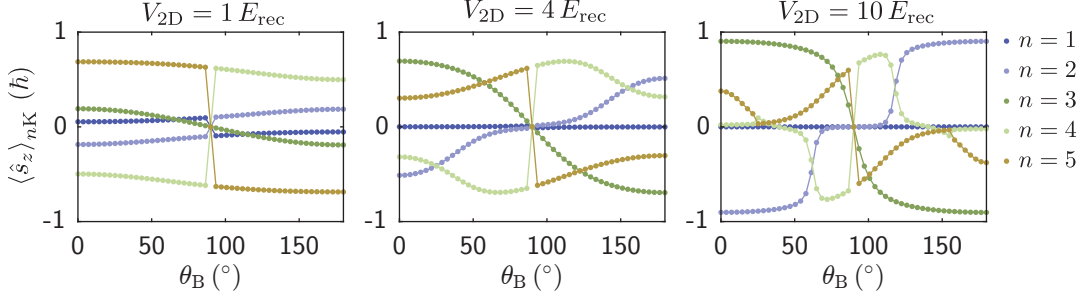
Fig. 3.6: Calculated intrinsic orbital angular momenta $\langle \hat{s}_z \rangle_{n\boldsymbol{k}}$ (OAM) for Bloch states $n = 1, \ldots, 5$ of the boron-nitride lattice at the quasimomentum $\boldsymbol{k} = $ K. The OAM are plotted as functions of the quantization axis angle θ_{B} for different lattice depths $V_{\mathrm{2D}} = (1, 4, 10)\, E_{\mathrm{rec}}$, assuming atoms in the Zeeman substate $|2, -2\rangle$. Note that the curves are symmetric under point reflection through $\theta_{\mathrm{B}} = 90°$, where the boron-nitride lattice corresponds to a honeycomb lattice and Bloch orbitals change their character. OAM for the high symmetry quasimomenta Γ and M evaluate to zero and have been omitted for clarity. In contrast, OAM at K′ are opposite to those at K. The corresponding curves can be obtained from the displayed data by reflection through the horizontal axis.

quasimomentum $\boldsymbol{k} = $ K. As depicted in Figure 3.4, the corresponding Bloch orbitals are characterized by nontrivial phase patterns that should result in a non-vanishing OAM. Indeed, we find that $\langle \hat{s}_z \rangle_{n\mathrm{K}}$ is generally finite on the order of $1\hbar$ per atom. In contrast, the OAM of Bloch orbitals to the quasimomenta Γ and M evaluates to zero, in agreement with the absence of phase windings.

Note that $\langle \hat{s}_z \rangle_{n\mathrm{K}}$ in the middle panel of Figure 3.6 for the value $\theta_{\mathrm{B}} = 0°$ originates from the Bloch orbitals (n, K) shown in Figure 3.4. For $n = 2$, for example, the OAM increases monotonically from a negative to a positive value as θ_{B} grows, with a zero-crossing at $\theta_{\mathrm{B}} = 90°$. This behavior is easily understood from the following point of view: The Bloch orbital $(2, \mathrm{K})$ for $\theta_{\mathrm{B}} = 0°$ is mainly localized on the sublattice sites $\mathbb{A}$ that host clockwise phase vortices, resulting in a maximum negative OAM. As θ_{B} is increased, the sublattice energy offset Δ_{AB} gets smaller and the Bloch orbital $(2, \mathrm{K})$ gradually spreads towards the shallower sublattice sites $\mathbb{B}$, leading to a reduced orbital weight on the phase vortices and thus a smaller absolute value of the OAM. Once $\theta_{\mathrm{B}} = 90°$ is passed, the roles reverse and the $\mathbb{B}$ sublattice sites become the deeper ones. At the same time, the Bloch orbital $(2, \mathrm{K})$ changes its character by acquiring an anti-clockwise phase winding on the sublattice sites $\mathbb{B}$, leading to a positive value of the OAM. The latter grows until the maximum localization on $\mathbb{B}$ is reached for $\theta_{\mathrm{B}} = 180°$.

A similar line of reasoning may be carried out to explain the OAM curves in Figure 3.6 for the remaining Bloch orbitals at different lattice depths. In this respect, it is illuminating to note that the OAM asymptotically approaches integral multiples of $\hbar$ in the limit of large lattice depths. Specifically, the OAM of the Bloch orbital $(2, \mathrm{K})$ for $\theta_{\mathrm{B}} = 0°$ converges to $-1\hbar$. Bloch orbitals become in this sense analogous to the wave functions of the two-dimensional harmonic oscillator. In general, however, Bloch states are no eigenstates to the angular momentum operator. Finally, note that the OAM of Bloch states to the quasimomentum K′ is opposite to the OAM of Bloch states to K, as expected from the fact that $|n, \mathrm{K}\rangle$ and $|n, \mathrm{K}'\rangle$ are TRS partner. In other words,

the corresponding Bloch orbitals (n, K) and (n, K') are related by complex conjugation, which simply inverts the orientation of phase windings.

3.2 Revealing momentum distributions

Given our discussion of various properties and aspects of atoms in optical lattices, it is natural to ask how these systems can be probed to obtain useful information about their state vector $|\psi\rangle$. In this section, we describe the corresponding standard techniques used in this work.

Recall that our central experimental observable is given by the optical density.[9] It is acquired through resonant absorption imaging of the atomic cloud after switching off all trapping potentials and allowing for a free expansion during a variable time-of-flight. Depending on how the trapping potentials are switched off in time, the corresponding TOF images can carry different information about the atomic ensemble. In what follows, we discuss the two important scenarios of sudden and adiabatic release from an optical lattice, which give access to the momentum and quasimomentum distribution of atoms in the lattice, respectively.

3.2.1 Sudden release

In the case of a sudden release, all trapping potentials are switched off abruptly. If interactions can be ignored, atoms will ballistically expand under the influence of gravity according to their initial in-trap momentum distribution. We may formalize this by

$$\hat{U}_0 \left(t_0 + t_{\mathrm{TOF}}, t_0\right) |\psi_{\mathrm{tr}}(t_0)\rangle = |\psi_{\mathrm{TOF}}\rangle, \tag{3.41}$$

where $\hat{U}_0$ denotes the time-evolution operator that describes the ballistic evolution of the in-trap state $|\psi_{\mathrm{tr}}(t_0)\rangle$ for a variable time-of-flight $t_{\mathrm{TOF}} \geq 0$ after switching off all trap potentials at time t_0. One can now show that the density distribution after time-of-flight $\langle \hat{n}(\boldsymbol{r}) \rangle_{\mathrm{TOF}}$, for sufficiently large times t_{TOF}, is linked to the in-trap momentum space density distribution $\langle \hat{n}(\boldsymbol{q}) \rangle_{\mathrm{tr}}$ via [148]

$$\langle \hat{n}(\boldsymbol{r}) \rangle_{\mathrm{TOF}} \approx \left(\frac{m}{\hbar t_{\mathrm{TOF}}}\right)^3 \langle \hat{n}(\boldsymbol{q_r}) \rangle_{\mathrm{tr}} (t_0). \tag{3.42}$$

Here, $\boldsymbol{q_r} \equiv m(\boldsymbol{r} - \mathbf{R}_0 - \mathbf{g}t_{\mathrm{TOF}}^2/2)/(\hbar t_{\mathrm{TOF}})$ reflects the ballistic condition, where $\mathbf{R}_0$ is the coordinate of the center of the trap and $\mathbf{g}$ refers to the gravitational acceleration. As $\langle \hat{n}(\boldsymbol{r}) \rangle_{\mathrm{TOF}}$ is directly probed by absorption imaging, we conclude that TOF images, in the limit where equation (3.42) holds, reveal the momentum distribution of atoms realized at the instant of the trap release. In particular, for N trapped atoms in a Bloch state $|n\boldsymbol{k}\rangle$, the momentum density distribution is given by (compare equation (3.32))

$$\langle \hat{n}(\boldsymbol{q}) \rangle_{n\boldsymbol{k}} = N f'_{n\boldsymbol{k}}(\boldsymbol{q}) = N \sum_{\mathbf{G}} |c_{n\boldsymbol{k}}(\mathbf{G})|^2 \, \delta\left(\boldsymbol{q} - (\mathbf{G} + \boldsymbol{k})\right). \tag{3.43}$$

---

[9]See subsection 2.4.1.

The resulting distribution $\langle \hat{n}(\boldsymbol{r}) \rangle_{\mathrm{TOF}}$ for large time-of-flight will thus exhibit pronounced peaks, known as *Bragg peaks*, at points that fulfill $\boldsymbol{q_r} = \boldsymbol{k} \pmod{\mathbf{G}}$. In other words, for a Bloch state, we expect to see a regular peak pattern with the periodicity of the reciprocal lattice. Note that each individual peak is weighted by a corresponding Fourier coefficient $|c_{n\boldsymbol{k}}(\mathbf{G})|^2$.

Now, the characteristic time scale where equation (3.42) can be considered accurate is given by the far field limit $t_{\mathrm{TOF}} > t_{\mathrm{FF}}$, with [197]

$$t_{\mathrm{FF}} = \frac{m l_{\mathrm{c}} \mathrm{R}_{\mathrm{tr}}}{\hbar}. \tag{3.44}$$

Here, l_{c} is the coherence length of the in-trap state and R_{tr} denotes the characteristic in situ extension of the atomic cloud. In our case, for a BEC with $l_{\mathrm{c}} \approx \mathrm{R}_{\mathrm{tr}} \approx 13\,\mu\mathrm{m}$, we may thus estimate $t_{\mathrm{FF}} \approx 230\,\mathrm{ms}$. Expansion times on this order, however, are out of reach with our current setup, where a typical time-of-flight amounts to $30\,\mathrm{ms}$ to $45\,\mathrm{ms}$. Nevertheless, these values still suffice to obtain useful information about the approximate momentum distribution of atoms in the optical lattice, specifically about the relative weights of Bragg peaks: As a result of the limited time-of-flight, Bragg peaks simply become broadened as compared to the ideal case of a Dirac delta.

In Figure 3.7, we present an exemplary time-of-flight measurement after sudden release from the boron-nitride lattice. Here, a BEC had been loaded into the ground state of the optical lattice by adiabatically ramping up the lattice depth to $V_{\mathrm{2D}} = 2.7\,E_{\mathrm{rec}}$ in $100\,\mathrm{ms}$. After holding for another $100\,\mathrm{ms}$, all trapping potentials were switched off abruptly and the atomic density distribution was recorded through resonant absorption imaging after $t_{\mathrm{TOF}} = 36\,\mathrm{ms}$. Zeroth and first order Bragg peaks are clearly visible, and numerical analysis of the momentum distribution of the Bloch state $|1, \Gamma\rangle$ for the same lattice parameters provides excellent agreement with the experimental results. This indicates that atoms indeed form a BEC in the lowest energy Bloch state of the optical.

Experimentally, a high visibility of Bragg peaks is often regarded as a clear signal of a BEC in an optical lattice, that is the presence of a large condensate or superfluid fraction [197]. To be precise, visibility is commonly defined as

$$\mathcal{V} \equiv \frac{N_{\mathrm{p}} - N_{\mathrm{h}}}{N_{\mathrm{p}} + N_{\mathrm{h}}}, \tag{3.45}$$

where N_{p} denotes the measured atom number in circular regions centered around the first order Bragg peaks, whereas N_{h} is the corresponding number for circular regions placed centrally in between them. The visibility can be considered a *heuristic* measure for the degree of long-range phase coherence of a bosonic many-body state in an optical lattice. This means that it will monotonically increase with the condensate fraction and reach $\mathcal{V} = 1$ for a pure condensate. We emphasize, however, that the mere appearance of Bragg peaks and a non-vanishing visibility in TOF images is no unequivocal signature of a finite BEC fraction in an optical lattice. In fact, even a pure thermal or normal fluid state in a lattice can exhibit analogous sharp features in the momentum distribution [200–203]. Therefore, to infer the presence of a finite condensate fraction from TOF images, it is usually required to identify more subtle characteristics. A widely accepted
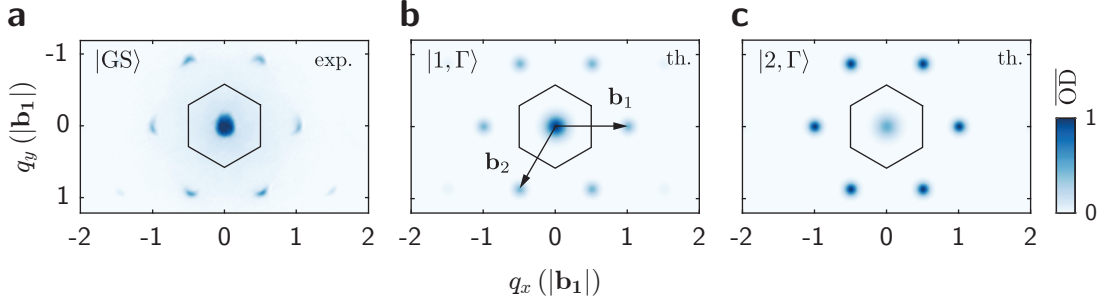
Fig. 3.7: Time-of-flight images for atoms in the Zeeman substate $|1, -1\rangle$ after sudden release from the boron-nitride lattice, with lattice depth $V_{2D} = 2.7\,E_{rec}$ and a quantization axis angle $\theta_B = 0°$. **a** Single-shot absorption image measured for $t_{TOF} = 36\,ms$. Due to the finite time-of-flight and harmonic confinement, individual momentum peaks show a finite width. The black hexagon depicts the Brillouin zone for reference. **b** The momentum distribution of the lowest energy Bloch state $|1, \Gamma\rangle$ for the same lattice potential provides reasonable agreement with the measurement. Results were obtained from equation (3.43) by replacing the Dirac delta function with a Gaussian of a fixed width. **c** For comparison: momentum distribution of the Bloch state $|2, \Gamma\rangle$. All densities have been normalized individually to the same peak amplitude.

one is a bimodal structure within Bragg peaks, which allows for an accurate estimate of the condensate fraction in the presence of a thermal or incoherent component (see, for example, [204]). A more rigorous but costly approach to assess the realized quantum many-body state through inspections of TOF images is given by a direct comparison to ab initio quantum Monte Carlo simulations as realized, for example, in [205].

In summary, TOF images after sudden release generally provide a good proxy for the momentum distribution of an atomic ensemble in an optical lattice. This in turn gives an essential characterization of the underlying many-body state. TOF imaging after sudden release is the central probing technique for experiments conducted in this work.

3.2.2 Band mapping

Another important type of release from an optical lattice is the so-called adiabatic band mapping (BM). Here, the lattice depth is slowly reduced in a way that a Bloch state $|n\boldsymbol{k}\rangle$ can follow its adiabatically connected eigenstate to the lattice potential $V(t)$ during the lattice ramp. In particular, the pair of quantum numbers $(n\boldsymbol{k})$ remains conserved. As a matter of fact, in the limit $V(t) \to 0$, the respective asymptotic Bloch sate $|n\boldsymbol{k}\rangle_0$ is composed only of momentum components $\{|\boldsymbol{G} + \boldsymbol{k}\rangle\}$ that lie exclusively within the n-th Brillouin zone (see Figure 3.5). BM therefore directly allows to identify the occupied band and quasimomentum of the initial Bloch state prior to the lattice ramp by imaging the momentum distribution after TOF, as in the case of sudden release. We stress that this identification is unique except for points that lie on the boundary of the Brillouin zone, which correspond to band touching points in the asymptotic band structure $\epsilon_n^0(\boldsymbol{k})$. Note that the latter is simply the free-particle dispersion relation folded back into the first Brillouin zone.

Experimentally, achieving true adiabaticity during BM is often challenging, if not impossible, for it usually conflicts with other constraints. For instance, performing

BM in the presence of gravity requires to maintain a residual trap potential that keeps atoms in the lattice during the ramp, in our case the XDT. To avoid excessive trap dynamics during BM, ramp times should be fast compared to the typical trap period. On the other hand, adiabaticity necessitates ramp times as large as possible. Even if the external trap can be circumvented, large ramp times may be in conflict with interaction-induced redistribution of the quasimomentum [198]. In our case, an adequate trade-off is achieved by an exponential ramp-down of the lattice within 2 ms to 3 ms, depending on the initial lattice depth. After completing the ramp, the XDT is switched off abruptly and the momentum distribution is imaged after TOF. The band mapping technique will be used extensively in chapter 4 to resolve and to quantify atom populations in higher Bloch bands of the boron-nitride lattice.

3.3 Lattice calibration techniques

A central experimental parameter for atoms in optical lattices is the lattice depth V_0. Specifying its exact value with high accuracy is crucial, for it has profound influence on almost all properties of the system. However, since the in situ intensities of lattice beams that determine the lattice depth generally cannot be measured directly, the lattice depth is usually not known a priori. On the other hand, experimentally, laser beam intensities can be controlled precisely, say in terms of some control parameter u_s. Typically, the control parameter is designed to scale linearly with the intensities and thus the lattice depth. This sets the stage for lattice depth calibration, whose aim is to provide a conversion factor between those two quantities, i.e. between the actual lattice depth V_0 and the set value for u_s.

In this section, we establish amplitude-modulation spectroscopy as our standard technique for lattice depth calibration of the spin-dependent boron-nitride lattice, as first discussed in [102]. In addition, we present Kapitza-Dirac diffraction as a useful method to calibrate and validate the in situ orientation of the quantization axis, which directly affects the sublattice energy offset for atoms with $m_F \neq 0$.

3.3.1 Amplitude-modulation spectroscopy

A variety of different techniques can be used to calibrate the lattice depth of an optical lattice. Often they rely on Landau-Zener tunneling [206, 207], Kapitza-Dirac diffraction [208–210], Stückelberg interferometry [211, 212], lattice phase shifts [213], or amplitude-modulation spectroscopy [214, 215]. All methods have in common that they probe, in one way or the other, the single-particle excitation spectrum. When the form of the lattice potential is completely specified, the single-particle spectrum for a given atomic species is uniquely determined by the lattice depth alone and provides, in principle, an injective mapping. By recording spectra at different set values u_s and comparing them to expectations from band structure calculations, one may thus arrive at the unknown lattice depths.

In our case, we directly probe the band gaps at quasimomentum Γ between the first and higher Bloch bands of our two-dimensional boron-nitride lattice through amplitude-modulation spectroscopy. The starting point is a BEC loaded into the ground state of the lattice for some fixed value u_s. We then apply a weak periodic intensity modulation
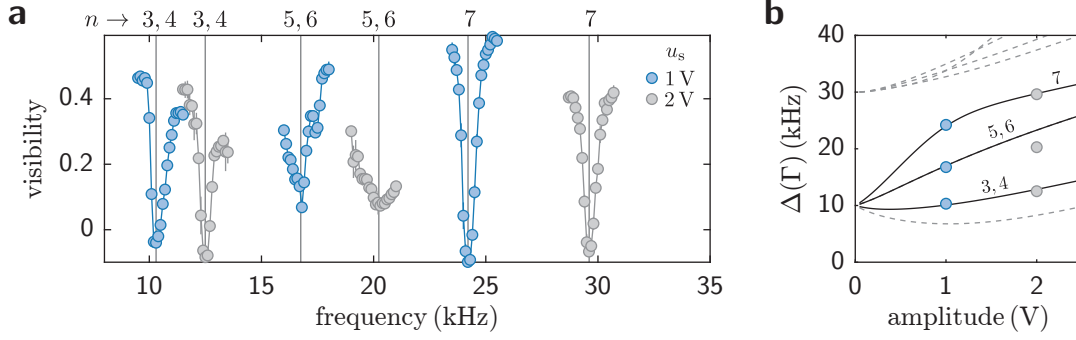
Fig. 3.8: Lattice depth calibration by amplitude-modulation spectroscopy: for a spin-dependent boron-nitride lattice, with $\theta_{\mathrm{B}} = 0°$ and atoms in the Zeeman substate $|1, -1\rangle$. **a** The measured visibility spectrum of first order Bragg peaks as a function of the modulation frequency for two different lattice depths encoded by the set voltages $u_{\mathrm{s}} = 1\,\mathrm{V}, 2\,\mathrm{V}$. Vertical lines indicate the resonance location (minima) extracted from a spline fit to the data. Numbers on the top denote band indices of the involved transitions. **b** By fitting the band gaps $\Delta_{1,n}(\Gamma)$ of all contributing transitions (black lines) simultaneously to the measured resonances, we obtain a conversion factor c_0 between the set voltage and lattice depth V_{2D}: here, $c_0 = 1.34(03)\,E_{\mathrm{rec}}\mathrm{V}^{-1}$. For data fitting with the multi-valued model function $\Delta_{1,n}(\Gamma; u_{\mathrm{s}})$, where $u_{\mathrm{s}} = V_{\mathrm{2D}}/c$, we assume an ideal boron-nitride lattice and take c as the only free parameter. Dashed lines in **b** denote transition frequencies to further bands.

of frequency ν_{m} and modulation depth δI_{m} to all three lattice beams simultaneously. Modulation depths amount to typically $1\,\%$ to $10\,\%$ with respect to the individual beam intensities. We scan the modulation frequency ν_{m} and record a band gap spectrum by evaluating the visibility of the first order Bragg peaks after TOF. Ideally, this is repeated for different set values u_{s}. Whenever the modulation frequency matches the transition $\Delta_{1,n}(\Gamma)$ into higher bands, the visibility in TOF images is strongly reduced as a result of parametric heating [214, 216].

In Figure 3.8, we show a corresponding visibility spectrum for atoms in the Zeeman substate $|1, -1\rangle$ and for a quantization axis angle $\theta_{\mathrm{B}} = 0°$. For this measurement, the lattice was ramped up exponentially within $100\,\mathrm{ms}$ to its final amplitude. After a hold time of $40\,\mathrm{ms}$, the modulation was turned on for $T_{\mathrm{m}} = 40\,\mathrm{ms}$, followed by sudden release and imaging after TOF. The resonance locations can be extracted from a fit and provide the observed band gap frequencies at Γ. By fitting the measured transitions with a multi-valued model function $\Delta_{1,n}(\Gamma; u_{\mathrm{s}})$, where $u_{\mathrm{s}} = V_{\mathrm{2D}}/c$ and c is the only free parameter, we obtain a best-fitting conversion factor c_0. We note that $\Delta_{1,n}(\Gamma)$ is obtained from exact numerical diagonalization of the Bloch Hamiltonian for an ideal boron-nitride lattice (equation (2.56)). The corresponding bands $(3, 4)$ and $(5, 6)$ are therefore degenerate at the Γ point. Remarkably, the model function fits well to all resonances except for the bands $(5, 6)$ at the largest set value u_{s}, which cannot be explained by lattice misalignment or small deviations from the quantization axis angle $\theta_{\mathrm{B}} = 0°$.

It is fair to ask whether assuming an ideal boron-nitride lattice for the fit is justified; after all, the actual lattice implementation will inevitably deviate from the ideal p-polarization configuration, which can have considerable impact on the band structure.

For example, even a small difference in the pairwise beam angles $\angle(\boldsymbol{k}_i, \boldsymbol{k}_j)_{i \neq j}$ within the lattice plane will cause a strong deformation of the lattice potential, resulting in a splitting of the degeneracy among Bloch bands $(3, 4)$ and $(5, 6)$, respectively. Before lattice depth calibration, however, we make sure to minimize these effects by carefully adjusting all lattice beam degrees of freedom. In particular, remaining with a slight lattice asymmetry, we *imbalance* the relative beam intensities so that the location of the minima in the second Bloch band coincide with the vertices of the Brillouin zone. This guarantees that the realized lattice potential matches the ideal boron-nitride lattice as close as possible and justifies working with the latter, though the final lattice beam parameters might in effect deviate strongly from the ideal p-polarization configuration. The fact that the model function $\Delta_{1,n}(\Gamma)$ fits well to all resonances, with one exception, can indeed be regarded as a confirmation for this. We leave a more elaborate discussion of this subject to Appendix A.

Finally, we note that lattice depth calibration should be performed preferably in the shallow lattice regime, with relatively small atom numbers: this reduces resonance shifts induced by mean-field interactions and avoids systematic errors in the conversion factor.

3.3.2 Kapitza-Dirac diffraction

We now turn our attention to the in situ orientation of the quantization axis. Knowing and controlling its precise alignment in terms of the angle θ_B is important, for it directly affects the sublattice energy offset of the spin-dependent boron-nitride lattice. Recall that θ_B was defined for the ideal p-polarization configuration as the angle between the z-axis, being collinear with the fictitious magnetic field, and the external magnetic field $\mathbf{B}_{\text{ext}}$ that determines the quantization axis. Typically, the external field is created by the subset $\{\mathbf{Q}_x, \mathbf{Q}_z\}$ of compensation coils (see subsection 2.2.2), which allow to align $\mathbf{B}_{\text{ext}}$ along an arbitrary direction in the xz-plane. In particular, based on the known characteristics of the coils, the angle $\theta_B' \equiv \angle(\mathbf{Q}_z, \mathbf{B}_{\text{ext}})$ can be set precisely. We note, however, that $\mathbf{Q}_z$ is slightly tilted with respect to the z-axis. For this reason, one might anticipate that $\theta_B = \theta_B' + \Delta\theta_B^{\text{set}}$, with some nonzero offset $\Delta\theta_B^{\text{set}}$.

A simple but time-consuming procedure to verify that θ_B is well-controlled and indeed follows the above prescription is to probe the excitation spectrum as in subsection 3.3.1 for varying angles θ_B'. For example, this has been conducted in the work of T. Klafka [107]. Here, we present a different and more convenient method that is based on an analysis of Kapitza-Dirac diffraction patterns. The idea is to examine a triangular contrast $\mathcal{C}$ among first order Bragg peaks as a function of θ_B' for otherwise fixed lattice parameters and interaction times τ_{KD}. Specifically, we define

$$\mathcal{C} \equiv \frac{N_+ - N_-}{N_+ + N_-}, \tag{3.46}$$

where $N_\pm$ is the atomic population in the first order Bragg peaks associated to reciprocal lattice vectors $\pm\mathbf{b}_1$, $\pm\mathbf{b}_2$, and $\pm\mathbf{b}_3$. Now, by comparing the measured contrast with the expected functional form of $\mathcal{C}(\theta_B)$, one may infer the offset $\Delta\theta_B^{\text{set}}$ and validate that the direction of the quantization axis is well-controlled and can be precisely aligned to any desired value of θ_B. Thus, the offset Δ_{AB} is known with high accuracy.
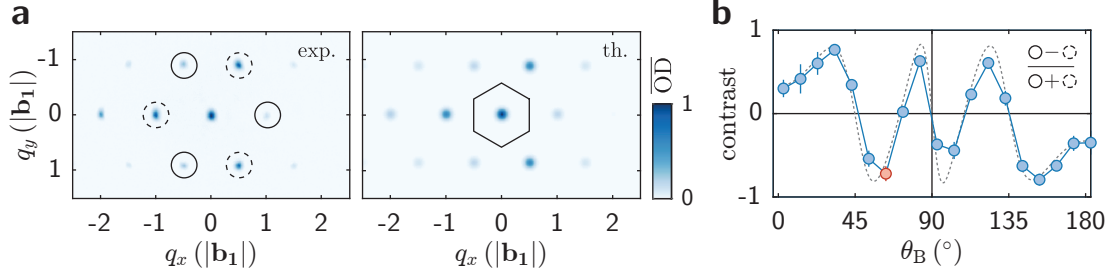
Fig. 3.9: Validating the alignment of the quantization axis through Kapitza-Dirac diffraction. **a** Exemplary Kapitza-Dirac diffraction pattern for atoms in $|1, -1\rangle$ in the boron-nitride lattice, with $\theta_{\mathrm{B}} = 63°$ and interaction time $\tau_{\mathrm{KD}} \approx 50\,\mu\mathrm{s}$. Left panel: measured single-shot absorption image after TOF. Right panel: Numerical calculation based on a coherent Bloch state expansion for the same lattice parameters. Circular regions around first order Bragg peaks are used to define a triangular contrast, as shown in the inset of subfigure **b**. The contrast as a function of θ_{B} is in excellent agreement with the numerical calculation (dashed line) for an interaction time $\tau_{\mathrm{KD}} = 45.7\,\mu\mathrm{s}$. The only free parameter is a uniform horizontal shift to account for an offset in the experimental set angle of the quantization axis: here, $\Delta\theta_{\mathrm{B}}^{\mathrm{set}} = +3°$. The red data point marks the realization in **a**.

In Figure 3.9, we depict an exemplary measurement of the triangular contrast. Here, a spin-polarized BEC was initially prepared in the XDT for some fixed value θ_{B}'. Subsequently, the lattice potential was turned on abruptly for a duration $\tau_{\mathrm{KD}} \approx 50\,\mu\mathrm{s}$ at a constant lattice depth $V_{2\mathrm{D}} = 10\,E_{\mathrm{rec}}$, followed by sudden release and imaging after TOF. This protocol was repeated for different set values of θ_{B}'. Note that a numerical calculation of $\mathcal{C}(\theta_{\mathrm{B}})$ for an interaction time $\tau_{\mathrm{KD}} = 45.7\,\mu\mathrm{s}$ is in excellent agreement with the experimental data. The slightly smaller value for τ_{KD} is readily explained by an observed delay of roughly $5\,\mu\mathrm{s}$ to reach the specified lattice depth. We stress that the numerical analysis of $\mathcal{C}(\theta_{\mathrm{B}})$ is based on a coherent Bloch state expansion, assuming an ideal boron-nitride lattice potential with the same parameters as used in the experiment. Apart from an overall offset $\Delta\theta_{\mathrm{B}}^{\mathrm{set}} = +3°$ that accounts for the misalignment of the compensation coils, there were no further free parameters. Also note that the simulated TOF image in Figure 3.9a, where higher order Bragg peaks are clearly visibly, is in excellent agreement with a corresponding experimental single-shot absorption image. All of this shows that the realized lattice potential is close to the ideal boron-nitride lattice and that the experimental rotation of the quantization axis provides reasonable and accurate control over the sublattice energy offset. This aspect will be essential in the following chapter 4.

3.4 Conclusion & Outlook

In this chapter, we have discussed several aspects of the physics of non-interacting atoms in a spin-dependent optical boron-nitride lattice. First, starting from the adiabatic approximation, we derived a reduced Hamiltonian for the center of mass motion of the atoms's m-th dressed internal state $|\eta_m(\boldsymbol{r})\rangle$. The latter is an element of the hyperfine subspace $\mathscr{H}_{\mathrm{int}}^F$ and exhibits, in general, a spatial dependence that results in the pres-

ence of artificial gauge fields, i.e. geometric scalar and vector potentials. These gauge fields can become significant for the spin-dependent lattice since the vector light shift combined with the external magnetic field allows for creating spatially varying, periodic magnetic landscapes. Future studies may focus on a detailed experimental and theoretical characterization of gauge fields that can be realized in this way. We point out that when the adiabatic approximation in the subspace $\mathscr{H}_{\mathrm{int}}^F$ breaks down, further exciting situations may arise that open new prospects for realizing two-dimensional spin-orbit coupling, which is ubiquitous in many phenomena of solid-state physics. Specifically, in the momentum-spin basis, the matrix elements of our lattice potential's vector light-shift are given by

$$\langle m\mathbf{G}| \, \hat{\mathcal{V}}_{\mathrm{L}}^v \, |m'\mathbf{G}'\rangle = \sum_i \mu_{\mathrm{B}} g_F \, \langle m| \, \hat{F}_i \, |m'\rangle \, B_{\mathrm{L}}^i(\mathbf{G} - \mathbf{G}') \,, \qquad (3.47)$$

where the $B_{\mathrm{L}}^i(\mathbf{J})$ denote the Fourier expansion coefficients of the fictitious magnetic field. Evidently, there is a non-vanishing coupling between spin and momentum, which can lead to band structures with non-trivial spin textures. We emphasize that a similar situation has been studied for the case $F = 1/2$, where the possibility of observing a spin Hall effect was predicted [217].

In the limit of a dominating uniform external magnetic field, the reduced Hamiltonian becomes a conventional Hamiltonian with a separate, tunable boron-nitride potential for each Zeeman substate. We have introduced the Bloch formalism and presented exact numerical calculations of band structures and Bloch states for different potential configurations. Particular emphasis was put on a detailed characterization of higher Bloch states in terms of their real-space representations, which reveal intricate phase patterns. Moreover, we have elaborated on the fundamental physical properties of Bloch states, including the momentum distribution and the intrinsic orbital angular momentum. For both quantities, we have presented explicit numerical calculations. In particular, it was shown that higher Bloch states in a boron-nitride lattice generally possess non-vanishing intrinsic orbital angular momentum, which can be tuned by changing the orientation of the external quantization field.

Furthermore, we have discussed sudden and adiabatic release from an optical lattice as probes for the momentum and quasimomentum distribution, which constitute our central experimental observables. Finally, we have introduced amplitude-modulation spectroscopy as our standard method for lattice depth calibration and elucidated how Kapitza-Dirac diffraction can be used to validate and calibrate the precise in situ orientation of the quantization axis. All notions and concepts established in this chapter will guide our studies in subsequent ones.

4 Bosonic superfluids in higher Bloch orbitals

In this chapter, I report on the realization of condensates in higher Bloch orbitals of an optical boron-nitride lattice. We start with a general overview of the field of ultracold bosonic atoms in higher lattice orbitals and elucidate the primary goals and prospects of studying these systems. Following this, we examine the main method used in this work for transferring atoms into higher Bloch bands via quenches of the sublattice energy offset. Next, we present measurements that provide compelling evidence for the emergence of unconventional orbital condensates in the second and fourth band of the boron-nitride lattice. Specifically, for condensates in the second band, we analyze signatures of time-reversal symmetry breaking and find evidence for a chiral superfluid order. Next, by examining the condensation and relaxation dynamics, we identify relevant processes that lead to an eventual dissolution of orbital condensates in higher bands. Finally, additional transfer methods into higher Bloch bands are explored.

Ultracold atoms in higher Bloch orbitals offer unique possibilities for realizing exotic quantum many-body states with no analogue in traditional condensed matter systems. The first pioneering theoretical works heading in this direction were largely concerned with weakly interacting superfluid bosons loaded into the second band of a monopartite square or cubic lattice. Perhaps one of the central insights in the study of these so-called p-band bosons was that a BEC with intrinsic angular momentum ordering can emerge that spontaneously breaks the time-reversal symmetry and is characterized by a complex order parameter [70, 71, 218]. In particular, the ground state of p-band bosons with weak repulsive interactions in a two-dimensional square lattice was predicted to feature staggered angular momentum ordering that can be understood in terms of a bosonic analogue of Hund's rule, as first elucidated by Liu and Wu [70]. Subsequent theoretical studies soon also focused on systems with strong interactions and on lattice geometries that exhibit geometrical frustration, predicting, for example, a quantum stripe ordering in a triangular lattice [69], Wigner crystallization in a honeycomb lattice [219], or exotic bond-algebraic liquid phases in the strongly correlated insulating regime of a square lattice [220]. Meanwhile, the phase diagram of p-band bosons has been extensively studied by mean-field and Gutzwiller theory [221] and complemented by quantum Monte Carlo simulations [222], showing that angular momentum ordering can extend into the Mott insulating phase. Similar analyses have been carried out in the context of p-band fermions in optical lattices [223–225]. Moreover, following the general trends in the solid state community, there has been increasing interest in all sorts of unique topological properties in higher lattice orbitals, as demonstrated by the ever-growing number of related publications [73–75, 226–229].

Besides facilitating the investigation of yet undiscovered phases of matter, ultracold atoms in higher lattice orbitals also give new impetus to the established field of quantum simulation of crystalline solids, owing to the orbital degrees of freedom that are inherent in both systems. As a matter of fact, orbital physics of electrons is ubiquitous in the study of condensed matter, including strongly correlated materials. For example, in transition metal oxides the electronic orbital degrees of freedom can be crucial for such diverse phenomena as high-temperature superconductivity, colossal magnetoresistance, or metal-insulator transitions [65, 230]. In view of this, atoms in higher lattice orbitals constitute ideal platforms to simulate and to investigate the role of orbital effects in solids [67]. Moreover, in the strongly interacting insulating regime, orbital degrees of freedom can be mapped to various paradigmatic spin models of quantum magnetism, such as the quantum Heisenberg model [231] or the J_1-J_2 model [232]. Arguably, our above considerations give only a brief overview of the fascinating physics of ultracold atoms in higher lattice orbitals: for comprehensive reviews we refer to [66, 68, 76].

On the experimental side, ultracold atoms in higher Bloch bands are still largely unexplored. In particular, experimental research on bosonic superfluids in higher bands has been confined almost exclusively to the bipartite square lattice geometry. In this chapter, we report on the experimental realization of unconventional bosonic superfluids or condensates in higher Bloch bands of a hexagonal boron-nitride optical lattice. At the beginning of this project, to the best of our knowledge, no systematic investigation of such condensates had been pursued. Only recently, two groups have reported on realizations of orbital condensates in a similar lattice geometry [82, 83]. Experimental data presented in this chapter has been acquired in collaboration with T. Klafka, J. Seeger, and P. Groß, with significant contributions from the author. Data analysis and theory calculations presented in this chapter have been performed by the author. A collaboration with G. Koutentakis, S. Mistakidis, and P. Schmelcher has been established to work on the theoretical description of the condensation process.

4.1 Condensates in higher Bloch bands

In this section, we give a brief introduction to the general notion of condensates in higher Bloch bands, which will be referred to as orbital condensates, and explain the role of orbital degrees of freedom. In addition, we have a glance on previous experimental efforts to realize orbital condensates and sketch the main difference between an orbital condensate in the second Bloch band of a bipartite square lattice and its counterpart in a hexagonal boron-nitride lattice.

4.1.1 General notions about orbital condensates

To a large extent, the intriguing physics encountered in the study of bosons in higher lattice orbitals can be attributed to orbital degeneracy. In fact, orbital degeneracy and the associated orbital degrees of freedom are a key feature of bosons in higher Bloch bands. For illustration, consider the many-body ground state of an ideal BEC in the usual setting of an optical lattice: Under fairly general conditions of time-reversal symmetry, it will be characterized by a macroscopic occupation of the lowest energy Bloch state $|1, \Gamma\rangle$ of the first band. The situation, however, may drastically change

if the BEC is excited into higher bands, where the respective lowest energy Bloch states are frequently degenerate. Let us assume that there are d such degenerate states $\{|\psi_i\rangle\}_{i=1,\dots,d}$ to a given target band, with $d > 1$. These states span a d-dimensional manifold M_d, which defines what we call the orbital degrees of freedom. We shall now be interested in the emerging many-body "ground" state of bosons in higher bands under the constraint that the only accessible single-particle states lie exclusively in M_d.[1] Although this constraint gives a considerable simplification with respect to the total band space, it is still not a priori evident what the new emerging many-body ground state should look like. For instance, one might imagine a *fragmented* BEC in which multiple states $|\psi_i\rangle$ are macroscopically occupied. Another possibility is a single BEC with macroscopic occupation of a single state $|\phi\rangle$, where $|\phi\rangle$ is given by a superposition of Bloch states $|\psi_i\rangle$ with a definite relative phase. All of this is primarily related to fundamental questions about condensates in degenerate manifolds (see, for example, [233–235]). In any case, it is obvious that interactions, no matter how weak, become determinant for selecting the minimal energy state. Given that interactions usually play a minor role for the ground state wave function of a superfluid bosonic ensemble, this is probably the most appealing aspect about condensates in higher Bloch bands.

Another important aspect of orbital physics in higher Bloch bands is the nontrivial character of higher Bloch states $|\psi_i\rangle$. In contrast to the wave function of the absolute ground state $|1,\Gamma\rangle$, which is necessarily positive definite, higher Bloch orbitals usually come along with complex phase patterns such as phase windings or intricate nodal structures (see subsection 3.1.4). Moreover, higher Bloch orbitals often have more complicated geometries with lower spatial symmetries than the underlying lattice potential and may thus induce anisotropy. All in all, the important ingredients of orbital physics may be summarized as follows: First, orbital degeneracy that puts interactions into a dominant position. Second, nontrivial Bloch orbitals with complex geometries and phase structures. While degeneracy defines the number of orbital degrees of freedom, the associated Bloch orbitals literally determine in what shape, so to say, these orbital degrees of freedom manifest. Naturally, both aspects will crucially depend on the particular band and lattice geometry at hand. Eventually, the interplay between orbital degrees of freedom, interaction, and lattice geometry gives rise to a variety of exotic superfluid states beyond the no-node theorem [68] and is responsible for a plethora of new physical phenomena.

4.1.2 State of experimental advances

So far, only a small number of groups has engaged in the experimental study of ultra-cold bosonic atoms in higher lattice orbitals. In part, this might be attributed to the experimental and conceptual challenges in creating and preparing long-lived states in higher Bloch bands. Bosons in higher bands can indeed, at best, only be metastable and will eventually decay into lower-lying states if not prevented by some ingenious mechanism.

First promising attempts to realize orbital condensates were made in a deep and highly anisotropic three-dimensional cubic lattice by Müller et al. [236]. The experi-

---

[1]This constraint is reasonable for a superfluid state with weak interactions as it can only be stable or at least metastable in the local minima of a given Bloch band.

mentalists used a stimulated two-photon Raman process to excite bosonic atoms from the Mott insulating ground state into the second Bloch band. Although they found evidence of coherence build-up along a single lattice dimension, the overall lifetimes of atoms in the second band remained rather small and no decisive cross-dimensional phase coherence could be observed.

The first true long-lived orbital condensates were achieved in a seminal experiment by Wirth et al. [77] in the Hamburg group of A. Hemmerich: The essential ingredient was a two-dimensional bipartite square lattice that allowed for a fast and controlled change of the sublattice energy offset. By rapidly tuning this offset, atoms could be excited into the second Bloch band. Subsequent thermalization revealed a coherent macroscopic occupation of degenerate quasimomenta X and X′ associated with the minimal energy Bloch states $|2, X\rangle$ and $|2, X'\rangle$, respectively. Theory suggested that the system should favor a single condensate in one of the two superposition states

$$|\psi_\pm\rangle \equiv \cos(\bar{\theta}) |2, X\rangle + \exp(i\phi_\pm) \sin(\bar{\theta}) |2, X'\rangle, \tag{4.1}$$

where $\bar{\theta} \equiv \pi/4$ and $\phi_\pm \equiv \pm\pi/2$. In this nomenclature, the angle $\theta \in [0, \pi/2)$ determines the weight of the two Bloch components and $\phi \in [-\pi, \pi)$ defines their relative phase. At that time, the true value of the relative phase remained experimentally unresolved. Subsequent interference experiments [237] managed to show that it indeed takes only one of two possible values in each experimental realization. This provided conclusive evidence for a chiral superfluid state compatible with equation (4.1), though the measurement setup did not allow to quantify those values exactly. A comprehensive review of these early studies as well as newer ones can be found in [79]. We stress that, among all possible values of θ and ϕ, the choices $\bar{\theta}$ and $\phi_\pm$ minimize the interaction energy in case of repulsive atoms. The states $|\psi_\pm\rangle$ are characterized by spontaneous time-reversal symmetry breaking and exhibit *staggered* angular momentum ordering along adjacent lattice sites, as illustrated in Figure 4.1 by the alternating orientation of phases vortices in the respective wave functions $\langle r|\psi_\pm\rangle$. Note the larger spatial extent of these wave functions as compared to the Bloch orbitals, leading to a reduced interaction energy. Note also that $\langle r|\psi_\pm\rangle$ give rise to a maximization of the local onsite angular momentum, reminiscent of Hund's rule. However, the total net orbital angular momentum remains zeros.

Until the start of this project, to the best of our knowledge, no orbital condensates had been realized in lattice geometries different from a bipartite square lattice. It has therefore been a central goal of our studies to advance research into this direction for the case of a hexagonal boron-nitride lattice; all the more because orbital condensates in a hexagonal boron-nitride lattice are expected to be of a different kind than those in a bipartite square lattice. For example, consider the minimal energy Bloch states $|2, K\rangle$ and $|2, K'\rangle$ in the second band of our boron-nitride lattice, where K and K′ denote the two distinct vertices of the Brillouin zone. Both states are visualized in Figure 4.2 for a common set of lattice parameters. In sharp contrast to $|2, X\rangle$ and $|2, X'\rangle$ (compare Figure 4.1), the states $|2, K\rangle$ and $|2, K'\rangle$ possess a genuinely complex phase profile, respectively. To be more precise, $|2, K\rangle$ ($|2, K'\rangle$) features anti-clockwise (clockwise) phase vortices on the deeper sublattice sites which gives rise to a *rectified* angular momentum ordering. We stress that this ordering is associated with a finite macroscopic
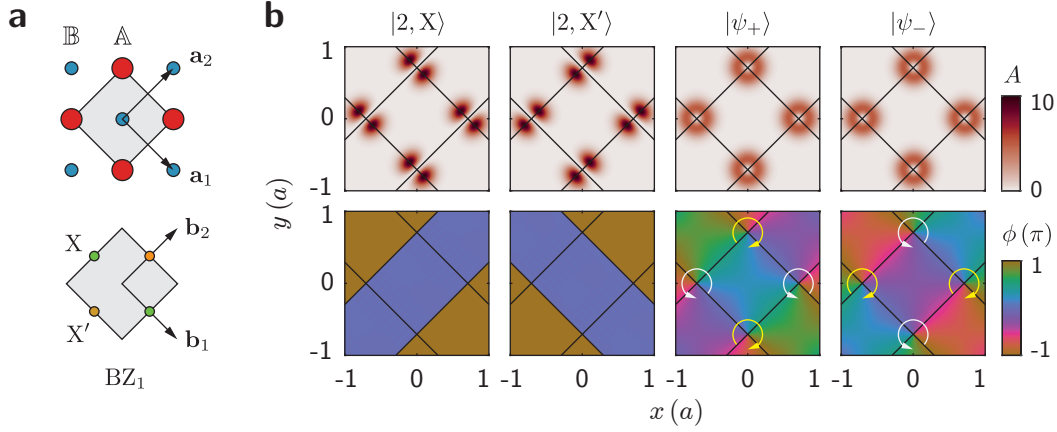
Fig. 4.1: Higher orbital states in a bipartite square lattice. **a** Top: Sketch of a bipartite square lattice with primitive lattice vectors $\mathbf{a}_1$, $\mathbf{a}_2$ that span the primitive unit cell (grey square). Blue sublattice sites denote shallow wells, red sublattice sites denote deep wells. Bottom: Associated Brillouin zone with reciprocal lattice vectors $\mathbf{b}_1$, $\mathbf{b}_2$. Quasimomenta X and X′ correspond to the typical location of the minima in the second band. **b** Wave functions to the states $|2, \mathrm{X}\rangle$, $|2, \mathrm{X}'\rangle$, $|\psi_\pm\rangle$ for a square lattice potential as defined in [79], with a lattice depth $V_0 = 6\,E_{\mathrm{rec}}$ and sublattice energy offset $\Delta_{\mathrm{AB}} \approx 14\,E_{\mathrm{rec}}$. Amplitudes (phases) of wave functions are depicted in the upper (lower) panel. Circular arrows indicate orientations of the phase windings. For convenience, wave functions have been normalized such that integration of A over a primitive unit cell gives the volume v of that cell. The global phase of Bloch orbitals has been gauged such that the zero-momentum component $c_{n\mathbf{k}}(\mathbf{G}_0)$ is real-valued.

value of the total angular momentum when the corresponding phase vortices have a non-vanishing orbital weight (see also subsection 3.1.5). Now, as before, a general single-particle state in the degenerate manifold spanned by $|2, \mathrm{K}\rangle$ and $|2, \mathrm{K}'\rangle$ may be written as

$$|\psi\rangle = \cos(\theta)\,|2, \mathrm{K}\rangle + \exp(\mathrm{i}\phi)\sin(\theta)\,|2, \mathrm{K}'\rangle. \tag{4.2}$$

One may ask for the states $|\psi\rangle$ that minimize the interaction energy among repulsive atoms. According to Figure 4.2, superpositions of Bloch states $|2, \mathrm{K}\rangle$ and $|2, \mathrm{K}'\rangle$ give rise to a density wave, which is usually energetically disfavored. In fact, as we show in Appendix B, the interaction energy for $|\psi\rangle$ is independent of the relative phase ϕ and takes a minimum value for $\theta = 0, \pi/2$. In other words, the system should favor condensation in one of the two Bloch states instead of a superposition of Bloch states. Of course, this line of reasoning builds on the assumption of a single condensate, i.e. the absence of fragmentation, and is only valid, strictly speaking, for a homogenous system within a simple mean-field treatment. Nevertheless, it gives a good estimate for an unconventional many-body state that might be approximately realized in the experiment within the weakly interacting superfluid regime. We emphasize that, since $|2, \mathrm{K}\rangle$ and $|2, \mathrm{K}'\rangle$ are TRS partner (see subsection 3.1.5), spontaneous condensation in one of the Bloch states necessitates spontaneous breaking of time-reversal symmetry.

In the rest of this chapter, we investigate and present the experimental realization of orbital condensates in the second and fourth band of our boron-nitride lattice. The observed orbital condensate in the second band is compatible with a macroscopic occu-
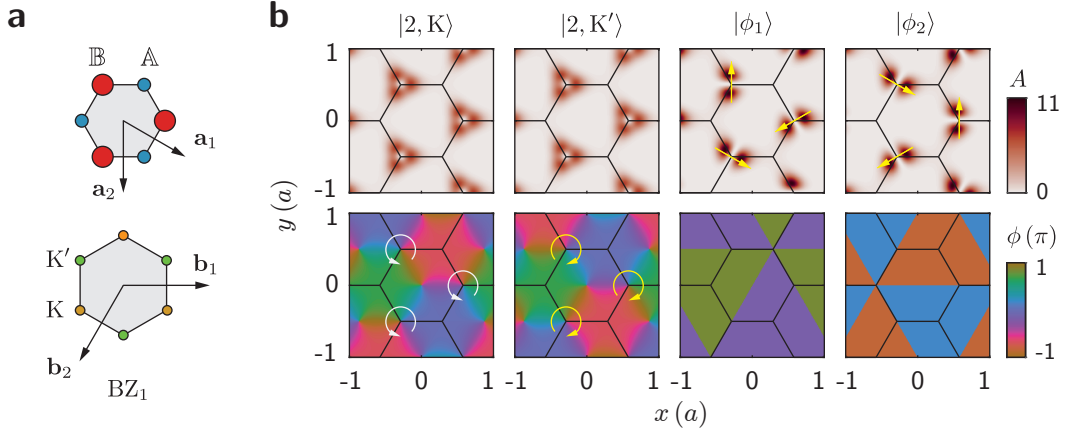
Fig. 4.2: Higher orbital states in a boron-nitride lattice. **a** Top: Sketch of a boron-nitride lattice with primitive lattice vectors $\mathbf{a}_1$, $\mathbf{a}_2$, which define the Wigner-Seitz cell (grey hexagon). Blue sublattice sites denote shallow wells, red sublattice sites denote deep wells. Bottom: Associated Brillouin zone with reciprocal lattice vectors $\mathbf{b}_1$, $\mathbf{b}_2$. Quasimomenta K and K′ correspond to the typical location of the minima in the second band. **b** Wave functions to the states $|2, \mathrm{K}\rangle$, $|2, \mathrm{K}'\rangle$, $|\psi_{1,2}\rangle$ for the spin-dependent boron-nitride potential with $\theta_{\mathrm{B}} = 180°$, $V_{2\mathrm{D}} = 6\,E_{\mathrm{rec}}$, and atoms in Zeeman substate $|2, -2\rangle$. Sublattice energy offset amounts to $\Delta_{\mathrm{AB}} \approx -14\,E_{\mathrm{rec}}$. Amplitudes (phases) of wave functions are depicted in the upper (lower) panel. Circular arrows indicate orientations of the phase windings. For convenience, wave functions have been normalized such that the integration of A over a primitive unit cell gives the volume v of that cell. The global phase of Bloch orbitals has been gauged such that the zero-momentum component $c_{n\boldsymbol{k}}(\mathbf{G}_0)$ is real-valued. Superposition states $|\psi_{1,2}\rangle$ are defined according equation (4.2), with $\theta = \pi/4$ and a relative phase $\phi_{1,2} = \pi/3, \pi$. Normal arrows in the top panel show the principal axis of the resulting onsite orbitals, revealing density waves with doubled periodicity.

pation of a single-particle state according to Equation 4.2 and shows a clear indication of symmetry breaking. Meanwhile, we note that two more groups have recently reported on orbital condensates in a similar lattice geometry: Jin et al. [82] claim the observation of a so-called Potts-nematic quantum phase for an ultracold bosonic ensemble in the second band of a hexagonal optical lattice. However, the results are controversial since the emergence of this order cannot be explained in terms of simple mean-field theory but relies on intricate renormalization effects. In contrast, the recent experimental observation of a chiral superfluid order in the second band of a boron-nitride lattice by Wang et al. [83] is in strong agreement with our findings.

4.2 Controlled transfer into higher Bloch bands

A selective and substantial population of higher Bloch bands is an essential prerequisite for the creation of an orbital condensate. In this section, we examine our standard method for preparing atoms in higher Bloch bands of a spin-dependent boron-nitride lattice. The method is based on a Landau-Zener type transfer induced by a quench of the sublattice energy offset through a rapid rotation of the external quantization axis. We emphasize that it is not the only efficient way to prepare atoms in higher Bloch bands of our optical lattice: a detailed survey and investigation of additional techniques

can be found in the PhD theses of T. Klafka [107] and J. Seeger [106].

4.2.1 Rapid quenches of the sublattice energy offset

Rapid quenches of the sublattice energy offset Δ_{AB} in a bipartite lattice provide a simple and direct means to prepare atoms in higher bands. One central reason for this is that the single-particle energy spectrum in a bipartite lattice generically exhibits several band crossings or avoided crossings as a function of Δ_{AB}. A band crossing is a point $\mathcal{P}_\varepsilon$ in the parameter space of Δ_{AB} where two or more bands approach close to each other such that there is at least one quasimomentum at which the bands touch. Analogous to the famous Landau-Zener tunneling, atoms prepared in a band that has a band crossing can undergo diabatic transitions into adjacent bands by a fast quench of Δ_{AB} across a point $\mathcal{P}_\varepsilon$. To achieve a large transfer fraction, the rate of change of the frequency separation among the relevant energy bands must be large compared to the square of the minimal band gap frequency.[2] In our spin-dependent boron-nitride lattice the sublattice energy offset is given by

$$\Delta_{\text{AB}} = 9V_{\text{2D}}\bar{m}_F \cos(\theta_{\text{B}})\eta(\omega_{\text{L}}; F)\,, \tag{4.3}$$

which can be tuned by changing the quantization axis angle θ_{B}, i.e. by rotating the direction of external magnetic field $\mathbf{B}_{\text{ext}}$. For clarity, we shall assume atoms in the Zeeman substate $|2, -2\rangle$, which is the typical internal state that we work with. Figure 4.3a displays the associated energy spectrum of the first five bands as a function of θ_{B} for a lattice depth $V_{\text{2D}} = 8\,E_{\text{rec}}$. Note that the third band is not resolved as its bandwidth is too small.

A typical experimental sequence starts with a spin-polarized BEC loaded into the lowest band of the optical lattice at an initial angle $\theta_{\text{B}}^{\text{i}} = 0°$. This corresponds to a maximum offset $\Delta_{\text{AB}}^{\text{i}} > 0$ at a given lattice depth for the internal state $|2, -2\rangle$. The starting point is illustrated by inset ① of Figure 4.3a for the weakly interacting superfluid regime, where atoms occupy the lowest band only at quasimomentum Γ. By rapidly rotating the quantization axis towards a final angle $\theta_{\text{B}}^{\text{f}} > 90°$, which results in a negative offset $\Delta_{\text{AB}}^{\text{f}} < 0$, the band crossing at $\theta_{\text{B}} = 90°$ (middle inset) is traversed and atoms can be elevated into the second band, as indicated by inset ② for a final angle $\theta_{\text{B}}^{\text{f}} = 106°$. Note that a fast rotation of the quantization axis and the associated quench of Δ_{AB} does not affect the quasimomentum. Hence, immediately after reaching the final angle, atoms in the second band will still be localized at Γ. We also note that a rapid quench to a final angle that involves further successive band crossings can lead to subsequent transitions into even higher bands. For instance, a final angle $\theta_{\text{B}}^{\text{f}} = 135°$ for the parameters in Figure 4.3 would result in a population transfer to the fourth band.

Before we proceed with some experimental details concerning the rotation of the quantization axis, we note that the number and location of band crossings $\mathcal{P}_\varepsilon$ generally depends on the lattice depth and other details of the lattice potential. Usually, additional band crossings between ever higher bands will emerge at the boundary values

---

[2]Compare also the more rigorous conditions in Morsch and Oberthaler [207] and Holthaus [238] in the context of accelerated optical lattices.
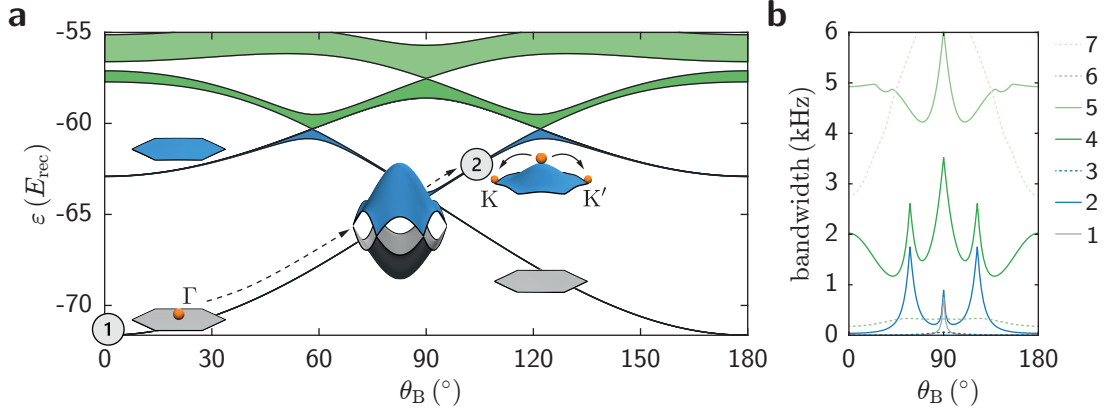
Fig. 4.3: Landau-Zener type transfer scheme into higher Bloch bands of the spin-dependent optical boron-nitride lattice. **a** Energy spectrum of the first five Bloch bands as a function of the quantization axis angle θ_B for a lattice depth $V_{2D} = 8\,E_{rec}$ and atoms in the Zeeman substate $|2, -2\rangle$. Multiple band crossings are visible. The third band is not resolved on this scale as its bandwidth is too small. ① Starting point at the initial angle $\theta_B^i = 0°$ with atoms localized at quasimomentum Γ of the lowest band. ② A rapid quench to a final angle $\theta_B^f = 106°$ across the first band crossing (central inset) transfers atoms diabatically into the second band, leaving the initial quasimomentum unaltered. Since Γ is an unstable point (local maximum), interactions will lead to a redistribution of the quasimomentum with a possible accumulation in the local, degenerate minima at K and K'. Note that the spectrum is symmetric around $\theta_B = 90°$ because lattice potentials on both sides are linked by inversion. **b** Related bandwidths of the first seven bands as a function of θ_B. Dashed lines correspond to bands that are not visible in **a**. Note the very small bandwidth of the third band, which stays below 60 Hz. Evidently, band crossings are signaled by pronounced cusps in the bandwidths.

$\theta_B = 0°, 180°$ for increasing lattice depths. For example, in Figure 4.3a an emerging band crossing between the fourth and fifth band becomes apparent. Meanwhile, the locations of already existing band crossings tend to shift towards the high symmetry point $\theta_B = 90°$. It is insightful to note that band crossings are signaled by cusps in the corresponding bandwidths, as visualized in Figure 4.3b. We stress that band crossings can be classified into accidental and essential degeneracies. The latter are relatively robust to changes of the lattice depth or the orientation of the quantization axis.

Experimental details The external magnetic field $\mathbf{B}_{ext}$ that defines the quantization axis for our spin-dependent boron-nitride lattice is created by the subset $\{\mathbf{Q}_x, \mathbf{Q}_y, \mathbf{Q}_z\}$ of compensation coils described in subsection 2.2.2. Initially, we take $\mathbf{B}_{ext} = B_{ext}\mathbf{e}_z$ to point along the z-direction, with a typical field magnitude $B_{ext} = 2.2\,\text{G}$. We perform a rotation of $\mathbf{B}_{ext}$ in the xz-plane by driving appropriate time-dependent currents through the coils $\mathbf{Q}_x$ and $\mathbf{Q}_z$, respectively. In particular, a uniform rotation starting at time t_0 and ending at $t_f = t_0 + \tau$, with $\tau > 0$, is achieved by setting currents according to $I_x(t) = I_x \sin(\omega_r(t - t_0))$ and $I_z(t) = I_z \cos(\omega_r(t - t_0))$, $t \in [t_0, t_f]$. This gives a time-dependent quantization field $\mathbf{B}_{ext}(t) = c_x I_x(t)\mathbf{e}_x + c_z I_z(t)\mathbf{e}_z$, where the constants $c_{x,z}$ denote the conversion factors from equation (2.4). The amplitudes $I_{x,z}$ are chosen such that the magnitude of $\mathbf{B}_{ext}(t)$ remains unaltered. Usually, the angular frequency

ω_r is set such that the rotation to the final angle $\theta_{\mathrm{B}}^{\mathrm{f}} \equiv \arccos\left(\langle \boldsymbol{e}_z, \mathbf{B}_{\mathrm{ext}}(t_{\mathrm{f}})\rangle\right)/B_{\mathrm{ext}}$ is accomplished within $\tau = 0.5\,\mathrm{ms}$. This results in a maximum angular rotation frequency $\omega_r^{\mathrm{max}} = 2\pi \cdot 2\,\mathrm{kHz}$ in case of a full revolution of the quantization axis.

Generally, in view of a large population transfer into higher bands, rotation frequencies ω_r as high as possible are desired, for they increase the Landau-Zener transition probabilities. Experimentally, the highest achievable rotation frequency is limited by the switching times of the coils including driving sources, which together effectively form an RLC circuit. Based on the characteristics of the coils and sources, the minimal switching time can be estimated to $\tau^{\mathrm{min}} = 0.2\,\mathrm{ms}$ [107]. Despite such technical limitations that prevent the increase of the rotation frequency ad infinitum, a theoretical bound is set by the Larmor frequency $\omega_{\mathrm{Z}} \equiv |\mu_{\mathrm{B}} g_F B_{\mathrm{ext}}|/\hbar \approx 2\pi \cdot 1.5\,\mathrm{MHz}$, which defines the time scale for an adiabatic following of the internal spin degree of freedom with respect to the instantaneous direction of $\mathbf{B}_{\mathrm{ext}}(t)$. In fact, adiabatic following of the spin is a necessary requirement for a successful transfer into higher bands, since our concept relies on the fact that the sublattice energy offset of the spin-dependent potential is well-defined at any instant of time and given by $\Delta_{\mathrm{AB}}(\theta_{\mathrm{B}}(t))$. Therefore, the condition $\omega_{\mathrm{Z}} \gg \omega_r$ should be fulfilled; clearly, this is the case for our typical parameters. Specifically, the condition guarantees that the bosonic ensemble remains spin-polarized during the rotation of the quantization axis and no spin flips occur, which would otherwise obstruct the transfer into higher bands.

Finally, we note that the experimental alignment of $\mathbf{B}_{\mathrm{ext}}$, i.e. the actual value of θ_{B} can be examined and calibrated through different methods (see section 3.3).

4.2.2 Maps of the transfer fraction

So far, we have merely considered the concepts as well as the experimental implementation of our transfer method. In the following, we have a close look at its central characteristic: the transfer fraction, i.e. the actual fraction of atoms that can be transferred into specific higher target bands. To this end, we present systematic measurements of the transfer fraction as a function of both lattice depth V_{2D} and final angle $\theta_{\mathrm{B}}^{\mathrm{f}}$, which constitute two basic variable parameters of the quench protocol described above. The results are compared to calculations of the overlap between Bloch states of the initial and respective final potential configuration.

In principle, an accurate theoretical treatment of the transfer process requires the solution of the full time-dependent Schrödinger equation. However, an upper bound for the transfer fraction into specific target bands can be obtained from the simple limiting case of a sudden potential quench $V(\theta_B^{\mathrm{i}}) \to V(\theta_B^{\mathrm{f}})$ for non-interacting atoms at fixed lattice depths V_{2D}. Consider some initial single-particle state $|\psi_{\mathrm{i}}\rangle$ prior to the quench. Let us denote by $\{|n\boldsymbol{k};\mathrm{f}\rangle\}$ the set of Bloch states to the final potential configuration. Since they form a complete basis, we may expand the initial state according to

$$|\psi_{\mathrm{i}}\rangle = \sum_n \int \mathrm{d}\boldsymbol{k}\, C_n(\boldsymbol{k}) |n\boldsymbol{k};\mathrm{f}\rangle \;, \tag{4.4}$$

where $C_n(\boldsymbol{k}) = \langle n\boldsymbol{k}; f|\psi_{\mathrm{i}}\rangle$ denote the expansion coefficients. Note that the sum in equation (4.4) is over all bands n, and integration should be restricted to quasimomenta
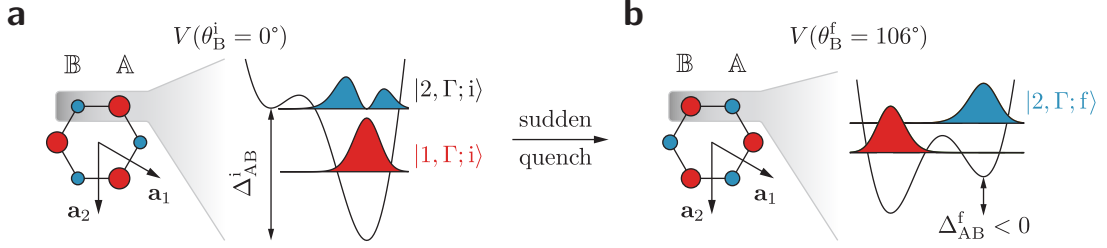
Fig. 4.4: Sudden quench $V(\theta_B^i) \to V(\theta_B^f) \iff \Delta_{AB}^i \to \Delta_{AB}^f$ of the boron-nitride lattice for parameters as in Figure 4.3. **a** In the initial potential configuration, sublattice sites $\mathbb{A}$ coincide with the deep wells (red), where Bloch states $|1, \Gamma; i\rangle$ and $|2, \Gamma; i\rangle$ are localized, as illustrated by the cross sections of their modulus squared. **b** In the final configuration, $\mathbb{A}$ coincides with the shallow wells (blue), where the Bloch state $|2, \Gamma; f\rangle$ is localized. Evidently, $|1, \Gamma; i\rangle$ and $|2, \Gamma; f\rangle$ have a large overlap, yielding efficient transfer into the second band after the quench if atoms initially occupy the ground state $|1, \Gamma; i\rangle$.

$\boldsymbol{k}$ of the first Brillouin zone. Assuming a sudden quench from the initial to the final potential configuration at time $t_0 = 0$, the general solution $|\psi(t)\rangle$ for $t \geq t_0$, with the initial condition $|\psi(t_0)\rangle = |\psi_i\rangle$, may therefore be directly written as

$$|\psi(t)\rangle = \sum_n \int \mathrm{d}\boldsymbol{k}\, C_n(\boldsymbol{k}) \exp\left(-\frac{\mathrm{i}}{\hbar}\epsilon_n^f(\boldsymbol{k})t\right) |n\boldsymbol{k}; f\rangle . \tag{4.5}$$

Here, $\epsilon_n^f(\boldsymbol{k})$ are the Bloch energies to the states $|n\boldsymbol{k}; f\rangle$. For clarity, we now consider an initial state that equals the atomic ground state in a lattice potential for an initial quantization axis angle $\theta_B^i = 0°$, i.e. $|\psi_i\rangle = |1, \Gamma; i\rangle$. Note that its expansion according to equation (4.4) yields non-vanishing coefficients $C_n(\boldsymbol{k})$ only for $\boldsymbol{k} = \Gamma$, which is clear from the fact that the quench does not affect the periodicity of the lattice potential. Starting from this particular initial state, a significant transfer into higher bands of the final potential is possible if there exists a set of lattice parameters $\{V_{2D}, \theta_B^f\}$ such that $|C_n(\Gamma)|^2 \sim 1$ for some $n \neq 1$. In other words, the overlap between the occupied Bloch state of the initial potential and higher Bloch states of the final potential should be one the order of one. For a bipartite lattice with a tunable sublattice energy offset, it turns out that there are indeed large regions of the parameter space where this is the case.

In Figure 4.4, we provide a simple visualization of a sudden quench that corresponds to the situation of the Landau-Zener transfer ① → ② displayed in Figure 4.3. Evidently, the initial and final Bloch states – $|1, \Gamma; i\rangle$ and $|2, \Gamma; f\rangle$ – have a large overlap, resulting in a substantial population of the second band after quenching to the final configuration. Note that the sudden quench paradigm provides a complementary and intuitive perspective on the transfer process: As the wave function cannot adapt to the fast change of the sublattice offset, atoms suddenly find themselves in a higher orbital state with respect to the new potential landscape. In this sense, the transfer via a quench of the sublattice offset is truly different from other methods that aim to evolve the initial state into higher orbital states with respect to the original potential by coupling to external perturbations, such as amplitude modulations or Raman excitations.

In Figure 4.5, we systematically analyze the overlap $S_n \equiv |C_n(\Gamma)|^2 = |\langle n, \Gamma; f | 1, \Gamma; i\rangle|^2$
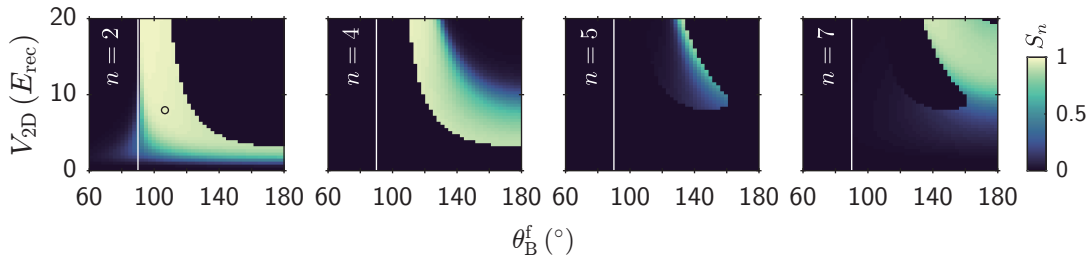
Fig. 4.5: Expected transfer fractions into higher Bloch bands $n \in \{2, 4, 5, 7\}$ of the boron-nitride lattice for a sudden quench of the sublattice energy offset, assuming atoms in the Zeeman substate $|2, -2\rangle$. Each plot depicts the corresponding overlap $S_n \equiv |C_n(\Gamma)|^2 = |\langle n, \Gamma; \mathrm{f}|1, \Gamma; \mathrm{i}\rangle|^2$ to the n-th target band as a function of lattice depth V_{2D} and final quench angle θ_B^{f}. White vertical lines mark the high symmetry angle $\theta_B^{\mathrm{f}} = 90°$, where the two sublattices of the boron-nitride lattice become degenerate. The circle in the first plot highlights the quench parameters $V_{2D} = 8\,E_{\mathrm{rec}}$, $\theta_B^{\mathrm{f}} = 106°$ from Figure 4.3, which are typically used to prepare a condensate in the second Bloch band with atoms in the internal state $|2, -2\rangle$.

into higher bands $n \in \{2, 4, 5, 7\}$ as a function of both lattice depth V_{2D} and final angle θ_B^{f}. Note that the overlaps into bands with $n \in \{3, 6\}$ are always zero and hence have been omitted. The circle in the first plot marks the parameters from Figure 4.3 and Figure 4.4. Based on these results, an almost complete transfer into higher bands can be achieved for realistic lattice depths over large portions of the parameter space. What is more, the individual bands can be addressed selectively as the respective supports of S_n are nearly disjoint.

Experimentally, we have characterized the maximum achievable transfer fraction over large regions of the relevant parameter space. The measurement sequence starts with a spin-polarized BEC in the internal state $|2, -2\rangle$ confined by an XDT (see chapter 2), where we choose $\theta_B^{\mathrm{i}} = 0°$ for the initial orientation of the external quantization field. Next, the BEC is loaded into the lowest band of our two-dimensional boron-nitride lattice for variable final lattice depths V_{2D}. The loading procedure is accomplished by an exponential ramp of the lattice depth to some desired value between $1\,E_{\mathrm{rec}}$ and $16\,E_{\mathrm{rec}}$ in a fixed ramp time $T_{\mathrm{R,2D}} = 100\,\mathrm{ms}$. We then wait for $T_0 = 2\,\mathrm{ms}$ before the quantization axis angle is quenched to a variable final value θ_B^{f} between 80° and 180° within $\tau = 0.5\,\mathrm{ms}$. After another hold time $T_{\mathrm{H}} = 0.5\,\mathrm{ms}$, we perform band mapping by exponentially reducing the lattice depth to zero value in $T_{\mathrm{BM}} = 2\,\mathrm{ms}$. Subsequently, all trapping potentials are switched off and absorption images are recorded after a time-of-flight $t_{\mathrm{TOF}} = 36\,\mathrm{ms}$. We stress that the quantization axis is adiabatically rotated back to is initial configuration during the ballistic expansion in TOF.

The results for the above measurement series are summarized in Figure 4.6. We determine a lower bound for the transfer fraction into higher bands from band mapping images by evaluating the relative atom number in corresponding Brillouin zone masks. Note that the Brillouin zones have been slightly modified to account for the finite experimental resolution of the imaging system and a redistribution of the quasimomentum during the band mapping ramp. The resulting transfer map in Figure 4.6b reveals distinct regions in the parameter space of V_{2D} and θ_B^{f}, similar to those in Figure 4.5, where a targeted transfer into specific higher bands can be accomplished. Each data point has
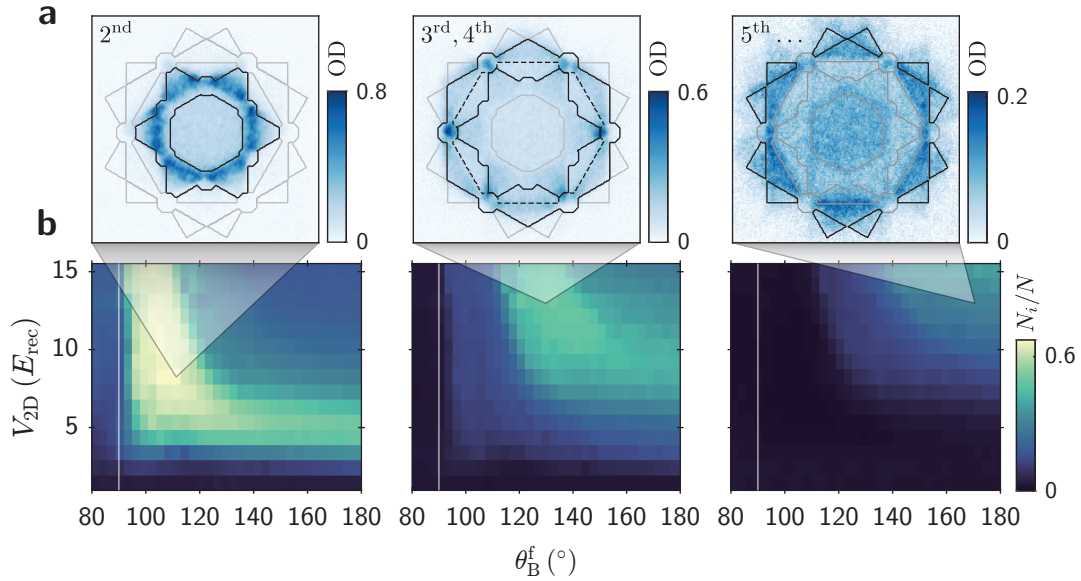
Fig. 4.6: Measured transfer fractions into higher bands of the boron-nitride lattice for atoms in the Zeeman substate $|2,-2\rangle$. After a quench from $\theta_B^i = 0°$ to a variable final angle θ_B^f at a fixed lattice depth V_{2D}, the atomic momentum distribution is recorded with the band mapping technique. **a** Exemplary single-shot absorption images show a population transfer into higher bands, as indicated by an increased optical density (OD) in the corresponding Brillouin zone masks. Left: the black polygon depicts the boundary of the mask that is used for evaluating the atom number N_2 in the second Brillouin zone BZ_2. Grey polygons correspond to higher Brillouin zones. Center: analogous mask for the union $BZ_3 \cup BZ_4$. The dashed contour shows the boundary between both zones. Right: BZ_5 mask. **b** Extracting the relative atom numbers N_i/N in each mask yields an estimated transfer fraction into respective higher bands as a function of the lattice depth V_{2D} and final angle θ_B^f. Left: measured transfer fractions into the second band. Center: transfer fractions into the third and fourth band. Right: transfer fractions into fifth and higher bands.

been averaged over three to four realizations. Note that the sudden quench model gives an adequate qualitative agreement, though the observed overall transfer fractions are clearly smaller. For example, for the second band we find a maximum transfer fraction of $n_2^{max} \approx 67\%$, while for the fourth band we obtain $n_4^{max} \approx 50\%$. These smaller values can be readily attributed to the finite quench time $\tau = 0.5\,\text{ms}$ as well as mean-field effects at large lattice depths, which typically result in a reduced overlap of the initial and finial Bloch states. We emphasize that we added atom numbers of the third and fourth Brillouin zone to determine the transfer fractions into the fourth band. This may be justified as follows: On the one hand, one does not expect transfer into the third band due to a vanishing overlap between the involved Bloch states. On the other hand, during the band mapping ramp, the fourth band encounters a touching point with the third band at quasimomentum Γ, where the fourth band has a minimum. In general, this may lead to an interaction-induced redistribution of atoms from the fourth to the third band and thus result in a false assignment of the initially populated band, which we effectively avoid.

The measured transfer fractions in Figure 4.6 provide a fundamental characterization of the transfer method and allow to assess quench parameters that are suitable for realizing orbital condensates in higher Bloch bands of the boron-nitride lattice, which is the subject of the following sections.

4.3 Emergence of an orbital condensate in the second band

We now show that we can create a metastable orbital condensate in the second band of the boron-nitride lattice by using the transfer method from the previous section. We analyze the dynamics of condensate formation and subsequent decay into the lowest band. Moreover, we investigate the manifestation of time-reversal symmetry breaking and discuss different possibilities for related many-body states.

4.3.1 Evidence for an orbital condensate

Initializing a bosonic ensemble of atoms in the second Bloch band via a quench $|1, \Gamma; i\rangle \rightarrow |2, \Gamma; f\rangle$ gives rise to a highly nonequilibrium state: First, the system is prone to decay into the lowest Bloch band, seeking for a global and total equilibration. Second, since Γ is a maximum point of the second band, the system will tend to relax towards the band minima at K and K$'$. The latter might be seen as the tendency to establish a kind of "local" equilibrium within the state manifold of the second band. Here, we directly investigate the dynamical evolution of the ensemble by probing the momentum and quasimomentum distribution for different hold times T_H after the quench. As a main result, we observe a transient macroscopic occupation of Bloch states $|2, K\rangle$ and $|2, K'\rangle$, which provides compelling evidence for the emergence of an orbital condensate in the second band.

The experimental sequence starts with a spin-polarized BEC in the Zeeman substate $|2, -2\rangle$ confined by the XDT, where $\theta_B^i = 0°$ is set for the initial orientation of the quantization axis. The BEC is then loaded into the ground state of the boron-nitride lattice by exponentially ramping up the lattice depth to $V_{2D} \approx 8\, E_{rec}$ within $100\,\text{ms}$. This gives an initial sublattice energy offset $\Delta_{AB}^i \approx 18\, E_{rec}$, resulting in a small bandwidth on the order of $1\,\text{Hz}$ for the lowest band. Hence, tunneling between the individual lattice sites is largely suppressed and the initial state shows no long-range phase coherence but exhibits a broad and fairly featureless momentum distribution. After a lattice hold time T_0 between $2\,\text{ms}$ and $20\,\text{ms}$, we induce a quench of the sublattice offset to $\Delta_{AB}^f \approx -5\, E_{rec}$ by rotating the quantization axis towards $\theta_B^f = 106°$ within $\tau = 0.5\,\text{ms}$. This promotes the bosonic ensemble into the second band. We vary the hold time T_H after the quench and probe the momentum and quasimomentum distribution through sudden switch-off and band mapping technique, respectively. The results are summarized in Figure 4.7 for hold times T_H ranging up to $50\,\text{ms}$.

Initially, immediately after the quench, the system does not exhibit long-range phase coherence. However, as depicted in Figure 4.7a, we observe a fast build-up of cross-dimensional phase coherence within $7\,\text{ms}$ after the quench, signaled by the appearance of sharp Bragg peaks in the momentum distribution. Most notably, two distinct classes of Bragg peaks appear that are associated with the quasimomenta K and K$'$, respectively, indicating the emergence of an unconventional BEC in the minimal energy Bloch states
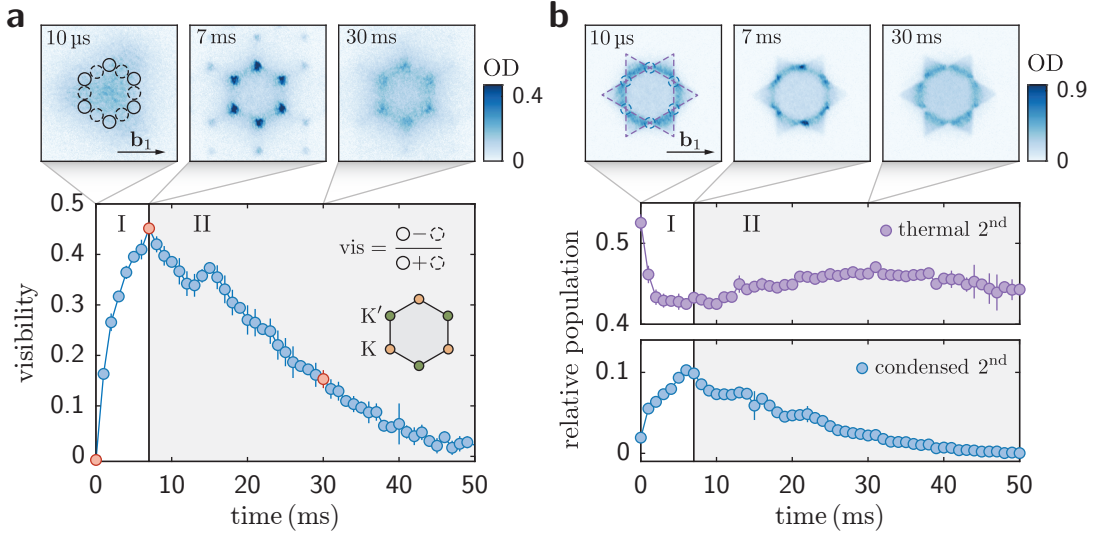
Fig. 4.7: Emergence of an orbital condensate in the second band of a boron-nitride lattice for atoms in the internal state $|2, -2\rangle$, after a quench to $\theta_B^f = 106°$ at a lattice depth $V_{2D} = 7.8\,E_{rec}$. **a** The visibility of zeroth order Bragg peaks associated with quasimomenta K and K′ is probed in TOF images as a function of the hold time after the quench. Single-shot absorption images on the top depict individual realizations for the data points highlighted in red. Higher order Bragg peaks are clearly visible at 7 ms, signaling long-range phase coherence and the emergence of an unconventional transient BEC. **b**. Complementary BM images reveal atoms in the second band (BZ_2), with strong occupation near K and K′. The time evolution of the condensate fraction in the second band follows the visibility, whereas the evolution of the thermal fraction in the second band relates inversely to it. Fractions, that is relative populations, are specified with respect to the total number of atoms distributed over all Brillouin zones and were extracted as detailed in Appendix C. Each data point is an average of 2-4 individual realizations, where error bars denote the corresponding standard deviations.

$|2, K\rangle$ and $|2, K'\rangle$ of the second band. We will refer to the corresponding period as stage I. Subsequently, during a second stage II, the visibility of Bragg peaks gradually fades within 40 ms and eventually vanishes. Complementary to these measurements, band mapping images presented in Figure 4.7b reveal a thermal, incoherent population of the second band at the beginning of stage I. From this thermal background, atoms condense near the quasimomenta K and K′, i.e. at the vertices of the Brillouin zone, reaching a maximum condensate fraction of roughly $n_c^{max} \approx 0.1$ within 7 ms. Then, following the behavior of the visibility, the fraction of condensed atoms gradually diminishes during stage II, while the thermal fraction in the second band shows a nearly opposite increase. Taken together, the TOF images of the momentum and quasimomentum distribution provide evidence for the emergence of a transient orbital condensate in the second band.

Before we move on with a more elaborate discussion of the dynamical evolution, we emphasize that condensate fractions stated here were extracted from band mapping images using a ring-mask method as detailed in Appendix C. In a nutshell, we count thermal atoms in a ring-shaped neighborhood centered on the vertices of the Brillouin zone and then extrapolate their number into the inner condensation region at K and K′. By subtracting this number from the total population at K and K′, we arrive at an

estimate for the number of condensed atoms.

We have checked that condensate fractions obtained in this way are consistent with those determined by more elaborate methods. For example, fitting Bragg peaks in the momentum distribution via two-dimensional, multimodal Gaussian mixture models usually gives similar results for the peak condensate fraction. However, a drawback is that the underlying empirical model functions require a large number of free parameters and therefore tend to give unreliable or unstable results in the sense that small variations of the initial estimates for fit parameters can lead to large deviations of the determined condensate fractions. In a way, this problem can be amplified by experimental fluctuations of the Bragg peak positions or widths, and generally makes two-dimensional fits of the momentum distribution badly conditioned. For this reason, we typically do not rely on this approach. Another method we have tried, which effectively avoids the former difficulties, was to mask off the Bragg peaks and to perform a two-dimensional fit or extrapolation only on the broad diffuse background. The difference to the original momentum distribution then directly yields an estimate of the condensate fraction, again resulting in similar peak values on the order of $10\,\%$.

Finally, note that about $50\,\%$ of the atoms remain in the lowest band due to the finite transfer efficiency. Thus, specifying the relative number of condensed atoms with respect to the total population in the second band gives a peak condensate fraction of almost $20\,\%$.

4.3.2 Condensation and band dynamics

We now have a closer look at the details of the condensation and band dynamics. As mentioned above, the observed dynamical evolution in the second band naturally splits into two stages of different time scales: A fast condensation and build-up of coherence, followed by a slower dissolution. In fact, for hold times $T_\mathrm{H} > 50\,\mathrm{ms}$ another dynamical stage III can be identified that is characterized by the onset and presence of a pronounced band decay. Moreover, on rather short time scales, intriguing oscillations between the first and second band can be observed.

Band decay In Figure 4.8, we analyze the dynamical evolution for hold times T_H up to $200\,\mathrm{ms}$. Evidently, just before the condensate fraction has completely vanished, mostly by transitioning into thermal atoms of the second band, the thermal fraction reaches a maximum and starts to continuously decrease (see Figure 4.8a), giving rise to stage III. By evaluating the total populations within individual Brillouin zones, i.e. the respective total band populations, we find that a decay occurs into the first band, as evidenced in Figure 4.8b. Note that the relative population in $\mathrm{BZ_2}$ is just the sum of the condensed and thermal fraction in the second band, since by counting total populations we do not discriminate between atoms of the condensate and thermal ones. As a matter of fact, band populations of the first ($\mathrm{BZ_1}$) and second band ($\mathrm{BZ_2}$) remain nearly constant during stage I and II, and the onset of band decay into the lowest band, marked by the vertical dashed line, basically coincides with the vanishing of the condensate fraction.

Remarkably, the sum of band populations in the first and second band is not constant over time but shows a visible decrease during stage III: this means that less atoms are accumulating in the first band than are leaving the second one. Moreover, even the
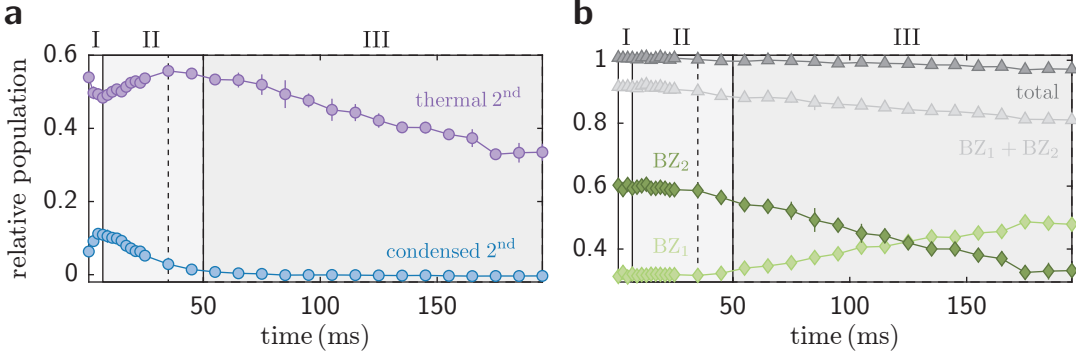
Fig. 4.8: Condensation and band dynamics for an experimental sequence as in Figure 4.7, stemming from an independent measurement series with hold times up to 200 ms. **a** Time evolution of the condensed and thermal fraction in the second band. During stage I, thermal atoms rapidly condense within the second band, leading to a maximum overall condensate fraction $n_c^{max} \approx 0.1$. During stage II, condensed atoms gradually transition into the thermal fraction of the second band. At the beginning of stage III, no condensed atoms are left and a strong band decay sets in. In fact, band decay sets in slightly earlier as marked by the vertical dashed line. **b** Time evolution of relative band populations in BZ_1, BZ_2, $BZ_1 \cup BZ_2$, and in the total union of zones up to BZ_5. Populations were extracted from band mapping images as described in Appendix C. Each data point is an average of 7-10 individual experimental realizations, where error bars denote the corresponding standard deviations.

cumulated band population up to the fifth band gradually diminishes, albeit with a smaller slope. Possibly, this indicates processes where two atoms from the second band collide such that one is transferred into the lowest band, while the other gets excited into higher bands to account for energy conservation. A more elaborate discussion of this subject will be given in section 4.6. Another explanation, which cannot be ruled out entirely, could be extrinsic heating induced by technical noise in the lattice setup as discussed, for example, by T. Klafka [107]. In any case, the population increase of the first band predominantly accounts for the decrease in the second band, which means that direct transitions from the second to the first band dominate.

In summary, we have identified three stages of the dynamical evolution after the quench, which are characterized by distinct physical processes and time scales. Specifically, during stage III, no condensed atoms are left in the second band, and a pronounced decay is observed over several hundred milliseconds. We note that similar results were found in the context of orbital condensates in a bipartite square lattice. Here, a detailed analysis along the lines of three dynamical stages has been conducted by Nuske et al. [81]. Our findings reveal excellent qualitative agreement with this study.

Band oscillations Investigating the band dynamics during the first and second stages at high time resolution is illuminating. Here, one generally finds damped oscillations in the population of the first and second Brillouin zone, as shown in Figure 4.9a. In particular, the oscillations in BZ_2 and BZ_1 are complementary, indicating a periodic particle exchange between the second and first band right after the quench. Also note that a slight overall population decay from BZ_2 into BZ_1 occurs already at this point, which can be viewed as a precursor to the pronounced band decay during stage III. We
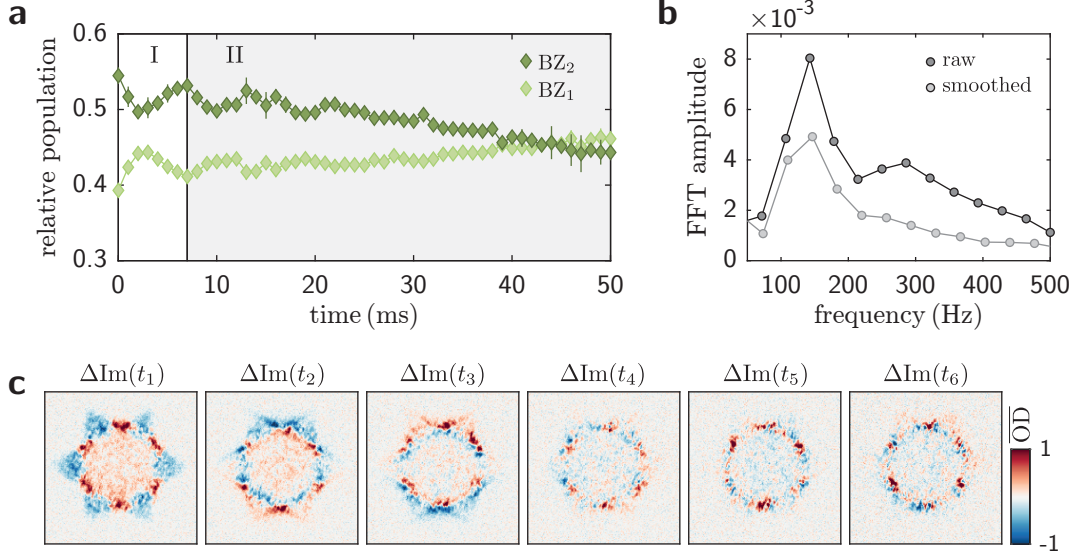
Fig. 4.9: Band dynamics during stages I and II for the same measurement as in Figure 4.7. **a** Evolution of the relative population in the first (BZ$_1$) and second Brillouin zone (BZ$_2$) as a function of the hold time after the quench, showing damped and complementary oscillations with opposite sign. **b** Fast Fourier transform of data points to BZ$_1$ reveals a dominant frequency component at 140 Hz. **c** Difference images of averaged consecutive BM images for the first six time steps. Red (blue) color corresponds to population increase (decrease) as compared to the density distribution at time t_{n-1}. All images are normalized to a common scale.

stress that each data point has been averaged over two to three experimental realizations. By performing a fast Fourier transform of the corresponding signals, we find a dominant frequency component at about 140 Hz for the quench parameters employed here. Our general observation is that the frequency increases for increasing sublattice energy offsets.

To further analyze the oscillations, we have examined difference images of consecutive quasimomentum distributions. More explicitly, each BM image was first normalized to the same fictitious particle number. Next, the normalized BM images were averaged for each time step t_n of the hold time T_H, yielding an image sequence $(\mathrm{Im}(t_n))_n$. Finally, we consider the difference $\Delta\mathrm{Im}(t_n) \equiv \mathrm{Im}(t_n) - \mathrm{Im}(t_{n-1})$. The results are depicted in Figure 4.9c for the first six time steps after the quench and visualize the averaged flow of particles. Evidently, the first three time steps reveal a particle influx to BZ$_1$ (red densities), whereas the last three time steps show an outgoing flux from this region, i.e. predominant blue densities, in agreement with Figure 4.9a. Regarding the second Brillouin zone BZ$_2$, the particle flow exhibits a much richer and complex behavior due to the intriguing condensation dynamics that takes place during stage I. For example, $\Delta\mathrm{Im}(t_1)$ nicely confirms that atoms accumulating near K and K' originate from the broad thermal distribution in the second band. The interpretation of subsequent images, however, is less straightforward, and it is difficult to assess whether there are specific points from which atoms preferably oscillate into the lowest band, or whether this happens in terms of a uniform background oscillation.

Taken as a whole, the origin of the observed oscillations is currently unclear, but we note that similar ones have been reported by Müller et al. [236], leading to speculations about an oscillating superfluid order parameter [239–241]. The situation studied by Tuchman et al. [241] is, in fact, closely related to ours: the initial state before the quench resembles a number-squeezed state, since tunneling between individual lattice sites is largely suppressed owing to the small bandwidth of the lowest band below 1 Hz. As atoms are promoted into the second band, they suddenly experience a bandwidth of about 270 Hz. This reestablishes tunneling and therefore effectively realizes a quench into a superfluid state, as evidenced experimentally by the appearance of Bragg peaks. For such a quench, it has been shown that phase coherence oscillates at a frequency proportional to the generalized Josephson frequency [241]. In fact, we observe reminiscent oscillatory features in the visibility and condensate fraction of the second band, which become apparent from a close inspection of Figure 4.7. What is more, these features have a similar period as the band oscillations, suggesting that both phenomena are intimately linked. In view of this, it is an open question whether the observed band oscillations are genuine oscillations of particles between bands or rather an artefact from the band mapping technique, given the presence of an oscillating superfluid fraction. For instance, at the start of band mapping, an increased condensate fraction at the Dirac points could lead to an enhanced decay during the lattice ramp, resulting in a seemingly larger initial population of the lowest band. In this context, one should keep in mind that BM is generally performed in our case with ramp times $T_{\mathrm{BM}} = 2\,\mathrm{ms}$ during which significant redistribution of quasimomenta can occur, especially for hold times T_{H} within stage I.

4.3.3 Evidence for a chiral superfluid

Following our presentation and analysis of the emergence and dynamical evolution of an orbital condensate in the second band of a boron-nitride lattice, we now focus on possible realizations of the underlying (approximate) many-body state vector $|\Psi\rangle$. For our theoretical description, we will neglect the thermal fraction and posit that the system has reached some kind of quasi-stationary equilibrium such that any reference to time can be ignored. In particular, following our preliminary discussion in section 4.1, we shall assume that the relevant single-particle Hilbert space $\mathscr{H}_1^{\mathrm{c}}$ for the condensate is spanned by the basis set of degenerate Bloch states $|2, \mathrm{K}\rangle$ and $|2, \mathrm{K}'\rangle$. Recall that the basis states are TRS partner and degeneracy is guaranteed for a time-reversal symmetric Bloch Hamiltonian (see subsection 3.1.5). Now, given that a general state in $\mathscr{H}_1^{\mathrm{c}}$ may be written as

$$|\psi\rangle = \cos(\theta)\,|2, \mathrm{K}\rangle + \exp\left(\mathrm{i}\phi\right)\sin(\theta)\,|2, \mathrm{K}'\rangle\,, \tag{4.6}$$

the central question is: What values of the mixing angles $\theta \in [0, \pi/2)$ and $\phi \in [-\pi, \pi)$ are realized in the experiment? Or, to put it differently: What type of orbital condensate do we actually have? For instance, condensation in a single basis state necessarily involves breaking of the time-reversal symmetry and gives rise to a chiral superfluid that can exhibit rectified angular momentum ordering.

To address these questions experimentally and, especially, to investigate possible manifestations of time-reversal symmetry breaking, we have measured and analyzed
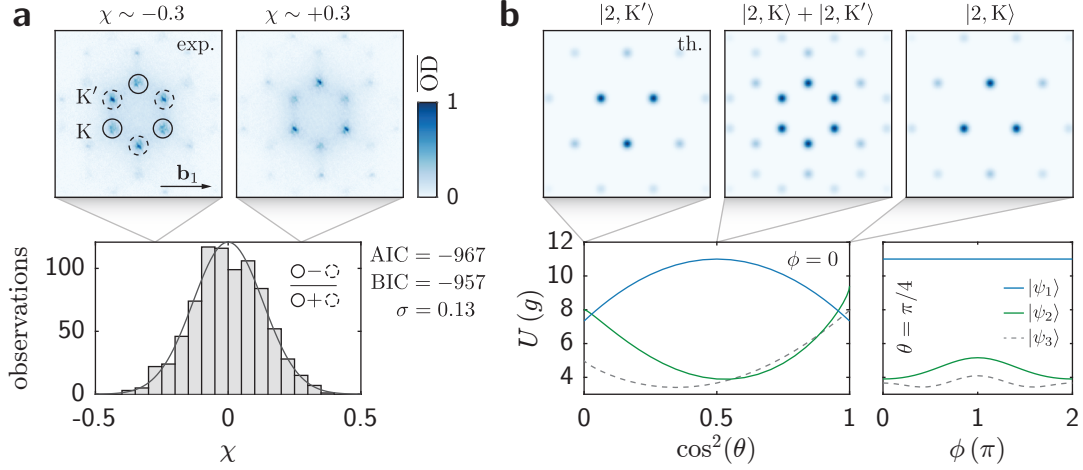
Fig. 4.10: Probing chiral symmetry breaking in the momentum distribution. **a** Top: Exemplary single-shot TOF images of orbital condensates with finite chirality χ. The latter is defined as the difference in the relative occupation of quasimomenta K and K' (see inset below). TOF images were obtained for a hold time $T_H = 7\,\text{ms}$ after a quench to $\theta_B^f = 106°$; with a lattice depth $V_{2D} = 8.1\,E_{\text{rec}}$ and atoms in the Zeeman substate $|2, -2\rangle$. Bottom: Histogram of observed chirality for a measurement series with 1900 runs at constant parameters as stated above. The continuous line shows a fit of a Gaussian model distribution, yielding a standard deviation $\sigma = 0.13$, Akaike information criterion AIC $= -967$, and Bayes information criterion BIC $= -957$. **b** Top: Numerical calculation of TOF images for three different states, labeled on top, and lattice parameters as used in **a**. Bottom: Interaction parameter U of a two-component superposition state $|\psi_i\rangle$ as defined in equation (4.6), with components $\{|2, K\rangle, |2, K'\rangle\}$, $\{|1, \Gamma\rangle, |2, \Gamma\rangle\}$, and $\{|2, \Gamma\rangle, |3, \Gamma\rangle\}$, respectively. Left panel: U as a function of the relative weight $\cos^2(\theta)$ for $\phi = 0$. Right panel: U as a function of the relative phase ϕ for $\theta = \pi/4$.

the chirality

$$\chi \equiv \frac{N_K - N_{K'}}{N_K + N_{K'}}\,, \tag{4.7}$$

which defines the difference in the relative occupation of the two basis states. In Figure 4.10a, we present results of a corresponding measurement series that comprises 1900 runs at fixed parameters of the quench protocol. We stress that the experimental sequence we used is identical to the one described in subsection 4.3.1. Here, however, we probe the momentum distribution after TOF only for a fixed hold time $T_H = 7\,\text{ms}$, i.e. when the condensate fraction has reached a maximum. By evaluating the number of condensed atoms in the respective zeroth order Bragg peaks, one directly arrives at χ. Most notably, we observe values as large as $\chi \sim \pm 0.35$, corresponding to a maximum relative occupation at K and K' of nearly 70 %, respectively. In other words, single realizations of the orbital condensate reveal a strongly symmetry-broken momentum distribution. Nevertheless, the overall symmetry breaking in the system remains rather weak in the sense that the observed probability distribution for χ is well-described by a single Gaussian with mean $\mu = -0.0005$ and standard deviation $\sigma = 0.132$, where respective 95 % confidence intervals are $C_\mu = [-0.01, 0.01]$ and $C_\sigma = [0.126, 0.139]$. In contrast, for strong symmetry breaking, one expects to see a bimodal distribution, which is evidently not manifested in our case: More precisely, in terms of Akaike and Bayes

information criteria, which provide an estimate for the relative quality of a statistical model, a *bimodal* Gaussian fit to the observed distribution of χ is rejected.

For a single condensate in the mode $|\psi\rangle$ as defined in equation (4.6), a simple mean-field analysis suggest that the system should favor condensation in one of the two basis states: Explicitly, let us consider the interaction parameter

$$U(\theta, \phi) \equiv g \int d\boldsymbol{r} \, |\langle \boldsymbol{r} | \psi \rangle|^4 \,, \quad \text{with} \quad g = 4\pi\hbar^2 a_s / m \,, \tag{4.8}$$

where g characterizes the contact interaction strength that depends on the s-wave scattering length a_s. In Figure 4.10b, we show the results of a numerical calculation of U as a function of the mixing angles θ and ϕ (blue lines) for identical lattice parameters as used in the experiment. For comparison, we also plot analogous interaction parameters for two-component superposition states that are defined in terms of another basis set of Bloch states. Details of the calculation are provided in Appendix B. Evidently, for the state $|\psi\rangle$, it turns out that U is independent of the relative phase ϕ and takes a minimum value for $\theta = 0, \pi/2$. Thus, for positive interaction energies ($g > 0$), as in our case for Rubidium-87, the system should favor condensation in either the Bloch state $|2, \mathrm{K}\rangle$ or $|2, \mathrm{K}'\rangle$, as compared to a superposition. For clarity, the expected momentum distribution of a condensate in $|2, \mathrm{K}\rangle$ and $|2, \mathrm{K}\rangle$ is visualized in the top panel of Figure 4.10b. Note the close similarity to the experimental TOF images on the left.

Now, although we do not observe strong symmetry breaking in the momentum distribution, our data still indicates an increased tendency towards condensation in one of the basis states, which in turn provides evidence for a *weak* chiral superfluid. In fact, the observed distribution of chirality is incompatible with a time-reversal symmetric single-mode BEC, as I will show in the following: To this end, we first define the Fock basis $\{|N_1, N_2\rangle_\mathrm{F}\}$ of the associated N-body Hilbert space $\mathscr{H}_N^c$ as the occupation number basis for states $|2, \mathrm{K}\rangle$ and $|2, \mathrm{K}'\rangle$. In this notation, we have $N_1 = N_\mathrm{K}$ and $N_2 = N_{\mathrm{K}'}$ with the constraint $N_1 + N_2 = N$, where N is the total number of condensed atoms. To proceed, we note that a general *single-mode* N-body state that corresponds to a BEC in the mode $|\psi\rangle$ is given by

$$|\Psi\rangle = \frac{1}{\sqrt{N!}} \left(\cos(\theta)\hat{b}_\mathrm{K}^\dagger + \exp(\mathrm{i}\phi)\sin(\theta)\hat{b}_{\mathrm{K}'}^\dagger \right)^N |0\rangle \,. \tag{4.9}$$

Here, $\hat{b}_{\boldsymbol{k}}^\dagger$ denotes the bosonic creation operator for a Bloch state $|2, \boldsymbol{k}\rangle$ in the second band with quasimomentum $\boldsymbol{k}$, and $|0\rangle$ refers to the vacuum state. Next, to establish connection with the observable χ, it is illuminating to rewrite $|\Psi\rangle$ in the following form:

$$|\Psi\rangle = [\alpha |2, \mathrm{K}\rangle + \beta |2, \mathrm{K}'\rangle]^{\otimes N} = \sum_{m=0}^{N} \binom{N}{m}^{1/2} \alpha^{N-m}\beta^m |N-m, m\rangle_\mathrm{F} \,, \tag{4.10}$$

where we employed the abbreviations $\alpha \equiv \cos(\theta)$, $\beta \equiv \exp(\mathrm{i}\phi)\sin(\theta)$ for compactness. From equation (4.10), one directly infers that the occupation number of individual Bloch states $|2, \mathrm{K}\rangle$ and $|2, \mathrm{K}'\rangle$ follows a binomial distribution. It is straightforward to show that the expectation value μ_χ and variance σ_χ^2 of the chirality for the state $|\Psi\rangle$ is

given by

$$\mu_\chi = 1 - 2|\beta|^2, \qquad \sigma_\chi^2 = \frac{4|\alpha|^2|\beta|^2}{N} \, . \qquad (4.11)$$

While the experimental value for the mean is consistent with a time-reversal symmetric condensate, which requires $|\alpha|^2 = |\beta|^2 = 1/2$, the observed variance is more than two orders of magnitude larger than would be expected. The latter follows from the fact that the total number of condensed atoms for the data presented here amounts to roughly $N \approx 2.0(2) \times 10^4$. We may thus conclude that a time-reversal symmetric state vector $|\Psi\rangle$ is generally not realized. Instead, individual realizations of the orbital condensate exhibit broken time-reversal symmetry, which means $|\alpha|^2 \neq |\beta|^2$. Whether the symmetry is broken spontaneously or induced by an external perturbation cannot be answered adequately. We note, however, that we were able to produce strong chiral superfluids in a single basis state $|2, \mathrm{K}\rangle$ ($|2, \mathrm{K}'\rangle$) by explicitly breaking TRS via clockwise (anti-clockwise) circular lattice shaking.

The single-mode BEC we considered above should be contrasted with more general states that are, in principle, also possible. For example, a state $|\mathcal{F}\rangle \equiv |N_1, N_2\rangle_\mathrm{F}$ where $N_1 \sim N_2$ are both macroscopically large would correspond to a fragmented state, i.e. a state that consists of two separate BECs in different modes. Another interesting case is the so-called *cat state*, which is a macroscopic superposition of two distinct BECs of the form $|\mathrm{cat}\rangle \equiv \cos(\theta) |N, 0\rangle_\mathrm{F} + \sin(\theta) |0, N\rangle_\mathrm{F}$.

Finally, we note that Wang et al. [83] have recently observed strong symmetry breaking in a similar system. Specifically, the chirality in their case exhibits a clear bimodal distribution. This becomes manifest, however, only for hold times on the order $T_\mathrm{H} > 100\,\mathrm{ms}$, which is much larger than the current lifetime of our orbital condensate. In view of this, it will be exciting to explore and pinpoint the relevant parameters that facilitate the formation of a long-lived chiral superfluid.

4.4 Condensates in the fourth band

In addition to orbital condensates in the second band, we have realized condensates in the fourth band of the boron-nitride lattice. Though they are, technically speaking, condensates in higher Bloch orbitals, here they do not comply with orbital condensates in the strict sense: Namely, they do not possess orbital degeneracies, since the fourth band has generally only a single global minimum at the quasimomentum Γ. As a result, no genuine orbital features can be observed at this point. Still, the investigation of condensates in the fourth band provides important insights into the dynamics of the condensation process in higher bands. Furthermore, it gives a good starting point for realizing genuine orbital condensates that are distinct from those in the second Bloch band: For example, by tuning the lattice parameters appropriately, one can reach a regime where the third and fourth band become degenerate at the Γ point over a large region of the parameter space.

To create condensates in the fourth Bloch band, we essentially proceed in a similar way as for the second band (see subsection 4.3.1). For the lattice quench, however, we typically choose lattice depths on the order of $V_\mathrm{2D} \approx 15\,E_\mathrm{rec}$ and final angles $\theta_\mathrm{B}^\mathrm{f} = 122°$. These parameters guarantee that two successive band crossings are encountered during
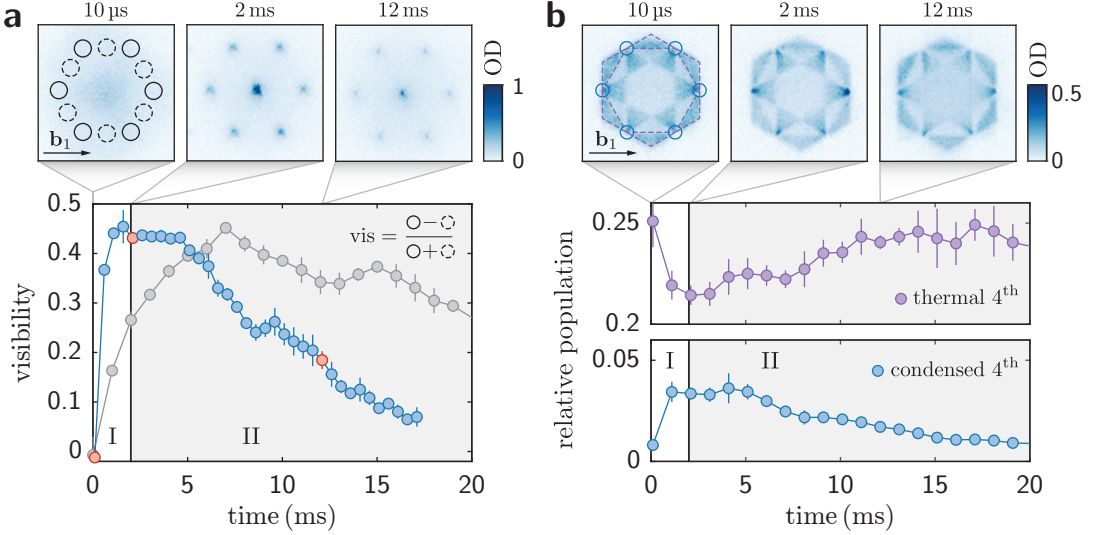
Fig. 4.11: Emergence of a condensate in the fourth band of a boron-nitride lattice for atoms in the internal state $|2, -2\rangle$, after a quench to $\theta_B^f = 122°$ at a lattice depth $V_{2D} = 14.7\,E_{rec}$. **a** The visibility of first order Bragg peaks associated with the quasimomentum Γ is probed as a function of the hold time after the quench (blue data points). Single-shot absorption images on the top depict individual realizations for data points highlighted in red. Higher order Bragg peaks are clearly visible after 2 ms, signaling long-range phase coherence and the emergence of a BEC. For comparison, grey data points show the time-evolution of the visibility for the orbital condensate in the second band (see Figure 4.7). **b**. Complementary BM images from an independent measurement series at $V_{2D} = 15\,E_{rec}$ reveal atoms in the fourth band (BZ$_4$), with strong occupation at six points that are equivalent to Γ. The time evolution of the condensate fraction in the fourth band follows the visibility, whereas the evolution of the thermal fraction in the fourth band relates inversely. Fractions, that is relative populations, are specified with respect to the total number of atoms distributed over all Brillouin zones and were extracted as detailed in Appendix C. Each data point is an average of 4-6 experimental realizations, where error bars denote the corresponding standard deviations.

the quench, which promotes atoms into the fourth band. We note that the final lattice parameters correspond to a final sublattice offset $\Delta_{AB}^f \approx -18\,E_{rec}$ and result in a bandwidth of about 230 Hz for the fourth band. We have analyzed the dynamical evolution of the system after the quench by probing the momentum and quasimomentum distribution as explained in subsection 4.3.1. The results are summarized in Figure 4.11 and Figure 4.12. In close analogy to the second band, three distinct stages can be identified, which are discussed in the following.

Initially, right after the quench, the system does not exhibit any long-range phase coherence, as evidenced by the first TOF image in Figure 4.11a. However, we observe a fast build-up of cross-dimensional coherence within 2 ms after the quench, signaled by the appearance of sharp Bragg peaks in the momentum distribution (stage I). The Bragg peaks are associated with the quasimomentum Γ, as expected for a condensate in the minimal energy Bloch state $|4, \Gamma\rangle$ of the fourth band. During the subsequent stage II, the visibility of Bragg peaks forms a plateau for about 3 ms and then gradually fades until it vanishes for a hold time of about 15 ms to 20 ms. For comparison, in Figure 4.11a,
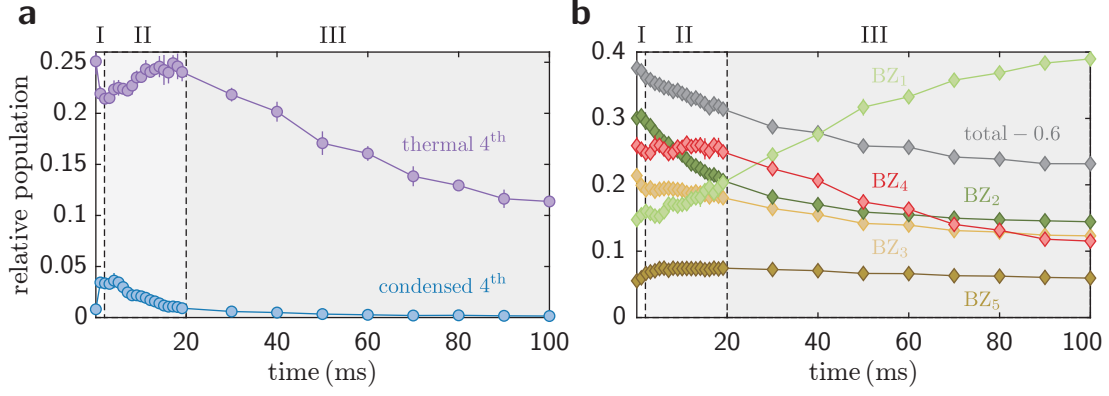
Fig. 4.12: Condensation and band dynamics for the experimental sequence in Figure 4.11b, with hold times T_H up to 100 ms. **a** Time evolution of the condensed and thermal fraction in the fourth band. During stage I, thermal atoms rapidly condense within the fourth band, leading to a maximum overall condensate fraction $n_c^{max} \approx 0.05$. During stage II, condensed atoms gradually transition into the thermal fraction of the fourth band. At the beginning of stage III, the condensate has vanished and a pronounced decay of thermal atoms from the fourth band sets in. **b** Time evolution of the relative band populations in different Brillouin zones, including their total sum, during all three stages. Populations were extracted from band mapping images as described in Appendix C. Each data point is an average of six individual experimental realizations, where error bars denote the corresponding standard deviations.

we also plot the time evolution of the visibility for the orbital condensate in the second band. Clearly, for the fourth band, the rise and subsequent loss of coherence happens on a notably shorter time scale. The faster increase of visibility may well be attributed to the fact that atoms in the fourth band do not need to redistribute quasimomenta in order to reach the lowest energy Bloch state. We note that the bandwidths of the two different target bands are nearly identical.

Regarding the quasimomentum distribution in Figure 4.11b, we make the following observation: During stage I, thermal atoms of the fourth band rapidly condense within the fourth band by accumulating near the Γ point. Note that there are six equivalent ones for the Brillouin zone of the fourth band. The maximal overall condensate fraction is reached at the crossover to stage II and amounts to roughly $n_c^{max} \approx 0.05$. Next, during stage II, the number of condensed atoms gradually diminishes, evidently by transitioning back into the thermal fraction of the fourth band, which shows a complementary increase until the condensate has vanished. Finally, this gives rise to the last stage III that is characterized by the onset and presence of a pronounced band decay, as analyzed in Figure 4.12 for hold times T_H up to 100 ms.

We point out that the total population of the fourth band remains nearly constant during stages I and II (see Figure 4.12b). However, note the locked oscillations for the first (BZ_1) and fourth band (BZ_4), reminiscent of those observed for a quench into the second Bloch band (compare subsection 4.3.2). All in all, the band dynamics here are somewhat more complicated than in the latter case, owing to considerable initial populations in more than just two bands. For example, the finite experimental transfer efficiency results in an unwanted thermal population of the second band, which rapidly decays into the lowest band during stage I and II. Certainly, this will cause intrinsic

heating and eventually limit the lifetime of condensed atoms in the fourth band. In fact, it might be an important reason why the observed coherence time is notably shorter than in the case of orbital condensates in the second band (see Figure 4.11). It should be emphasized that the cumulated band population up to the fifth band shows a visible decrease during all three stages, which slows down by the end of stage III. As before, this could indicate band-changing collisions where atoms are excited into even higher bands.

Finally, we like to point out that the condensate fractions stated above were extracted from band mapping images, as explained in Appendix C. Here, these fractions should be considered as a lower bound estimate, for we presume that there is significant loss of condensed atoms during the band mapping ramp, which lasts 2 ms. As compared to the orbital condensate in the second band, this loss should be more severe, since a band crossing with the flat third band is encountered at the Γ point at an early stage of the band mapping ramp. Indeed, estimating the condensate fraction from the momentum distribution (after sudden release), as discussed in subsection 4.3.1, yields larger values on the order of $\tilde{n}_\mathrm{c}^\mathrm{max} \approx 0.2$. While this clarifies that the actual condensate fraction in the fourth band might be larger than provided by Figure 4.11b, it has no consequence for our discussion of the temporal evolution itself.

4.5 Exploring the parameter space: Islands of coherence

In the previous sections, we have studied the emergence of orbital condensates in the second and fourth band of a boron-nitride lattice for a specific set of quench parameters. In fact, those parameters have turned out to be optimal: they yield maximal condensate fractions and longest lifetimes, respectively. In the following, we shall present related measurements over a large region of the relevant parameter space. We find characteristic parameter "islands" where condensation in higher bands is possible.

The experimental sequence follows the usual protocol described earlier. We vary the lattice depth V_2D and final quench angle $\theta_\mathrm{B}^\mathrm{f}$ of the quantization axis and observe the momentum distribution for a fixed hold time $T_\mathrm{H} = 7$ ms after the quench. By evaluating the visibility of Bragg peaks, we obtain a density map as shown in Figure 4.13a. Specifically, the visibility here is defined as the sum of visibilities for the second and fourth band: $\mathcal{V} = \mathcal{V}_2 + \mathcal{V}_4$, which is a useful quantity as $\mathcal{V}_{2,4}$ derive from two disjoint sets of masks. Clearly, the map reveals two separated islands of high visibility or coherence, which correspond to parameter regions that are suitable for metastable condensates in the second and fourth band, respectively.

Modeling the exact forms of the observed islands is quite challenging: On the one hand, a simple theoretical approach for tracing the full nonequilibrium dynamics of a quantum many-body system with particle numbers as large as $N \approx 3 \times 10^5$ is not available. On the other hand, besides obvious variables such as bandwidths or band gaps, there are additional, more intricate ones that will certainly affect the visibility and that depend on V_2D or $\theta_\mathrm{B}^\mathrm{f}$. For example, the (quasi-)momentum distribution of the initial state before the quench, the finite transfer fraction into the target band, the final longitudinal confinement, and so on. In general, these variables will have an influence on thermalization and decay rates and must therefore be characterized beforehand.
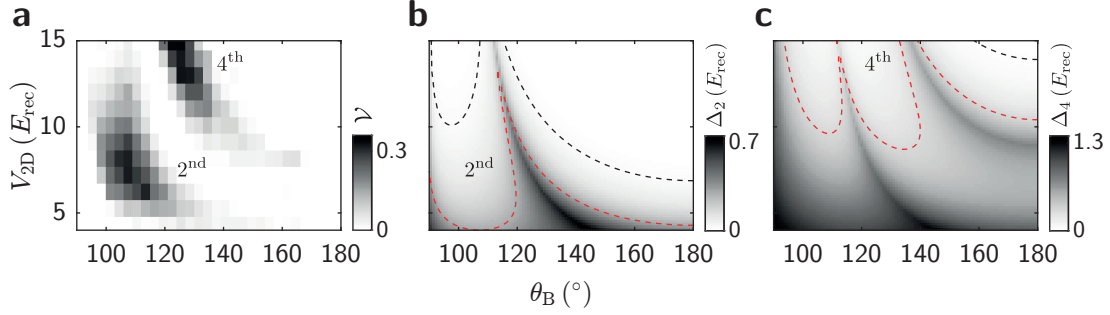
Fig. 4.13: Islands of visibility for condensates in higher bands. **a** Measured Bragg peak visibility $\mathcal{V}$ in the second and fourth band as a function of the quench parameters $\theta_{\mathrm{B}}^{\mathrm{f}}$ and V_{2D}, revealing separated regions (islands) where condensation in higher bands is possible. Measurements were performed for a fixed hold time $T_{\mathrm{H}} = 7\,\mathrm{ms}$ and atoms in the Zeeman substate $|2, -2\rangle$. **b** Bandwidth of the second band over the same parameter space. Dashed black and red lines highlight contours where the bandwidth equals 100 Hz and 1000 Hz, respectively. **c** Similar plot for the bandwidth of the fourth band. Note that certain lobe-like regions bounded by contours in **b** and **c** are in good agreement with islands in **a**.

Despite this, basic insights can be gained by examining the bandwidths.

In Figure 4.13b-c, we plot the results of a numerical calculation of the bandwidths for the second and fourth band, respectively. In addition, we show the contour lines that correspond to a bandwidth of 100 Hz (black line) and 1000 Hz (red line). The most simplistic argument that one can make now is the following: If the bandwidth of the target band becomes too large, the excess energy that must be deposited to reach the corresponding lowest energy Bloch states will exceed a certain threshold, above which condensation cannot be accomplished. In other words, after thermalization in the target band, the finite temperature will eventually exceed the critical temperature for condensation in the given manifold. Thus, no visibility will be observed. In contrast, if the bandwidth becomes too small, the excess energy will be low but tunneling will be strongly suppressed, such that phase coherence cannot be established on an adequate time scale: Again, no visibility will be observed. Of course, these arguments ignore the true complexity of the condensation process with all its genuine nonequilibrium dynamical features and will necessarily fail to reproduce details of the visibility map. But still, they may serve as a simple guideline or a starting point for more refined considerations. For example, T. Klafka has verified that the ridge line for a given island almost perfectly coincides with the line of minimal ratio $(\Delta_n/\delta_n)^2$, where Δ_n denotes the bandwidth of the n-th target band and δ_n is its band gap to the next subjacent band [107]. We note that this relation was motivated by a recent study of recondensation dynamics in a one-dimensional bipartite optical lattice [242]. To understand whether this is indeed the relevant figure of merit for our system, however, requires further theoretical investigation. At the same time, it leads us to the important question: What are the basic and general requirements for long-lived metastable condensates in higher bands? We will try to give an adequate answer in the next section.

4.6 Basic aspects of condensate formation and dissolution

Certainly, an indispensable prerequisite for the emergence of metastable condensates in higher bands is a separation of time scales for intraband relaxation and interband decay, which relates to the concept of prethermalization [243, 244]. While intraband relaxation seeks to establish a *local* equilibrium within the state manifold of a give target band, interband decay constantly promotes equilibration towards a *global* thermal state. Under realistic experimental scenarios, thermalization within the target band will always compete with decay into lower bands, and it is not a priori clear whether and under what specific conditions separation of the relevant time scales can exist. Addressing these questions requires to invoke the full machinery of quantum many-body systems out of equilibrium, which is way beyond the scope of this thesis. Meanwhile, the sheer existence of separated time scales will not guarantee that an eventual prethermalized state is compatible with a macroscopic occupation of a particular minimal energy Bloch state. In general, additional requirements must be satisfied for condensation in a given target band.

In this section, we examine such additional requirements, assuming a system with separated time scales, as manifested in the experiment. More precisely, we give a brief summary of basic and general aspects of condensate formation and dissolution in higher bands, aiming to develop a simple understanding of processes that enable, facilitate, or obstruct the realization of long-lived metastable condensates. For clarity, we mainly focus on the case of condensation in the second Bloch band of our boron-nitride lattice. The considerations, however, can be generalized to arbitrary bands and different settings as well.

4.6.1 Excess energy and lattice dimensionality

Consider a bosonic ensemble initialized in the Bloch state $|2, \Gamma; f\rangle$ after a corresponding quench of the lattice potential. As Γ corresponds to a maximum of the second band, interactions will generally induce a redistribution of quasimomenta towards the minimal energy Bloch states $|2, \mathrm{K}\rangle$ and $|2, \mathrm{K}'\rangle$, which is the essence of intraband relaxation. Obviously, relaxation from a band maximum to a minimum involves a certain amount of excess energy $\Delta\epsilon_{\mathrm{exc}}$. For an isolated system, this energy must be redistributed across spatial degrees of freedom other than the lattice plane to decrease the overall band energy and enable the formation of a condensate.[3] This is where the longitudinal (axial) confinement along the lattice tubes, i.e. the confinement orthogonal to the lattice plane, comes into play: It literally acts as an entropy or energy reservoir, where the excess energy can be deposited.

Commonly, the orthogonal confinement is realized through a harmonic trap potential, which is uniquely characterized by its trap frequency ω_z. Based on this, a necessary condition for condensation should be that ω_z is not larger than the bandwidth of the target band. Otherwise, intraband relaxation will be frozen out effectively, since no longitudinal modes with energy $E_l \equiv \hbar\omega_z(l + 1/2)$ can be excited. For the same reason, it appears that condensation in higher bands is generally not feasible in case of a three-

---

[3]For closed and open systems, $\Delta\epsilon_{\mathrm{exc}}$ may also dissipate into another subsystem. This leads to exciting additional possibilities, as we touch on by the end of this section.

dimensional optical lattices, at least not for an isolated system as considered here: The lowest energy Bloch state in a target band simply cannot be reached in any obvious way. In accordance with that, condensation in higher Bloch bands could not be observed as soon as the orthogonal lattice (compare subsection 2.2.4) was ramped up in addition to the boron-nitride lattice, which illustrates the importance of lattice dimensionality: Condensates in higher Bloch bands of an optical lattice can perhaps only be realized for one- or two-dimensional lattice geometries.

In our case, the longitudinal trap frequencies at sublattice sites $\mathbb{A}$ and $\mathbb{B}$ in the center of the lattice are given by

$$\Omega_z(\mathbb{A}, \mathbb{B}) = \left(\Omega_{\mathrm{h},z}^2 + \omega_z^2(\mathbb{A}, \mathbb{B})\right)^{1/2}. \tag{4.12}$$

Here, $\Omega_{\mathrm{h},z}$ denotes the contribution from the XDT as defined in equation (2.8), whereas $\omega_z(\mathbb{A}, \mathbb{B})$ refers to the longitudinal trap frequency of the boron-nitride lattice. In terms of the lattice parameters V_{2D} and θ_{B}, it is explicitly given by

$$\omega_z^2(\mathbb{A}, \mathbb{B}) = \frac{18}{mw_0^2}V_{\mathrm{2D}}\left[2 \pm \bar{m}_F \cos(\theta_{\mathrm{B}})\eta(\omega_{\mathrm{L}}; F)\right], \tag{4.13}$$

where the plus (minus) sign refers to the $\mathbb{A}$ ($\mathbb{B}$) sublattice site, and $w_0 = 115\,\mu\mathrm{m}$ is the lattice beam waist, with remaining variables as usual. We stress that, with increasing lattice depth, the longitudinal trap frequency is quickly dominated by the contribution of the lattice potential due to the relatively small lattice beam waists. For example, we have $\omega_z(\mathbb{A}) \approx 2\pi \cdot 90\,\mathrm{Hz}$ for quench parameters as in Figure 4.7, whereas the XDT is generally set to $\Omega_{\mathrm{h},z} \approx 2\pi \cdot 20\,\mathrm{Hz}$. Equation (4.12) has some important implications: Following our previous arguments we do not expect to observe condensation in the second Bloch band for final lattice parameters that yield bandwidths below approximately $100\,\mathrm{Hz}$. This value is roughly where the longitudinal trap frequencies will begin to exceed the bandwidth of the second band. Note that the $100\,\mathrm{Hz}$ contour for the bandwidth of the second band has been plotted in Figure 4.13b. Indeed, rather little visibility is observed above this line. The observed finite visibility may be explained by additional relaxation channels that are realized through interactions with remaining atoms in the lowest band.

In the following, we shall sketch how to formalize the above considerations to arrive at reasonable quantitative predictions on condensate fractions in higher bands. For simplicity, we will assume that all atoms occupy a single target band and that decay into lower bands can be ignored. Based on a local thermal equilibrium for an isolated band, a sufficient condition for condensation would be that the final temperature T^{f} associated with $\Delta\epsilon_{\mathrm{exc}}$ after equilibration in the target band is compatible with a macroscopic occupation of the respective lowest energy Bloch states. In other words, it should not exceed the critical temperature T_{c} in the energy landscape of the target band.

Let us denote by $\epsilon_n(\boldsymbol{k}, l) \equiv \epsilon_n(\boldsymbol{k}) + \hbar\omega_z(l + 1/2)$ the total band space energy of the n-th band, where l describes the harmonic oscillator quanta into longitudinal direction. Assume some initial, normalized distribution $g_1^{\mathrm{i}}(\boldsymbol{k}, l)$ for the quantum numbers in the lowest band prior to the lattice quench. For example, it could be a thermal distribution. During the lattice quench, the distribution of quantum numbers $\boldsymbol{k}$ and l remains

approximately unaltered, while atoms become elevated into a higher target band, where $g_1^i(\boldsymbol{k}, l)$, in general, does not correspond to any thermal distribution. In particular, it will be associated with the following excess energy within the target band:

$$\Delta\epsilon_n^{\text{exc}} \equiv -\min(\epsilon_n) + \sum_l \int \mathrm{d}\boldsymbol{k} \, g_1^i(\boldsymbol{k}, l)\epsilon_n(\boldsymbol{k}, l) \,. \tag{4.14}$$

After intraband relaxation, the final distribution $g_n^f(\boldsymbol{k}, l)$ of quasimomenta and oscillator quanta shall correspond to a local thermal equilibrium that is described by the Bose-Einstein distribution $\mathcal{B}_n(\epsilon_n(\boldsymbol{k}, l), \mu, T^f)$ for a given band index n and final temperature T^f, where $\mu = \mu(N, T^f)$ is the chemical potential that fixes the number of total atoms N. Since we assume an isolated band, the excess energy $\Delta\epsilon_n^{\text{exc}}$ must be conserved such that T^f is uniquely determined by

$$\sum_l \int \mathrm{d}\boldsymbol{k} \, g_n^f(\boldsymbol{k}, l)\epsilon_n(\boldsymbol{k}, l) = \min(\epsilon_n) + \Delta\epsilon_n^{\text{exc}} \,, \tag{4.15}$$

where we explicitly set $g_n^f(\boldsymbol{k}, l) \equiv \mathcal{B}_n(\epsilon_n(\boldsymbol{k}, l), \mu, T^f)$. If it happens that $T^f < T_c^n$, the excess energy will allow for a finite condensate fraction in the target band to the zero mode $l = 0$. Here, the critical temperature T_c^n in the n-th band is determined as usual by requiring that the thermal fraction is saturated, i.e. $\langle N_{\text{th}}(T_c^n, \mu = 0) \rangle = N$. The equations (4.14) and (4.15) highlight several important aspects: Condensation depends crucially on the excess energy $\Delta\epsilon_n^{\text{exc}}$, which should be small to give low final temperatures T^f. As $\Delta\epsilon_n^{\text{exc}}$ can be reduced by decreasing the bandwidth of the target band, small bandwidths should facilitate condensation and therefore be preferred. On the other hand, the critical temperature will typically likewise decrease with decreasing bandwidth and oscillator frequency ω_z, counteracting the lowering of T^f. Eventually, there is a trade-off that leads to a maximum finite condensate fraction at a certain bandwidth. Besides, since $\Delta\epsilon_n^{\text{exc}}$ additionally depends on the initial distribution $g_1^i(\boldsymbol{k}, l)$, the optimal bandwidth will also be affected by the latter. Finally, we note that the total particle number N or, equivalently, the total density in the target band should generally be as large as possible, for it increases the critical temperature.

We emphasize that the above formulas are only valid for an isolated target band. They may, however, be refined in the sense of a closed system to include energy transfer with atoms remaining in the lowest band. This is particularly important in view of finite experimental transfer fractions into higher bands. Explicit calculations with such a model have been performed by G. Koutentakis within our theory collaboration. The results show excellent agreement with experimentally observed values of the condensate fraction. Most strikingly, they indicate that atoms remaining in the lowest band can support condensation in higher bands by acting as an efficient heat sink, i.e. an additional energy reservoir. Our joint work will be published later this year.

4.6.2 Interband relaxation and band decay

Once the atoms have reached a prethermalized state with a finite condensate fraction in a higher target band, the lifetime of the condensate will ultimately be limited by collision-mediated band decay. For example, two atoms can undergo an elastic collision
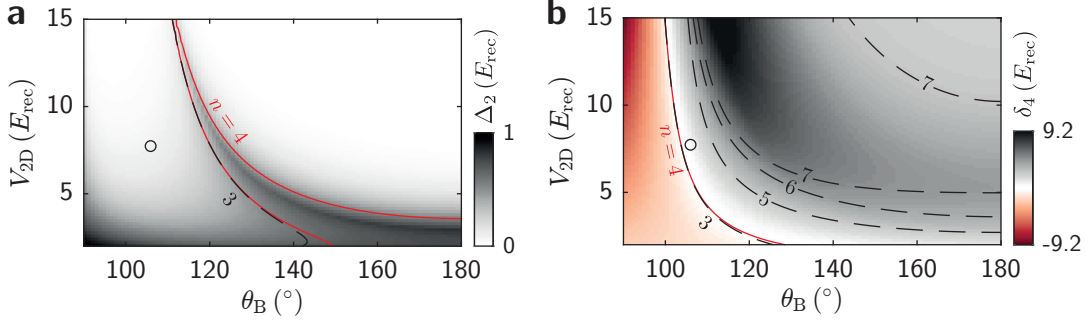
Fig. 4.14: Energy landscape for relaxation and decay in the second band of a boron-nitride lattice for atoms in $|2, -2\rangle$. **a** The bandwidth $\Delta_2 \equiv \epsilon_2(\Gamma) - \epsilon_2(K)$ of the second Bloch band as a function of lattice depth V_{2D} and quantization axis angle θ_B. White regions correspond to small excess energy for relaxation into the local minima K and K' of the second band. Here, condensation should be facilitated. The dashed black line marks the boundary where the bandwidth equals the minimal energy separation to the 3rd band. To the left of it, relaxation cannot induce transitions into higher bands. To the right of it, transitions into the 3rd band are energetically possible. Similarly, excitations into the 4th band are energetically possible within the region that is bounded by the red contour. Outside of it, the 4th and higher bands cannot be reached by relaxation alone. **b** The energy difference $\delta_4 \equiv 2\epsilon_2(K) - \epsilon_1(\Gamma) - \epsilon_4^{min}$ provides an necessary condition for open decay channels. If $\delta_4 < 0$, band-changing transition $22 \to 14$ from K or K' are not possible. If $\delta_4 \geq 0$, they are energetically allowed. The different contour lines for $\delta_n = 0$ correspond to transitions $22 \to 1n$. Inside the regions bounded by the contours the respective transitions are energetically possible. The circles highlight experimental parameters in Figure 4.7.

whereby one is transferred into a lower band, while the other gets excited into even higher bands. Similarly, atoms in higher bands may collide and both decay into a lower band, with the excess energy being released into the direction orthogonal to the lattice plane. Of course, all such processes are subject to energy and momentum conservation, which can be used to engineer band structures that effectively limit the number of allowed decay channels. In particular, specific types of band-changing collisions can be strongly suppressed by choosing appropriate lattice parameters.

In Figure 4.14, we plot the energy landscape for band-changing transitions of the form $22 \to 2n$ and $22 \to 1n$, assuming $n > 2$, as a function of lattice depth V_{2D} and quantization axis angle θ_B, where the circle highlights our optimal parameters for condensation in the second band. Here, transitions $22 \to 2n$ correspond to band relaxation in the second band, involving excitations of atoms into higher bands. As apparent from Figure 4.14a, relaxation in the second band cannot induce band-changing transitions at typical parameters, meaning it is literally *intraband* relaxation. This is readily understood from the fact that the band gap to the next higher band is larger than the bandwidth of the second band.[4] In contrast, for decay processes of the form $22 \to 1n$, excitations into higher bands $n > 2$ are usually energetically allowed. Specifically, Figure 4.14b clarifies that decay processes involving excitations up to the fourth band may occur at our optimal parameters. This is consistent with our experimental observation

---

[4]Incidentally, this justifies the restriction to a single band space n in our consideration of the local equilibrium for condensation as discussed in the previous subsection.
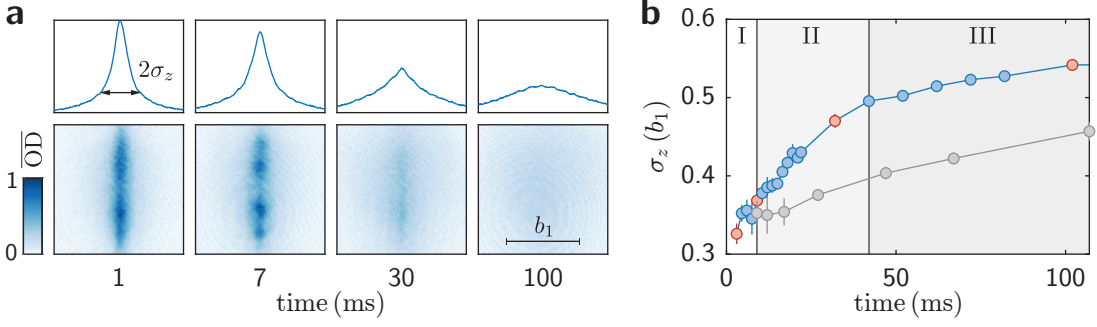
Fig. 4.15: Energy redistribution into lattice tube direction (longitudinal z-direction) after a quench into the second band for $\theta_{\mathrm{B}}^{\mathrm{f}} = 106°$, $V_{\mathrm{2D}} = 8\,E_{\mathrm{rec}}$, and atoms in $|2, -2\rangle$. **a** Bottom: PCO single-shot TOF images for different hold times T_{H} after the quench. Top: corresponding row sum profiles yield the longitudinal momentum distribution and associated standard deviation σ_z, defined by the square root of the second central moment. **b** The time evolution of σ_z after the quench is depicted by blue data points. Data points highlighted in red refer to TOF images in **a**. For comparison, grey data points show σ_z for a measurement at identical parameters $\theta_{\mathrm{B}}^{\mathrm{f}}$ and V_{2D}, where the lattice hold time *before* the quench was varied and T_{H} was fixed to 7 ms. For both curves, the time axis corresponds to equal total hold times in the lattice. Each data point is an average of 6-8 measurements, where error bars denote the corresponding standard deviations.

that less atoms aggregate in the lowest band than are decaying from the second band during stage III of the dynamical evolution (see subsection 4.3.2). Note that for slightly smaller angles θ_{B} these transitions can be tuned out of resonance.

Though fine-tuning of lattice parameters can inhibit certain decay paths, transitions such as $22 \rightarrow 12(11)$ and $21 \rightarrow 11$, implying excitations orthogonal to the lattice plane, most likely cannot be avoided, at least not for the thermal fraction. These transitions are particularly problematic because they do not only decrease the number of atoms in the second band but, which is much more severe, they impart a lot of kinetic energy to the system. This in turn will cause strong heating and thus deplete the condensate. At our optimal parameters, for example, we have a large band gap on the order of $\Delta_{12} \approx 4\,E_{\mathrm{rec}}$. For this reason, even a small number of decaying atoms will suffice to rapidly increase the temperature of the bosonic ensemble and to destroy the condensate.

Experimentally, we have evidenced the decay-induced increase of energy along the lattice tubes by observing the longitudinal momentum distribution for varying hold times T_{H} after the lattice quench. In Figure 4.15, we present results of a corresponding measurement. Here, the momentum distribution is imaged from the transverse direction (-x-axis) by means of the PCO camera (compare section 2.4). For TOF images that are displayed in Figure 4.15a, the lattice plane is oriented vertically, whereas the horizontal axis corresponds to the tube direction. By analyzing the horizontal profiles, we extract the second central moment σ_z^2 of the longitudinal momentum distribution. In Figure 4.15b, we plot the time evolution of σ_z for hold times up to 100 ms (blue data points). Obviously, there is a substantial and rapid increase of the momentum width during stages I and II. Meanwhile, it slows down during stage III, where the condensate has vanished. We stress that it is unclear whether the increase of σ_z during stage I can be uniquely attributed to the excess energy of the condensation process or is merely

a consequence of an early decay from the second band. Most probably, it stems from both. For comparison, we also show a reference curve (grey data points) for the time evolution of the momentum width, where the hold time *before* the quench was varied and we had chosen $T_H = 7\,\text{ms}$ at otherwise identical quench parameters. Here, the increase of the momentum width is considerably slower, which proves that the rapid increase in the former case is indeed a result of intra- and interband relaxation dynamics and cannot be explained, for example, by intrinsic lattice heating. Besides, it directly visualizes the role of the transverse confinement as an energy and entropy reservoir.

We note that decay rates for all transitions as discussed above can be, in principle, estimated from Fermi's golden rule. Based on this, extensive analyses of intraband relaxation and band kinetics have been performed by Paul and Tiesinga [245] in the context of a two-dimensional bipartite square lattice, as well as by Sharma et al. [242] for a one-dimensional double-well lattice. In addition to it, general stability properties of condensates in higher bands have been studied for similar one- and two-dimensional lattice systems in the conventional framework of order parameters, showing that lifetimes in higher bands can be affected by the presence of dynamical instabilities [246, 247]. We emphasize that similar work for two-dimensional hexagonal lattices, as in our case, is currently lacking. Anyway, as valuable as such studies might be, they will usually miss an important ingredient that is notoriously hard to keep track of, namely coherences and interferences among various decay channels, which can be crucial to explain the stability of orbital condensates.

For condensed atoms in a chiral state of a bipartite square lattice, it has been shown that decay is inhibited by destructive inference of two principal decay channels [81]. Here, the condensate gives rise to an effective many-body dark state with respect to internal de-excitation into the lowest band, while its observed depletion happens only via successive rethermalization with the decaying thermal background. A similar mechanism might be at work in our case, which is, however, yet an open question. Nevertheless, we emphasize that the observed time evolution of the thermal and condensed fraction in the second band of the boron-nitride lattice is perfectly amenable to the same physical interpretation as provided by the authors. In fact, our data is almost in one-to-one correspondence with the simulated data presented in that work. Following the same narrative, the condensed fraction is protected from decay, whereas thermal atoms continuously relax into the lowest band. The latter leads to heating and causes condensed atoms to transition into the thermal fraction of the second band, which can overcompensate the decay and cause an increasing thermal fraction during the dynamical stage II, as clearly evidenced in our case in Figure 4.8. In view of this, it seems that a general strategy for engineering long lifetimes of orbital condensates should be to avoid thermal atoms in higher bands in the first place. Giving the intriguing condensation process in higher bands, this is of course only possible to a limited extent. Alternatively, one could use the large longitudinal momentum transfer to achieve a spatial separation between decaying thermal atoms and the condensate before thermalization can set in. For example, additional laser beams at the periphery might serve as a trap for hots atoms that are able to surpass a certain potential hill, allowing for their selective isolation. In any case, there are many exciting possibilities yet to be explored.
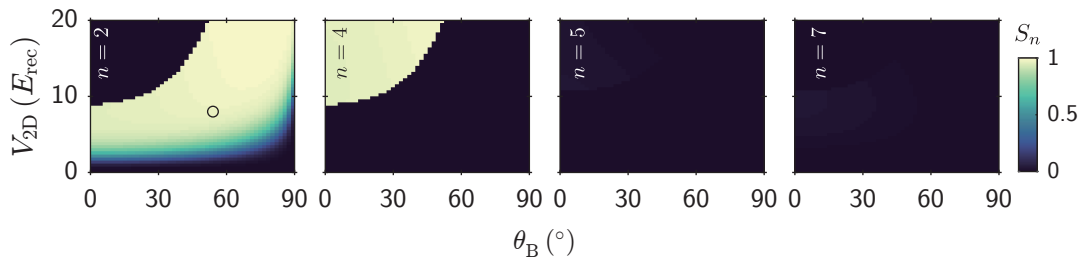
Fig. 4.16: Expected transfer fractions into higher Bloch bands $n \in \{2, 4, 5, 7\}$ of the boron-nitride lattice for a sudden quench via a spin flip $|1, -1\rangle \rightarrow |1, +1\rangle$. Each plot depicts the corresponding overlap $S_n \equiv |\langle n, \Gamma; m_F = +1 | 1, \Gamma; m_F = -1 \rangle|^2$ to the n-th target band as a function of lattice depth V_{2D} and quantization axis angle θ_B. During the quench, θ_B is held constant. For experimentally accessible lattice depths, spin flips allow only for a transfer into the second and fourth band but not into higher ones. The circle in the first plot highlights the parameters from Figure 4.17.

4.7 Condensation via spin flip

In addition to a fast rotation of the quantization axis, we have investigated spin flips $|F, \bar{m}_F\rangle \rightarrow |F, -\bar{m}_F\rangle$ in the boron-nitride lattice as an alternative method to induce quenches of the sublattice energy offset and to create orbital condensates in the second band. Here, spin flips are accomplished by applying a π-pulse as explained in subsection 2.4.2. Similar to a rotation, for certain lattice depths V_{2D} and quantization axis angles θ_B, there is a finite overlap between the initial ground state and higher Bloch states of the final potential configuration, allowing for a targeted transfer into higher bands. In fact, for a given angle θ_B, a spin flip is equivalent to a rotation $\theta_B \rightarrow \theta_B^f = 180° - \theta_B$. Spin flips, however, can often be accomplished on a much shorter time scale than the rotation of the quantization field, thus promising larger transfer fractions.

In Figure 4.16, we plot the expected transfer fractions into higher bands as a function of V_{2D} and θ_B for a sudden lattice quench based on a spin flip $|1, -1\rangle \rightarrow |1, +1\rangle$. Clearly, a targeted population transfer into the second and fourth band is possible for realistic lattice depths over large regions of the parameter space. However, a systematic experimental investigation is more involved than in the case of a rotation of the quantization field. The reason is twofold: First, light shifts and mean-field interactions in the lattice may shift the resonance position for a spin flip to a new, a priori unknown frequency $\nu_r(V_{2D}, \theta_B)$ as compared to the value ν_0 in the absence of the lattice. Second, the Rabi frequency Ω for the spin rotation depends on the driving field component $B_{rf}^\perp$ that is perpendicular to the external quantization field $\mathbf{B}_{ext}(\theta_B)$. Therefore, each time V_{2D} and θ_B is varied, new parameters of the π-pulse, namely driving frequency ν_{RF} and pulse duration τ, must be found to yield a proper spin flip. In particular, for certain θ_B, the component $B_{rf}^\perp$ can be so small that spin flips become impossible for short pulse durations τ, say below $200\,\mu s$. Keeping short pulse durations would require rotating the RF antenna in order to change its polarization, which is not practicable in our setup. Despite all this, it is possible to find reasonable parameters that allow the realization of an orbital condensate in the second band, as we demonstrate in the following.
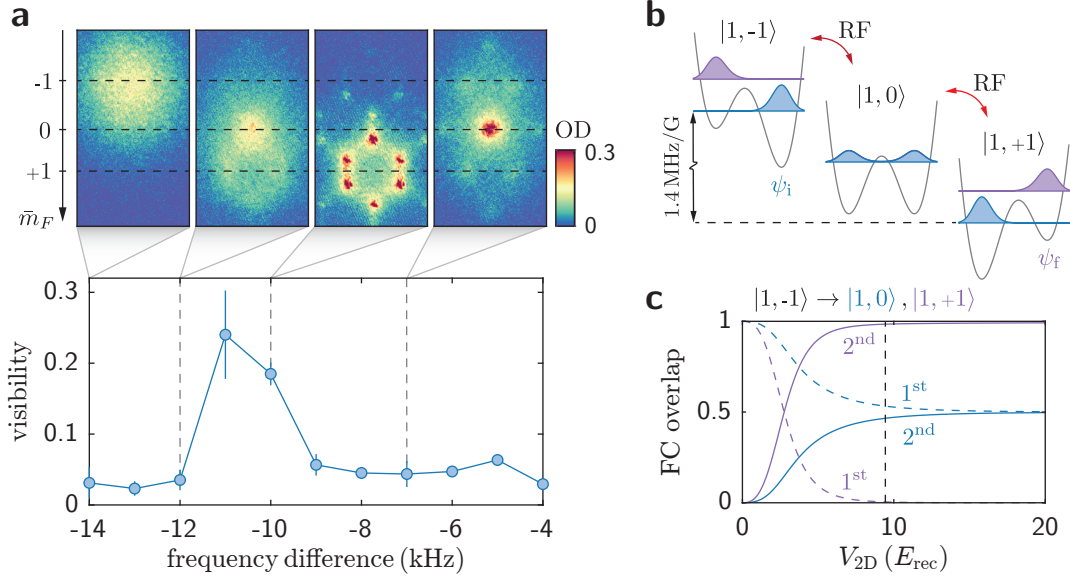
Fig. 4.17: Spin-flip-induced condensation in the second band for an initial potential configuration with $\theta_B = 54°$, $V_{2D} = 9.4\,E_{rec}$, and atoms in $|1, -1\rangle$. **a** Top panel: Single-shot absorption images after sudden release and Stern-Gerlach separation for different frequencies ν_{RF} of the RF driving field. Images were obtained for a fixed hold time $T_H = 7\,\text{ms}$ after the RF pulse. Lower panel: Visibility in the second band as a function of $\nu_{RF} - \nu_0$, where ν_0 denotes the resonance frequency for a π-pulse in the absence of the lattice. Each data point is an average of 2-3 measurements, where error bars denote the corresponding standard deviations. **b** Schematic energy diagram for RF coupling in the manifold $F = 1$ in presence of the boron-nitride lattice. A cross section of the lattice potential and individual Bloch orbitals $(1, \Gamma; \bar{m}_F)$ and $(2, \Gamma; \bar{m}_F)$ is visualized for each $\bar{m}_F$ substate. The large overlap between $\psi_i = (1, \Gamma; -1)$ and $\psi_f = (2, \Gamma; +1)$ leads to efficient transfer into the second band in case of a spin flip $|1, -1\rangle \rightarrow |1, +1\rangle$. **c** Frank-Condon (FC) overlaps between initial and different final Bloch states $(n, \Gamma; \bar{m}_F)$ as a function of the lattice depth V_{2D}. The vertical dashed line marks the experimental value in **a**.

Figure 4.17 presents a measurement where the frequency ν_{RF} was varied across the resonance for a spin flip $|1, -1\rangle \rightarrow |1, +1\rangle$ in a lattice with $V_{2D} = 9.4\,E_{rec}$ and $\theta_B = 54°$. These parameters provide a final sublattice energy offset as in the case of the field rotation in section 4.3. The experimental data has been obtained by the following sequence: First, we create a spin-polarized BEC in the XDT in the Zeeman substate $|1, -1\rangle$. Next, the external quantization axis is adiabatically rotated to an angle $\theta_B = 54°$ at a field magnitude $B_{ext} \approx 2.17\,\text{G}$, corresponding to a Larmor frequency $\nu_0 = 1.519\,\text{MHz}$. Subsequently, the lattice is ramped up exponentially within 100 ms to its final lattice depth. After a wait time of 2 ms, a π-pulse with a variable frequency ν_{RF} is applied for the duration $\tau = 145\,\text{µs}$. We then wait for another 7 ms to allow for recondensation and eventually observe the momentum distribution after TOF, where we use Stern-Gerlach separation to distinguish between different $\bar{m}_F$ components. We stress that the value of the pulse duration τ is determined beforehand by verifying that it gives a pure spin flip for $\theta_B = 54°$ in the absence of the lattice.

In the top panel of Figure 4.17a, we show exemplary single-shot absorption images for different set values of ν_{RF}. Note that the initial component $\bar{m}_F = -1$ exhibits no

long-range phase coherence due the very small bandwidth in the lowest band, which amounts to roughly $5\,\text{Hz}$. As we scan from left to right, we clearly encounter a resonance where atoms are transferred to the new spin state $\bar{m}_F = +1$ and establish long-range phase coherence in the second band. This shows that condensates in the second band can be realized also via spin flips. By evaluating the visibility of Bragg peaks in the component $\bar{m}_F = +1$ at quasimomenta K and K′, we obtain the plot in the lower panel of Figure 4.17a. Note that the visibility is plotted as a function of the frequency difference $\nu_{\text{RF}} - \nu_0$. Specifically, one observes that the resonance frequency for a spin flip in the given lattice potential is shifted by nearly $\delta\nu \approx -10\,\text{kHz}$. We note that level shifts, as sketched in Figure 4.17b, yield a contribution $\delta\nu_{\text{L}} \approx -17\,\text{kHz}$. We suppose that the remaining difference to the observed value is explained by an additional positive shift from mean-field interactions.

Strikingly, by scanning the drive frequency one also observes a regime with an apparent finite long-range phase coherence in the component $\bar{m}_F = 0$, which is associated with the occupation of the Bloch state $|1, \Gamma\rangle$ and can be explained as follows: For an off-resonant RF pulse, the time evolution of the spin state (equation (2.63)) will generally lead to a non-vanishing population in the Zeeman substate $\bar{m}_F = 0$. A necessary condition, of course, is that there is a finite Frank-Condon overlap for the respective external orbitals, which is indeed the case for the given lattice parameters, as we clarify in Figure 4.17c. Besides, the bandwidth of the lowest band for $\bar{m}_F = 0$ amounts to approximately $60\,\text{Hz}$ as the sublattice energy offset vanishes, thus allowing for efficient tunneling and the manifestation of phase coherence.

In summary, we have examined spin flips as a method to create condensates in the second Bloch band of the boron-nitride lattice and verified that appropriate parameters exist to accomplish this goal. Future studies may focus on systematic investigations of attainable transfer fractions and resulting lifetimes of the metastable states, including condensates in the fourth band.

4.8 Conclusion & Outlook

In this chapter, we have demonstrated the successful realization of unconventional condensates in the second and fourth band of a spin-dependent optical boron-nitride lattice. As the main result of our studies, we observed evidence for a chiral superfluid order in the second band, i.e. an orbital condensate that breaks the time-reversal symmetry. At present, however, the lifetime of this metastable state does not suffice to reveal strong and unequivocal symmetry breaking in the momentum distribution.

Starting with an introduction to several fundamental aspects of orbital condensates, we have conducted detailed analyses of lattice quenches induced by rapid rotations of the external quantization field. In general, such quenches for the spin-dependent lattice provide efficient means for a population transfer from the lowest into specific higher target bands. The transfer is conveniently pictured as a Landau-Zener transition, where the finite rotation speed and the finite overlaps between initial and final Bloch states limit the transfer probability. The experimental transfer fractions have been mapped over the full accessible parameter space, demonstrating that targeted transfer can be achieved up to the fifth band and beyond.
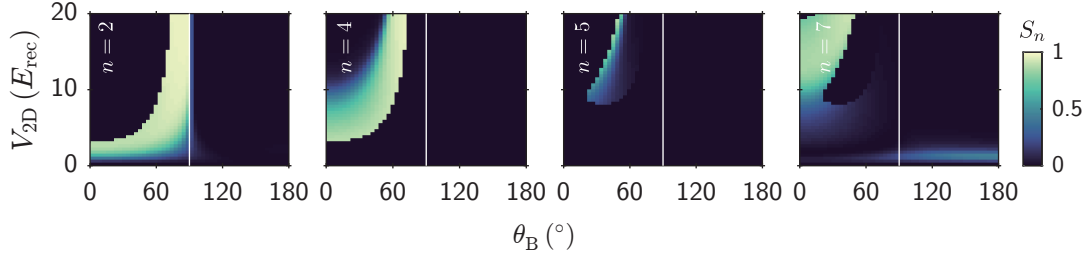
Fig. 4.18: Expected transfer fractions into higher Bloch bands $n \in \{2, 4, 5, 7\}$ of the boron-nitride lattice for a sudden quench via a lattice translation $\Delta \mathbf{R} = -(\mathbf{a}_1 + \mathbf{a}_2)/3$, with atoms in the Zeeman substate $|2, -2\rangle$. Each plot depicts the corresponding overlap $S_n \equiv |\langle n, \Gamma; \mathrm{f} | 1, \Gamma; \mathrm{i}\rangle|^2$ to the n-th target band as a function of the lattice depth $V_{2\mathrm{D}}$ and quantization axis angle θ_B. Labels i and f refer to the Bloch states of the initial and final potential configuration, respectively, i.e. before and after the lattice shift. During the shift, θ_B is held constant. White vertical lines mark the high symmetry angle $\theta_\mathrm{B} = 90°$, where the two sublattices of the boron-nitride lattice become degenerate.

Using this method, we have studied the nonequilibrium dynamics induced by a quench into the second and fourth Bloch band, respectively, and identified three distinct stages with separated time scales: During stage I, atoms quickly condense in a transient metastable state of the target band. During stage II, the number of condensed atoms gradually diminishes by transitioning into thermal atoms of the target band. Finally, during stage III, no condensed atoms are left and a pronounced decay of thermal atoms, mainly into the lowest band, sets in. Our findings are in excellent agreement with a related study [81] in the context of a bipartite square lattice, which indicates that destructive many-body interference may play a crucial role in the hexagonal lattice for stabilizing orbital condensates against decay.

Furthermore, coherence in higher bands was analyzed over large regions of the parameter space, revealing characteristic islands where condensation is possible. Based on this, we have discussed several basic aspects of condensate formation and dissolution in higher bands and elaborated on relevant intraband and interband relaxation processes. In particular, we clarified the importance of the longitudinal confinement as an energy and entropy reservoir: The energy redistribution along the lattice tubes was directly evidenced for all three dynamical stages. While band structures can be engineered that allow to suppress decay channels involving excitations into higher bands, certain processes implying excitations orthogonal to the lattice plane likely cannot be avoided, at least not for thermal atoms. At the same time, it is these processes that introduce strong heating and thus constitute a major limitation for the lifetimes of the realized orbital condensates.

Finally, we have demonstrated that condensation in higher bands of a spin-dependent optical boron-nitride lattice is also possible via RF-induced spin flips. Here, further systematic investigations need to be conducted. Another promising route towards large transfer fractions into higher bands – and perhaps smaller thermal fractions – that we have not yet considered is provided by abrupt lattice shifts. The main advantage compared to the rotation of the quantization axis is that lattice shifts can be readily accomplished on a much shorter time scale of a few microseconds only. In Figure 4.18,

we plot the expected transfer fractions for an exemplary lattice shift of the boron-nitride lattice that allows direct population transfer up to the seventh band, in contrast to the spin flip. Moreover, lattice shifts could also be used to excite atoms into higher bands of lattice potentials that have a vanishing vector light shift, such as the triangular lattice that is realized for an out-of-plane polarization of the lattice beams. The triangular lattice opens up new exciting possibilities for creating orbital condensates in a threefold degenerate manifold. For example, for atoms in the second band of a triangular lattice, a quantum stripe ordering [69] as well as intertwined superfluidity and density wave order [72] have been predicted. In this regard, it would be particularly illuminating to apply new probing techniques, such as the recently presented quantum gas magnifier [248], for resolving these states directly in real space.

5 Time-resolved measurements of the anomalous Hall velocity

In this chapter, I report on measurements of the anomalous velocity for bosonic atoms in an accelerated optical boron-nitride lattice. We start with a brief introduction to the Berry calculus and provide results of a numerical calculation of the Berry curvature. Based on this, we discuss the semiclassical equations of motion for Bloch states subject to a uniform force field and illustrate the resulting trajectories in momentum and real space for different types of forcing. Next, the experimental approach for inertial forcing via lattice acceleration is presented, and the transformation into the comoving frame is reviewed. Following this, we examine the coherent evolution of Bloch states in a moving lattice to first order in adiabatic perturbation theory and establish an explicit connection to experimentally observed momentum distributions after time-of-flight. Finally, we present measurements of the anomalous velocity for different forcing protocols and compare the results to numerical calculations.

The response of Bloch electrons to external forces is one of the oldest problems in the physics of crystalline solids. A rather late insight was that the geometric structure of Bloch bundles over the Brillouin zone can have fundamental implications for the induced dynamics of electrons. Specifically, in the realm of semiclassical wave-packet dynamics, the geometry of Bloch bundles enters the equations of motion via the Berry curvature, which acts similar to a magnetic field: Upon external forcing, in the presence of a non-vanishing Berry curvature, Bloch states will acquire a velocity component that is perpendicular to the instantaneous direction of the force. This so-called *anomalous velocity* is a purely intrinsic effect that lies at the heart of the anomalous Hall response and gives rise to many fascinating transport phenomena, including the anomalous Hall effect (AHE) [249], the spin Hall effect (SHE) [250], as well as their quantized versions, the QAHE and QSHE [88, 251–253]. The latter two, for example, manifest in what has become known as Chern insulators and topological insulators, respectively [176, 254–256].

In real crystal solids, observing induced electron wave-packet dynamics is notoriously hard, mostly due to inherent short times for scattering off lattice defects. Though certain semiconductor nanostructures may provide a remedy, measured Hall response data is in general influenced by the presence of additional extrinsic effects, whose strength may not be known a priori. In practice, it therefore proves difficult to disentangle individual contributions and to unequivocally identify the intrinsic one associated with the anomalous velocity.[1] In this chapter, we report on the direct observation of the

---

[1]See, for example, a recent measurement by Schmidt et al. [257].

anomalous velocity for ultracold bosonic atoms in an accelerated optical boron-nitride lattice, where the measured time-resolved Hall response reveals the local Berry curvature along the forced trajectory in reciprocal space. In addition, by forcing condensed atoms in the second band, we demonstrate geometric "charge" pumping reminiscent of the valley Hall effect [96, 97].

Probing the anomalous Hall response in ultracold atom systems is not new. In fact, Hall drift measurements have been employed successfully in a number of experiments to reveal the topological character of engineered quantum states [54, 56, 57]. So far, existing probe schemes, however, have exclusively focused on detecting the real-space in situ deflection of atomic clouds and did not provide quantitative measurements of the anomalous velocity itself. At typical experimental parameters, real-space Hall deflections are rather small, amounting to only a few lattice sites per forcing cycle, which can be demanding to resolve. In contrast, here we study the dynamical response in momentum space, which is readily accessible from conventional time-of-flight images. In particular, we trace the coherent evolution of Bloch states under an adiabatic perturbation. This approach has basically two advantages: First, even when the real-space Hall deflections are too small to be resolved, the momentum distribution can still yield accurate results for the instantaneous anomalous velocity. Second, observing the momentum distribution naturally provides insights into the coherent interference mechanism that underlies the anomalous velocity: Though, at its core, it builds on a purely geometrical property encoded in the Berry curvature, the physical manifestation as a dynamical effect invokes the coherent admixture of higher Bloch states, making it a genuine interference transport phenomenon. This aspect usually does not become apparent from in situ observations.

Experimental data presented in this chapter has been acquired by the author in the team of J. Simonet and T. Klafka. The measurements have been conceived and proposed by the author. Data analysis and numerical calculations have been performed by the author. Theoretical work related to our considerations can be found in [258, 259]. In what follows, we assume that the reader is familiar with some basic aspects of topological band theory and the quantum geometric phase. A general and comprehensive presentation is given by Bohm et al. [163]. For topological band theory in the context of cold atoms we encourage to consult the recent review by Cooper et al. [92]. An excellent review on semiclassical wave-packet dynamics is provided by Xiao et al. [88] and references therein.

The structure of this chapter is the following: In the first section 5.1, we give a brief review on the Berry calculus and present exact numerical calculations of the Berry curvature for our tunable boron-nitride lattice. Based on this, we discuss the semiclassical motion of Bloch states subject to a uniform force and illustrate exemplary trajectories in the momentum and real space. In section 5.2, we elucidate our experimental approach for inertial forcing and review transformations into the comoving frame. Following this, in section 5.3, we examine the coherent evolution of Bloch states in the comoving frame to first order in adiabatic perturbation theory and establish explicit connection to the observed momentum distribution after time-of-flight. Finally, in section 5.4, we present direct measurements of the anomalous velocity and compare the results to numerical calculations. We conclude and give a brief outlook on further experiments in this direction in section 5.5.

5.1 Berry calculus

In this section, we briefly review the Berry calculus and present exact numerical calculations of the Berry curvature tensor for our tunable boron-nitride lattice. Based on this, we discuss the effects of a non-vanishing Berry curvature on the motion of forced atoms prepared in a non-degenerate band at a quasimomentum $\boldsymbol{k}$.

5.1.1 Berry curvature calculation

Consider a Bloch Hamiltonian $\hat{h}(\boldsymbol{k})$ with associated Bloch modes $\{|u_{n\boldsymbol{k}}\rangle\}$ and eigenenergies $\{\epsilon_n(\boldsymbol{k})\}$, as introduced in subsection 3.1.2. In what follows, we define the Berry curvature 2-form of the n-th Bloch band at quasimomentum $\boldsymbol{k}$ as

$$\Omega^n(\boldsymbol{k}) \equiv \mathrm{i} \sum_{m \neq n} \frac{\langle u_{n\boldsymbol{k}}| [\mathrm{d}\hat{h}(\boldsymbol{k})] |u_{m\boldsymbol{k}}\rangle \wedge \langle u_{m\boldsymbol{k}}| [\mathrm{d}\hat{h}(\boldsymbol{k})] |u_{n\boldsymbol{k}}\rangle}{[\epsilon_n(\boldsymbol{k}) - \epsilon_m(\boldsymbol{k})]^2} = \frac{1}{2} \Omega^n_{\mu\nu}(\boldsymbol{k}) \, \mathrm{d}k^\mu \wedge \mathrm{d}k^\nu \,, \quad (5.1)$$

where summation over repeated indices is implied. Here, d is the exterior derivative and $\wedge$ denotes the wedge product. Besides, we define the Berry curvature tensor

$$\Omega^n_{\mu\nu}(\boldsymbol{k}) \equiv \mathrm{i} \sum_{m \neq n} \frac{\langle u_{n\boldsymbol{k}}| \partial_\mu \hat{h}(\boldsymbol{k}) |u_{m\boldsymbol{k}}\rangle \langle u_{m\boldsymbol{k}}| \partial_\nu \hat{h}(\boldsymbol{k}) |u_{n\boldsymbol{k}}\rangle - (\nu \leftrightarrow \mu)}{[\epsilon_n(\boldsymbol{k}) - \epsilon_m(\boldsymbol{k})]^2} \,, \quad (5.2)$$

with the abbreviation $\partial_\mu \equiv \partial/\partial k_\mu$. We stress that the individual contra- and covariant components labeled by Greek indices μ, ν can refer to any basis for the local coordinate representation of $\Omega^n(\boldsymbol{k})$, but will usually imply cartesian coordinates. For compactness, let us now introduce the expression

$$S^{nm}_\mu(\boldsymbol{k}) \equiv \langle u_{n\boldsymbol{k}}| \partial_\mu \hat{h}(\boldsymbol{k}) |u_{m\boldsymbol{k}}\rangle \,. \quad (5.3)$$

Since the Bloch Hamiltonian is Hermitian, it follows that $S^{nm}_\mu = [S^{mn}_\mu]^*$. With this, we may write the Berry curvature tensor in the compact notation

$$\Omega^n_{\mu\nu}(\boldsymbol{k}) = -2 \sum_{m \neq n} \frac{\mathrm{Im}\left(S^{nm}_\mu(\boldsymbol{k}) S^{mn}_\nu(\boldsymbol{k})\right)}{[\epsilon_n(\boldsymbol{k}) - \epsilon_m(\boldsymbol{k})]^2} \,. \quad (5.4)$$

By expanding the Bloch modes according to equation (3.20) and noting that $\partial_\mu \hat{h}(\boldsymbol{k}) = \hbar(\hat{p}_\mu + \hbar k_\mu)/m_{\mathrm{a}}$, where m_{a} denotes the atomic mass, we obtain

$$S^{nm}_\mu(\boldsymbol{k}) = \frac{\hbar^2}{m_{\mathrm{a}}} \left(k_\mu \delta_{nm} + \sum_{\mathbf{G}} c^*_{n\boldsymbol{k}}(\mathbf{G}) c_{m\boldsymbol{k}}(\mathbf{G}) G_\mu \right) \,. \quad (5.5)$$

Once the expansion coefficients $\{c_{n\boldsymbol{k}}(\mathbf{G})\}$ and $\{c_{m\boldsymbol{k}}(\mathbf{G})\}$ are determined from a numerical diagonalization of the Bloch Hamiltonian, equation (5.5) is easily evaluated for all $m < M$, where M denotes an upper bound for summation over band indices. Using equation (5.4), we then directly arrive at an approximation for the Berry curvature. It is worth noting that the Berry curvature tensor, by definition, is an antisymmetric tensor:
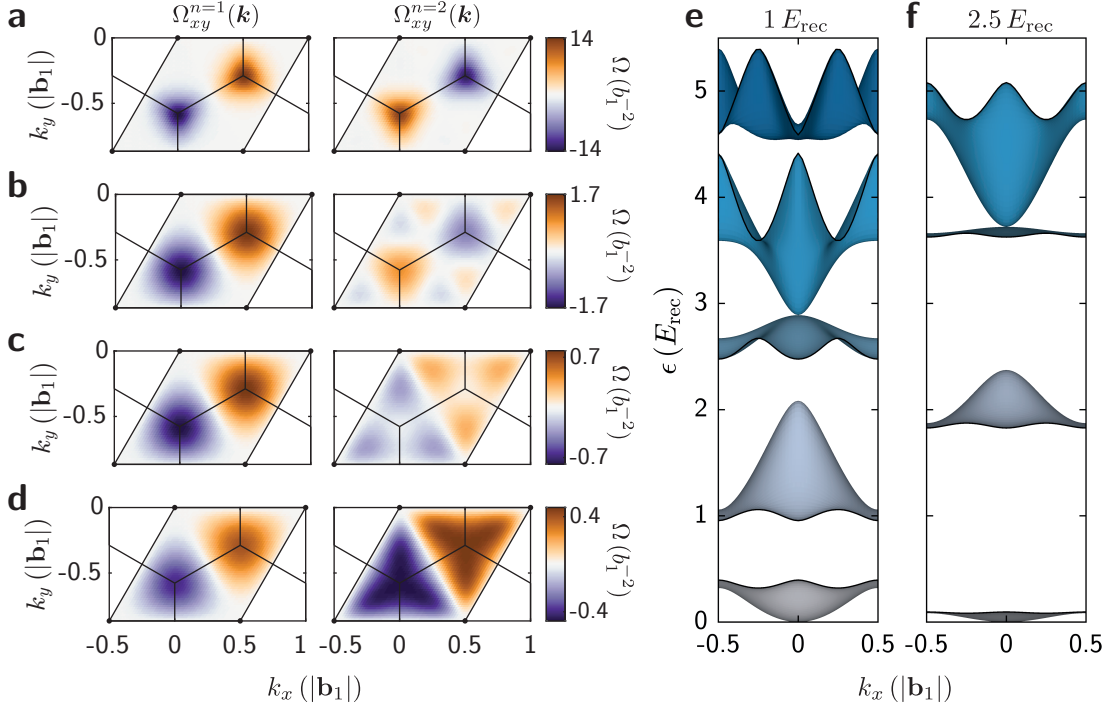
Fig. 5.1: Berry curvature tensor components $\Omega_{xy}^n(\boldsymbol{k})$ for the first ($n = 1$) and second ($n = 2$) band of the boron-nitride lattice, plotted over a primitive reciprocal unit cell (grey rhombus). For the lattice potential, we assume atoms in the Zeeman substate $|1, -1\rangle$ and a quantization axis angle $\theta_{\mathrm{B}} = 0°$. **a-d** For lattice depths $V_{\mathrm{2D}} = (1, 2, 2.5, 3)\, E_{\mathrm{rec}}$, respectively. In general, there is a concentration of Berry curvature at the vertices of the Brillouin zone, i.e. at quasimomenta K and K′. Note that $\Omega_{xy}^n(\mathrm{K}) = -\Omega_{xy}^n(\mathrm{K}')$, as expected for a time-reversal symmetric Bloch Hamiltonian. With increasing lattice depth, the Berry curvature in the second band acquires a non-trivial texture due to the increased relative proximity of higher bands. **e-f** Exemplary band structures for the lattice depths $V_{\mathrm{2D}} = 1\, E_{\mathrm{rec}}$ and $2.5\, E_{\mathrm{rec}}$.

$\Omega_{\mu\nu}^n(\boldsymbol{k}) = -\Omega_{\nu\mu}^n(\boldsymbol{k})$. Moreover, it is real-valued and gauge invariant. For time-reversal symmetric Bloch Hamiltonians, it obeys the symmetry relation $\Omega_{\mu\nu}^n(\boldsymbol{k}) = -\Omega_{\mu\nu}^n(-\boldsymbol{k})$.

In Figure 5.1, we plot the tensor component $\Omega_{xy}^n(\boldsymbol{k})$ for an exemplary configuration of our spin-dependent boron-nitride lattice. Specifically, we consider the potential for atoms in the Zeeman substate $|1, -1\rangle$ with the parameter $\theta_{\mathrm{B}} = 0°$, leading to broken inversion symmetry with a maximal sublattice energy offset and opened Dirac cones between the two lowest Bloch bands. Clearly, for shallow lattices, the Berry curvature of the first and second band is well-localized around the vertices of the Brillouin zone, i.e. at the quasimomenta K and K′, as expected from the minimal band gap at these points. In this regime, the Berry curvature distribution features opposite signs for the first and second Bloch band. For increasing lattice depths, the respective distributions get broader and can acquire more complicated structures due to the enhanced relative proximity of higher bands: For example, the Berry curvature of the second band may vanish at K and K′ and even undergo a sign change, as evident from Figure 5.1c-d. We note that Berry curvature distributions as shown here can be mapped out directly via

special tomographic techniques, as demonstrated by Fläschner et al. [94].

For completeness, we mention that a Bloch state in the n-th band picks up, in addition to a dynamical phase factor, a geometric phase factor $\exp(\mathrm{i}\gamma_n)$ upon adiabatic transport along a closed path $\mathcal{C}$ in reciprocal space [84]. Here, the phase

$$\gamma_n(\mathcal{C}) \equiv \mathrm{i} \oint_{\mathcal{C}} \mathrm{d}\boldsymbol{k} \, \langle u_{n\boldsymbol{k}} | \, \nabla_{\boldsymbol{k}} \, | u_{n\boldsymbol{k}} \rangle = \frac{1}{2} \int_S \Omega^n_{\mu\nu}(\boldsymbol{k}) \, \mathrm{d}k^\mu \wedge \mathrm{d}k^\nu \tag{5.6}$$

is known as the adiabatic Berry phase to the n-th band, which depends only on the Berry curvature flux through the surface element S bounded by the closed path $\mathcal{C} \equiv \partial S$. In particular, for the first band, this phase is in general nonzero for a path enclosing a single Dirac point. We note that the associated geometric phase becomes a topological one in the limit $\theta_{\mathrm{B}} \to 90°$, i.e. when the Dirac cones of the first and second Bloch band intersect. In fact, the Berry curvature in this case approaches zero everywhere except at the Dirac points, where it diverges such that $\gamma_1(\mathcal{C}^*) \to \pm\pi$ for any path $\mathcal{C}^*$ that encloses a Dirac point exactly once.[2] We emphasize that the geometric and topological phase around such degeneracy points has been successfully measured and studied in cold atom experiments by means of interferometric techniques in momentum space [93].

For gapped two-dimensional periodic systems, it is well-known that Bloch bands can be classified by a topological invariant known as the first Chern number [164], which is an integer. It is defined for the n-th Bloch band via

$$\mathrm{C}_1^n \equiv \frac{1}{2\pi} \int_{\tilde{\mathbf{T}}^2} \Omega^n = \frac{1}{4\pi} \int_{\mathrm{BZ}} \Omega^n_{xy}(\boldsymbol{k}) \, \mathrm{d}k^x \mathrm{d}k^y \,, \tag{5.7}$$

where integration has to be performed over the Brillouin zone torus $\tilde{\mathbf{T}}^2$, i.e. over the entire first Brillouin zone. It immediately follows from our above symmetry considerations that the first Chern number of any Bloch band must vanish for time-reversal symmetric Bloch Hamiltonians. This is in perfect agreement with results obtained by numerical integration of the calculated Berry curvatures.

5.1.2 Semiclassical equations of motion

We now focus on the effects of a non-vanishing Berry curvature on the motion of atoms subject to a uniform force $\mathbf{F}(t)$ in a periodic potential, where the force can be time-dependent in general. We will assume atoms prepared in a single band n at some initial quasimomentum $\boldsymbol{k}_0$. When the force remains sufficiently weak such that transitions into other bands can be neglected on a relevant time scale, an adequate description of the semiclassical wave-packet dynamics is provided by the following single-band equations of motion, stated for a three-dimensional lattice system [88–90]:

$$\dot{\boldsymbol{k}}(t) = \mathbf{F}(t)/\hbar \,, \tag{5.8a}$$

$$\boldsymbol{v}^n(t) = \hbar^{-1}\nabla\epsilon_n(\boldsymbol{k}(t)) - \dot{\boldsymbol{k}}(t) \times \boldsymbol{\Omega}^n(\boldsymbol{k}(t)). \tag{5.8b}$$

---

[2]The sign depends on the Dirac point and the limiting procedure, i.e. whether $\theta_{\mathrm{B}} = 90°$ is approached from above or below.

In this notation, $\boldsymbol{k}(t)$ denotes the time-dependent gauge-invariant quasimomentum, and $\boldsymbol{v}^n(t)$ is the mean velocity of the time-evolved Bloch state. Here, $\boldsymbol{\Omega}^n(\boldsymbol{k})$ is the so-called pseudovector form of the Berry curvature: Its components are given by [88]

$$(\boldsymbol{\Omega}^n(\boldsymbol{k}))_\rho \equiv \frac{1}{2}\Omega_{\mu\nu}^n(\boldsymbol{k})\varepsilon_{\mu\nu\rho}\,, \tag{5.9}$$

where $\varepsilon_{\mu\nu\rho}$ is the Levi-Civita tensor and summation over repeated indices is implied. The first term on the right-hand side of equation (5.8b) is known as the group velocity $\boldsymbol{v}_g^n(\boldsymbol{k}(t))$, whereas the second term is the *anomalous velocity* $\boldsymbol{v}_a^n(\boldsymbol{k}(t))$. Evidently, the anomalous velocity is proportional to the Berry curvature and forcing strength. Moreover, it points perpendicular to the force $\mathbf{F}(t)$. In other words, whenever $\boldsymbol{k}(t)$ passes regions with non-vanishing Berry curvature in a given band n, one acquires a velocity component transverse to the time derivative of $\boldsymbol{k}(t)$.

Since we are dealing with a uniform force $\mathbf{F}(t)$, which does not depend on the position coordinate $\boldsymbol{r}$, equation (5.8) decouples and is particularly easy to solve: For the sake of clarity, assume that the force is turned on at $t_0 = 0$. The solution for $\boldsymbol{k}(t)$ is then simply given by

$$\boldsymbol{k}(t) = \boldsymbol{k}_0 + \frac{1}{\hbar}\int_0^t \mathrm{d}\tau\,\mathbf{F}(\tau)\,, \qquad t > 0. \tag{5.10}$$

Then, by plugging this into the right-hand side of equation (5.8b), one directly obtains the time evolution of the mean velocity $\boldsymbol{v}^n(t) = \boldsymbol{v}_g^n(\boldsymbol{k}(t)) + \boldsymbol{v}_a^n(\boldsymbol{k}(t))$. We emphasize that equation (3.35) can be used to calculate the group velocity without invoking derivates of the band structure, which is advantageous for numerical calculations. In the following, let us focus on a two-dimensional lattice with a uniform force that lies within the lattice plane. We denote by $\{\boldsymbol{e}_x, \boldsymbol{e}_y, \boldsymbol{e}_z\}$ an orthonormal basis, where $\boldsymbol{e}_x, \boldsymbol{e}_y$ are vectors in the lattice plane. With the convention that $\Omega_{\mu\nu}^n = 0$ if μ or ν is equal to z, the anomalous term can be recast as

$$\boldsymbol{v}_a^n(t) = -\left[\dot{k}_y(t)\boldsymbol{e}_x - \dot{k}_x(t)\boldsymbol{e}_y\right]\Omega_{xy}^n(\boldsymbol{k}(t))\,. \tag{5.11}$$

To gain insights into solutions of the semiclassical equations of motion for our boron-nitride lattice, we consider constant forcing in the lowest Bloch band along three distinct orbits in reciprocal space, as illustrated in Figure 5.2a: In all cases, the quasimomentum follows a straight path or geodesic. The corresponding time evolution of the mean velocity is depicted in Figure 5.2b-c. For convenience, we introduce the gauge-invariant quantity $\boldsymbol{\kappa}^n(t) \equiv m_a \hbar^{-1}\boldsymbol{v}^n(t)$, which has same units as the quasimomentum and will be called *mean momentum* for short. It is illuminating to decompose $\boldsymbol{\kappa}^n(t)$ into longitudinal and transverse components according to

$$\kappa_{l,t}^n(t) \equiv \frac{m_a}{\hbar}\left\langle \boldsymbol{v}^n(t), \boldsymbol{e}_{l,t}\right\rangle\,, \tag{5.12}$$

where $(\boldsymbol{e}_l, \boldsymbol{e}_t)$ denotes a local right-handed orthonormal basis in which $\boldsymbol{e}_l$ points in the direction of the force. Obviously, when the group velocity has vanishing contribution to κ_t^n, the transverse component is a direct measure of the anomalous velocity and thus the Berry curvature, i.e. one has $\kappa_t^n \boldsymbol{e}_t = m_a \hbar^{-1}\boldsymbol{v}_a^n$. For example, this is the case for
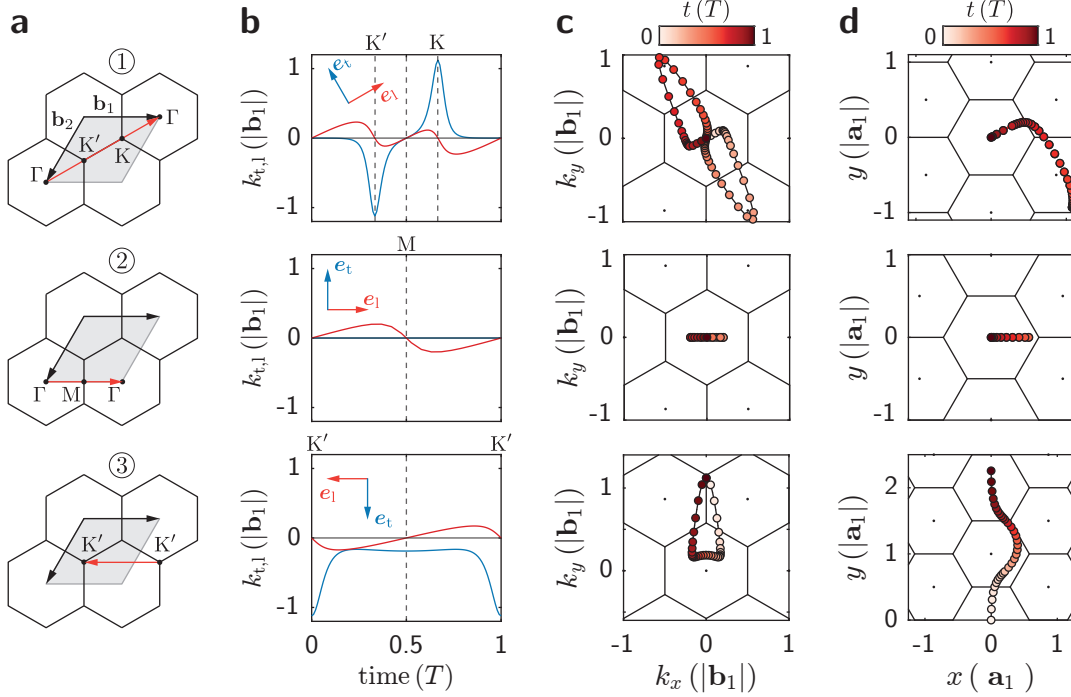
Fig. 5.2: Semiclassical dynamics of Bloch states under uniform forcing in a hexagonal boron-nitride lattice. **a** Sketch of three different forcing orbits in the reciprocal space: ① From $\Gamma \to \Gamma$ across the vertices K', K of the Brillouin zone, ② from $\Gamma \to \Gamma$ across the M point, and ③ from K' $\to$ K' parallel to the previous direction. **b** Resulting time evolution of the respective longitudinal (red) and transverse (blue) momenta $\hbar\kappa_{\mathrm{l,t}}(t) \equiv m_a \langle \boldsymbol{v}(t), \boldsymbol{e}_{\mathrm{l,t}} \rangle$ of the first band for an exemplary configuration of the boron-nitride lattice: atoms in the Zeeman substate $|1, -1\rangle$, lattice depth $V_{\mathrm{2D}} = 1\,E_{\mathrm{rec}}$, and quantization axis angle $\theta_{\mathrm{B}} = 60°$. Here, $(\boldsymbol{e}_{\mathrm{l}}, \boldsymbol{e}_{\mathrm{t}})$ denotes a local right-handed orthonormal basis, where $\boldsymbol{e}_{\mathrm{l}}$ points into the direction of the external force. The time on the horizontal axis is specified in units of the corresponding Bloch period T. We consider a forcing strength $F/\hbar = 2.31\,|\mathbf{b}_1|\,\mathrm{ms}^{-1}$ in all three cases, which gives $T_1 \approx 0.75\,\mathrm{ms}$, $T_{2,3} \approx 0.43\,\mathrm{ms}$. **c** Associated time evolution of the total momentum $\boldsymbol{\kappa}$ in reciprocal space, where time is encoded by the colormap. **d** Similarly, related trajectories in real space, where ① and ② yield closed periodic orbits, while ③ results in a net transverse Hall drift.

protocols ① and ② in Figure 5.2, where forcing is performed along high-symmetry lines of the Brillouin zone. Specifically, in ①, the traversed path in reciprocal space visits the K' and K points, where atoms encounter a strong Berry curvature that causes large transverse deflections in opposite directions, respectively. If there was no transverse component due to the anomalous velocity, atoms would just perform ordinary Bloch oscillations as described by the longitudinal component κ_{l}^n. This is indeed the case for the protocol ② as the Berry curvature always vanishes along the corresponding path (compare Figure 5.1). Meanwhile, the situation is more complicated for ③, where the orbit $\boldsymbol{k}(t)$ periodically visits regions of one and the same sign of the Berry curvature, leading to a nonzero net anomalous Hall drift after each cycle. The resulting trajectory in real space is depicted in the lowest panel of Figure 5.2d. In fact, this constitutes an example of geometric pumping in which periodic particle transport into transverse direction of the force can be achieved by exploiting the non-vanishing local character

of the Berry curvature. It should be stressed, however, that the transverse component κ_{t}^n in ③ has contributions from both the group and anomalous velocity, as evidenced from the nonzero value in between the two equivalent K$'$ points. The same is true for a general forcing orbit starting at the quasimomentum $\boldsymbol{k}_0 = \Gamma$. As we will further see in the section 5.4, where we present time-resolved measurements of the transverse mean momentum for the above forcing schemes, the anomalous contribution may still be uniquely identified by applying a time-reversed protocol. Before we come to that, we review our experimental approach for generating uniform forcing in the lattice frame of reference.

5.2 Lattice forcing: experimental approach

For the Hall measurements we are going to present, we do not apply a direct force to atoms within the laboratory frame of reference. Instead, we use lattice acceleration via frequency modulation to create inertial forces in the comoving frame. Here, we elucidate our experimental approach and establish formulas and transformations that are relevant for further analysis.

5.2.1 Lattice orbits

Recall that our 2D lattice potential $V_{\mathrm{L}}(\boldsymbol{r})$ in the limit of strong external quantization fields takes the general form

$$V_{\mathrm{L}}(\boldsymbol{r}) = \sum_{k}^{3} \alpha_k \cos(\mathbf{b}_k \boldsymbol{r} + \Delta_k) + \sum_{k}^{3} \beta_k \sin(\mathbf{b}_k \boldsymbol{r} + \Delta_k) + \mathrm{const.} \,, \qquad (5.13)$$

where α_k and β_k denote some constants that may depend on the internal state of the atom, and $\{\mathbf{b}_1, \mathbf{b}_2, \mathbf{b}_3\}$ is the set of reciprocal lattice vectors. The latter span a two-dimensional subspace that defines the lattice plane. So far, we have ignored the relative phases $\Delta_k \equiv \epsilon_{ijk}(\phi_i - \phi_j)/2$. As we show below, they can be used to move the lattice along an arbitrary orbit in the lattice plane.

As before, let us denote by $\{\boldsymbol{e}_x, \boldsymbol{e}_y\}$ an orthonormal basis within the lattice plane. In this subspace, we now define the origin $\mathbf{R}_0 = R_x \boldsymbol{e}_x + R_y \boldsymbol{e}_y$ of our optical lattice as the solution to the following linear equation:

$$\begin{pmatrix} b_{2,x} & b_{2,y} \\ b_{3,x} & b_{3,y} \end{pmatrix} \cdot \begin{pmatrix} R_x \\ R_y \end{pmatrix} + \begin{pmatrix} \Delta_2 \\ \Delta_3 \end{pmatrix} = 0 \,. \qquad (5.14)$$

The solution is easily obtained by inverting the matrix, giving

$$\mathbf{R}_0 = \frac{(b_{2,y}\Delta_3 - b_{3,y}\Delta_2)}{\xi} \boldsymbol{e}_x + \frac{(b_{3,x}\Delta_2 - b_{2,x}\Delta_3)}{\xi} \boldsymbol{e}_y \,. \qquad (5.15)$$

Here, we have defined $\xi \equiv b_{2,x} b_{3,y} - b_{2,y} b_{3,x}$. Without loss of generality, we will assume that $\phi_1 = 0$, such that $\Delta_2 = \phi_3$ and $\Delta_3 = -\phi_2$. Ideally, in the static case, the phases of the individual lattice beams are constant over time, i.e. $\phi_i(t) = \phi_i$. If their frequencies, however, undergo a small time-dependent variation $\delta\omega_i(t)$, the beams will pick up an

additional phase. Assuming that the variation starts at $t_0 = 0$, with the initial condition $\phi_i(t \leq t_0) = 0$, the total time-dependent phases become

$$\phi_i(t) = -\int_0^t \mathrm{d}t' \, \delta\omega_i(t'), \qquad t \geq 0. \tag{5.16}$$

Hence, if only the frequencies ω_2 and ω_3 get modulated, the origin of the lattice potential will exert a motion along the following orbit:

$$\mathbf{R}_0(t) = -\frac{b_{2,y}\phi_2(t) + b_{3,y}\phi_3(t)}{\xi}\boldsymbol{e}_x + \frac{b_{2,x}\phi_2(t) + b_{3,x}\phi_3(t)}{\xi}\boldsymbol{e}_y, \tag{5.17}$$

with the corresponding velocity vector

$$\dot{\mathbf{R}}_0(t) = \frac{b_{2,y}\delta\omega_2(t) + b_{3,y}\delta\omega_3(t)}{\xi}\boldsymbol{e}_x - \frac{b_{2,x}\delta\omega_2(t) + b_{3,x}\delta\omega_3(t)}{\xi}\boldsymbol{e}_y. \tag{5.18}$$

Frequently, the inverted equation is more useful. In other words, one considers some carefully designed velocity orbit $\dot{\mathbf{R}}_0(t)$ that one likes to implement experimentally by appropriately setting the frequency modulations, i.e. according to

$$\delta\omega_2(t) = -\mathbf{b}_3\dot{\mathbf{R}}_0(t), \qquad \delta\omega_3(t) = \mathbf{b}_2\dot{\mathbf{R}}_0(t). \tag{5.19}$$

Evidently, the individual frequency modulations must increase or decrease at constant rates to realize constant lattice accelerations.

As an example for a typical lattice orbit, consider the case where only $\delta\omega_3(t)$ is nonzero. It then follows that both $\dot{\mathbf{R}}_0(t)$ and $\ddot{\mathbf{R}}_0(t)$ are perpendicular to $\mathbf{b}_3$. For an ideal hexagonal lattice, this also implies that they are parallel to $\boldsymbol{k}_3$, which is the wave vector of the lattice beam that is modulated. In other words, lattice motion or forcing is exerted along high-symmetry lines of the underlying Brillouin zone. We note, however, that this does not hold universally: In the presence of lattice asymmetries, modulating the frequency of a single lattice beam will in general not result in a lattice motion that is exactly oriented along the corresponding directions of high symmetry.

5.2.2 Inertial forces in the comoving frame

Clearly, for a moving lattice, the single particle Hamiltonian for atoms in the laboratory frame takes the form

$$\hat{H}(t) = \frac{\hat{\boldsymbol{p}}^2}{2m_\mathrm{a}} + V_\mathrm{L}(\hat{\boldsymbol{r}} - \mathbf{R}_0(t)). \tag{5.20}$$

It is insightful to transform the Hamiltonian into the comoving frame, i.e. into the lattice frame of reference. Specifically, this is achieved by applying the following time-dependent unitary transformation [174] $\hat{U}(t) = \hat{U}_3(t)\hat{U}_2(t)\hat{U}_1(t)$, with the position shift operator

$$\hat{U}_1(t) \equiv \exp\left(\frac{\mathrm{i}}{\hbar}\mathbf{R}_0(t)\hat{\boldsymbol{p}}\right), \tag{5.21}$$

the time-dependent energy shift

$$\hat{U}_2(t) \equiv \exp\left(-\frac{\mathrm{i}}{\hbar}\frac{m_\mathrm{a}}{2}\int_{t_0}^{t}\mathrm{d}\tau\left[\dot{\mathbf{R}}_0(\tau)\right]^2\right),\tag{5.22}$$

and the momentum shift operator

$$\hat{U}_3(t) \equiv \exp\left(-\frac{\mathrm{i}}{\hbar}m_\mathrm{a}\dot{\mathbf{R}}_0(t)\hat{\boldsymbol{r}}\right).\tag{5.23}$$

The transformed Hamiltonian $\hat{H}_\mathrm{cm}(t) \equiv \hat{U}(t)\hat{H}(t)\hat{U}^\dagger - \mathrm{i}\hbar\hat{U}(t)\partial_t\hat{U}^\dagger(t)$ reads

$$\hat{H}_\mathrm{cm}(t) = \frac{\hat{\boldsymbol{p}}^2}{2m_\mathrm{a}} + V_\mathrm{L}(\hat{\boldsymbol{r}}) - \mathbf{F}(t)\hat{\boldsymbol{r}}\,,\quad\text{with}\quad \mathbf{F}(t)\equiv -m_\mathrm{a}\ddot{\mathbf{R}}_0(t)\,,\tag{5.24}$$

where $\mathbf{F}(t)$ denotes the fictitious force felt by atoms as seen from the non-inertial lattice frame of reference. We have thus shown that lattice acceleration can be used to create a uniform force field, leading to a bilinear term $-\mathbf{F}(t)\hat{\boldsymbol{r}}$ in the Hamiltonian $\hat{H}_\mathrm{cm}(t)$ of the comoving frame. The semiclassical equation (5.8) refers exactly to a Hamiltonian of this form.

For static force fields $\mathbf{F}(t) = \mathbf{F}$, the Hamiltonian $\hat{H}_\mathrm{cm}$ is known as the Wannier-Stark Hamiltonian. Finding its eigenstates and eigenenergies constitutes the so-called Wannier-Stark problem, which we shall not delve into.[3] In fact, for our purpose it will be sufficient to consider only the approximate adiabatic state evolution under the action of $\hat{H}_\mathrm{cm}(t)$ for short durations τ, assuming a system initialized in a Bloch state. This is the focus of the next section 5.3: As a main result, it will provide clear understanding of the momentum distributions after time-of-flight as observed in the *laboratory frame*, and, most importantly, clarify the coherent interference nature that underlies the anomalous velocity in the semiclassical equations.

5.3 State evolution in adiabatic perturbation theory

Obviously, a nonzero force $\mathbf{F}(t)$ breaks the translational invariance of the Hamiltonian $\hat{H}_\mathrm{cm}(t)$ in the comoving frame. As a consequence, Bloch states are no longer eigenstates to it. Translational invariance, however, can be reestablished by switching to an intermediate gauge in which the state evolution of Bloch states is studied in the most transparent manner. For this, we revert the last unitary transformation from $\hat{U}_3(t)$, yielding the intermediate-gauge Hamiltonian

$$\hat{H}_\mathrm{I}(t) = \frac{(\hat{\boldsymbol{p}} - \hbar\mathbf{K}_0(t))^2}{2m_\mathrm{a}} + V_\mathrm{L}(\hat{\boldsymbol{r}})\,,\quad\text{with}\quad \mathbf{K}_0(t)\equiv\hbar^{-1}m_\mathrm{a}\dot{\mathbf{R}}_0(t).\tag{5.25}$$

The price one must pay, so to speak, is that $\hat{H}_\mathrm{I}(t)$ becomes explicitly time-dependent even when the force in the comoving frame is static, i.e. $\hat{H}_\mathrm{cm}$ is time-independent. If the introduced comoving quasimomentum $\mathbf{K}_0(t)$ describes a periodic orbit in reciprocal space, in the sense that $\mathbf{K}_0(t) = \mathbf{K}_0(t+T)$ (mod $\mathbf{G}$) for some reciprocal lattice vector

---

[3]For a rigorous treatment see, for example, Glück [260].

G and a fixed period T, then a natural strategy to solve the Schrödinger equation for $\hat{H}_{\mathrm{I}}(t)$ is provided by the Floquet formalism, giving rise to spatio-temporal Bloch states [261]. Here, we shall not assume such a $\mathbf{K}_0(t)$ and instead follow a perturbative approach.

To proceed, we consider the instantaneous eigenstates of $\hat{H}_{\mathrm{I}}(t)$ for some fixed time $t = \tau$. Since $\hat{H}_{\mathrm{I}}(\tau)$ is translationally invariant, the instantaneous eigenstates are given by conventional Bloch states

$$|n\boldsymbol{k}_{\mathrm{I}}(\tau)\rangle \equiv e^{\mathrm{i}\boldsymbol{k}\hat{\boldsymbol{r}}} |u_{n\boldsymbol{k}}^{\mathrm{I}}(\tau)\rangle \ , \tag{5.26}$$

which we label with an additional index for clarity. Here, the Bloch modes $|u_{n\boldsymbol{k}}^{\mathrm{I}}(\tau)\rangle$ are eigenstates to the associated Bloch Hamiltonian

$$\hat{h}_{\mathrm{I}}(\boldsymbol{k};\tau) \equiv \frac{(\hat{\boldsymbol{p}} - \hbar\mathbf{K}_0(\tau) + \hbar\boldsymbol{k})^2}{2m_{\mathrm{a}}} + V_{\mathrm{L}}(\hat{\boldsymbol{r}}) \,, \tag{5.27}$$

with corresponding eigenvalues $\epsilon_n(\boldsymbol{k};\tau)$. Note that equation (5.27) has the same form as the standard Bloch Hamiltonian in equation (3.19) if we introduce a new parameter $\mathbf{q}(\tau) \equiv \boldsymbol{k} - \mathbf{K}_0(\tau)$, such that $\hat{h}_{\mathrm{I}}(\boldsymbol{k},\tau) = \hat{h}(\mathbf{q}(\tau))$ and $\epsilon_n(\boldsymbol{k};\tau) = \epsilon_n(\mathbf{q}(\tau))$. Eventually, it follows that the Bloch modes can be expanded in the conventional Fourier basis as

$$|u_{n\boldsymbol{k}}^{\mathrm{I}}(\tau)\rangle \equiv |u_{n\mathbf{q}(\tau)}\rangle = \sum_{\mathbf{G}} c_{n(\boldsymbol{k}-\mathbf{K}_0(\tau))}(\mathbf{G}) |\mathbf{G}\rangle = \sum_{\mathbf{G}} c_{n\mathbf{q}(\tau)}(\mathbf{G}) |\mathbf{G}\rangle \,. \tag{5.28}$$

Note that the parametric time-dependence of the Bloch modes is incorporated in the expansion coefficients $\{c_{n\mathbf{q}(\tau)}(\mathbf{G})\}$ via the dependence on the quasimomentum $\mathbf{q}$.

Now, if the external parameter $\mathbf{K}_0(t)$ and thus $\mathbf{q}(t)$ upon real dynamical evolution varies sufficiently slowly, the adiabatic theorem will hold: Hence, a system prepared in an instantaneous eigenstate $|n\boldsymbol{k}_{\mathrm{I}}(t_0)\rangle$ at time t_0 will remain in the corresponding manifold of adiabatically connected eigenstates. Specifically, for times $t \geq t_0$, the state will evolve to zeroth order according to [84, 163]

$$|\psi_{\mathrm{I}}(t)\rangle^{(0)} = e^{-\mathrm{i}\alpha_n(t)} |n\boldsymbol{k}_{\mathrm{I}}(t)\rangle \ , \tag{5.29}$$

where the phase angle $\alpha_n(t) = \alpha_n^{\mathrm{dyn}}(t) + \alpha_n^{\mathrm{geo}}(t)$ is conveniently split into a dynamical

$$\alpha_n^{\mathrm{dyn}}(t) \equiv \frac{1}{\hbar} \int_{t_0}^{t} \mathrm{d}\tau \, \epsilon_n(\mathbf{q}(\tau)) \,, \tag{5.30}$$

and geometric contribution

$$\alpha_n^{\mathrm{geo}}(t) \equiv -\mathrm{i} \int_{t_0}^{t} \mathrm{d}\tau \, \langle u_{n\boldsymbol{k}}^{\mathrm{I}}(\tau)| \, \partial_\tau \, |u_{n\boldsymbol{k}}^{\mathrm{I}}(\tau)\rangle = -\mathrm{i} \int_{\mathcal{C}} \mathrm{d}\mathbf{q} \, \langle u_{n\mathbf{q}}| \nabla_{\mathbf{q}} |u_{n\mathbf{q}}\rangle \,. \tag{5.31}$$

In the last term, $\mathcal{C}$ is the path traced out by $\mathbf{q}$ with starting point $\mathbf{q}(t_0)$ and endpoint $\mathbf{q}(t)$. Note that, in the case of a closed path $\mathcal{C}$, the geometric phase defined here is just the negative of the adiabatic Berry phase $\gamma_n(t)$ (equation (5.6)). Here, we assume a smooth gauge for the phase of the Bloch mode $|u_{n\mathbf{q}}\rangle$ along $\mathcal{C}$. We do not, however, require that it is necessarily single-valued. For example, by choosing a parallel transport

gauge, the phase $\alpha_n^{\text{geo}}(t)$ would vanish while being incorporated directly in the Bloch mode $|u_{n\mathbf{q}}\rangle$.

The zeroth-order adiabatic expansion in equation (5.29) cannot account for the anomalous velocity. It is merely responsible for the group velocity via equation (3.35). To explain the anomalous response, one must include admixtures from adjacent bands due to higher order corrections: To first order in adiabatic perturbation theory one finds [262]

$$|\psi_{\text{I}}(t)\rangle^{(1)} = e^{-\mathrm{i}\alpha_n(t)} \left(|n\boldsymbol{k}_{\text{I}}(t)\rangle - \mathrm{i}\hbar \sum_{m\neq n} b_m(t) |m\boldsymbol{k}_{\text{I}}(t)\rangle \right), \qquad (5.32)$$

where the coefficients $b_m(t)$, with $m \neq n$, are given by

$$b_m(t) \equiv \frac{\langle m\boldsymbol{k}_{\text{I}}(t)| \, \partial_t \, |n\boldsymbol{k}_{\text{I}}(t)\rangle}{\epsilon_n(\boldsymbol{k};t) - \epsilon_m(\boldsymbol{k};t)} = \frac{\langle u_{m\mathbf{q}(t)}| \left[\frac{\mathrm{d}}{\mathrm{d}t}\hat{h}(\mathbf{q}(t)) \right] |u_{n\mathbf{q}(t)}\rangle}{[\epsilon_n(\mathbf{q}(t)) - \epsilon_m(\mathbf{q}(t))]^2}$$
$$= \sum_\mu \frac{\dot{q}^\mu(t) S_\mu^{mn}(\mathbf{q}(t))}{[\epsilon_n(\mathbf{q}(t)) - \epsilon_m(\mathbf{q}(t))]^2} . \quad (5.33)$$

Here, $S_\mu^{mn}(\mathbf{q})$ is defined as in equation (5.5), such that the different $b_m(t)$ are readily obtained from the numerical calculation of the Berry curvature. We like to stress the following point: Without loss of generality, we may choose a gauge such that the expansion coefficients $\{c_{n\mathbf{q}}(\mathbf{G})\}$ of Bloch modes admit the relation

$$c_{n,\mathbf{q}+\mathbf{J}}(\mathbf{G}) = c_{n\mathbf{q}}(\mathbf{G} + \mathbf{J}) \qquad (5.34)$$

for arbitrary quantum numbers n, $\mathbf{q}$, and reciprocal lattice vectors $\mathbf{J}$, $\mathbf{G}$. Then, if the orbit described by $\mathbf{q}(t)$ is periodic in the sense that $\mathbf{q}(t) = \mathbf{q}(t+T)$ (mod $\mathbf{J}$), it follows that all coefficients $b_m(t)$ are also periodic, with the same period T.

Momentum distribution in the intermediate gauge   To understand the momentum distribution of $|\psi_{\text{I}}(t)\rangle^{(1)}$, consider the expansion in the Fourier basis:

$$|\psi_{\text{I}}(t)\rangle^{(1)} = e^{-\mathrm{i}\alpha_n(t)} \sum_{\mathbf{G}} \left(c_{n\mathbf{q}(t)}(\mathbf{G}) - \mathrm{i}\hbar \sum_{m\neq n} b_m(t) c_{m\mathbf{q}(t)}(\mathbf{G}) \right) |\mathbf{G} + \boldsymbol{k}\rangle$$
$$\equiv e^{-\mathrm{i}\alpha_n(t)} \sum_{\mathbf{G}} \left(c_{n\mathbf{q}(t)}(\mathbf{G}) + d_{n\mathbf{q}(t)}(\mathbf{G}) \right) |\mathbf{G} + \boldsymbol{k}\rangle \qquad (5.35)$$
$$\equiv e^{-\mathrm{i}\alpha_n(t)} \sum_{\mathbf{G}} C_{n\mathbf{q}(t)}(\mathbf{G}) |\mathbf{G} + \boldsymbol{k}\rangle .$$

From this, we see that the Bragg peaks represented by $\{|\mathbf{G} + \boldsymbol{k}\rangle\}$ remain stationary, while their weights $\{C_{n\mathbf{q}(t)}(\mathbf{G})\}$ "move" along $\mathbf{q}(t)$ through reciprocal space. Specifically, for a periodic orbit in the above sense, the momentum distribution recurs after time T, being just translated by a corresponding reciprocal lattice vector $-\mathbf{J}$.

Momentum distribution in the comoving frame   Complementary, consider the time-evolved Bloch state $|\psi_{\mathrm{I}}(t)\rangle^{(1)}$ transformed into the original comoving frame:

$$|\psi_{\mathrm{cm}}(t)\rangle^{(1)} \equiv \hat{U}_3(t)\,|\psi_{\mathrm{I}}(t)\rangle^{(1)} = e^{-\mathrm{i}\mathbf{K}_0(t)\hat{\mathbf{r}}}\,|\psi_{\mathrm{I}}(t)\rangle^{(1)} \tag{5.36}$$

$$= e^{-\mathrm{i}\alpha_n(t)} \sum_{\mathbf{G}} C_{n\mathbf{q}(t)}(\mathbf{G})\,|\mathbf{G}+\mathbf{q}(t)\rangle\,. \tag{5.37}$$

Here, we see that both the Bragg peaks as well as their weights move along $\mathbf{q}(t)$. Obviously, for periodic orbits $\mathbf{q}(t)$, this describes a cyclic state with a periodically recurring momentum distribution, i.e. $|\psi_{\mathrm{cm}}(t+T)\rangle^{(1)} \sim |\psi_{\mathrm{cm}}(t)\rangle^{(1)}$, meaning equality up to a phase factor. In fact, without the first-order adiabatic correction $d_{n\mathbf{q}(t)}(\mathbf{G})$ in $C_{n\mathbf{q}(t)}(\mathbf{G})$, this would just describe ordinary Bloch oscillations. The connection to the semiclassical equations becomes immediately apparent by noting that the mean velocity of the time-evolved Bloch state in the comoving frame is given by

$$\boldsymbol{v}^n(t) \equiv {}^{(1)}\langle\psi_{\mathrm{cm}}(t)|\,m_{\mathrm{a}}^{-1}\hat{\boldsymbol{p}}\,|\psi_{\mathrm{cm}}(t)\rangle^{(1)} = \frac{\hbar}{m_{\mathrm{a}}} \sum_{\mathbf{G}} |c_{n\mathbf{q}(t)}(\mathbf{G})|^2\,[\mathbf{G}+\mathbf{q}(t)]$$

$$+ \frac{\hbar}{m_{\mathrm{a}}} \sum_{\mathbf{G}} 2\mathrm{Re}\Big(c_{n\mathbf{q}(t)}^*(\mathbf{G})\cdot d_{n\mathbf{q}(t)}(\mathbf{G})\Big)[\mathbf{G}+\mathbf{q}(t)] + \mathcal{O}(d_{n\mathbf{q}}(t)\cdot d_{n\mathbf{q}}^*(t)). \tag{5.38}$$

The first term on the right-hand side is equal to the group velocity $\boldsymbol{v}_{\mathrm{g}}^n(t)$, whereas the second term gives rise to the anomalous velocity $\boldsymbol{v}_{\mathrm{a}}^n(t)$. Indeed, using equations (5.4) and (5.33) it is straightforward to verify that

$$\frac{\hbar}{m_{\mathrm{a}}} \sum_{\mathbf{G}} 2\mathrm{Re}\Big(c_{n\mathbf{q}(t)}^*(\mathbf{G})\cdot d_{n\mathbf{q}(t)}(\mathbf{G})\Big)[\mathbf{G}+\mathbf{q}(t)] = \sum_{\mu\nu} \dot{q}_\mu(t)\Omega_{\mu\nu}^n(\mathbf{q}(t))\boldsymbol{e}_\nu\,, \tag{5.39}$$

which is equal to the anomalous velocity defined in equation (5.11).

Momentum distribution in the laboratory frame   Finally, let us consider the time-evolved Bloch state in the laboratory frame:

$$|\psi(t)\rangle^{(1)} \equiv U_1^\dagger(t)U_2^\dagger(t)U_3^\dagger(t)\,|\psi_{\mathrm{cm}}(t)\rangle^{(1)}$$
$$= e^{-\mathrm{i}\alpha_n(t)}e^{-\mathrm{i}\theta(t)} \sum_{\mathbf{G}} e^{-\mathrm{i}\chi(t,\mathbf{G},\boldsymbol{k})}C_{n\mathbf{q}(t)}(\mathbf{G})\,|\mathbf{G}+\boldsymbol{k}\rangle\,, \tag{5.40}$$

where we defined the following phase factors:

$$\theta(t) \equiv \frac{m_{\mathrm{a}}}{2\hbar} \int_{t_0}^t \mathrm{d}\tau\,\Big[\dot{\mathbf{R}}_0(\tau)\Big]^2\,, \qquad \chi(t,\mathbf{G},\boldsymbol{k}) \equiv \mathbf{R}_0(t)[\mathbf{G}+\boldsymbol{k}]. \tag{5.41}$$

Hence, in the laboratory frame, similar to the intermediate gauge, Bragg peaks remain stationary, while the associated weights $C_{n\mathbf{q}(t)}(\mathbf{G})$ evolve through reciprocal space. Note that the individual phase factors in equation (5.40) are unimportant for the observed momentum distribution: While $e^{-\mathrm{i}\alpha_n(t)}$ and $e^{-\mathrm{i}\theta(t)}$ correspond to global phase factors, the local phase factors $e^{-\mathrm{i}\chi(t,\mathbf{G},\boldsymbol{k})}$ do not affect the Bragg peak weights.

5.4 Measurements of the anomalous velocity

We now present systematic measurements of the coherent evolution of Bloch states in an accelerated optical boron-nitride lattice. Knowing the precise lattice geometry, we can readily infer the full time evolution of the anomalous velocity, which gives access to the local Berry curvature along the forced trajectory in reciprocal space. In the following, we focus on the three quasimomentum orbits ①, ②, and ③ as introduced in subsection 5.1.2.

The experimental sequence starts with the creation of a spin-polarized BEC in a crossed optical dipole trap (see chapter 2). For a predefined quantization axis angle θ_B, the condensate is then adiabatically loaded into the ground state $|1, \Gamma\rangle$ of the optical boron-nitride lattice by exponentially ramping up the lattice depth V_{2D} to a desired value in $T_R = 100\,\text{ms}$. Following a hold time $T_H = 50\,\text{ms}$, we apply inertial forcing by sweeping the lattice beam frequencies $\omega_{2,3}(t)$ according to a prescribed protocol. After a variable forcing time τ_F, all confining potentials are switched off abruptly, and we observe the momentum distribution after 36 ms time-of-flight.

Type-1 orbit According to equation (5.18), forcing along the orbit ①, i.e. along the high-symmetry line $\Gamma \to K' \to K \to \Gamma$ or vice versa, is readily achieved by setting all frequency modulations to zero except for $\delta\omega_3(t)$. In particular, here we consider $\dot{\omega}_3(t) = \pm 2\pi \cdot 40\,\text{MHz s}^{-1}$. This leads to an inertial force of magnitude $F/\hbar = 2.41\,|\mathbf{b}_1|\,\text{ms}^{-1}$ with a positive and negative sign, respectively. To be precise, we mention that due to the presence of a small breaking of the hexagonal lattice symmetry (compare Appendix A), the resulting orbits $\mathbf{q}^\pm(t)$ for our modulation scheme do not exactly trace out high-symmetry lines of the Brillouin zone. In general, they are not even closed. Though one may compensate for this by introducing an appropriate $\dot{\omega}_2(t) \neq 0$, the deviations from the ideal orbit ① in our case remain small, and we do not invoke this complication.

In Figure 5.3, we show exemplary TOF images of the momentum distribution probed for different times τ_F and for a positive and negative inertial force, respectively. We compare the experimental results to theoretical predictions based on equation (5.40). For the calculations, we neglect effects from the external harmonic confinement and assume atoms localized at a single quasimomentum $\mathbf{k}(t)$. Evidently, the calculated TOF images show excellent agreement with the observed momentum distributions. We note that the momentum space origin in the laboratory frame has been chosen such that it corresponds to the "center of mass" of the momentum distribution when no forcing is applied.

As explained in the previous section 5.3, Bragg peaks in the laboratory frame remain stationary during lattice acceleration, while the peak weight or Wannier envelope follows the comoving quasimomentum $\mathbf{K}_0(t) \equiv \hbar^{-1} m_a \dot{\mathbf{R}}_0(t)$. Recall that the latter is uniquely determined by equation (5.18) once the reciprocal lattice vectors and frequency modulations are specified. Here, we directly derive the reciprocal lattice vectors from the observed locations of Bragg peaks, which provide a calibration of the momentum scale. The corresponding $\mathbf{K}_0(t)$ at times τ_F are visualized in Figure 5.3 by blacked filled circles. For completeness, we also plot the associated comoving Brillouin zones, depicted by black hexagons. Note that, with $\mathbf{K}_0(t)$, also the inertial force $\mathbf{F}(t) \equiv \hbar \dot{\mathbf{K}}_0(t)$ as well as the local coordinate basis $(\mathbf{e}_l, \mathbf{e}_t)$ is now uniquely specified so that the longitudinal
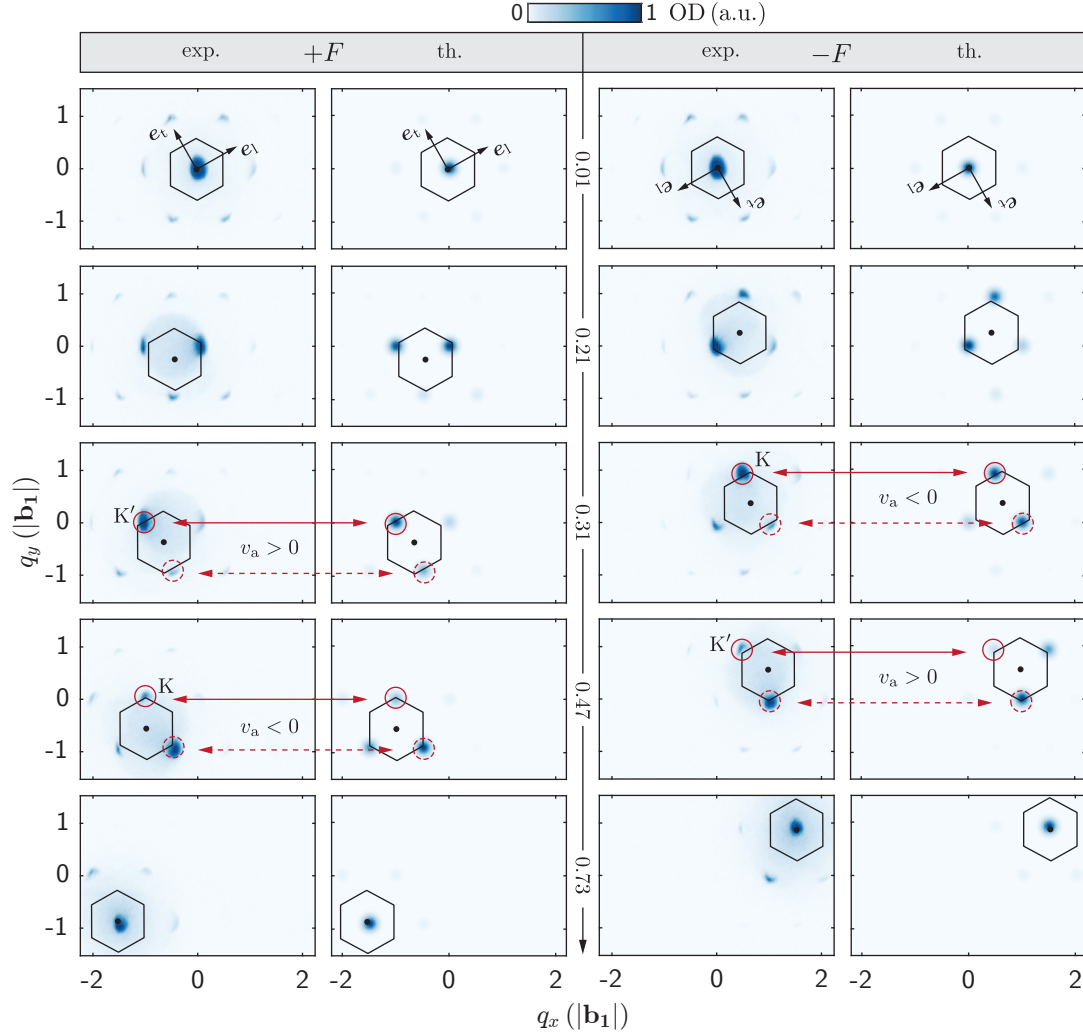
Fig. 5.3: Comparison between measured and calculated momentum distributions of Bloch states in the lowest band subject to forcing ① along $\Gamma \rightarrow K' \rightarrow K \rightarrow \Gamma$ as shown in Figure 5.2: For atoms in the Zeeman substate $|1, -1\rangle$, in a boron-nitride lattice with $V_{2D} = 1.3\,E_{rec}$ and $\theta_B = 180°$. Momentum distributions were probed for a positive $(+F)$ and time-reversed negative $(-F)$ force at increasing times τ_F (top to bottom) after switching on a frequency sweep $\dot{\omega}_3(t) = \pm 2\pi \cdot 40\,\text{MHz s}^{-1}$, respectively. Times are indicated by numbers in the middle column, in units of millisecond. Simulated TOF images were obtained from numerical analysis of equation (5.40) for lattice and forcing parameters as used in the experiment, with Bragg peaks represented by Gaussians of a common fixed width without additional free parameters. We also account for the actual lattice geometry (compare Appendix A), determined from the observed locations of Bragg peaks, which provide a common length scale $|\mathbf{b_1}|$. Small axes in the first row indicate the local coordinate basis $(\boldsymbol{e}_l, \boldsymbol{e}_t)$, where $\boldsymbol{e}_l$ points in the direction of the resulting inertial force. Black hexagons depict Brillouin zones of the comoving lattice frame, traveling in the opposite direction. The anomalous velocity becomes manifest as an imbalance or transverse symmetry breaking between Bragg peaks on opposite sides of the Brillouin zone, as highlighted in the third and fourth row for quasimomenta close to K' and K. All images have been normalized individually to the same colormap. Experimental images depict typical single-shot absorption images recorded after $36\,\text{ms}$ time-of-flight.

and transverse mean momentum components $\kappa_{l,t}(t)$ can be directly deduced: For this, we first extract the central moment $\boldsymbol{\kappa}(t)$ of the TOF distribution with respect to $\mathbf{K}_0(t)$, yielding the mean momentum as measured from the comoving frame, and then project it onto the local basis vectors. The results are summarized in Figure 5.4b,e,h. We like to point out that the anomalous velocity, since it is aligned into either the positive or negative transverse direction, must manifest as an imbalance in the occupation of Bragg peaks on opposite sides of the line that is spanned by $\boldsymbol{e}_l$. In Figure 5.3, such an imbalance becomes clearly evident for TOF images in the third and fourth row, where the relevant Bragg peaks are highlighted by red circles. Note that the imbalance undergoes a sign change when passing from the quasimomentum K$'$ to K and vice versa, as one would anticipate from the alternating sign of the Berry curvature. For forcing along the orbit ①, where the group velocity has a vanishing or at least negligible contribution to the transverse momentum, this is indeed an unequivocal signature of the anomalous Hall response.

To give a more quantitative analysis of the anomalous velocity, we now have a closer look at the time evolution of the longitudinal and transverse momentum components $\kappa_{l,t}(\pm F, t)$ for the two forcing orientations $\pm F$. Let us first write the mean momentum as a sum of group and anomalous momentum: $\boldsymbol{\kappa}(\pm F, t) = \boldsymbol{\kappa}_g(\pm F, t) + \boldsymbol{\kappa}_a(\pm F, t)$. In general, $\boldsymbol{\kappa}_g(\pm F, t)$ can have a non-vanishing contribution $\kappa_{g,t}(\pm F, t) \equiv \langle \boldsymbol{\kappa}_g(\pm F, t), \boldsymbol{e}_t(\pm F) \rangle$ to the transverse momentum. To disentangle the anomalous part, one should note that the initial state is localized at a time-reversal invariant quasimomentum $\mathbf{q}(0) = \Gamma$. It then follows that $\boldsymbol{\kappa}_g(\pm F, t) = -\boldsymbol{\kappa}_g(\mp F, t)$ and hence $\kappa_{g,t}(\pm F, t) = \kappa_{g,t}(\mp F, t)$. Consequently, the anomalous contribution $\kappa_a(\pm F, t)$ can be directly obtained by

$$\kappa_a(\pm F, t) = \frac{\kappa_t(\pm F, t) - \kappa_t(\mp F, t)}{2} \,.$$ (5.42)

We stress that this implies $\kappa_a(+F, t) = -\kappa_a(-F, t)$, such that we may focus only on the component $\kappa_a(+F, t)$ in the following.

Figure 5.4 depicts the extracted time evolution of the various momenta $\kappa_{t,l,a}(t)$ for the above measurement (Figure 5.3). In addition, we present results for two further lattice configurations characterized by larger and smaller band gaps to the second band, respectively. For all measurements, we used the same forcing protocol ①, and each data point is an average of two to three experimental realizations. The individual plots are arranged in decreasing order of the band gaps (from left to right): For the largest band gap (Figure 5.4a,d,g), we find an excellent agreement with predictions of the semiclassical equations. Bloch oscillations are clearly resolved in the measured longitudinal momentum. Moreover, the measured transverse momentum reveals a nonzero anomalous Hall response $\kappa_a(+F, t)$ that reaches a positive maximum near the Dirac point at K$'$ and a negative minimum near the second Dirac point at K, exhibiting a characteristic sign change in between. For a reduced band gap (Figure 5.4b,e,h), the individual momentum components exhibit similar oscillatory features but with a larger amplitude, as expected from the increased magnitude of the Berry curvature and band width. In this regime, the semiclassical single-band equations still provide a reasonable description, though deviations to the measured data become more noticeable. Most strikingly, the maximum in the measured anomalous momentum $\kappa_a(+F, t)$ is reached at signifi-
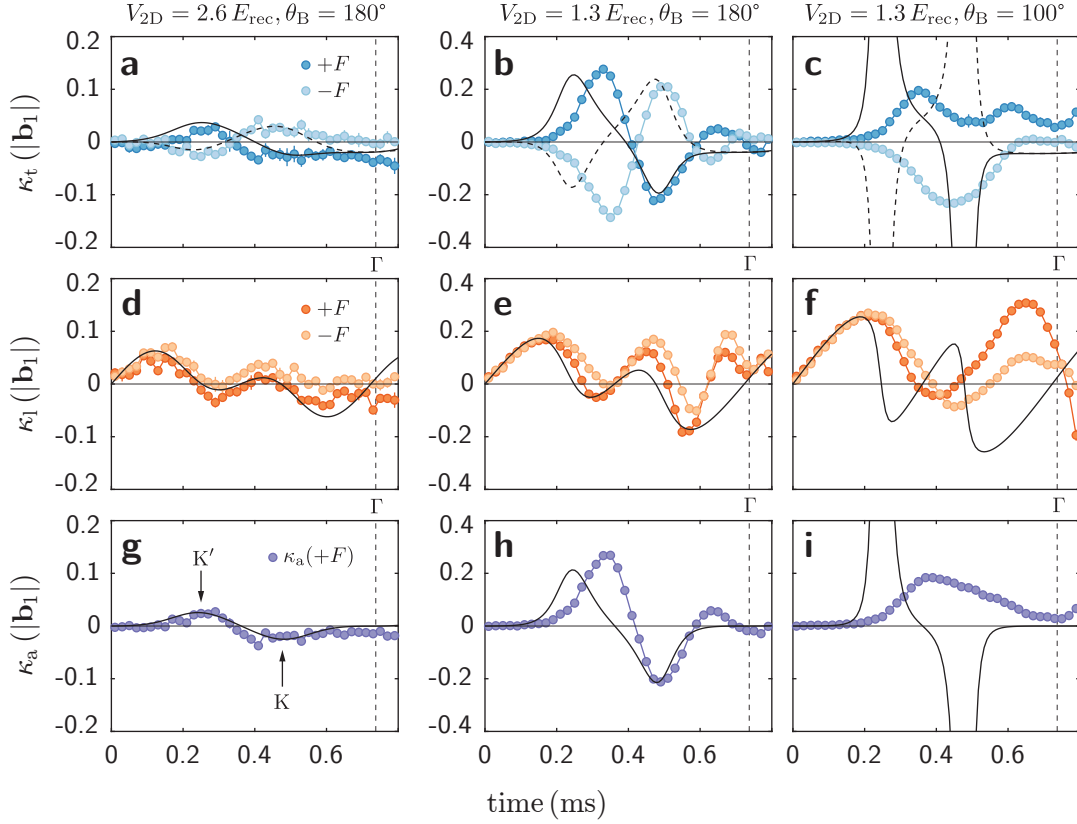
Fig. 5.4: Time evolution of the mean velocity of Bloch states in the lowest band in response to forcing ① along $\Gamma \to K \to K' \to \Gamma$ and the opposite direction, realized by frequency sweeps $\dot{\omega}_3(t) = \pm 2\pi \cdot 40\,\mathrm{MHz}\,\mathrm{s}^{-1}$, respectively: For atoms in the Zeeman substate $|1, -1\rangle$ and varying lattice configurations (left to right). The sweeps result in corresponding forces $(\pm F)$ with a magnitude $F/\hbar = 2.41\,|\mathbf{b}_1|\,\mathrm{ms}^{-1}$. **a-c** Dark (light) blue data points depict the measured transverse momentum $\kappa_{\mathrm{t}}(\pm F, t)$ for a positive (negative) force. Solid (dashed) lines show the results of the semiclassical equation (5.8). **d-f** Corresponding longitudinal momenta $\kappa_{\mathrm{l}}(\pm F, t)$. One expects $\kappa_{\mathrm{l}}(+F, t) = \kappa_{\mathrm{l}}(-F, t)$ from time-reversal symmetry. **g-i** Time evolution of the anomalous momentum $\kappa_{\mathrm{a}}(+F, t)$ as obtained from $\kappa_{\mathrm{a}}(+F, t) \equiv [\kappa_{\mathrm{t}}(+F, t) - \kappa_{\mathrm{t}}(-F, t)]/2$. In all plots, vertical dashed lines indicate the Bloch period for atoms in a lattice with ideal hexagonal symmetry, forced with the same strength. Plots in the central column show the results of the measurement in Figure 5.3. Each data point is an average of 2-3 measurements, and error bars denote the standard deviations. All theory curves have been obtained for lattice and forcing parameters as used in the experiment, incorporating measured lattice asymmetries (compare Appendix A).

cantly later times. We attribute this behavior to the growing influence of non-adiabatic transitions into higher bands. Finally, for the smallest band gap (Figure 5.4c,f,i), we still observe a nonzero Hall response but with a completely different trace that remains positive over the observed time span. The increasing deviation from the semiclassical description indicates the breakdown of the first-order adiabatic approximation. Within the calculations, this is likewise signaled by the diverging anomalous response.

The possible inadequacy of the first-order adiabatic approximation can be checked by evaluating the sum of the squared amplitudes of the expansion coefficients $b_m(t)$ from equation (5.33). Naturally, a necessary condition for adiabaticity to hold is that

$$B_n(t) \equiv \sum_{m \neq n} |b_n(t)|^2 \ll 1 \,, \tag{5.43}$$

up to all relevant times t. Specifically, for the three lattice configurations in Figure 5.4, we obtain $\max(B_1(t)) \approx 0.007, 0.22, 84$, respectively. We thus conclude that data points in Figure 5.4g constitute a direct measure of the Berry curvature along the traversed orbit ① in reciprocal space, i.e. we have

$$\Omega_{xy}(\mathbf{q}(t)) = \frac{\hbar}{m_{\mathrm{a}}} \kappa_{\mathrm{a}}(t) \left[\dot{q}_x(t) \langle \boldsymbol{e}_y, \boldsymbol{e}_{\mathrm{t}} \rangle - \dot{q}_y(t) \langle \boldsymbol{e}_x, \boldsymbol{e}_{\mathrm{t}} \rangle \right]^{-1} \,. \tag{5.44}$$

Type-2 orbit   The preceding forcing orbit was designed to visit the K and K′ points in the lowest band, where the Berry curvature is localized, and thus a large Hall response was measured. For comparison, we now focus on forcing along the orbit ②, i.e. along a high-symmetry line $\Gamma \to \mathrm{M} \to \Gamma$ (see Figure 5.2) for which no such response should occur. This time, we choose $\dot{\omega}_3(t) = \mp \dot{\omega}_2(t) = \pm 2\pi \cdot 23.094\,\mathrm{MHz\,s^{-1}}$, which leads to the required inertial force, with a similar magnitude $F/\hbar = 2.42\,|\mathbf{b}_1|\,\mathrm{ms^{-1}}$ as before. We note that in our convention, the sign of the inertial force ($\pm F$) is identified with the sign of $\dot{\omega}_3(t)$.

In Figure 5.5, we show exemplary TOF images of the resulting momentum distributions probed for different times τ_F and for a positive and negative inertial force, respectively. As in the previous paragraph, we compare the experimental results to theoretical predictions based on equation (5.40). Once again, the calculated TOF images are in excellent agreement with measured momentum distributions. Most strikingly, no apparent transverse symmetry breaking in the momentum distributions becomes manifest. This is further confirmed by evaluating the respective longitudinal and transverse momentum components $\kappa_{\mathrm{t,l}}(\pm F, t)$, which is summarized in Figure 5.6 for the same set of lattice configurations as in Figure 5.4: Across all configurations, no significant transverse momentum is observable. The slight modulations that are noticeable in Figure 5.6b-c are largely attributable to contributions from the group velocity, as a result of lattice asymmetries and forcing that is not exactly along a high-symmetry line. Most importantly, the resulting anomalous momentum curves $\kappa_{\mathrm{a}}(+F, t)$ are consistently zero within the error bounds. In other words, no anomalous Hall response is discernible, in agreement with a vanishing Berry curvature along the given forcing orbit ②. Hence, the system essentially performs ordinary Bloch oscillations, as evidenced by the time evolution of the longitudinal momentum $\kappa_{\mathrm{l}}(\pm F, t)$. Note that we resolve nearly two Bloch periods for the observed time span, since the path length is reduced
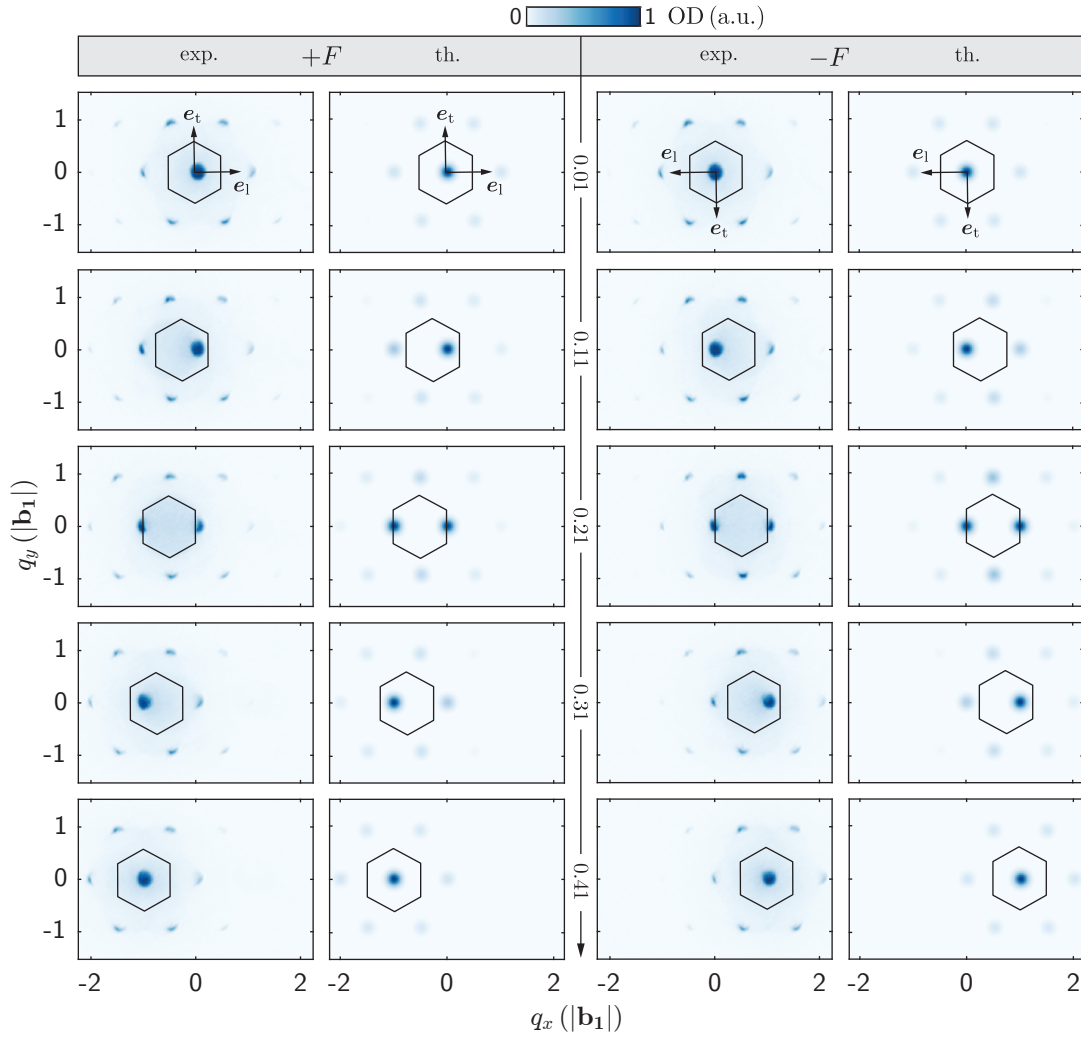
Fig. 5.5: Comparison between measured and calculated momentum distributions of Bloch states in the lowest band subject to forcing ② along $\Gamma \to M \to \Gamma$ as illustrated in Figure 5.2: For atoms in the Zeeman substate $|1, -1\rangle$, in a boron-nitride lattice with $V_{2D} = 2.6\,E_{\mathrm{rec}}$ and $\theta_B = 180°$. Momentum distributions were probed for a positive $(+F)$ and time-reversed negative $(-F)$ force at increasing times τ_F (top to bottom) after switching on frequency sweeps $\dot{\omega}_3(t) = \mp\dot{\omega}_2(t) = \pm 2\pi \cdot 23.094\,\mathrm{MHz\,s^{-1}}$, respectively. Times are indicated by numbers in the middle column, in units of millisecond, and span a full Bloch period. As before, simulated TOF images were obtained by numerical analysis of equation (5.40) for lattice and forcing parameters as used in the experiment. Small axes in the first row indicate the local coordinate basis (e_l, e_t), where e_l points in the direction of the resulting inertial force. Black hexagons depict Brillouin zones of the comoving lattice frame, traveling in the opposite direction. In contrast to Figure 5.3, no transverse symmetry breaking in the momentum distribution is discernible, which indicates the absence of an anomalous Hall response. All images have been normalized individually to the same colormap. Experimental images depict typical single-shot absorption images after $36\,\mathrm{ms}$ time-of-flight.
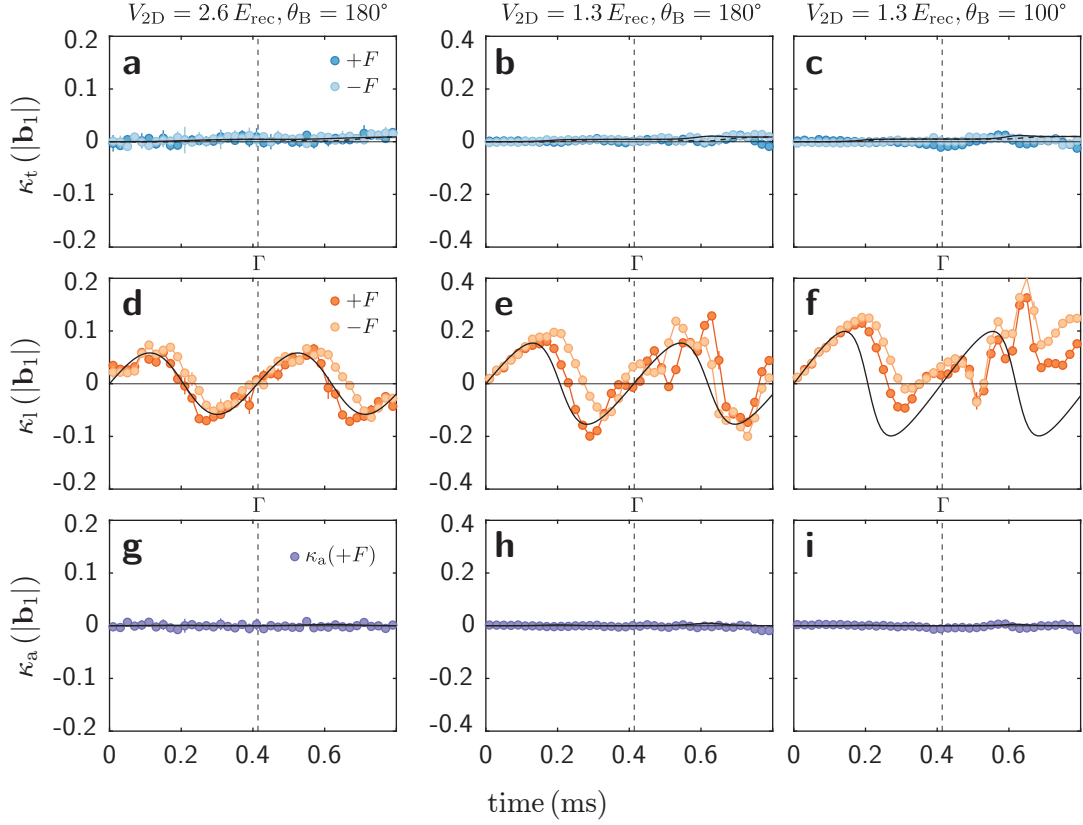
Fig. 5.6: Time evolution of the mean velocity of Bloch states in the lowest band in response to forcing ② along $\Gamma \rightarrow M \rightarrow \Gamma$: For sweep slopes $\dot{\omega}_3(t) = \mp\dot{\omega}_2(t) = \pm 2\pi \cdot 23.094\,\mathrm{MHz\,s^{-1}}$, atoms in the Zeeman substate $|1, -1\rangle$, and varying lattice configurations (left to right) as in Figure 5.4. Sweep slopes were chosen to yield a similar forcing strength $F/\hbar = 2.42\,|\mathbf{b}_1|\,\mathrm{ms^{-1}}$ as for measurements in Figure 5.4. **a-c** Dark (light) blue data points depict the measured transverse momentum $\kappa_\mathrm{t}(\pm F, t)$ for a positive (negative) force. Solid (dashed) lines show the results of the semiclassical equation (5.8). **d-f** Corresponding longitudinal momenta $\kappa_\mathrm{l}(\pm F, t)$. **g-i** Time evolution of the anomalous momentum $\kappa_\mathrm{a}(+F, t)$ as obtained from $\kappa_\mathrm{a}(+F, t) \equiv [\kappa_\mathrm{t}(+F, t) - \kappa_\mathrm{t}(-F, t)]/2$. In all plots, vertical dashed lines indicate the Bloch period for atoms in a lattice with ideal hexagonal symmetry, forced with the same strength. Plots in the left column depict the results of the measurement in Figure 5.5. Each data point is an average of 2-3 measurements, where error bars denote the standard deviations. All theory curves have been obtained for lattice and forcing parameters as used in the experiment, incorporating measured lattice asymmetries (compare Appendix A).

compared to ① while the forcing strength remains constant. Specifically, data points for the largest band gap (Figure 5.6a,d,g) are in excellent agreement with results of the semiclassical equation (5.8). With decreasing band gap, deviations become more pronounced and reflect the influence of non-adiabatic transitions into higher bands. In this context, we stress that the maximum value of $B_1(t)$ along the orbit ② amounts to $\max(B_1(t)) \approx 0.009, 0.15, 0.65$ for the three lattice configurations, respectively.

Type-3 orbit The orbits ① and ② considered so far have in common that they pass through a time-reversal symmetric point, namely Γ. For a closed orbit, this implies that the integrated anomalous Hall response is always zero. In other words, though a non-vanishing anomalous velocity may occur, as for the orbit ①, no net transport into transverse direction will arise. As outlined in subsection 5.1.2, the situation can be different for orbits that do not conform to this restriction, such as the orbit ③, which we explore in the following.

The experimental sequence we employ is essentially identical to the previous ones. Instead of atoms in the ground state, however, here we initialize atoms in the Bloch states $|2, \mathrm{K}\rangle$ and $|2, \mathrm{K}'\rangle$ of the second band, as presented in chapter 4. Forcing is applied for a duration τ_F by setting $\dot{\omega}_3(t) = \mp\dot{\omega}_2(t) = \pm 2\pi \cdot 80\,\mathrm{MHz\,s^{-1}}$. This produces the desired orbits $\mathrm{K} \to \mathrm{K}$ and $\mathrm{K}' \to \mathrm{K}'$, which get traversed in positive and negative orientation ($\pm F$) with a strength $F/\hbar = 8.39\,|\mathbf{b}_1|\,\mathrm{ms^{-1}}$. For the two independent Bloch state components we, then separately analyze the individual Hall response in the momentum distribution.

For the sake of clarity, in Figure 5.7, we present the resulting TOF images probed for different times τ_F and a positive and negative inertial force, respectively. Note that the simulated TOF images included for comparison match well, although we do not account for the thermal incoherent background. The associated time evolution of the transverse and anomalous momentum for components K and K' are displayed in Figure 5.8. We stress that the anomalous momentum can be obtained by generalizing equation (5.42) for time-reversal symmetric partner $\mathbf{q}_{1,2}$:

$$\kappa_\mathrm{a}(\pm F, t, \mathbf{q}_{1,2}) = \frac{\kappa_\mathrm{t}(\pm F, t, \mathbf{q}_{1,2}) - \kappa_\mathrm{t}(\mp F, t, \mathbf{q}_{2,1})}{2}\,, \tag{5.45}$$

from which $\kappa_\mathrm{a}(\pm F, t, \mathbf{q}_{1,2}) = -\kappa_\mathrm{a}(\mp F, t, \mathbf{q}_{2,1})$ follows. Consider now $\kappa_\mathrm{a}(+F, t, \mathrm{K})$ as shown in Figure 5.8c. Evidently, it reaches a negative minimum upon each visit of K, where a negative Berry curvature is encountered. In between, $\kappa_\mathrm{a}(+F, t, \mathrm{K})$ also acquires a small positive value, which stems from the Berry curvature distribution of K' slightly extending into the corresponding orbit ③. Nevertheless, the total integrated anomalous Hall response over one forcing cycle, i.e. for one orbit revolution, is nonzero and hence realizes geometric pumping with a net transverse current of atoms in $|2, \mathrm{K}\rangle$. For the observed time span, we find a total Hall drift $r_\mathrm{a}(\mathrm{K}) \approx -1.9(3) \times 10^{-8}\,\mathrm{m}$. The reasoning is similar for the Bloch state $|2, \mathrm{K}'\rangle$ and its anomalous momentum $\kappa_\mathrm{a}(+F, t, \mathrm{K}')$ shown in Figure 5.8d. Due to the reversed sign of the Berry curvature, however, the total Hall drift points in the opposite direction. Here, it amounts to $r_\mathrm{a}(\mathrm{K}') \approx 1.6(3) \times 10^{-8}\,\mathrm{m}$. We emphasize that larger Hall drifts can be achieved by decreasing the lattice depth or rotating the quantization axis towards the degeneracy point $\theta_\mathrm{B} = 90°$, thereby
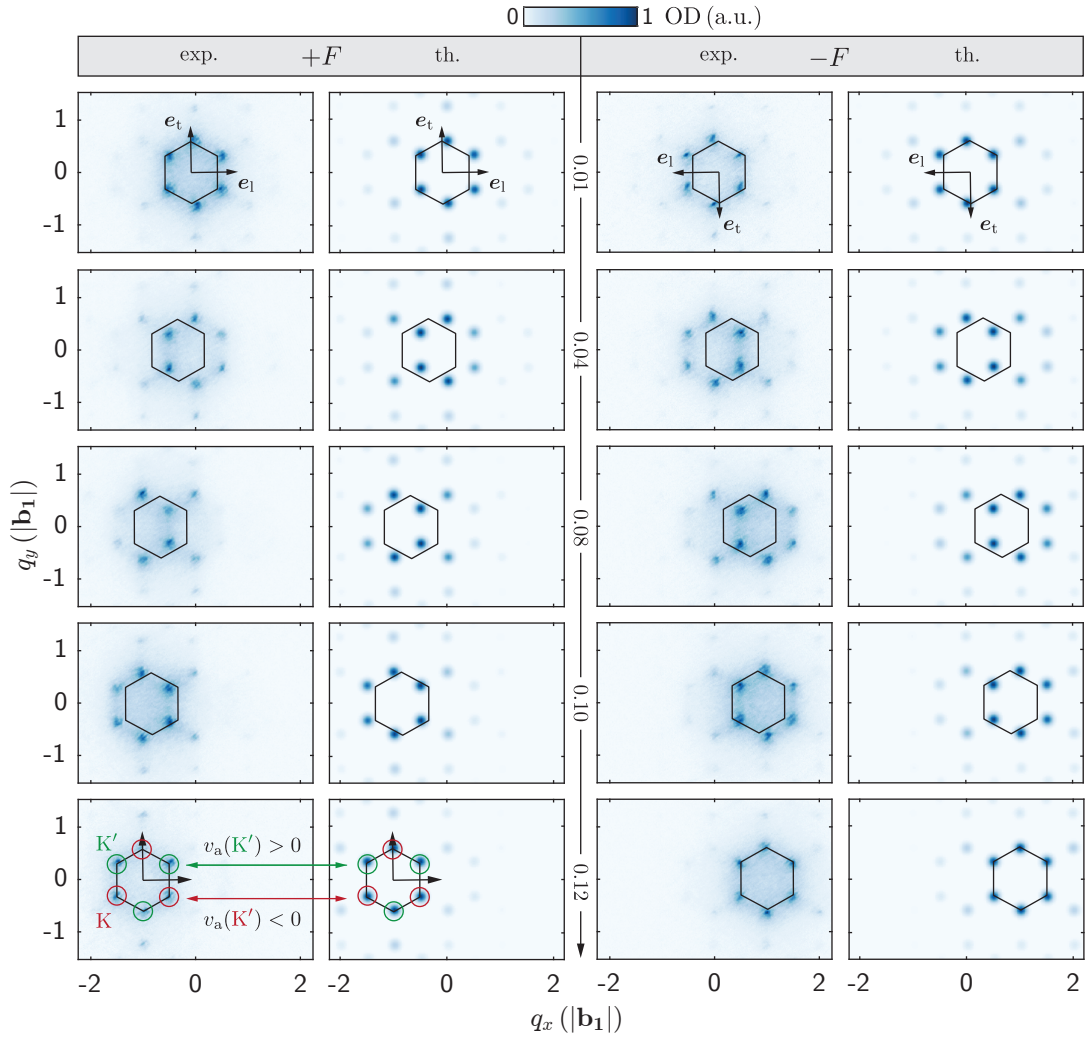
Fig. 5.7: Comparison between measured and calculated momentum distributions of Bloch states in the second band subject to forcing ③ along K → K (K′ → K′) as illustrated in Figure 5.2: For atoms in the Zeeman substate $|2, -2\rangle$, in a boron-nitride lattice with $V_{2D} = 7.5\,E_{rec}$ and $\theta_B = 74°$. Momentum distributions were probed for a positive $(+F)$ and time-reversed negative $(-F)$ force at increasing times τ_F (top to bottom) after switching on frequency sweeps $\dot{\omega}_3(t) = \mp\dot{\omega}_2(t) = \pm 2\pi \cdot 80\,\mathrm{MHz\,s^{-1}}$, respectively. Times are indicated by numbers in the middle column, in units of millisecond, and span a full Bloch period. As before, simulated TOF images were obtained by numerical analysis of equation (5.40) for lattice and forcing parameters as used in the experiment. Small axes in the first row indicate the local coordinate basis $(\boldsymbol{e}_l, \boldsymbol{e}_t)$, where $\boldsymbol{e}_l$ points in the direction of the resulting inertial force. Black hexagons depict Brillouin zones of the comoving lattice frame, traveling in the opposite direction. The anomalous velocity for each individual valley K and K′ manifests as a slight, almost imperceptive transverse imbalance among zeroth order Bragg peaks, as highlighted in the last row for a positive force. All images have been normalized individually to the same colormap. Experimental images depict typical single-shot absorption images after 36 ms time-of-flight.
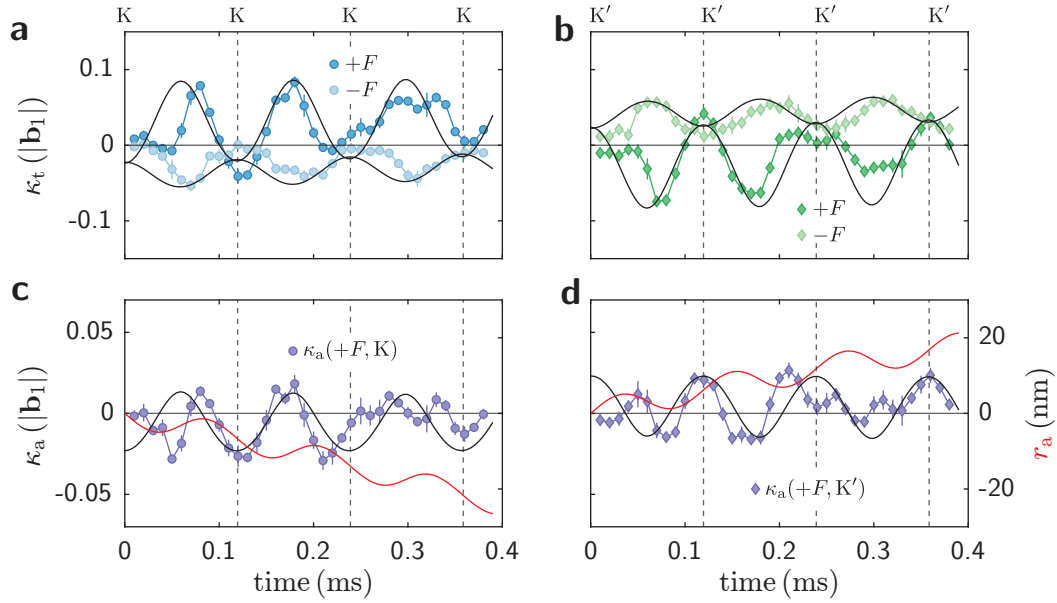
Fig. 5.8: Geometric pumping and valley Hall effect for measurements in Figure 5.7. **a** Transverse momentum $\kappa_{\mathrm{t}}(\pm F, t, \mathrm{K})$ of the Bloch state $|2, \mathrm{K}\rangle$ for a positive and time-reversed negative force. Black lines show respective momenta obtained by numerical analysis of the semiclassical equation (5.8). **b** As before, but for the Bloch state $|2, \mathrm{K}'\rangle$. **c** Time evolution of the anomalous momentum $\kappa_{\mathrm{a}}(+F, t, \mathrm{K})$ for atoms at valley K. The red line shows the expected Hall drift in real space, indicating net anomalous Hall transport after each cycle. Integration of data points yields an estimated Hall drift $r_{\mathrm{a}}(\mathrm{K}) \approx -1.9(3) \times 10^{-8}\,\mathrm{m}$. **d** As before, but for atoms at valley K', with a Hall drift $r_{\mathrm{a}}(\mathrm{K}') \approx 1.6(3) \times 10^{-8}\,\mathrm{m}$ in the opposite direction. All theory curves have been obtained for lattice and forcing parameters as used in the experiment, incorporating measured lattice asymmetries. Vertical dashed lines indicate the Bloch period for atoms in a lattice with ideal hexagonal symmetry, forced with the same strength $F/\hbar = 8.39\,|\mathbf{b}_1|\,\mathrm{ms}^{-1}$. Each data point is an average of 2-3 measurements, where error bars denote the corresponding standard deviations.

increasing the magnitude of the Berry curvature.

The observed dynamics is reminiscent of the valley Hall effect [88, 96, 97], where electrons in different valleys K or K′ experience Hall drifts in opposite directions. In particular, by introducing a population imbalance between valleys, a finite transverse net current can be realized. The same is true in our case: Perfect imbalance could be achieved, for example, by a two-step forcing protocol starting with atoms in the ground state $|1, \Gamma\rangle$ that get forced to K and then along an orbit ③ as above.

5.5 Conclusion & Outlook

In this chapter, we have investigated the anomalous Hall response of ultracold bosonic atoms in an accelerated optical boron-nitride lattice. The essential insight is that the anomalous velocity can be accurately and easily accessed from conventional time-of-flight images. In particular, we have measured the time-dependent anomalous velocity along various orbits in reciprocal space. When the force is sufficiently weak such that first-order adiabatic perturbation theory applies, the semiclassical single-band equations of motion adequately describe the observed wave-packet dynamics. In that case, it is possible to infer the value of the local Berry curvature along the forced trajectory directly from the measured Hall response. For instance, for the first and second Bloch band, we could explicitly show the localization of the Berry curvature at the K and K′ points, where it reveals equal magnitudes but opposite signs. In addition, we have demonstrated the realization of geometric pumping with bosons. In conclusion, inertial forcing combined with time-of-flight imaging is a valuable and sensitive tool for investigating the geometric properties of Bloch bands and their influence on wave-packet dynamics.

When the exerted force on atoms becomes so strong that transitions into nearby bands cannot be ignored, the semiclassical single-band equations naturally fail to reproduce the observed dynamics, as evidenced for lattice parameters that result in small band gaps. However, it is possible to generalize the equations of motion to multiple Bloch bands, entailing the appearance of non-Abelian gauge structures [263, 264]. Future experimental studies may focus on probing the associated non-Abelian wave-packet dynamics, especially in regimes that differ from the infinite-force degenerate band limit considered in the case of Wilson lines [95].

Our approach to examining the anomalous response in momentum space is entirely general and can be applied to any type of optical lattice and species, including fermionic systems. Furthermore, integrating Stern-Gerlach separation during time-of-flight allows probing spin-dependent Hall drifts, which is essential for studying systems exhibiting spin Hall phyiscs. Apart from the dynamical response to external force fields, one may likewise probe the effects of time-dependent Bloch bands, leading to geometric scalar potentials that mimic intrinsic electric fields [265]. The observed dynamics can provide complementary information about the geometry of Bloch states.

A central goal of future experimental and theoretical studies will be to understand how interactions in quantum many-body systems modify or even give rise to geometric and topological features. In fact, for interacting systems, especially strongly correlated ones, the very notion of topological characteristics and how they manifest, for example,

in the dynamical properties of quasiparticles or collective modes is far from being fully understood. While theoretical research has flourished, experimental studies in this field are still in their infancy. There is little doubt that many connections between topology and the physics of quantum many-body systems are yet to be uncovered.

A Lattice imperfections

Naturally, our experimental implementation of the boron-nitride lattice exhibits certain deviations from the ideal p-polarization configuration discussed in subsection 2.2.4. This in turn gives rise to so-called lattice imperfections, i.e. deviations from the ideal potential in equation (2.56). In particular, as a consequence of the in-plane polarization, even small differences in the mutual lattice beam angles $\Delta\phi_{ij} \equiv \angle(\boldsymbol{k}_i, \boldsymbol{k}_j) \neq 120°$ can result in strong distortions of the potential, accompanied by a deformation of the unit cell. Other sources for lattice imperfections include polarization maladjustment and intensity imbalance among the individual lattice beams.

Often, lattice imperfections will cause undesired splittings of degeneracies in the band structure, which may impede the observation of certain physical effects. Besides, lattice imperfections that remain unrecognized as such can lead to serious errors in the calibration of the lattice depth. Here, we elucidate how a potential deformation that stems from a geometrical misalignment of the lattice beams is cured by introducing an appropriate intensity imbalance. Most importantly, the band structure can be restored almost perfectly with a minimal and minor splitting of degeneracies. Our experimental approach for "restoration" makes sure that the realized lattice potential approaches the ideal boron-nitride lattice as close as possible.

First, we characterize the experimental lattice geometry, that is the angles between the lattice beams: By analyzing Kapitza-Dirac diffraction patterns we determine the set of primitive reciprocal lattice vectors $\{\mathbf{b}_1, \mathbf{b}_2, \mathbf{b}_3\}$. Next, assuming that all lattice beams lie within the imaging plane, one obtains a system of linear equations that is easily solved to yield the individual wave vectors $\boldsymbol{k}_i$. Specifically, we obtain for the corresponding polar angles ϕ_i with respect to the experimental x-axis:

$$\phi_1 = 91.1(3)°, \qquad \phi_2 = 327.7(7)°, \qquad \phi_3 = 212.2(3)° . \tag{A.1}$$

Though the assumption that the lattice beams lie in the image plane is not completely justified, the error introduced by neglecting a small out-of-plane tilting is insignificant and will have no profound influence on what follows.

In Figure A.1, we compare potentials for the ideal and actual lattice beam configurations. Evidently, if the individual beam intensities remain balanced, the experimental angles from equation (A.1) will result in a strong lattice anisotropy. By imbalancing the beam intensities as detailed in Figure A.1c, the lattice anisotropy can be cured, leaving behind only a small deformation of the unit cell (white hexagon). We stress that the unit cell itself cannot be restored in this way, since it is a pure geometrical property that depends only on the polar angles ϕ_i. Despite this, the potential form is reestablished and the band structure likewise becomes restored, as evidenced by the band gap spectrum in Figure A.1d, where the dashed black and beige lines almost perfectly coincide over the entire range of lattice depths. When this situation is reached, it is well-justified
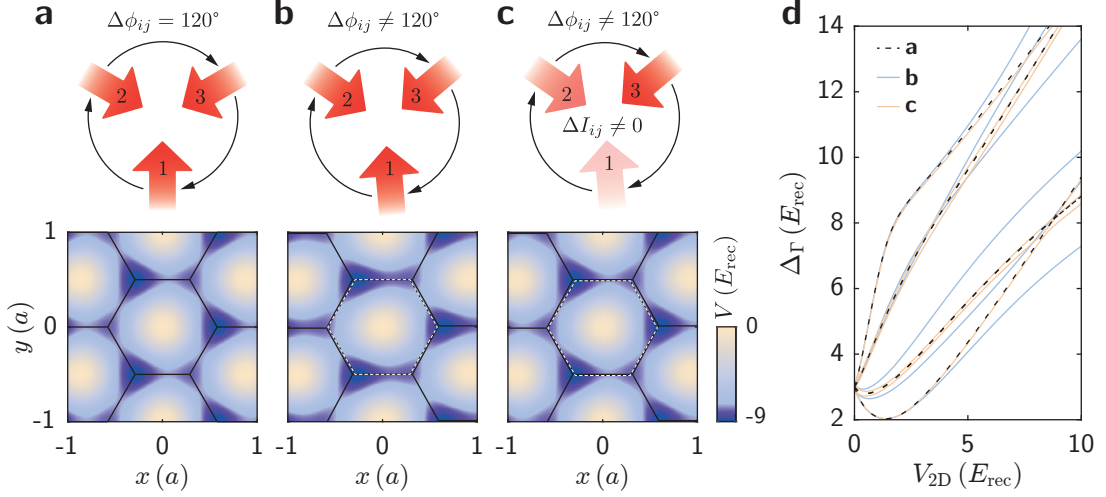
Fig. A.1: Boron-nitride potentials for different lattice beam configurations and atoms in the Zeeman substate $|1, -1\rangle$, with $\theta_B = 0°$. **a** The ideal boron-nitride potential is realized for relative beam angles $\Delta\phi_{ij} = 120°$ and balanced beam strengths $E_i = E_0$. For the sake of clarity, we set $V_{2D} = \alpha_F^s E_0^2 = 8\,E_{rec}$. **b** For $\Delta\phi_{ij} \neq 120°$ but still balanced beam strengths, the potential is strongly deformed. Here, we assume individual polar angles as realized in the experiment: $\phi_1 = 91.1°$, $\phi_2 = 327.7°$, $\phi_3 = 212.2°$. The white hexagon indicates the unit cell from **a**, revealing a slight deviation from the ideal hexagonal symmetry. **c** By imbalancing the lattice beams according to $E_1/E_3 = 0.78$, $E_2/E_3 = 0.94$, the form of the potential can be reestablished almost perfectly. However, the unit cell remains as in **b**. All potentials have been scaled to the same depth V by setting $E_3 = 0.998 E_0$ in **b**, and $E_3 = 1.10 E_0$ in **c**. **d** For each case, we plot the band gaps between the first and higher bands at the quasimomentum Γ as a function of the lattice depth $V_{2D} = \alpha_F^s E_0^2$. Note that band gaps for **a** and **c** almost perfectly coincide. Although degeneracies in **a** cannot be fully restored in **c**, the associated bands remain sufficiently close. In contrast, band gaps in **b** are strongly altered as compared to the ideal case.

to assume the validity and applicability of the ideal potential in equation (2.56) instead of reverting to the general form in equation (2.48).

Experimentally, in order to precisely set the required relative beam intensities for optimal lattice restoration, we use the fact that the locations of minima in the second Bloch band are extremely sensitive to lattice anisotropy. First, we excite a cold bosonic ensemble into the second band as explained in section 4.2. Next, we wait for a certain time to allow for condensation in the minima. The locations of observed Bragg peaks in the momentum distribution after TOF then directly reflects the locations of the minima in the second band. In particular, the observed pattern of the first order Bragg peaks will conform to the respective density distributions in Figure A.2, where we visualize the locations of minima in the second Bloch band for different exemplary lattice beam configurations. By iteratively adjusting the individual lattice beam intensities, we symmetrize the observed momentum distribution to yield an optimal hexagonal symmetry as in Figure A.2f. This approach guarantees that the realized potential resembles the one in Figure A.1c. In other words, the boron-nitride lattice becomes almost perfectly restored. We emphasize that the locations of minima in the second Bloch band will in general slightly depend on the quantization axis angle θ_B, as evidenced in Figure A.2c.
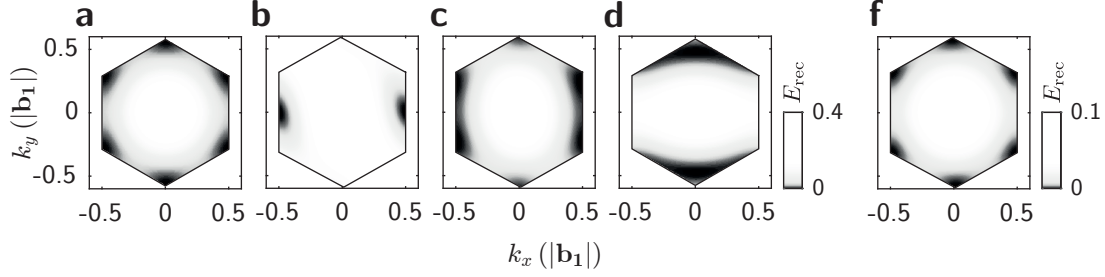
Fig. A.2: Energy spectrum $\epsilon_2(\boldsymbol{k}) - \min(\epsilon_2)$ of the second Bloch band for different lattice beam configurations of the boron-nitride potential. For the sake of clarity, we assume atoms in the Zeeman substate $|1, -1\rangle$ with lattice parameters $V_{2\mathrm{D}} = \alpha_F^s E_0^2 = 8\, E_{\mathrm{rec}}$ and $\theta_{\mathrm{B}} = 0°$. **a** Band minima (Dirac points) are located at the vertices of the hexagonal Brillouin zone for the ideal potential: $\Delta\phi_{ij} = 120°$, $E_i = E_0$. **b** For a distorted lattice with angles $\Delta\phi_{ij} \neq 120°$ as defined in Figure A.1b, the two-fold degeneracy of band minima is removed. They become localized at a single M point. **c** By imbalancing the lattice beams, the minima are moved back towards the vertices and the two-fold degeneracy is restored. Here: $E_1/E_3 = 0.78$ and $E_2/E_3 = 0.94$, as in Figure A.1c. We set $E_3 = 0.998E_0$ in **b** and $E_3 = 1.10E_0$ in **c** to arrive at the same depths as for the ideal potential. **d** For comparison, ideal potential as in **a** but for $E_1/E_0 = 0.95$. **f** As in **c** but for $\theta_{\mathrm{B}} = 126°$, revealing fully restored locations of the Dirac points.

We also note that the remaining deformation of the unit cell involves a corresponding deformation of the Brillouin zone, which is almost imperceptible here but can still be relevant for designing and engineering precise forcing protocols (compare subsection 5.2.1). Finally, we remark that we have focused on compensating the effects from a geometrical misalignment of the lattice beams. However, the same line of reasoning applies also in the presence of other lattice imperfections, such as maladjusted polarizations.

B Interaction integrals for Bloch state superpositions

Consider a general two-component Bloch state superposition $|\psi\rangle$ of the form

$$|\psi\rangle = \cos(\theta)\,|n\boldsymbol{k}\rangle + \exp(\mathrm{i}\phi)\sin(\theta)\,|m\boldsymbol{l}\rangle\,, \tag{B.1}$$

where $|n\boldsymbol{k}\rangle$, $|m\boldsymbol{l}\rangle$ denote two arbitrary Bloch states of the underlying lattice potential, with band indices m, n and quasimomenta $\boldsymbol{k}, \boldsymbol{l}$. Specifically, $\theta \in [0, \pi/2)$ determines their relative weight, while $\phi \in [-\pi, \pi)$ defines their relative phase. We are interested in the related interaction parameter

$$U(\theta, \phi) \equiv gV \int \mathrm{d}\boldsymbol{r}\,|\langle \boldsymbol{r}|\psi\rangle|^4\,, \quad \text{with} \quad g = 4\pi\hbar^2 a_s/m. \tag{B.2}$$

Here, V denotes the system volume and g characterizes the contact interaction strength, which depends on the s-wave scattering length a_s. The integral in equation (B.2) should be evaluated with respect to the torus topology imposed by the periodic boundary conditions as discussed in subsection 3.1.2. For convenience, we treat the case of equal quasimomenta ($\boldsymbol{l} = \boldsymbol{k}$) and distinct quasimomenta ($\boldsymbol{l} \neq \boldsymbol{k}$) separately.

Case 1: $\boldsymbol{l} = \boldsymbol{k}$ By expanding the Bloch states according to

$$|n\boldsymbol{k}\rangle = e^{\mathrm{i}\boldsymbol{k}\hat{\boldsymbol{r}}}\,|u_{n\boldsymbol{k}}\rangle = e^{\mathrm{i}\boldsymbol{k}\hat{\boldsymbol{r}}}\sum_{\mathbf{G}}c_{n\boldsymbol{k}}(\mathbf{G})\,|\mathbf{G}\rangle = \sum_{\mathbf{G}}c_{n\boldsymbol{k}}(\mathbf{G})\,|\mathbf{G}+\boldsymbol{k}\rangle\,, \tag{B.3}$$

where the sum is over all reciprocal lattice vectors $\mathbf{G}$, it immediately follows that an equal-quasimomentum superposition state can be written as

$$|\psi_1\rangle = \sum_{\mathbf{G}}s_{\boldsymbol{k}}(\mathbf{G})\,|\mathbf{G}+\boldsymbol{k}\rangle\,, \tag{B.4}$$

where we employ the definition

$$s_{\boldsymbol{k}}(\mathbf{G}) \equiv \cos(\theta)c_{n\boldsymbol{k}}(\mathbf{G}) + \exp(\mathrm{i}\phi)\sin(\theta)c_{m\boldsymbol{k}}(\mathbf{G})\,. \tag{B.5}$$

For the related interaction parameter U_1, we then obtain

$$U_1(\theta, \phi) = gV \int \mathrm{d}\boldsymbol{r}\,|\langle \boldsymbol{r}|\psi_1\rangle|^4 = g\sum_{\mathbf{J}}S(\mathbf{J})S^*(\mathbf{J}),$$

$$S(\mathbf{J}) \equiv \sum_{\mathbf{G}}s_{\boldsymbol{k}}(\mathbf{G}+\mathbf{J})s_{\boldsymbol{k}}^*(\mathbf{G}). \tag{B.6}$$

B Interaction integrals for Bloch state superpositions

Here, the sum is over all reciprocal lattice vectors $\mathbf{G}$ and $\mathbf{J}$. Given the expansion coefficients $\{c_{nk}(\mathbf{G})\}$ and $\{c_{ml}(\mathbf{G})\}$ for the two Bloch states, we can easily evaluate these expressions numerically for different mixing angles θ and ϕ, as done for Figure 4.10b.

Case 2: $l \neq k$ We now focus on Bloch states that have distinct quasimomenta. In this case, the associated superposition state $|\psi_2\rangle$ cannot be written as in equation (B.4). To proceed, we note that the related interaction parameter U_2 naturally splits into six terms:

$$U_2(\theta, \phi) = gV \int \mathrm{d}\boldsymbol{r} \; |\langle \boldsymbol{r} | \psi_2 \rangle|^4 = g \sum_{i=1}^{6} M_i \,, \tag{B.7}$$

where we use the following abbreviations:

$$M_1 = \cos^4(\theta) V \int \mathrm{d}\boldsymbol{r} \; [u_{nk}^*(\boldsymbol{r}) u_{nk}(\boldsymbol{r})]^2 \,, \tag{B.8}$$

$$M_2 = \sin^4(\theta) V \int \mathrm{d}\boldsymbol{r} \; [u_{ml}^*(\boldsymbol{r}) u_{ml}(\boldsymbol{r})]^2 \,, \tag{B.9}$$

$$M_3 = 4 \cos^2(\theta) \sin^2(\theta) V \int \mathrm{d}\boldsymbol{r} \, u_{nk}^*(\boldsymbol{r}) u_{nk}(\boldsymbol{r}) u_{ml}^*(\boldsymbol{r}) u_{ml}(\boldsymbol{r}), \tag{B.10}$$

$$M_4 = 4 \cos^3(\theta) \sin(\theta) V \int \mathrm{d}\boldsymbol{r} \, u_{nk}^*(\boldsymbol{r}) u_{nk}(\boldsymbol{r}) \mathrm{Re} \left(e^{\mathrm{i}\phi} u_{nk}^*(\boldsymbol{r}) u_{ml}(\boldsymbol{r}) e^{\mathrm{i}(l-k)r} \right), \tag{B.11}$$

$$M_5 = 4 \sin^3(\theta) \cos(\theta) V \int \mathrm{d}\boldsymbol{r} \, u_{ml}^*(\boldsymbol{r}) u_{ml}(\boldsymbol{r}) \, \mathrm{Re} \left(e^{\mathrm{i}\phi} u_{nk}^*(\boldsymbol{r}) u_{ml}(\boldsymbol{r}) e^{\mathrm{i}(l-k)r} \right), \tag{B.12}$$

$$M_6 = 2 \cos^2(\theta) \sin^2(\theta) V \int \mathrm{d}\boldsymbol{r} \, \mathrm{Re} \left(e^{2\mathrm{i}\phi} u_{nk}^*(\boldsymbol{r}) u_{nk}^*(\boldsymbol{r}) u_{ml}(\boldsymbol{r}) u_{ml}(\boldsymbol{r}) e^{2\mathrm{i}(l-k)r} \right). \tag{B.13}$$

Here, the functions $u_{nk}(\boldsymbol{r})$ denote the lattice-periodic Bloch mode functions

$$u_{nk}(\boldsymbol{r}) = \langle \boldsymbol{r} | u_{nk} \rangle = \frac{1}{\sqrt{V}} \sum_{\mathbf{G}} c_{nk}(\mathbf{G}) e^{\mathrm{i}\mathbf{G}\boldsymbol{r}} \,. \tag{B.14}$$

Note that the integrals M_i are all unitless. After a few lines of algebra, one obtains the following expressions for M_1, M_2, and M_3:

$$M_1 = \cos^4(\theta) \sum_{\mathbf{J}} C_{nk}(\mathbf{J}) C_{nk}^*(\mathbf{J}), \quad M_2 = \sin^4(\theta) \sum_{\mathbf{J}} C_{ml}(\mathbf{J}) C_{ml}^*(\mathbf{J}),$$
$$M_3 = 4 \cos^2(\theta) \sin^2(\theta) \sum_{\mathbf{J}} C_{nk}(\mathbf{J}) C_{ml}^*(\mathbf{J}) \,, \tag{B.15}$$

with the short notation

$$C_{nk}(\mathbf{J}) \equiv \sum_{\mathbf{G}} c_{nk}(\mathbf{G} + \mathbf{J}) c_{nk}^*(\mathbf{G}). \tag{B.16}$$

We stress that M_1, M_2, and M_3 are all independent of the relative phase ϕ. As regards the integrals M_4 and M_5, one may show that they always vanish, as a result of the periodicity of Bloch mode functions and the periodic boundary conditions, unless $(\boldsymbol{l} - \boldsymbol{k})$ is equal to some reciprocal lattice vector $\mathbf{P} \in \mathcal{G}_{\mathrm{B}}$. The latter would imply, however, that $(\boldsymbol{l} - \boldsymbol{k}) \sim \Gamma$, which contradicts our assumption that $\boldsymbol{l}$ and $\boldsymbol{k}$ are distinct. Thus, we
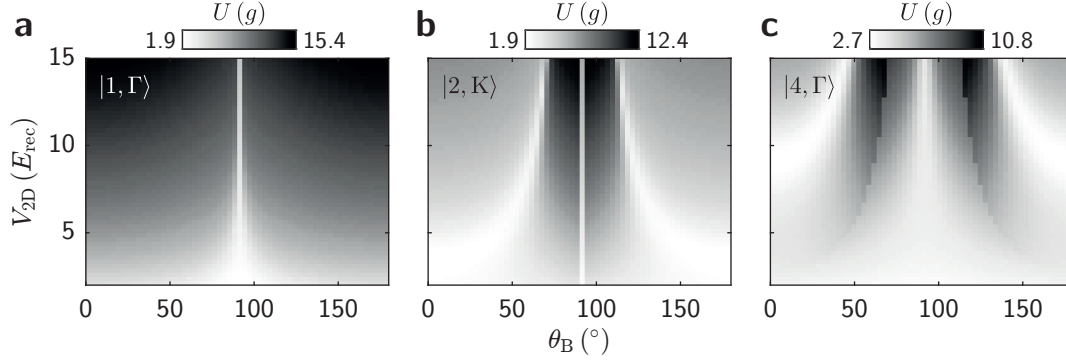
Fig. B.1: Interaction parameters U in the boron-nitride lattice as a function of the lattice depth V_{2D} and quantization axis angle θ_B. **a** For the lowest energy Bloch state $|1, \Gamma\rangle$, corresponding to the superfluid ground state in an optical lattice. **b** For the state $|2, K\rangle$, equivalent to a chiral condensate in the second band. **c** For the Bloch state $|4, \Gamma\rangle$, corresponding to a condensate in the fourth band.

have

$$M_4 = M_5 = 0 \,. \tag{B.17}$$

Meanwhile, a similar argument applies to the last integral M_6, which will vanish if $2(\boldsymbol{l} - \boldsymbol{k}) \neq \mathbf{P} \in \mathcal{G}_B$. For example, this is the case for a superposition of Bloch states with quasimomenta $\boldsymbol{k} = \mathrm{K}$ and $\boldsymbol{l} = \mathrm{K}'$, as examined in chapter 4. Clearly, $2(\mathrm{K}' - \mathrm{K}) = \mathrm{K}' \nsim \Gamma$. We stress, however, that non-trivial solutions to $2(\boldsymbol{l} - \boldsymbol{k}) = \mathbf{P} \in \mathcal{G}_B$ exist, which are characterized by $\boldsymbol{l} \nsim \boldsymbol{k}$. Up to a reciprocal lattice vector, these are given by $(\boldsymbol{l} - \boldsymbol{k}) \in \{\mathbf{b}_1/2, \mathbf{b}_2/2, (\mathbf{b}_1 + \mathbf{b}_2)/2\}$, where the $\mathbf{b}_i$ denote the reciprocal (primitive) basis vectors. In any case, if $2(\boldsymbol{l} - \boldsymbol{k}) = \mathbf{P} \in \mathcal{G}_B$, we find

$$M_6 = \cos^2(\theta)\sin^2(\theta)e^{2\mathrm{i}\phi} \sum_{\mathbf{J}} D_{n\boldsymbol{k}}^*(\mathbf{J}) F_{ml}(\mathbf{J}; \mathbf{P}) + \mathrm{c.c.} \,, \tag{B.18}$$

where we make use of the following definitions:

$$D_{n\boldsymbol{k}}(\mathbf{J}) \equiv \sum_{\mathbf{G}} c_{n\boldsymbol{k}}(\mathbf{J} + \mathbf{G})c_{n\boldsymbol{k}}(-\mathbf{G}), \quad F_{ml}(\mathbf{J}; \mathbf{P}) \equiv \sum_{\mathbf{G}} c_{ml}(\mathbf{J} + \mathbf{G} - \mathbf{P})c_{ml}(-\mathbf{G}). \tag{B.19}$$

As before, given the expansion coefficients $\{c_{n\boldsymbol{k}}(\mathbf{G})\}$ and $\{c_{ml}(\mathbf{G})\}$ for the two Bloch states, we can easily evaluate expressions M_1, M_2, M_3, and M_6 numerically for different mixing angles θ and ϕ. For illustration, in Figure B.1, we show exemplary plots of the interaction parameter U in the boron-nitride lattice as a function of the lattice depth V_{2D} and quantization axis angle θ_B for three different Bloch states.

The term $U(\theta, \phi)$ is also often denoted as g_{1D}^{eff} in the context of two-dimensional lattices. Besides, for a homogenous system with uniform extension L along the direction perpendicular to the lattice plane, one may define a Hubbard-like interaction energy U_H according to

$$U_H \equiv \frac{U(\theta, \phi)}{vL} \,. \tag{B.20}$$

Here, v denotes the surface volume of a primitive unit cell. For example, for the Bloch

state $|1, \Gamma\rangle$ of our boron-nitride lattice in case of a lattice depth $V_{\mathrm{2D}} = 8\,E_{\mathrm{rec}}$, atoms in the Zeeman substate $|2, -2\rangle$, and an estimated longitudinal extension $L_z \approx 2 \times 20\,\mu\mathrm{m}$, we obtain $U_{\mathrm{H}} \approx 8.5\,\mathrm{Hz}$ for the choice $\theta_{\mathrm{B}} = 0°$. In contrast, we have $U_{\mathrm{H}} \approx 3.1\,\mathrm{Hz}$ for the choice $\theta_{\mathrm{B}} = 90°$. For comparison, the corresponding bandwidths of the lowest band amount to $\Delta_1 \approx 0.3\,\mathrm{Hz}$ and $\Delta_1 \approx 750\,\mathrm{Hz}$, respectively, indicating that Bragg peak visibility should vanish in the former case, whereas it should still be finite for $\theta_{\mathrm{B}} = 90°$. Experimentally, this is indeed confirmed.

C Extracting condensate fractions

We obtain estimates for the condensate fractions in the second and fourth band from band mapping images via a ring-mask method as explained in the following.

Given the respective masks for the n-th Brillouin zone (BZ_n), inner circles (ic), and outer circles (oc) as defined in Figure C.1, we first construct the ring mask according to $\mathcal{R} \equiv \text{oc} \setminus \text{ic}$. We note that the size of the inner circles is chosen such that they fully comprise the support region of the condensate. Next, we define individual ring segments $\mathcal{R}_n \equiv \mathcal{R} \cap BZ_n$ and inner circle segments $\text{ic}_n \equiv \text{ic} \cap BZ_n$. By construction, $\mathcal{R}_n$ is populated only by thermal atoms of the n-th Brillouin zone. We directly count this population and obtain the number $N(\mathcal{R}_n)$. We now estimate the number of thermal atoms that belong to BZ_n and lie in the inner circles via

$$N_{\text{th}}(\text{ic}_n) = \frac{N(\mathcal{R}_n)}{|\mathcal{R}_n|}|\text{ic}_n|. \tag{C.1}$$

Here, the vertical bars refer to the size of the corresponding masks. The number of condensed atoms N_{c} is then simply defined as the total number of atoms in the inner circles minus the number of thermal atoms in the inner circles:

$$N_{\text{c}} \equiv N(\text{ic}) - \sum_n N_{\text{th}}(\text{ic}_n). \tag{C.2}$$

Moreover, we determine the number of thermal atoms in the n-th Brillouin zone according to

$$N_{\text{th}}(BZ_n) = N(BZ_n \setminus \text{ic}) + N_{\text{th}}(\text{ic}_n). \tag{C.3}$$

Finally, condensate fractions and respective thermal fractions are obtained through division by the total number of atoms N in the entire band mapping image.
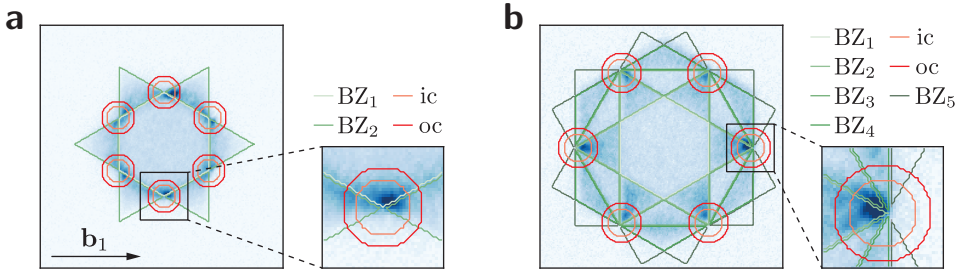
Fig. C.1: Masks for estimating condensate fractions from band mapping (BM) images. **a** For a condensate in the second band, where inner circle (ic) and outer circle (oc) masks are centered at the zeroth order K and K′ points. **b** For a condensate in the fourth band, where ic and oc masks are centered at the six first order Γ points.

Bibliography

[1] M. H. Anderson, J. R. Ensher, M. R. Matthews, C. E. Wieman, and E. A. Cornell, "Observation of Bose-Einstein Condensation in a Dilute Atomic Vapor", Science **269**, 198–201 (1995).

[2] C. C. Bradley, C. A. Sackett, J. J. Tollett, and R. G. Hulet, "Evidence of Bose-Einstein Condensation in an Atomic Gas with Attractive Interactions", Physical Review Letters **75**, 1687–1690 (1995).

[3] K. B. Davis, M. O. Mewes, M. R. Andrews, N. J. van Druten, D. S. Durfee, D. M. Kurn, and W. Ketterle, "Bose-Einstein Condensation in a Gas of Sodium Atoms", Physical Review Letters **75**, 3969–3973 (1995).

[4] B. DeMarco and D. S. Jin, "Onset of Fermi Degeneracy in a Trapped Atomic Gas", Science **285**, 1703–1706 (1999).

[5] M. W. Zwierlein, C. A. Stan, C. H. Schunck, S. M. F. Raupach, S. Gupta, Z. Hadzibabic, and W. Ketterle, "Observation of Bose-Einstein Condensation of Molecules", Physical Review Letters **91**, 250401 (2003).

[6] T. Bourdel, L. Khaykovich, J. Cubizolles, J. Zhang, F. Chevy, M. Teichmann, L. Tarruell, S. J. J. M. F. Kokkelmans, and C. Salomon, "Experimental Study of the BEC-BCS Crossover Region in Lithium 6", Physical Review Letters **93**, 050401 (2004).

[7] W. Zwerger, ed., *The BCS-BEC Crossover and the Unitary Fermi Gas*, Vol. 836, Lecture Notes in Physics (Springer Berlin Heidelberg, Berlin, Heidelberg, 2012).

[8] T. Kraemer, M. Mark, P. Waldburger, J. G. Danzl, C. Chin, B. Engeser, A. D. Lange, K. Pilch, A. Jaakkola, H.-C. Nägerl, and R. Grimm, "Evidence for Efimov quantum states in an ultracold gas of caesium atoms", Nature **440**, 315–318 (2006).

[9] S. E. Pollack, D. Dries, and R. G. Hulet, "Universality in Three- and Four-Body Bound States of Ultracold Atoms", Science **326**, 1683–1685 (2009).

[10] M. Zaccanti, B. Deissler, C. D'Errico, M. Fattori, M. Jona-Lasinio, S. Müller, G. Roati, M. Inguscio, and G. Modugno, "Observation of an Efimov spectrum in an atomic system", Nature Physics **5**, 586–591 (2009).

[11] S. Knoop, F. Ferlaino, M. Mark, M. Berninger, H. Schöbel, H.-C. Nägerl, and R. Grimm, "Observation of an Efimov-like trimer resonance in ultracold atom–dimer scattering", Nature Physics **5**, 227–230 (2009).

[12] Z. Hadzibabic, P. Krüger, M. Cheneau, B. Battelier, and J. Dalibard, "Berezinskii–Kosterlitz–Thouless crossover in a trapped atomic gas", Nature **441**, 1118–1121 (2006).

[13] V. Schweikhard, S. Tung, and E. A. Cornell, "Vortex Proliferation in the Berezinskii-Kosterlitz-Thouless Regime on a Two-Dimensional Lattice of Bose-Einstein Condensates", Physical Review Letters **99**, 030401 (2007).

[14] C.-L. Hung, X. Zhang, N. Gemelke, and C. Chin, "Observation of scale invariance and universality in two-dimensional Bose gases", Nature **470**, 236–239 (2011).

[15] J.-y. Choi, S. W. Seo, and Y.-i. Shin, "Observation of Thermally Activated Vortex Pairs in a Quasi-2D Bose Gas", Physical Review Letters **110**, 175302 (2013).

[16] P. A. Murthy, I. Boettcher, L. Bayha, M. Holzmann, D. Kedar, M. Neidig, M. G. Ries, A. N. Wenz, G. Zürn, and S. Jochim, "Observation of the Berezinskii-Kosterlitz-Thouless Phase Transition in an Ultracold Fermi Gas", Physical Review Letters **115**, 010401 (2015).

[17] T. Langen, R. Geiger, M. Kuhnert, B. Rauer, and J. Schmiedmayer, "Local emergence of thermal correlations in an isolated quantum many-body system", Nature Physics **9**, 640–643 (2013).

[18] T. Langen, S. Erne, R. Geiger, B. Rauer, T. Schweigler, M. Kuhnert, W. Rohringer, I. E. Mazets, T. Gasenzer, and J. Schmiedmayer, "Experimental observation of a generalized Gibbs ensemble", Science **348**, 207–211 (2015).

[19] A. M. Kaufman, M. E. Tai, A. Lukin, M. Rispoli, R. Schittko, P. M. Preiss, and M. Greiner, "Quantum thermalization through entanglement in an isolated many-body system", Science **353**, 794–800 (2016).

[20] T. Langen, R. Geiger, and J. Schmiedmayer, "Ultracold Atoms Out of Equilibrium", Annual Review of Condensed Matter Physics **6**, 201–217 (2015).

[21] M. Schreiber, S. S. Hodgman, P. Bordia, H. P. Lüschen, M. H. Fischer, R. Vosk, E. Altman, U. Schneider, and I. Bloch, "Observation of many-body localization of interacting fermions in a quasirandom optical lattice", Science **349**, 842–845 (2015).

[22] J.-y. Choi, S. Hild, J. Zeiher, P. Schauß, A. Rubio-Abadal, T. Yefsah, V. Khemani, D. A. Huse, I. Bloch, and C. Gross, "Exploring the many-body localization transition in two dimensions", Science **352**, 1547–1552 (2016).

[23] D. A. Abanin and Z. Papić, "Recent progress in many-body localization", Annalen der Physik **529**, 1700169 (2017).

[24] C. Chin, R. Grimm, P. Julienne, and E. Tiesinga, "Feshbach resonances in ultracold gases", Reviews of Modern Physics **82**, 1225–1286 (2010).

[25] C. J. Vale and M. Zwierlein, "Spectroscopic probes of quantum gases", Nature Physics **17**, 1305–1315 (2021).

[26] C. Gross and W. S. Bakr, "Quantum gas microscopy for single atom and spin detection", Nature Physics **17**, 1316–1323 (2021).

[27] M. Stecker, H. Schefzyk, J. Fortágh, and A. Günther, "A high resolution ion microscope for cold atoms", New Journal of Physics **19**, 043020 (2017).

[28] C. Veit, N. Zuber, O. A. Herrera-Sancho, V. S. V. Anasuri, T. Schmid, F. Meinert, R. Löw, and T. Pfau, "Pulsed Ion Microscope to Probe Quantum Gases", Physical Review X **11**, 011036 (2021).

[29] R. P. Feynman, "Simulating physics with computers", International Journal of Theoretical Physics **21**, 467–488 (1982).

[30]I. M. Georgescu, S. Ashhab, and F. Nori, "Quantum simulation", Reviews of Modern Physics **86**, 153–185 (2014).

[31]E. Altman, K. R. Brown, G. Carleo, L. D. Carr, E. Demler, C. Chin, B. DeMarco, S. E. Economou, M. A. Eriksson, K.-M. C. Fu, M. Greiner, K. R. Hazzard, R. G. Hulet, A. J. Kollár, B. L. Lev, M. D. Lukin, R. Ma, X. Mi, S. Misra, C. Monroe, K. Murch, Z. Nazario, K.-K. Ni, A. C. Potter, P. Roushan, M. Saffman, M. Schleier-Smith, I. Siddiqi, R. Simmonds, M. Singh, I. Spielman, K. Temme, D. S. Weiss, J. Vučković, V. Vuletić, J. Ye, and M. Zwierlein, "Quantum Simulators: Architectures and Opportunities", PRX Quantum **2**, 017003 (2021).

[32]M. Lewenstein, A. Sanpera, and V. Ahufinger, *Ultracold Atoms in Optical Lattices* (Oxford University Press, Mar. 2012).

[33]C. Gross and I. Bloch, "Quantum simulations with ultracold atoms in optical lattices", Science **357**, 995–1001 (2017).

[34]F. Schäfer, T. Fukuhara, S. Sugawa, Y. Takasu, and Y. Takahashi, "Tools for quantum simulation with ultracold atoms in optical lattices", Nature Reviews Physics **2**, 411–425 (2020).

[35]D. Jaksch, C. Bruder, J. I. Cirac, C. W. Gardiner, and P. Zoller, "Cold Bosonic Atoms in Optical Lattices", Physical Review Letters **81**, 3108–3111 (1998).

[36]T. Stöferle, H. Moritz, C. Schori, M. Köhl, and T. Esslinger, "Transition from a Strongly Interacting 1D Superfluid to a Mott Insulator", Physical Review Letters **92**, 130403 (2004).

[37]I. Spielman, W. Phillips, and J. Porto, "Mott-Insulator Transition in a Two-Dimensional Atomic Bose Gas", Physical Review Letters **98**, 080404 (2007).

[38]C. Becker, P. Soltan-Panahi, J. Kronjäger, S. Dörscher, K. Bongs, and K. Sengstock, "Ultracold quantum gases in triangular optical lattices", New Journal of Physics **12**, 065025 (2010).

[39]P. Soltan-Panahi, J. Struck, P. Hauke, A. Bick, W. Plenkers, G. Meineke, C. Becker, P. Windpassinger, M. Lewenstein, and K. Sengstock, "Multi-component quantum gases in spin-dependent hexagonal lattices", Nature Physics **7**, 434–440 (2011).

[40]R. Jördens, N. Strohmaier, K. Günter, H. Moritz, and T. Esslinger, "A Mott insulator of fermionic atoms in an optical lattice", Nature **455**, 204–207 (2008).

[41]U. Schneider, L. Hackermüller, S. Will, T. Best, I. Bloch, T. A. Costi, R. W. Helmes, D. Rasch, and A. Rosch, "Metallic and Insulating Phases of Repulsively Interacting Fermions in a 3D Optical Lattice", Science **322**, 1520–1525 (2008).

[42]T. Volz, N. Syassen, D. M. Bauer, E. Hansis, S. Dürr, and G. Rempe, "Preparation of a quantum state with one molecule at each site of an optical lattice", Nature Physics **2**, 692–695 (2006).

[43]A. Mazurenko, C. S. Chiu, G. Ji, M. F. Parsons, M. Kanász-Nagy, R. Schmidt, F. Grusdt, E. Demler, D. Greif, and M. Greiner, "A cold-atom Fermi–Hubbard antiferromagnet", Nature **545**, 462–466 (2017).

[44] G. Salomon, J. Koepsell, J. Vijayan, T. A. Hilker, J. Nespolo, L. Pollet, I. Bloch, and C. Gross, "Direct observation of incommensurate magnetism in Hubbard chains", Nature **565**, 56–60 (2019).

[45] P. A. Lee, N. Nagaosa, and X.-G. Wen, "Doping a Mott insulator: Physics of high-temperature superconductivity", Reviews of Modern Physics **78**, 17–85 (2006).

[46] K. L. Hur and T. Maurice Rice, "Superconductivity close to the Mott state: From condensed-matter systems to superfluidity in optical lattices", Annals of Physics **324**, 1452–1515 (2009).

[47] C. Weitenberg and J. Simonet, "Tailoring quantum gases by Floquet engineering", Nature Physics, `10.1038/s41567-021-01316-x` (2021).

[48] J. Dalibard, F. Gerbier, G. Juzeliūnas, and P. Öhberg, "Colloquium : Artificial gauge potentials for neutral atoms", Reviews of Modern Physics **83**, 1523–1543 (2011).

[49] N. Goldman, G. Juzeliūnas, P. Öhberg, and I. B. Spielman, "Light-induced gauge fields for ultracold atoms", Reports on Progress in Physics **77**, 126401 (2014).

[50] J. Struck, C. Ölschläger, R. Le Targat, P. Soltan-Panahi, A. Eckardt, M. Lewenstein, P. Windpassinger, and K. Sengstock, "Quantum Simulation of Frustrated Classical Magnetism in Triangular Optical Lattices", Science **333**, 996–999 (2011).

[51] J. Struck, M. Weinberg, C. Ölschläger, P. Windpassinger, J. Simonet, K. Sengstock, R. Höppner, P. Hauke, A. Eckardt, M. Lewenstein, and L. Mathey, "Engineering Ising-XY spin-models in a triangular lattice using tunable artificial gauge fields", Nature Physics **9**, 738–743 (2013).

[52] M. Aidelsburger, M. Atala, M. Lohse, J. T. Barreiro, B. Paredes, and I. Bloch, "Realization of the Hofstadter Hamiltonian with Ultracold Atoms in Optical Lattices", Physical Review Letters **111**, 185301 (2013).

[53] H. Miyake, G. A. Siviloglou, C. J. Kennedy, W. C. Burton, and W. Ketterle, "Realizing the Harper Hamiltonian with Laser-Assisted Tunneling in Optical Lattices", Physical Review Letters **111**, 185302 (2013).

[54] M. Aidelsburger, M. Lohse, C. Schweizer, M. Atala, J. T. Barreiro, S. Nascimbène, N. R. Cooper, I. Bloch, and N. Goldman, "Measuring the Chern number of Hofstadter bands with ultracold bosonic atoms", Nature Physics **11**, 162–166 (2015).

[55] C. J. Kennedy, W. C. Burton, W. C. Chung, and W. Ketterle, "Observation of Bose–Einstein condensation in a strong synthetic magnetic field", Nature Physics **11**, 859–864 (2015).

[56] G. Jotzu, M. Messer, R. Desbuquois, M. Lebrat, T. Uehlinger, D. Greif, and T. Esslinger, "Experimental realization of the topological Haldane model with ultracold fermions", Nature **515**, 237–240 (2014).

[57] K. Wintersperger, C. Braun, F. N. Ünal, A. Eckardt, M. D. Liberto, N. Goldman, I. Bloch, and M. Aidelsburger, "Realization of an anomalous Floquet topological system with ultracold atoms", Nature Physics **16**, 1058–1063 (2020).

[58] C. Booker, B. Buča, and D. Jaksch, "Non-stationarity and dissipative time crystals: spectral properties and finite-size effects", New Journal of Physics **22**, 085007 (2020).

[59]K. Sacha and J. Zakrzewski, "Time crystals: a review", Reports on Progress in Physics **81**, 016401 (2018).

[60]A. Celi, P. Massignan, J. Ruseckas, N. Goldman, I. B. Spielman, G. Juzeliūnas, and M. Lewenstein, "Synthetic Gauge Fields in Synthetic Dimensions", Physical Review Letters **112**, 043001 (2014).

[61]H. M. Price, O. Zilberberg, T. Ozawa, I. Carusotto, and N. Goldman, "Four-Dimensional Quantum Hall Effect with Ultracold Atoms", Physical Review Letters **115**, 195303 (2015).

[62]T. Ozawa and H. M. Price, "Topological quantum matter in synthetic dimensions", Nature Reviews Physics **1**, 349–357 (2019).

[63]N. R. Cooper, "Optical Flux Lattices for Ultracold Atomic Gases", Physical Review Letters **106**, 175301 (2011).

[64]A. Sterdyniak, B. A. Bernevig, N. R. Cooper, and N. Regnault, "Interacting bosons in topological optical flux lattices", Physical Review B **91**, 035115 (2015).

[65]Y. Tokura and N. Nagaosa, "Orbital physics in transition-metal oxides", Science **288**, 462–468 (2000).

[66]M. Lewenstein and W. V. Liu, "Orbital dance", Nature Physics **7**, 101–103 (2011).

[67]O. Dutta, M. Gajda, P. Hauke, M. Lewenstein, D.-S. Lühmann, B. A. Malomed, T. Sowiński, and J. Zakrzewski, "Non-standard Hubbard models in optical lattices: a review", Reports on Progress in Physics **78**, 066001 (2015).

[68]C. Wu, "Unconventional Bose-Einstein condensation beyond the no-node theorem", Modern Physics Letters B **23**, 1–24 (2009).

[69]C. Wu, W. V. Liu, J. Moore, and S. D. Sarma, "Quantum stripe ordering in optical lattices", Physical Review Letters **97**, 3–6 (2006).

[70]W. V. Liu and C. Wu, "Atomic matter of nonzero-momentum Bose-Einstein condensation and orbital current order", Physical Review A - Atomic, Molecular, and Optical Physics **74**, 1–10 (2006).

[71]A. B. Kuklov, "Unconventional strongly interacting Bose-Einstein condensates in optical lattices", Physical Review Letters **97**, 1–4 (2006).

[72]S. Lieu, A. F. Ho, D. K. K. Lee, and P. Coleman, "Intertwined superfluidity and density wave order in a p-orbital Bose condensate", Physical Review B **99**, 014504 (2019).

[73]Z. F. Xu, L. You, A. Hemmerich, and W. V. Liu, "π-Flux Dirac Bosons and Topological Edge Excitations in a Bosonic Chiral p-Wave Superfluid", Physical Review Letters **117**, 1–11 (2016).

[74]M. Di Liberto, A. Hemmerich, and C. Morais Smith, "Topological Varma Superfluid in Optical Lattices", Physical Review Letters **117**, 163001 (2016).

[75]G.-Q. Luo, A. Hemmerich, and Z.-F. Xu, "Bosonic topological excitations from the instability of a quadratic band crossing", Physical Review A **98**, 053617 (2018).

[76]X. Li and W. V. Liu, "Physics of higher orbital bands in optical lattices: a review", Reports on Progress in Physics **79**, 116401 (2016).

[77] G. Wirth, M. Ölschläger, and A. Hemmerich, "Evidence for orbital superfluidity in the P-band of a bipartite optical square lattice", Nature Physics **7**, 147–153 (2011).

[78] M. Ölschläger, G. Wirth, and A. Hemmerich, "Unconventional superfluid order in the F band of a bipartite optical square lattice", Physical Review Letters **106**, 7–10 (2011).

[79] T. Kock, C. Hippler, A. Ewerbeck, and A. Hemmerich, "Orbital optical lattices with bosons", Journal of Physics B: Atomic, Molecular and Optical Physics **49**, 042001 (2016).

[80] M. Hachmann, Y. Kiefer, J. Riebesehl, R. Eichberger, and A. Hemmerich, "Quantum Degenerate Fermi Gas in an Orbital Optical Lattice", Physical Review Letters **127**, 033201 (2021).

[81] M. Nuske, J. Vargas, M. Hachmann, R. Eichberger, L. Mathey, and A. Hemmerich, "Metastable order protected by destructive many-body interference", Physical Review Research **2**, 043210 (2020).

[82] S. Jin, W. Zhang, X. Guo, X. Chen, X. Zhou, and X. Li, "Evidence of Potts-Nematic Superfluidity in a Hexagonal sp^2 Optical Lattice", Physical Review Letters **126**, 035301 (2021).

[83] X.-Q. Wang, G.-Q. Luo, J.-Y. Liu, W. V. Liu, A. Hemmerich, and Z.-F. Xu, "Evidence for an atomic chiral superfluid with topological excitations", Nature **596**, 227–231 (2021).

[84] M. V. Berry, "Quantal phase factors accompanying adiabatic changes", Proceedings of the Royal Society of London. A. Mathematical and Physical Sciences **392**, 45–57 (1984).

[85] D. J. Thouless, "Quantization of particle transport", Physical Review B **27**, 6083–6087 (1983).

[86] M. Lohse, C. Schweizer, O. Zilberberg, M. Aidelsburger, and I. Bloch, "A Thouless quantum pump with ultracold bosonic atoms in an optical superlattice", Nature Physics **12**, 350–354 (2016).

[87] S. Nakajima, T. Tomita, S. Taie, T. Ichinose, H. Ozawa, L. Wang, M. Troyer, and Y. Takahashi, "Topological Thouless pumping of ultracold fermions", Nature Physics **12**, 296–300 (2016).

[88] D. Xiao, M.-C. Chang, and Q. Niu, "Berry phase effects on electronic properties", Reviews of Modern Physics **82**, 1959–2007 (2010).

[89] G. Sundaram and Q. Niu, "Wave-packet dynamics in slowly perturbed crystals: Gradient corrections and Berry-phase effects", Physical Review B **59**, 14915–14925 (1999).

[90] M.-C. Chang and Q. Niu, "Berry phase, hyperorbits, and the Hofstadter spectrum: Semiclassical dynamics in magnetic Bloch bands", Physical Review B **53**, 7010–7023 (1996).

[91] D. J. Thouless, M. Kohmoto, M. P. Nightingale, and M. den Nijs, "Quantized Hall Conductance in a Two-Dimensional Periodic Potential", Physical Review Letters **49**, 405–408 (1982).

[92] N. R. Cooper, J. Dalibard, and I. B. Spielman, "Topological bands for ultracold atoms", Reviews of Modern Physics **91**, 015005 (2019).

[93] L. Duca, T. Li, M. Reitter, I. Bloch, M. Schleier-Smith, and U. Schneider, "An Aharonov-Bohm interferometer for determining Bloch band topology", Science **347**, 288–292 (2015).

[94] N. Fläschner, B. S. Rem, M. Tarnowski, D. Vogel, D.-S. Lühmann, K. Sengstock, and C. Weitenberg, "Experimental reconstruction of the Berry curvature in a Floquet Bloch band", Science **352**, 1091–1094 (2016).

[95] T. Li, L. Duca, M. Reitter, F. Grusdt, E. Demler, M. Endres, M. Schleier-Smith, I. Bloch, and U. Schneider, "Bloch state tomography using Wilson lines", Science **352**, 1094–1097 (2016).

[96] D. Xiao, W. Yao, and Q. Niu, "Valley-contrasting physics in graphene: Magnetic moment and topological transport", Physical Review Letters **99**, 1–4 (2007).

[97] W. Yao, D. Xiao, and Q. Niu, "Valley-dependent optoelectronics from inversion symmetry breaking", Physical Review B **77**, 235406 (2008).

[98] H. Schmaljohann, "Spindynamik in Dissertation", PhD Thesis (Universität Hamburg, 2004).

[99] M. Erhard, "Experimente mit mehrkomponentigen Bose-Einstein-Kondensaten", PhD Thesis (Universität Hamburg, 2004).

[100] J. Kronjäger, "Coherent dynamics of spinor Bose-Einstein condensates", PhD Thesis (Universität Hamburg, 2007).

[101] C. Becker, "Multi component Bose-Einstein Condensates: From mean field physics to strong correlations", PhD Thesis (Universität Hamburg, 2008).

[102] P. Soltan-Panahi, "Multi-component quantum gases in spin-dependent hexagonal lattices", PhD Thesis (Universität Hamburg, 2010).

[103] J. Struck, "Artificial Gauge Fields in Driven Optical Lattices From Frustrated XY Models to Ising Ferromagnetism", PhD Thesis (Universität Hamburg, 2013).

[104] M. Weinberg, "Band Structure Engineering for Ultracold Quantum Gases in Optical Lattices", PhD Thesis (Universität Hamburg, 2014).

[105] C. Ölschläger, "Floquet Engineering of Bloch Bands in Shaken Optical Lattices", PhD Thesis (Universität Hamburg, 2016).

[106] J. Seeger, *Bose-Einstein-Kondensate in höheren Bändern des hexagonalen Gitters* (Springer Fachmedien Wiesbaden, Wiesbaden, 2022).

[107] T. Klafka, "Bose-Einstein condensation in higher Bloch bands of the optical honeycomb lattice", PhD Thesis (Universität Hamburg, 2021).

[108] C. D'Errico, M. Zaccanti, M. Fattori, G. Roati, M. Inguscio, G. Modugno, and A. Simoni, "Feshbach resonances in ultracold 39K", New Journal of Physics **9**, 223–223 (2007).

[109] A. Marte, T. Volz, J. Schuster, S. Dürr, G. Rempe, E. G. M. van Kempen, and B. J. Verhaar, "Feshbach Resonances in Rubidium 87: Precision Measurement and Analysis", Physical Review Letters **89**, 283202 (2002).

[110]D. Vogel, "Measuring Geometry and Topology of Floquet-Bloch States in and out of Equilibrium with ultracold fermions", PhD Thesis (Universität Hamburg, 2018).

[111]C. Ölschläger, "Quantensimulation von frustriertem Magnetismus in einem optischen Dreiecksgitter", Diploma Thesis (Universität Hamburg, 2011).

[112]A. Kerkmann, "A novel Apparatus for Quantum Gas Microscopy of Lithium Atoms", PhD Thesis (Universität Hamburg, 2019).

[113]R. Dinter, "Aufbau und Charakterisierung einer Magnetfalle zur simultanen Speicherung von K und Rb", Diploma Thesis (Universität Hamburg, 2004).

[114]S. Rosi, A. Burchianti, S. Conclave, D. S. Naik, G. Roati, C. Fort, and F. Minardi, "Λ-enhanced grey molasses on the D2 transition of Rubidium-87 atoms", Scientific Reports **8**, 1301 (2018).

[115]R. S. Conrad, "Graue Melasse für ultrakaltes Rubidium", Bachelor Thesis (Universität Hamburg, 2020).

[116]P. Groß, "Design of a Hybrid Trap for Ultracold Rubidium", Master Thesis (Universität Hamburg, 2020).

[117]A. T. Grier, I. Ferrier-Barbut, B. S. Rem, M. Delehaye, L. Khaykovich, F. Chevy, and C. Salomon, "Λ-enhanced sub-Doppler cooling of lithium atoms in D1 gray molasses", Physical Review A **87**, 063411 (2013).

[118]F. Sievers, N. Kretzschmar, D. R. Fernandes, D. Suchet, M. Rabinovic, S. Wu, C. V. Parker, L. Khaykovich, C. Salomon, and F. Chevy, "Simultaneous sub-Doppler laser cooling of fermionic 6Li and 40K on the D1 line: Theory and experiment", Physical Review A **91**, 023426 (2015).

[119]J. Dalibard and C. Cohen-Tannoudji, "Laser cooling below the Doppler limit by polarization gradients: simple theoretical models", Journal of the Optical Society of America B **6**, 2023 (1989).

[120]G. Grynberg and J.-Y. Courtois, "Proposal for a Magneto-Optical Lattice for Trapping Atoms in Nearly-Dark States", Europhysics Letters (EPL) **27**, 41–46 (1994).

[121]M. Weidemüller, T. Esslinger, M. A. Ol'shanii, A. Hemmerich, and T. W. Hänsch, "A Novel Scheme for Efficient Cooling below the Photon Recoil Limit", Europhysics Letters (EPL) **27**, 109–114 (1994).

[122]D. Boiron, C. Triché, D. R. Meacher, P. Verkerk, and G. Grynberg, "Three-dimensional cooling of cesium atoms in four-beam gray optical molasses", Physical Review A **52**, R3425–R3428 (1995).

[123]T. Esslinger, H. Ritsch, M. Weidemüller, F. Sander, A. Hemmerich, and T. W. Hänsch, "Purely optical dark lattice", Optics Letters **21**, 991 (1996).

[124]M. Kottke, "Magnetfallen und Signaturen der Eindimensionalität für Bose-Einstein-Kondesate", PhD Thesis (Universität Hannover, 2004).

[125]A. Bick, "Interfacing Ultracold Atoms and a Cryogenic Micromechanical Oscillator", PhD Thesis (Universität Hamburg, 2015).

[126]D. E. Pritchard, "Cooling Neutral Atoms in a Magnetic Trap for Precision Spectroscopy", Physical Review Letters **51**, 1336–1339 (1983).

[127]T. P. Meyrath, *Electromagnet Design Basics for Cold Atom Experiments*, tech. rep. (2001).

[128]W. H. Wing, "On neutral particle trapping in quasistatic electromagnetic fields", Progress in Quantum Electronics **8**, 181–199 (1984).

[129]C. Ospelkaus, "Fermi-Bose mixtures — From mean-field interactions to ultracold chemistry", PhD Thesis (Universität Hamburg, 2006).

[130]W. Ketterle, D. S. Durfee, and D. M. Stamper-Kurn, "Making, probing and understanding Bose-Einstein condensates", (1999).

[131]S. E. Dörscher, "Creation of ytterbium quantum gases with a compact 2D-/3D-MOT setup", PhD Thesis (Universität Hamburg, 2013).

[132]N. L. Manakov, V. D. Ovsiannikov, and L. P. Rapoport, "Atoms in a laser field", Physics Reports **141**, 320–433 (1986).

[133]W. Happer and B. S. Mathur, "Effective Operator Formalism in Optical Pumping", Physical Review **163**, 12–25 (1967).

[134]B. S. Mathur, H. Tang, and W. Happer, "Light Shifts in the Alkali Atoms", Physical Review **171**, 11–19 (1968).

[135]F. Le Kien, P. Schneeweiss, and A. Rauschenbeutel, "Dynamical polarizability of atoms in arbitrary light fields: general theory and application to cesium", The European Physical Journal D **67**, 92 (2013).

[136]I. H. Deutsch and P. S. Jessen, "Quantum control and measurement of atomic spins in polarization spectroscopy", Optics Communications **283**, 681–694 (2010).

[137]C. Cohen-Tannoudji and D. Guéry-Odelin, *Advances in Atomic Physics* (World Scientific, Sept. 2011).

[138]R. W. Boyd, *Nonlinear Optics*, 4th ed. (Elsevier, 2020).

[139]R. Grimm, M. Weidemüller, and Y. B. Ovchinnikov, "Optical Dipole Traps for Neutral Atoms", in *Advances in atomic, molecular, and optical physics* (2000), pp. 95–170.

[140]D. A. Steck, *Quantum and Atom Optics* (2007), revision 0.13.4, 24 September 2020.

[141]C. Cohen-Tannoudji and J. Dupont-Roc, "Experimental Study of Zeeman Light Shifts in Weak Magnetic Fields", Physical Review A **5**, 968–984 (1972).

[142]M. Rosatzin, D. Suter, and J. Mlynek, "Light-shift-induced spin echoes in a J =1/2 atomic ground state", Physical Review A **42**, 1839–1841 (1990).

[143]M. Zielonkowski, J. Steiger, U. Schünemann, M. DeKieviet, and R. Grimm, "Optically induced spin precession and echo in an atomic beam", Physical Review A **58**, 3993–3998 (1998).

[144]J. Kobayashi, K. Shibata, T. Aoki, M. Kumakura, and Y. Takahashi, "Fictitious magnetic resonance by quasielectrostatic field", Applied Physics B **95**, 361–365 (2009).

[145]V. V. Flambaum, V. A. Dzuba, and A. Derevianko, "Magic Frequencies for Cesium Primary-Frequency Standard", Physical Review Letters **101**, 220801 (2008).

[146] A. Derevianko and H. Katori, "Colloquium : Physics of optical lattice clocks", Reviews of Modern Physics **83**, 331–347 (2011).

[147] Q.-Q. Hu, C. Freier, Y. Sun, B. Leykauf, V. Schkolnik, J. Yang, M. Krutzik, and A. Peters, "Observation of vector and tensor light shifts in Rb87 using near-resonant, stimulated Raman spectroscopy", Physical Review A **97**, 013424 (2018).

[148] I. Bloch, J. Dalibard, and W. Zwerger, "Many-body physics with ultracold gases", Reviews of Modern Physics **80**, 885–964 (2008).

[149] G. Reinaudi, T. Lahaye, Z. Wang, and D. Guéry-Odelin, "Strong saturation absorption imaging of dense clouds of ultracold atoms", Optics Letters **32**, 3143 (2007).

[150] W. J. Kwon, J.-y. Choi, and Y.-i. Shin, "Calibration of saturation absorption imaging of ultracold atom clouds", Journal of the Korean Physical Society **61**, 1970–1974 (2012).

[151] K. Hueck, N. Luick, L. Sobirey, J. Siegl, T. Lompe, H. Moritz, L. W. Clark, and C. Chin, "Calibrating high intensity absorption imaging of ultracold atoms", Optics Express **25**, 8670 (2017).

[152] I. Sobel'Man, *Introduction to the Theory of Atomic Spectra* (Pergamon Press, 1972).

[153] N. V. Vitanov, T. Halfmann, B. W. Shore, and K. Bergmann, "Laser-induced population transfer by adiabatic passage techniques", Annual Review of Physical Chemistry **52**, 763–809 (2001).

[154] M. P. A. Fisher, P. B. Weichman, G. Grinstein, and D. S. Fisher, "Boson localization and the superfluid-insulator transition", Physical Review B **40**, 546–570 (1989).

[155] M. Greiner, O. Mandel, T. Esslinger, T. W. Hänsch, and I. Bloch, "Quantum phase transition from a superfluid to a Mott insulator in a gas of ultracold atoms", Nature **415**, 39–44 (2002).

[156] L. Pitaevskii and S. Stringari, *Bose-Einstein Condensation and Superfluidity* (Oxford University Press, Jan. 2016).

[157] C. J. Pethick and H. Smith, *Bose-Einstein Condensation in Dilute Gases* (Cambridge University Press, Cambridge, Dec. 2008).

[158] E. Zaremba, T. Nikuni, and A. Griffin, "Dynamics of Trapped Bose Gases at Finite Temperatures", Journal of Low Temperature Physics **116**, 277–345 (1999).

[159] A. Griffin, T. Nikuni, and E. Zaremba, *Bose-Condensed Gases at Finite Temperatures* (Cambridge University Press, Cambridge, 2009).

[160] A. Griffin, "Conserving and gapless approximations for an inhomogeneous Bose gas at finite temperatures", Physical Review B **53**, 9341–9347 (1996).

[161] D. Baillie and P. B. Blakie, "Finite-temperature theory of superfluid bosons in optical lattices", Physical Review A - Atomic, Molecular, and Optical Physics **80**, 1–19 (2009).

[162] M. Born and R. Oppenheimer, "Zur Quantentheorie der Molekeln", Annalen der Physik **389**, 457–484 (1927).

[163] A. Bohm, A. Mostafazadeh, H. Koizumi, Q. Niu, and J. Zwanziger, *The Geometric Phase in Quantum Systems* (Springer Berlin Heidelberg, Berlin, Heidelberg, 2003).

[164]M. Nakahara, *Differentialgeometrie, Topologie und Physik* (Springer Berlin Heidelberg, Berlin, Heidelberg, Oct. 2015).

[165]G. Grynberg and C. Robilliard, "Cold atoms in dissipative optical lattices", Physics Reports **355**, 335–451 (2001).

[166]M. Cheneau, S. P. Rath, T. Yefsah, K. J. Günter, G. Juzeliūnas, and J. Dalibard, "Geometric potentials in quantum optics: A semi-classical interpretation", EPL (Europhysics Letters) **83**, 60001 (2008).

[167]M. Aidelsburger, S. Nascimbene, and N. Goldman, "Artificial gauge fields in materials and engineered systems", Comptes Rendus Physique **19**, 394–432 (2018).

[168]C. A. Mead and D. G. Truhlar, "On the determination of Born–Oppenheimer nuclear motion wave functions including complications due to conical intersections and identical nuclei", The Journal of Chemical Physics **70**, 2284–2296 (1979).

[169]A. Eckardt and E. Anisimovas, "High-frequency approximation for periodically driven quantum systems from a Floquet-space perspective", New Journal of Physics **17**, 093039 (2015).

[170]N. Goldman and J. Dalibard, "Periodically Driven Quantum Systems: Effective Hamiltonians and Engineered Gauge Fields", Physical Review X **4**, 031027 (2014).

[171]A. Eckardt, P. Hauke, P. Soltan-Panahi, C. Becker, K. Sengstock, and M. Lewenstein, "Frustrated quantum antiferromagnetism with ultracold bosons in a triangular lattice", EPL (Europhysics Letters) **89**, 10010 (2010).

[172]J. Struck, C. Ölschläger, M. Weinberg, P. Hauke, J. Simonet, A. Eckardt, M. Lewenstein, K. Sengstock, and P. Windpassinger, "Tunable Gauge Potential for Neutral and Spinless Particles in Driven Optical Lattices", Physical Review Letters **108**, 225304 (2012).

[173]P. Hauke, O. Tieleman, A. Celi, C. Ölschläger, J. Simonet, J. Struck, M. Weinberg, P. Windpassinger, K. Sengstock, M. Lewenstein, and A. Eckardt, "Non-Abelian Gauge Fields and Topological Insulators in Shaken Optical Lattices", Physical Review Letters **109**, 145301 (2012).

[174]E. Arimondo, D. Ciampini, A. Eckardt, M. Holthaus, and O. Morsch, "Kilohertz-Driven Bose–Einstein Condensates in Optical Lattices", in *Advances in atomic, molecular and optical physics*, Vol. 61 (Academic Press, July 2012).

[175]J. Sólyom, *Fundamentals of the Physics of Solids. Volume 1: Structure and Dynamics* (Springer, Berlin, Heidelberg, 2007).

[176]M. Z. Hasan and C. L. Kane, "Colloquium: Topological insulators", Reviews of Modern Physics **82**, 3045–3067 (2010).

[177]M. König, S. Wiedmann, C. Brüne, A. Roth, H. Buhmann, L. W. Molenkamp, X.-L. Qi, and S.-C. Zhang, "Quantum Spin Hall Insulator State in HgTe Quantum Wells", Science **318**, 766–770 (2007).

[178]D. Hsieh, D. Qian, L. Wray, Y. Xia, Y. S. Hor, R. J. Cava, and M. Z. Hasan, "A topological Dirac insulator in a quantum spin Hall phase", Nature **452**, 970–974 (2008).

[179] A. Roth, C. Brüne, H. Buhmann, L. W. Molenkamp, J. Maciejko, X.-L. Qi, and S.-C. Zhang, "Nonlocal Transport in the Quantum Spin Hall State", Science **325**, 294–297 (2009).

[180] A. Alase, E. Cobanera, G. Ortiz, and L. Viola, "Generalization of Bloch's theorem for arbitrary boundary conditions: Theory", Physical Review B **96**, 195133 (2017).

[181] R. E. Peierls, *Quantum Theory of Solids* (Oxford University Press, Feb. 2001).

[182] C. Kittel, *Introduction to solid state physics*, 8th ed. (John Wiley & Sons, New York, 2004).

[183] P. R. Wallace, "The Band Theory of Graphite", Physical Review **71**, 622–634 (1947).

[184] A. H. Castro Neto, F. Guinea, N. M. R. Peres, K. S. Novoselov, and A. K. Geim, "The electronic properties of graphene", Reviews of Modern Physics **81**, 109–162 (2009).

[185] M. Weinberg, C. Staarmann, C. Ölschläger, J. Simonet, and K. Sengstock, "Breaking inversion symmetry in a state-dependent honeycomb lattice: artificial graphene with tunable band gap", 2D Materials **3**, 024005 (2016).

[186] Y. Hasegawa, R. Konno, H. Nakano, and M. Kohmoto, "Zero modes of tight-binding electrons on the honeycomb lattice", Physical Review B **74**, 033413 (2006).

[187] S.-L. Zhu, B. Wang, and L.-M. Duan, "Simulation and Detection of Dirac Fermions with Cold Atoms in an Optical Lattice", Physical Review Letters **98**, 260402 (2007).

[188] B. Wunsch, F. Guinea, and F. Sols, "Dirac-point engineering and topological phase transitions in honeycomb optical lattices", New Journal of Physics **10**, 103027 (2008).

[189] G. Montambaux, F. Piéchon, J.-N. Fuchs, and M. O. Goerbig, "Merging of Dirac points in a two-dimensional crystal", Physical Review B **80**, 153412 (2009).

[190] L. Tarruell, D. Greif, T. Uehlinger, G. Jotzu, and T. Esslinger, "Creating, moving and merging Dirac points with a Fermi gas in a tunable honeycomb lattice", Nature **483**, 302–305 (2012).

[191] K. Kishigi, H. Hanada, and Y. Hasegawa, "Energy Gap and Averaged Inversion Symmetry of Tight-Binding Electrons on Generalized Honeycomb Lattice", Journal of the Physical Society of Japan **77**, 074707 (2008).

[192] K. Kishigi, R. Takeda, and Y. Hasegawa, "Energy gap of tight-binding electrons on generalized honeycomb lattice", Journal of Physics: Conference Series **132**, 012005 (2008).

[193] J.-M. Hou and W. Chen, "Hidden symmetry and protection of Dirac points on the honeycomb lattice", Scientific Reports **5**, 17571 (2015).

[194] G. van Miert and C. M. Smith, "Dirac cones beyond the honeycomb lattice: A symmetry-based approach", Physical Review B **93**, 035401 (2016).

[195] C. Fefferman and M. Weinstein, "Honeycomb lattice potentials and Dirac points", Journal of the American Mathematical Society **25**, 1169–1220 (2012).

[196] F. Schwabl, *Advanced Quantum Mechanics*, 4th ed. (Springer Berlin Heidelberg, Berlin, Heidelberg, 2008).

[197]F. Gerbier, S. Trotzky, S. Fölling, U. Schnorrberger, J. D. Thompson, A. Widera, I. Bloch, L. Pollet, M. Troyer, B. Capogrosso-Sansone, N. V. Prokof'ev, and B. V. Svistunov, "Expansion of a quantum gas released from an optical lattice", Physical Review Letters **101**, 1–4 (2008).

[198]S. S. Natu, D. C. McKay, B. DeMarco, and E. J. Mueller, "Evolution of condensate fraction during rapid lattice ramps", Physical Review A **85**, 061601 (2012).

[199]D. Dürr, S. Goldstein, J. Taylor, R. Tumulka, and N. Zanghì, "Quantum mechanics in multiply-connected spaces", Journal of Physics A: Mathematical and Theoretical **40**, 2997–3031 (2007).

[200]W. Yi, G. D. Lin, and L. M. Duan, "Signal of Bose-Einstein condensation in an optical lattice at finite temperature", Physical Review A - Atomic, Molecular, and Optical Physics **76**, 1–4 (2007).

[201]R. B. Diener, Q. Zhou, H. Zhai, and T. L. Ho, "Criterion for bosonic superfluidity in an optical lattice", Physical Review Letters **98**, 4–7 (2007).

[202]Y. Kato, Q. Zhou, N. Kawashima, and N. Trivedi, "Sharp peaks in the momentum distribution of bosons in optical lattices in the normal state", Nature Physics **4**, 617–621 (2008).

[203]G.-D. Lin, W. Zhang, and L.-M. Duan, "Characteristics of Bose-Einstein condensation in an optical lattice", Physical Review A **77**, 043626 (2008).

[204]I. Spielman, W. Phillips, and J. Porto, "Condensate Fraction in a 2D Bose Gas Measured across the Mott-Insulator Transition", Physical Review Letters **100**, 120402 (2008).

[205]S. Trotzky, L. Pollet, F. Gerbier, U. Schnorrberger, I. Bloch, N. V. Prokof'ev, B. Svistunov, and M. Troyer, "Suppression of the critical temperature for superfluidity near the Mott transition", Nature Physics **6**, 998–1004 (2010).

[206]M. Cristiani, O. Morsch, J. H. Müller, D. Ciampini, and E. Arimondo, "Experimental properties of Bose-Einstein condensates in one-dimensional optical lattices: Bloch oscillations, Landau-Zener tunneling, and mean-field effects", Physical Review A **65**, 063612 (2002).

[207]O. Morsch and M. Oberthaler, "Dynamics of Bose-Einstein condensates in optical lattices", Reviews of Modern Physics **78**, 179–215 (2006).

[208]Y. B. Ovchinnikov, J. H. Müller, M. R. Doery, E. J. D. Vredenbregt, K. Helmerson, S. L. Rolston, and W. D. Phillips, "Diffraction of a Released Bose-Einstein Condensate by a Pulsed Standing Light Wave", Physical Review Letters **83**, 284–287 (1999).

[209]B. Gadway, D. Pertot, R. Reimann, M. G. Cohen, and D. Schneble, "Analysis of Kapitza-Dirac diffraction patterns beyond the Raman-Nath regime", Optics Express **17**, 19173 (2009).

[210]T. Zhou, K. Yang, Y. Zhai, X. Yue, S. Yang, J. Xiang, Q. Huang, W. Xiong, X. Zhou, and X. Chen, "High precision calibration of optical lattice depth based on multiple pulses Kapitza-Dirac diffraction", Optics Express **26**, 16726 (2018).

[211]A. Zenesini, D. Ciampini, O. Morsch, and E. Arimondo, "Observation of Stückelberg oscillations in accelerated optical lattices", Physical Review A **82**, 065601 (2010).

[212]S. Kling, T. Salger, C. Grossert, and M. Weitz, "Atomic Bloch-Zener Oscillations and Stückelberg Interferometry in Optical Lattices", Physical Review Letters **105**, 215301 (2010).

[213]C. Cabrera-Gutiérrez, E. Michon, V. Brunaud, T. Kawalec, A. Fortun, M. Arnal, J. Billy, and D. Guéry-Odelin, "Robust calibration of an optical-lattice depth based on a phase shift", Physical Review A **97**, 043617 (2018).

[214]R. Jáuregui, N. Poli, G. Roati, and G. Modugno, "Anharmonic parametric excitation in optical lattices", Physical Review A **64**, 033403 (2001).

[215]N. Fläschner, M. Tarnowski, B. S. Rem, D. Vogel, K. Sengstock, and C. Weitenberg, "High-precision multiband spectroscopy of ultracold fermions in a nonseparable optical lattice", Physical Review A **97**, 051601 (2018).

[216]S. Friebel, C. D'Andrea, J. Walz, M. Weitz, and T. W. Hänsch, "CO_2-laser optical lattice with cold rubidium atoms", Physical Review A **57**, R20–R23 (1998).

[217]A. M. Dudarev, R. B. Diener, I. Carusotto, and Q. Niu, "Spin-Orbit Coupling and Berry Phase with Ultracold Atoms in 2D Optical Lattices", Physical Review Letters **92**, 153005 (2004).

[218]A. Isacsson and S. M. Girvin, "Multiflavor bosonic Hubbard models in the first excited Bloch band of an optical lattice", Physical Review A - Atomic, Molecular, and Optical Physics **72**, 1–25 (2005).

[219]C. Wu, D. Bergman, L. Balents, and S. Das Sarma, "Flat bands and wigner crystallization in the honeycomb optical lattice", Physical Review Letters **99**, 1–4 (2007).

[220]C. Xu and M. P. A. Fisher, "Bond algebraic liquid phase in strongly correlated multiflavor cold atom systems", Physical Review B **75**, 104428 (2007).

[221]A. Collin, J. Larson, and J. P. Martikainen, "Quantum states of p-band bosons in optical lattices", Physical Review A - Atomic, Molecular, and Optical Physics **81**, `10.1103/PhysRevA.81.023605` (2010).

[222]F. Hébert, Z. Cai, V. G. Rousseau, C. Wu, R. T. Scalettar, and G. G. Batrouni, "Exotic phases of interacting p-band bosons", Physical Review B **87**, 224505 (2013).

[223]E. Zhao and W. V. Liu, "Orbital Order in Mott Insulators of Spinless p-Band Fermions", Physical Review Letters **100**, 160403 (2008).

[224]C. Wu, "Orbital Ordering and Frustration of p-Band Mott Insulators", Physical Review Letters **100**, 200406 (2008).

[225]P. Hauke, E. Zhao, K. Goyal, I. H. Deutsch, W. V. Liu, and M. Lewenstein, "Orbital order of spinless fermions near an optical Feshbach resonance", Physical Review A **84**, 051603 (2011).

[226]C. Wu, "Orbital analogue of the quantum anomalous hall effect in p-band systems", Physical Review Letters **101**, 1–4 (2008).

[227]K. Sun, H. Yao, E. Fradkin, and S. A. Kivelson, "Topological insulators and nematic phases from spontaneous symmetry breaking in 2D fermi systems with a quadratic band crossing", Physical Review Letters **103**, 1–4 (2009).

[228]K. Sun, W. V. Liu, A. Hemmerich, and S. Das Sarma, "Topological semimetal in a fermionic optical lattice", Nature Physics **8**, 67–70 (2012).

[229]G.-B. Zhu, Q. Sun, H.-M. Yang, L.-L. Wang, W.-M. Liu, and A.-C. Ji, "Interaction-driven topological phase transition in a p-orbital honeycomb optical lattice", Physical Review A **100**, 043608 (2019).

[230]M. Imada, A. Fujimori, and Y. Tokura, "Metal-insulator transitions", Reviews of Modern Physics **70**, 1039–1263 (1998).

[231]F. Pinheiro, G. M. Bruun, J.-P. Martikainen, and J. Larson, "XYZ Quantum Heisenberg Models with p-Orbital Bosons", Physical Review Letters **111**, 205302 (2013).

[232]P. Saugmann and J. Larson, "Magnetic phases of orbital bipartite optical lattices", New Journal of Physics **22**, 023023 (2020).

[233]P. Noziéres, "Some comments on Bose-Einstein condensation", in *Bose-Einstein condensation*, edited by A. Griffin, D. W. Snoke, and S. Stringari (Cambridge University Press, 1995), pp. 15–30.

[234]D. S. Rokhsar, "Phase coherence and "fragmented" Bose condensates", (1998).

[235]E. J. Mueller, T.-L. Ho, M. Ueda, and G. Baym, "Fragmentation of Bose-Einstein condensates", Physical Review A **74**, 033612 (2006).

[236]T. Müller, S. Fölling, A. Widera, and I. Bloch, "State Preparation and Dynamics of Ultracold Atoms in Higher Lattice Orbitals", Physical Review Letters **99**, 200405 (2007).

[237]T. Kock, M. Ölschläger, A. Ewerbeck, W.-M. Huang, L. Mathey, and A. Hemmerich, "Observing Chiral Superfluid Order by Matter-Wave Interference", Physical Review Letters **114**, 115301 (2015).

[238]M. Holthaus, "Bloch oscillations and Zener breakdown in an optical lattice", Journal of Optics B: Quantum and Semiclassical Optics **2**, 589–604 (2000).

[239]E. Altman and A. Auerbach, "Oscillating Superfluidity of Bosons in Optical Lattices", Physical Review Letters **89**, 250404 (2002).

[240]A. Polkovnikov, S. Sachdev, and S. M. Girvin, "Nonequilibrium Gross-Pitaevskii dynamics of boson lattice models", Physical Review A **66**, 053607 (2002).

[241]A. K. Tuchman, C. Orzel, A. Polkovnikov, and M. A. Kasevich, "Nonequilibrium coherence dynamics of a soft boson lattice", Physical Review A **74**, 051601 (2006).

[242]V. Sharma, S. Choudhury, and E. J. Mueller, "Dynamics of Bose-Einstein recondensation in higher bands", Physical Review A **101**, 033609 (2020).

[243]J. Eisert, M. Friesdorf, and C. Gogolin, "Quantum many-body systems out of equilibrium", Nature Physics **11**, 124–130 (2015).

[244]T. Mori, T. N. Ikeda, E. Kaminishi, and M. Ueda, "Thermalization and prethermalization in isolated quantum systems: a theoretical overview", Journal of Physics B: Atomic, Molecular and Optical Physics **51**, 112001 (2018).

[245]S. Paul and E. Tiesinga, "Formation and decay of Bose-Einstein condensates in an excited band of a double-well optical lattice", Physical Review A **88**, 033615 (2013).

[246]J.-P. Martikainen, "Dynamical instability and loss of p-band bosons in optical lattices", Physical Review A **83**, 013610 (2011).

[247]Y. Xu, Z. Chen, H. Xiong, W. V. Liu, and B. Wu, "Stability of p-orbital Bose-Einstein condensates in optical checkerboard and square lattices", Physical Review A **87**, 013635 (2013).

[248]L. Asteria, H. P. Zahn, M. N. Kosch, K. Sengstock, and C. Weitenberg, "Quantum gas magnifier for sub-lattice-resolved imaging of 3D quantum systems", Nature **599**, 571–575 (2021).

[249]N. Nagaosa, J. Sinova, S. Onoda, A. H. MacDonald, and N. P. Ong, "Anomalous Hall effect", Reviews of Modern Physics **82**, 1539–1592 (2010).

[250]J. Sinova, S. O. Valenzuela, J. Wunderlich, C. H. Back, and T. Jungwirth, "Spin Hall effects", Reviews of Modern Physics **87**, 1213–1260 (2015).

[251]M. König, H. Buhmann, L. W. Molenkamp, T. Hughes, C.-X. Liu, X.-L. Qi, and S.-C. Zhang, "The Quantum Spin Hall Effect: Theory and Experiment", Journal of the Physical Society of Japan **77**, 031007 (2008).

[252]J. Maciejko, T. L. Hughes, and S.-C. Zhang, "The Quantum Spin Hall Effect", Annual Review of Condensed Matter Physics **2**, 31–53 (2011).

[253]C.-X. Liu, S.-C. Zhang, and X.-L. Qi, "The Quantum Anomalous Hall Effect: Theory and Experiment", Annual Review of Condensed Matter Physics **7**, 301–321 (2016).

[254]X.-L. Qi and S.-C. Zhang, "Topological insulators and superconductors", Reviews of Modern Physics **83**, 1057–1110 (2011).

[255]M. Fruchart and D. Carpentier, "An introduction to topological insulators", Comptes Rendus Physique **14**, 779–815 (2013).

[256]C.-K. Chiu, J. C. Y. Teo, A. P. Schnyder, and S. Ryu, "Classification of topological quantum matter with symmetries", Reviews of Modern Physics **88**, 035005 (2016).

[257]C. B. Schmidt, S. Priyadarshi, and M. Bieler, "Sub-picosecond temporal resolution of anomalous Hall currents in GaAs", Scientific Reports **7**, 11241 (2017).

[258]H. M. Price and N. R. Cooper, "Mapping the Berry curvature from semiclassical dynamics in optical lattices", Physical Review A **85**, 033620 (2012).

[259]D. Shin, S. A. Sato, H. Hübener, U. De Giovannini, J. Kim, N. Park, and A. Rubio, "Unraveling materials Berry curvature and Chern numbers from real-time evolution of Bloch states", Proceedings of the National Academy of Sciences **116**, 4135–4140 (2019).

[260]M. Glück, "Wannier–Stark resonances in optical and semiconductor superlattices", Physics Reports **366**, 103–182 (2002).

[261]M. Holthaus, "Floquet engineering with quasienergy bands of periodically driven optical lattices", Journal of Physics B: Atomic, Molecular and Optical Physics **49**, 13001 (2015).

[262]P. Weinberg, M. Bukov, L. D'Alessio, A. Polkovnikov, S. Vajna, and M. Kolodrubetz, "Adiabatic perturbation theory and geometry of periodically-driven systems", Physics Reports **688**, 1–35 (2017).

[263]D. Culcer, Y. Yao, and Q. Niu, "Coherent wave-packet evolution in coupled bands", Physical Review B **72**, 085110 (2005).

[264]R. Shindou and K.-I. Imura, "Noncommutative geometry and non-Abelian Berry phase in the wave-packet dynamics of Bloch electrons", Nuclear Physics B **720**, 399–435 (2005).

[265]H. Koizumi and Y. Takada, "Geometric phase current in solids: Derivation in a path-integral approach", Physical Review B **65**, 153104 (2002).

Danksagung

Sofern in dieser Dissertation Raum für Persönliches bleibt, dann doch für die Menschen, die mich auf dem Weg zur Promotion unterstützend – in welcher Hinsicht auch immer – begleiten oder begleitet haben. All diesen Menschen möchte ich dafür danken, zuvorderst meinem Doktorvater Klaus Sengstock: Lieber Klaus, von Herzen vielen Dank für deine Geduld, dein Vertrauen, deinen Rat, deine offene und motivierende Art, all die unschätzbare Arbeit im „Vorder-" und „Hintergrund", mit der Du stetig die besten Bedingungen fürs Forschen schaffst. Nichts davon ist selbstverständlich, danke!

Herrn Professor Henning Moritz danke ich vielmals für die bereitwillige Übernahme des Zweitgutachtens.

Besonderen Dank möchte ich ausrichten an Dich, Juliette Simonet: Du bist eine geduldige, einfühlsame, zuversichtliche und zuvorkommende Betreuerin, eine fantastische Forscherin, ein großartiger Mensch! Danke für deine permanente Unterstützung in allen Angelegenheiten.

Lieber Tobias Klafka, auch Dir möchte ich besonders danken: für dein Verständnis, deine Zuverlässigkeit, deine Zielstrebigkeit, deine Tatkraft, deine Heiterkeit, deine Initiative und deinen Einsatz für die YAO2019, für all den Spaß abseits der Forschung, nicht zuletzt für den regen fachlichen Austausch, die kollegiale Zusammenarbeit und den Zusammenhalt. Kurzum: vielen Dank für die gemeinsame Zeit!

Liebe Julia Bergmann, danke auch an Dich. Obwohl die Zusammenarbeit am Spinor-Projekt leider viel zu kurz kam, war sie stets eine große Bereicherung. Auf deinem neuen Weg viel Glück und Erfolg! Herzlichen Dank auch an die ehemaligen Bachelor- und Master-Studierenden David Nak, Ruven Conrad, Amir Khan und Phillip Groß, die maßgeblich zum Fortschritt des Spinor-Projekts beigetragen haben.

Meinen geschätzten Kollegen und Freunden Benjamin Abeln, Tobias Kroker und Koen Sponselee danke ich vielmals für den stets willkommenen fachlichen und privaten Austausch bei unzähligen erheiternden und ermutigenden Zusammentreffen. Vor allem danke ich euch für die gelungene Organisation und Veranstaltung der YAO2019. Es war ein großes Vergnügen und eine bereichernde Erfahrung!

Ich danke Herrn Professor Peter Schmelcher, Simos Mistakidis und Georgios Koutentakis für die inspirierende Zusammenarbeit und die vielen Einblicke in die Theorie der Kondensationsdynamik. Von den zahlreichen Meetings und Diskussionen habe ich enorm profitiert. Vielen Dank!

Für die Hilfe bei allen administrativen Belangen möchte ich mich herzlich bei Ellen Gloy und Loreen Tornier bedanken. Darüber hinaus danke ich herzlichst Sylke Strien und Irmgard Flick, ohne deren tatkräftige Unterstützung die YAO2019 nicht möglich gewesen wäre. Herrn Reinhard Mielck danke ich für seine hilfsbereite Art und den unermüdlichen Einsatz an der Gebäudetechnik. Es war mir eine Freude mit all diesen Menschen sowie den vielen weiteren Mitgliedern der Gruppe Sengstock zusammenzuarbeiten.

Danksagung

Meiner Familie, meinen Freunden und Freundinnen danke ich für das Wichtigste in dieser Zeit: Liebe, Geborgenheit, Zuversicht, Lachen, Weinen, Freude. Danke für alles!